

Nonlinear Effects of Energetic Particle
Driven Instabilities in Tokamaks

Michael Brüdgam

TECHNISCHE UNIVERSITÄT MÜNCHEN

Fakultät für Physik
Max-Planck-Institut für Plasmaphysik

Nonlinear Effects of Energetic Particle Driven Instabilities in Tokamaks

Michael Brüdgam

Vollständiger Abdruck der von der Fakultät für Physik der
Technischen Universität München zur Erlangung des akademischen
Grades eines Doktors der Naturwissenschaften (Dr. rer. nat.)
genehmigten Dissertation.

Vorsitzender: Univ.-Prof. Dr. R. Gross

Prüfer der Dissertation: 1. Hon.-Prof. Dr. S. Günter
2. Univ.-Prof. Dr. K. Krischer

Die Dissertation wurde am 20.01.2010 bei der Technischen Universität
München eingereicht und durch die Fakultät für Physik am 25.03.2010
angenommen.

Contents

1. Introduction	9
2. Theoretical Background	13
2.1. MHD Model	13
2.2. Equilibrium Magnetic Field and Coordinate Systems in a Tokamak	14
2.3. Stability and MHD Modes	18
2.3.1. Continuum Spectrum	22
2.3.2. Toroidicity-induced Alfvén Eigenmodes	22
2.3.3. Beta-induced Alfvén Eigenmodes	24
2.3.4. Growth and Damping of Alfvén Eigenmodes	25
2.3.5. Neoclassical Tearing Mode	27
2.4. Fast Particles in a Tokamak	30
2.5. Heating Systems and Diagnostics at ASDEX Upgrade	36
2.5.1. Ion Cyclotron Resonance Heating	36
2.5.2. Neutral Beam Injection	38
2.5.3. Fast Ion Loss Detector	39
3. Code Development	41
3.1. Introduction to the HAGIS code	41
3.1.1. Boozer Coordinates	42
3.1.2. Wave-Particle Equations	45
3.1.3. The δf Method	49
3.2. Extension of the HAGIS Code	52
3.2.1. Vacuum Coordinates	52
3.2.2. Connection of two Equilibrium Reconstructions	58
3.2.3. Equations of Motion	61
3.2.4. Virtual Fast Ion Loss Diagnostic	64
3.2.5. ICRH-generated Fast Particle Distribution	66
3.3. Validation of Vacuum Coordinates	69
4. Simulation Results	75
4.1. Experimental Measurements	76
4.2. TAE-induced Fast Particle Losses	79
4.2.1. Initial Conditions and Mode Drive	79
4.2.2. Fast Particle Losses	90
4.3. Enhanced Fast Particle Losses due to Multiple Modes	94
4.3.1. Mode Drive and Transport Phenomena	94
4.3.2. Fast Ion Losses	104
4.3.3. Summary	107
4.4. Fast Particle Losses for ICRH-generated distributions	108

4.5. Comparison of Fast Ion Losses: Simulation vs Experiment	113
4.6. Particle Redistribution due to NTMs	122
5. Summary and Outlook	129
5.1. Summary	129
5.2. Conclusions and Further Work	130
A. Appendix	133
A.1. Useful Vector- and Tensor Transformation	133
A.2. Guiding Centre Lagrangian and Equations of Motion	133
A.3. Decomposition of the Equations of Motion in the Vacuum	139
B. Nomenclature	143
C. Acronyms	145
Bibliography	147
Publications and Conference Presentations	151
Acknowledgements	153

Abstract

In a tokamak plasma, a population of superthermal particles generated by heating methods can lead to a destabilization of various MHD modes. Due to nonlinear wave-particle interactions, a consequential fast particle redistribution reduces the plasma heating and can cause severe damages to the wall of the fusion device.

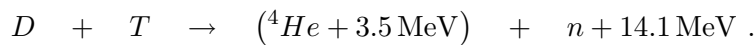
In order to describe the wave-particle interaction, the drift-kinetic perturbative HAGIS code is applied which evolves the particle trajectories and the waves nonlinearly. For a simulation speed-up, the 6-d particle phase-space is reduced by the guiding centre approach to a 5-d description. The eigenfunction of the wave is assumed to be invariant, but its amplitude and phase is altered in time. A sophisticated δf -method is employed to model the change in the fast particle distribution so that numerical noise and the excessive number of simulated Monte-Carlo points are reduced significantly. The original code can only calculate the particle redistribution inside the plasma region. Therefore, a code extension has been developed during this thesis which enlarges the simulation region up to the vessel wall.

By means of numerical simulations, this thesis addresses the problem of nonlinear wave-particle interactions in the presence of multiple MHD modes with significantly different eigenfrequencies and the corresponding fast particle transport inside the plasma. In this context, a new coupling mechanism between resonant particles and waves has been identified that leads to enhanced mode amplitudes and fast particle losses.

The extension of the code provides for the first time the possibility of a quantitative and qualitative comparison between simulation results and recent measurements in the experiment. The findings of the comparison serve as a validation of both the theoretical model and the interpretation of the experimental results. Thus, a powerful interface tool has been developed for a deeper insight of nonlinear wave-particle interaction.

1. Introduction

The controlled nuclear fusion of hydrogen isotopes provides a possibility of an energy source which is practically inexhaustible. Future fusion power plants will possess an available power of 1–3 GW as nuclear fission devices but in addition offer much higher environmental safety. In order to reach a burning plasma, among all reactions the fusion between Tritium (T) and deuterium ions (D) is most favourable,



If the plasma temperature is large enough, $T \geq 20 \text{ keV}$, the probability of the production of energetic α -particles is sufficiently increased to keep the plasma in the burning state. However, this state can only be reached if the Lawson criterion [1] is fulfilled,

$$n\tau_E > 1.5 \cdot 10^{20} \text{ m}^{-3} \text{ s}$$

where n is the D - T fuel density. The quantity τ_E is the energy confinement time which is defined as the ratio between the stored plasma energy to the heat loss rate.

The most advanced approach to achieve the required fusion parameters is the confinement of the plasma in a tokamak configuration [2] as shown in figure 1.1. The tokamak is an axisymmetric device which consists of magnetic field coils (green). These coils generate a large toroidal magnetic field. A transformer in the centre of the torus induces a toroidal current within the plasma which creates a poloidal magnetic field that is usually smaller compared to the toroidal magnetic field. Together, both magnetic fields form helical field lines. Such a configuration has the crucial advantage that it avoids open field lines in the plasma compared to linear devices and therefore has favourable plasma confinement properties.

However, auxiliary heating must be applied to the plasma before a burning state is reached. This is done by the injection of highly energetic beam ions or by launching electromagnetic waves which accelerate the plasma particles. Since energetic ions move approximately along the magnetic field lines and their orbits are closed in a tokamak, they are in principle well confined. Unfortunately, the fast particle confinement is diminished by particle transport due to turbulence [3], static perturbations like field ripples [4] or dynamical instabilities like shear Alfvén waves [5]. Due to the tokamak configuration, extended global modes [6, 7] in the frequency range of $\mathcal{O}(10 - 100 \text{ kHz})$ with phase velocities of the order of the fast particles velocity are of particular interest since they resonate with the highly energetic particles [8]. Experiments have shown that these modes are driven unstable by the fast particle distribution due to inverse Landau damping leading to significantly increased ion losses [9]. Such a particle ejection can cause severe damages to the vessel wall. Furthermore, the efficiency of the heating is reduced due to the particle redistribution.

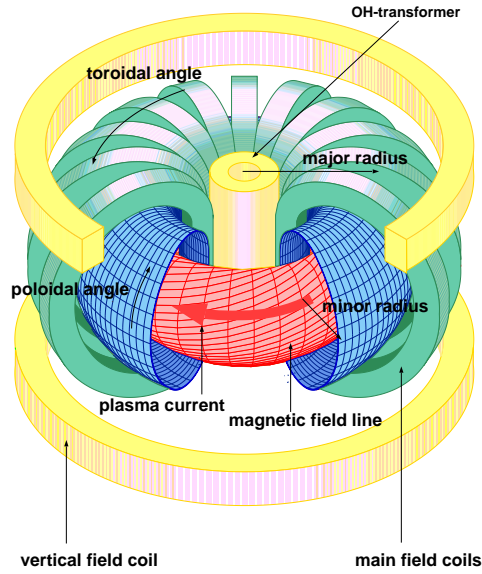


Figure 1.1.: Tokamak configuration

In this PhD thesis, resonant wave-particle interactions due to dynamical instabilities are discussed. The general shear Alfvén wave [5] describes a perpendicular plasma oscillation which propagates along the magnetic field lines with the Alfvén speed,

$$v_A = \frac{B}{\sqrt{\mu_0 \rho}}$$

where B and ρ are the magnetic field strength and the plasma mass density, respectively. Due to the high phase velocity of the order $\mathcal{O}(10^6 m/s)$, the waves only resonate with the highly energetic ions. Therefore, it is appropriate to separate the total particle population into a thermal background component which represents the bulk plasma and a smaller fraction of supra-thermal ions. The background ions are strongly magnetized and are described by the magnetohydrodynamic (MHD) approach [10]. However, the highly energetic ions are best treated by a kinetic description. The assumption of a guiding centre motion [11] neglects the rapid circular motion around the magnetic field lines. It reduces the particle trajectory to a parallel motion along the field line and a slow drift motion perpendicular to it.

Due to the fact that the trajectory of the highly energetic ions is determined by the magnetic field, a coordinate system is applied which is aligned on the field lines. Based on this coordinate system, the wave-particle interactions are calculated by the drift-kinetic, perturbative HAGIS code [12, 13]. The spatial structure of the Alfvén eigenmodes is assumed to be invariant but its amplitude and phase changes in time. Both the wave and the particle distribution are evolved nonlinearly and they interact due to inverse Landau damping. Therefore, a sophisticated Monte-Carlo method known as δf -method [14] is applied to calculate the change in the distribution function rather than the whole particle ensemble and the corresponding mode evolution. This leads to a reduction of numerical noise without using an excessive number of particles.

However, the calculation of the wave-particle interactions and the corresponding fast particle redistribution [15, 16] is limited to the plasma region in the original HAGIS code. For this reason, this PhD thesis deals with the extension of the HAGIS code into the region between the plasma and the vessel wall. This provides the possibility to simulate fast particle losses up to the wall. Due to a large proposed α -particle population in future fusion devices like ITER and DEMO, this is of enhanced importance. Therefore, energetic particle losses are compared to experimental measurements [17] by the fast ion loss diagnostic FILD [18] installed at ASDEX Upgrade [19]. The fundamental connection between numerical predictions and experimental results allows the elucidation of physical mechanisms and a validation of theoretical assumptions. Beside the comparison of fast ions losses to the experiment, this thesis addresses the questions of various coupling mechanisms between modes and the collective fast particle redistribution due to multiple modes with significantly different eigenfrequencies.

This thesis is organized as follows: In chapter 2, the physical background is presented by introducing the equilibrium magnetic field representation with the problem-adapted coordinate system, the MHD model as well as the fast ion generation with the corresponding particle motion. At the beginning of chapter 3, the implementation of the model in the original HAGIS code is summarized shortly. Based on this, the code extension is described in detail. In chapter 4, the experimental measurements are presented briefly. They constitute the basis for extensive numerical simulations investigating the fast particle losses due to nonlinear wave-particle interactions. In this context, coupling mechanisms between eigenmodes and different fast particle distributions are examined. Afterwards, the results are compared to the experiment. In chapter 5, a summary is given and conclusions with indications for future work are drawn.

2. Theoretical Background

In order to investigate the complex, physical problem of resonant wave-particle interaction, it is favourable to first introduce the models used in the following. Due to its relative simplicity, the MHD approach provides the possibility to treat the plasma as a continuous medium. The corresponding equations describe the plasma behaviour which can easily be separated into equilibrium and a perturbative part. A coordinate system is applied to the equilibrium which represents the magnetic field configuration adequately and simplifies the description of the perturbation significantly. In the presence of the equilibrium, the behaviour of the energetic ions due to given forces is evolved by the equations of motion. These equations are derived from a kinetic approach known as guiding centre motion. Both models allow for the calculation of the wave-particle interaction which is influenced by the initialization of the fast particle distribution in the plasma.

Therefore, the outline of this chapter is as follows: after the introduction of the MHD model [10], the representation of the equilibrium field and the problem-adapted coordinate system [20] is shown. Afterwards, the perturbations which are relevant in the following are presented with their features in the plasma. At the end, the equations of motion for the energetic ions and the particle properties are briefly outlined following the description of Pinches [12] in the broadest sense. With respect to the energetic ions, a particular interest is also directed on their generation of the fast particle population in the plasma due to various heating methods. Therefore, the properties of the fast particle distributions are presented.

2.1. MHD Model

By taking the velocity moments of the kinetic equations for the ion and electron distribution function, a moment approach is used which describes the plasma behaviour adequately. It reduces the kinetic equations to a single fluid model but still consists of the main physical conservation laws. This is known as the magnetohydrodynamic (MHD) approach [10]. Together with Maxwell's equations, the ideal MHD equations allow for the analysis of the plasma confinement in a complex magnetic configuration,

$$\frac{\partial \rho}{\partial t} + \nabla \cdot (\rho \mathbf{v}) = 0 \quad (\text{Mass continuity}) \quad (2.1a)$$

$$\rho \frac{\partial \mathbf{v}}{\partial t} + \rho \mathbf{v} \cdot \nabla \mathbf{v} + \nabla p - \mathbf{j} \times \mathbf{B} = 0 \quad (\text{Momentum balance}) \quad (2.1b)$$

$$\frac{\partial p}{\partial t} + \mathbf{v} \cdot \nabla p + \gamma p \nabla \cdot \mathbf{v} = 0 \quad (\text{Adiabatic equation of state}) \quad (2.1c)$$

$$\mathbf{E} + \mathbf{v} \times \mathbf{B} = 0 \quad (\text{Ohm's law}) \quad (2.1d)$$

$$\nabla \cdot \mathbf{B} = 0 \quad (\text{Divergence-free magnetic field}) \quad (2.1e)$$

$$\nabla \times \mathbf{B} - \mu_0 \mathbf{j} = 0 \quad (\text{Ampère's law}) \quad (2.1f)$$

$$\frac{\partial \mathbf{B}}{\partial t} + \nabla \times \mathbf{E} = 0 \quad (\text{Faraday's law}) \quad (2.1g)$$

where ρ is the mass density of the plasma, \mathbf{v} is the plasma velocity, p is the plasma pressure, γ is the adiabatic index, t is the time, \mathbf{j} is the current density, μ_0 is the permeability, \mathbf{B} and \mathbf{E} are the magnetic and electric field, respectively. The MHD equations are valid under the condition that the scale lengths are greater than the Debye length. Furthermore, the plasma is treated to be quasi-neutral, i.e. $n_e = Z n_i$, and is assumed to possess an infinite plasma conductivity.

2.2. Equilibrium Magnetic Field and Coordinate Systems in a Tokamak

As described at the beginning of chapter 2, the ideal MHD equations of zeroth order describe the plasma equilibrium. In order to generate a plasma first, the magnetic field is of crucial importance. In the introduction, it has been explained how the magnetic field of the plasma is generated in a tokamak. Due to several external field coils for the plasma shaping and position, the total magnetic field is divided into a magnetic field connected to the plasma and a vacuum field as shown in figure 2.1. Whilst the helical magnetic field lines inside the plasma constitute closed surfaces (red closed lines), the vacuum field lines (red dashed lines) are open and intersect with the vessel wall. The closed and open field lines are separated by the separatrix (bold solid line). The intersection of the separatrix with itself is called the X-point.

Considering the magnetic field configuration inside the separatrix for a static equilibrium only, the closed surfaces are determined by momentum balance (Eqn. 2.1b),

$$\nabla p = \mathbf{j} \times \mathbf{B} , \quad (2.2)$$

It is obvious by dotting with both \mathbf{j} and \mathbf{B} that both vectors lie in surfaces of constant pressure. For this reason, these surfaces are usually referred to as magnetic surfaces or flux surfaces since the magnetic flux within each surface is constant.

In this case, it is appropriate to use flux coordinates which constitute a non-orthogonal, curvi-linear coordinate system. This involves the use of both a covariant and a contravariant representation. The radial coordinate ψ is chosen so that it is constant over each flux surfaces

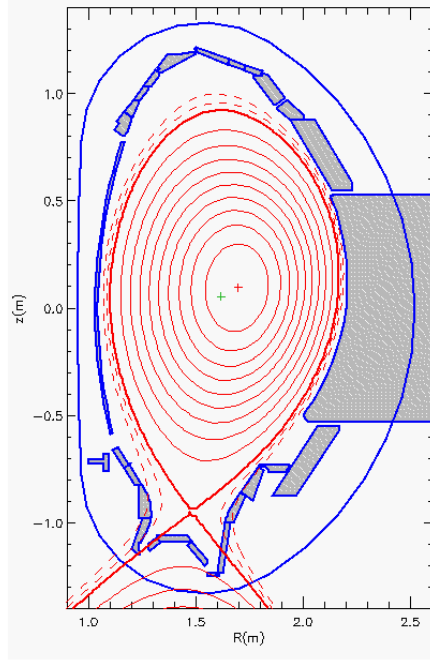


Figure 2.1.: ASDEX Upgrade discharge #21083 at $t = 1.19$ s: Closed (solid) and open (dashed) surfaces inside the vessel. The bold line is the separatrix. The green and red cross represent the geometric and magnetic axis, respectively.

as shown in figure 2.2. This means that ψ is a flux label of the surface. Due to this definition $\psi = const.$, the flux surfaces form nested tori with

$$\mathbf{B} \cdot \nabla \psi = B^\psi = 0 . \quad (2.3)$$

The other two coordinates are determined to be the angles ζ and θ which close upon themselves in toroidal and poloidal direction.

Since the magnetic field in radial direction vanishes (2.3), the divergence-free magnetic field implies that

$$\nabla \cdot \mathbf{B} = \frac{1}{\mathcal{J}} \left[\frac{\partial}{\partial \theta} (\mathcal{J} B^\theta) + \frac{\partial}{\partial \zeta} (\mathcal{J} B^\zeta) \right] = 0 , \quad (2.4)$$

where \mathcal{J} is the Jacobian of the coordinate system defined by

$$\mathcal{J} = \frac{1}{\nabla \psi \cdot \nabla \theta \times \nabla \zeta} . \quad (2.5)$$

Equation (2.4) is expressed by introducing a stream function ν [20] so that

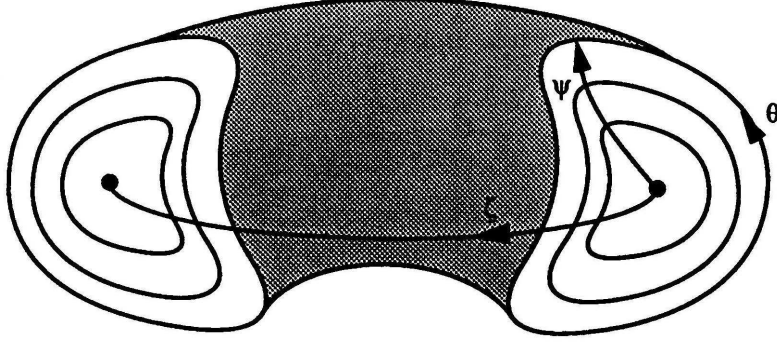


Figure 2.2.: General curvi-linear flux coordinates with the radial coordinate ψ , the poloidal angle θ and the toroidal angle ζ (from [21], p. 22).

$$\mathcal{J}B^\theta = -\frac{\partial\nu}{\partial\zeta}, \quad \mathcal{J}B^\zeta = \frac{\partial\nu}{\partial\theta}. \quad (2.6)$$

To ensure that the magnetic field is single-valued, the stream function $\nu(\psi, \theta, \zeta)$ is a sum of terms which are linear or periodic in θ and ζ ,

$$\nu = u(\psi)\theta + v(\psi)\zeta + w(\psi, \theta, \zeta). \quad (2.7)$$

Such a definition of a function like ν is known as a surface potential, i.e. the gradient of the function only is of physical significance,

$$\nabla\nu = \frac{\partial\nu}{\partial\psi}\nabla\psi + \frac{\partial\nu}{\partial\theta}\nabla\theta + \frac{\partial\nu}{\partial\zeta}\nabla\zeta. \quad (2.8)$$

Using the contravariant representation of the magnetic field \mathbf{B} and substituting the field components by the expressions (2.6) yields

$$\mathbf{B} = \frac{\partial\nu}{\partial\theta}\nabla\psi \times \nabla\theta + \frac{\partial\nu}{\partial\zeta}\nabla\psi \times \nabla\zeta.$$

This implies with (2.8) that the magnetic field can be represented [21] by

$$\mathbf{B} = \nabla\psi \times \nabla\nu, \quad (2.9)$$

where ψ is an arbitrary flux label. The function ν need to be determined now and it is expected that the linear functions u and v are related to the toroidal and poloidal flux, ψ_t and ψ_p . Calculating the toroidal flux gives

$$\begin{aligned}
 \psi_t &= \int \mathbf{B} \cdot \nabla \zeta \, d^3x \\
 &= d\psi \int_0^{2\pi} \int_0^{2\pi} B^\zeta \mathcal{J} \, d\theta \, d\zeta \\
 &= d\psi \int_0^{2\pi} \int_0^{2\pi} \frac{\partial \nu}{\partial \theta} \, d\theta \, d\zeta \\
 &= d\psi \int_0^{2\pi} \int_0^{2\pi} \left(u(\psi) + \frac{\partial w}{\partial \theta} \right) \, d\theta \, d\zeta \\
 \Rightarrow d\psi_t &= u(\psi) d\psi .
 \end{aligned}$$

A similar procedure for the poloidal flux yields for the functions u and v ,

$$u(\psi) = \frac{d\psi_t}{d\psi} \quad \text{and} \quad v(\psi) = -\frac{d\psi_p}{d\psi} . \quad (2.10)$$

Since the poloidal and the toroidal angle have not been specified yet, it is possible to construct coordinates in which the magnetic field lines appear straight (Fig. 2.3). Such a representation is obtained if the equation of the field line, i.e. $\nu = \text{const.}$ for a constant ψ , is linear in θ and ζ . From equation (2.7), it can be seen that this occurs when the periodic function w is cancelled. Typically, the toroidal angle is deformed,

$$\theta_{\text{new}} = \theta_{\text{old}} \quad \text{and} \quad \zeta_{\text{new}} = \zeta_{\text{old}} - \frac{w}{v(\psi)} ,$$

so that the new flux potential is expressed by

$$\nu = u(\psi)\theta + v(\psi)\zeta .$$

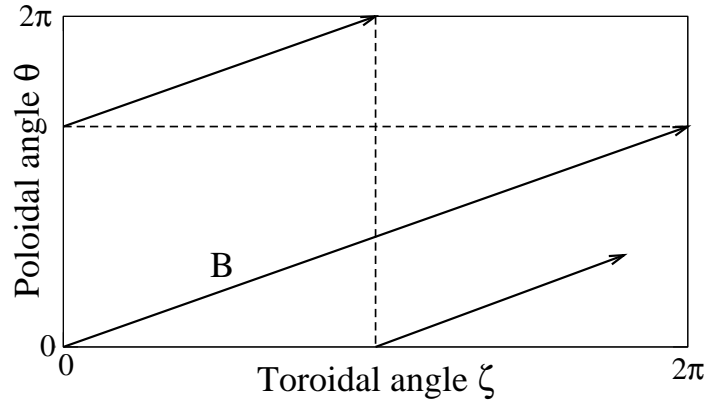


Figure 2.3.: Flux surface which shows a straight magnetic field line if the angles θ and ζ are chosen adequately.

Inserting this expression into the contravariant representation of B gives

$$\mathbf{B} = u(\psi) \cdot \nabla\psi \times \nabla\theta - v(\psi) \cdot \nabla\zeta \times \nabla\psi ,$$

which can be further rewritten by the expressions (2.10) to

$$\mathbf{B} = \frac{\partial\psi_t}{\partial\psi} \nabla\psi \times \nabla\theta + \frac{\partial\psi_p}{\partial\psi} \nabla\zeta \times \nabla\psi . \quad (2.11)$$

It can be shown [20] that the field line in a straight field line representation is described by contours of a constant linear flux potential ν on a flux surface, i.e.

$$\zeta - q\theta = \text{const} \quad \text{for} \quad \psi = \text{const}.$$

where q is the safety factor and denotes the reciprocal slope of the magnetic field line, $1/q = d\theta/d\zeta$, in figure 2.3. Thus, it is also the ratio between the contravariant components of the magnetic field, $q = B^\zeta/B^\theta$. Substituting (2.10) into equation (2.11), it reveals that

$$q = \frac{d\psi_t}{d\psi_p} . \quad (2.12)$$

Thus in every straight field line coordinate representation, the derivative of the toroidal flux with respect to the poloidal flux is constant on a flux surface.

Altogether, such a flux coordinate system represents the equilibrium magnetic field in a tokamak inside the separatrix appropriately. The form of the flux surfaces in realistic geometry is calculated by the HELENA code [22] that solves the Grad-Shafranov equation [2]. The calculated grid which is expressed in straight field line coordinates is given to the HAGIS code. This grid serves as the basis on which the nonlinear interaction between the energetic particles and the perturbations are evolved.

2.3. Stability and MHD Modes

In this section, the stability of the equilibrium and the corresponding instabilities are investigated. In order to understand the phenomena of the nonlinear equations and its properties, it is advisable to apply them to the simplest physical background first and to extend the model by additional effects gradually. At the end, the existence criteria and the properties of the eigenmodes relevant for the following wave-particle investigations are outlined.

Since the ideal MHD equations are nonlinear, an analysis is simplified by linearizing them to identify the classes of instabilities. This proceeding [10] is justified by the fact that the plasma remains static and occurring perturbations are small compared to the equilibrium quantities, $Q(\mathbf{r}, t) = Q_0(\mathbf{r}) + \delta Q(\mathbf{r}, t)$. Furthermore, the time scale on which the plasma evolves, i.e. $\mathcal{O}(10^{-1} \text{ s})$, is long in contrast to the instabilities which oscillate on the Alfvén

time scale of $\mathcal{O}(10^{-6} \text{ s})$. Introducing the fluid displacement vector $\xi(\mathbf{r}, t)$,

$$\mathbf{v} = \frac{\partial \xi}{\partial t} ,$$

the complete linearized set of equations can be further reduced to three equations

$$\begin{aligned} \rho_0 \frac{\partial^2 \xi}{\partial t^2} + \nabla \delta p + [\delta \mathbf{B} \times (\nabla \times \mathbf{B}_0)] + [\mathbf{B}_0 \times (\nabla \times \delta \mathbf{B})] &= 0 , \\ \delta p + \xi \cdot \nabla p_0 + \gamma p_0 \nabla \cdot \xi &= 0 , \\ \delta \mathbf{B} - \nabla \times (\xi \times \mathbf{B}_0) &= 0 . \end{aligned}$$

The first equation is the linearized momentum balance equation. Using the other two equations to eliminate the perturbed plasma pressure δp and the perturbed magnetic field $\delta \mathbf{B}$, the force-operator equation is given by

$$\rho_0 \frac{\partial^2 \xi}{\partial t^2} = \mathbf{F}(\xi) \tag{2.13}$$

with the force-operator

$$\begin{aligned} \mathbf{F}(\xi) &= \nabla(\xi \cdot \nabla p_0 + \gamma p_0 \nabla \cdot \xi) + (\nabla \times \nabla \times (\xi \times \mathbf{B}_0)) \times \mathbf{B}_0 \\ &\quad + (\nabla \times \mathbf{B}_0) \times (\nabla \times (\xi \times \mathbf{B}_0)) . \end{aligned}$$

Analyzing the linear stability and the waves, it is advantageous to apply the following ansatz to the force-operator equation,

$$\delta Q(\mathbf{r}, t) = Q(\mathbf{r}) e^{-i\omega t} . \tag{2.14}$$

This form represents periodic perturbations with amplitude Q and frequency ω which have always been present in the plasma and do not require an initial condition. With this mode representation, equation (2.13) becomes

$$-\omega^2 \xi = \frac{1}{\rho_0} \mathbf{F}(\xi) . \tag{2.15}$$

The equation is no longer time-dependent explicitly and represents an eigenvalue problem for the eigenvalue ω^2 with the boundary conditions on the fluid displacement vector ξ . Since the force-operator $\mathbf{F}(\xi)$ is Hermitian [23], the eigenvalues ω^2 are always real. However, the spectrum of the force-operator is confined to both the imaginary and the real axis. This implies that within the MHD model modes are obtained which are either oscillatory, $\omega^2 > 0$, or exponentially growing/decaying, $\omega^2 < 0$. A further distinction can be made by

$$\begin{aligned} \text{Im } \omega &> 0 \quad (\text{unstable}) \\ \text{Im } \omega &\leq 0 \quad (\text{stable}) . \end{aligned}$$

For the first case, the mode will grow exponentially (Eqn. 2.14) whereas in the latter case, the modes decays exponentially.

Applying these previous considerations to an infinite, homogeneous plasma slab where all equilibrium quantities are constant, the force-operator equation (2.15) can be simplified by a Fourier transform in space,

$$\omega^2 \rho_0 \xi + \gamma P_0 (\mathbf{k} \cdot \xi) \mathbf{k} + \frac{1}{\mu_0} [\mathbf{k} \times [\mathbf{k} \times (\xi \times \mathbf{B}_0)]] \times \mathbf{B}_0 = 0 ,$$

where \mathbf{k} is the wave vector. Due to the Fourier transform, the set of differential equations is transferred to simpler, algebraic equations. Assuming that the magnetic field is oriented in one direction, $\mathbf{B} = B_0 \hat{\mathbf{z}}$ and the wave vector is decomposed into $\mathbf{k} = k_\perp \hat{\mathbf{y}} + k_\parallel \hat{\mathbf{z}}$, the equation above is written as

$$\begin{pmatrix} \omega^2 - k_\parallel^2 v_A^2 & 0 & 0 \\ 0 & \omega^2 - k_\perp^2 v_S^2 - k^2 v_A^2 & -k_\perp^2 k_\parallel^2 C_S^2 \\ 0 & -k_\perp^2 k_\parallel^2 v_S^2 & \omega^2 - k_\parallel^2 v_S^2 \end{pmatrix} \begin{pmatrix} \xi_x \\ \xi_y \\ \xi_z \end{pmatrix} = 0 ,$$

where v_A and v_S are the Alfvén and the sound velocity, respectively, defined by

$$v_A^2 = \frac{B_0^2}{\mu_0 \rho_0} \quad \text{and} \quad v_S^2 = \frac{\gamma p_0}{\rho_0} . \quad (2.16)$$

Solutions from the set of equations are obtained if the determinant of the matrix is zero. This gives the dispersion relation,

$$(\omega^2 - k_\parallel^2 v_A^2) [\omega^4 - (v_A^2 + v_S^2) k^2 \omega^2 + (k k_\parallel v_A v_S)^2] = 0 . \quad (2.17)$$

Each solution represents an oscillation in the plasma. Since in the equation (2.17) the quantity ω^2 is a cubic polynomial, three different solution branches are expected. The simplest solution is

$$\omega^2 = k_\parallel^2 v_A^2 , \quad (2.18)$$

which denotes the shear Alfvén branch. The waves are independent of k_\perp , even if $k_\perp \gg k_\parallel$. They are incompressible transverse modes with both \mathbf{v} and δB perpendicular to the equilibrium magnetic field \mathbf{B}_0 . The shear Alfvén wave represents the balance between the plasma inertia and the field line tension. Since the wave is incompressible ($\delta p = \delta \rho = 0$), the plasma is carried along the magnetic field lines simultaneously.

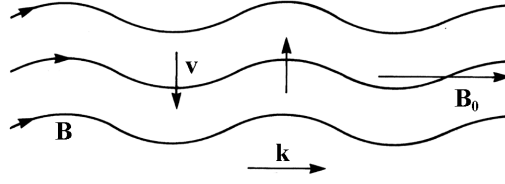


Figure 2.4.: Propagation of a transverse Alfvén wave within the equilibrium magnetic field \mathbf{B}_0 (from [2]).

The second term of equation (2.17) yields two further solutions which are the fast and slow magnetoacoustic waves. They arise from the coupling between the magnetic compression - Alfvénic branch - and the fluid compression - sonic branch - which gives

$$\omega_{2,3}^2 = \frac{k^2}{2} \left[v_S^2 + v_A^2 \pm \sqrt{(v_S^2 + v_A^2)^2 - 4v_S^2 v_A^2 \cos^2 \theta} \right], \quad (2.19)$$

where θ denotes the angle between the wave vector and the equilibrium magnetic field as shown in figure 2.5 here.

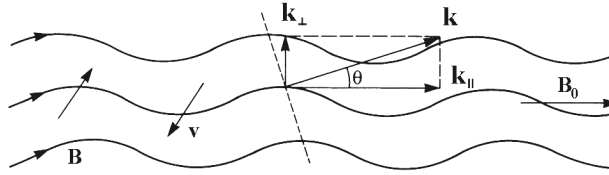


Figure 2.5.: Propagation of a magnetoacoustic wave across the magnetic field \mathbf{B}_0 (from [2]).

The positive sign in (2.19) corresponds to the fast magnetoacoustic wave and oscillates at frequencies always greater than the Alfvén wave (Eqn. 2.18). The negative sign corresponds to the slow magnetoacoustic waves which oscillates at frequencies always smaller than v_A . Both waves are compressional, i.e. they possess perturbative components in both parallel and perpendicular direction compared to \mathbf{B}_0 .

A useful parameter to characterize a plasma is the plasma beta defined by

$$\beta = \frac{2\mu_0 p}{B^2}. \quad (2.20)$$

It describes the ratio between the plasma energy density to the plasma field line density and is also related to the significant velocities [2] through

$$\beta = \frac{2}{\gamma} \frac{v_S^2}{v_A^2}. \quad (2.21)$$

This parameter indicates if most of the compression is carried out by the magnetic field, i.e.

in the low- β limit with $\beta \ll 1$, or if both the magnetic field and the plasma are compressed equally, $v_A \approx v_S$.

2.3.1. Continuum Spectrum

In figure 1.1, it is shown that the magnetic field is bent to a torus. The magnetic field is inhomogeneous and decrease with $1/R$ from the torus axis. Thus, the dispersion relation in a homogeneous plasma (2.18) is modified to

$$\omega^2 = k_{\parallel}^2(r)v_A^2(r) , \quad (2.22)$$

where r is the minor plasma radius which is related to the flux label ψ (Fig. 2.2). This shows that shear Alfvén waves with a radial extent are dispersive due to different phase velocities. Thus, excited Alfvén waves are strongly damped by resonant absorption from the shear Alfvén continuum (Eqn. 2.22), also known as continuum damping [24].

2.3.2. Toroidicity-induced Alfvén Eigenmodes

A further modification in the dispersion relation appears due to toroidicity. A wave perturbation ξ which propagates along the magnetic field line can be described by a Fourier decomposition in poloidal and toroidal harmonics due to the periodicity. However, the torus is rotational symmetric so that the toroidal harmonics decouple. So, the Fourier decomposition is given by

$$\xi(r, \theta, \zeta) = \sum_m \xi_m(r) e^{i(n\zeta - m\theta - \omega t)} , \quad (2.23)$$

where m and n are the poloidal and toroidal mode numbers, respectively. Due to an inhomogeneous magnetic field, \mathbf{B} is a function of the poloidal angle θ . Thus, a coupling between different poloidal harmonics appear for the perturbation ξ .

Considering a particular toroidal mode number n , for a small inverse aspect ratio $\epsilon = r_0/R_0 \ll 1$ it can be assumed that the poloidal harmonic ξ_m couples to its neighbouring harmonic ξ_{m+1} only. Then, the force-operator equation (2.15) can be rewritten as a set of coupled equations [25],

$$\begin{pmatrix} P_m & K \\ K & P_{m+1} \end{pmatrix} \begin{pmatrix} \xi_m \\ \xi_{m+1} \end{pmatrix} = 0$$

with

$$\begin{aligned} P_m &= \frac{d}{dr} r^3 \left(\frac{\omega^2}{v_A^2} - k_{\parallel, m}^2 \right) \frac{d}{dr} - (m^2 - 1)r \left(\frac{\omega^2}{v_A^2} - k_{\parallel, m}^2 \right) + \left(\frac{\omega^2}{v_A^2} \right)' r^2 \\ K &= \frac{5}{2} \epsilon \frac{d}{dr} \frac{\omega^2 r^4}{v_A^2} \frac{d}{dr} . \end{aligned}$$

The subscripts m and $m + 1$ denote the two dominant poloidal mode numbers. The final dispersion relation is given by

$$\begin{aligned}\omega^2 &= k_{\parallel,m}^2(r) v_A^2(r) \\ &= \frac{v_A^2(r)}{R^2} \left(n - \frac{m}{q(r)} \right)^2 + \mathcal{O}(\epsilon^2)\end{aligned}\quad (2.24)$$

with

$$q = \frac{r B_{tor}}{R B_{pol}} + \mathcal{O}(\epsilon) .$$

This means that solutions for the eigenvalue ω^2 still exist in the torus which form a continuous spectrum for the shear Alfvén waves. In the cylindrical limit, i.e. $\epsilon = 0$, the two poloidal harmonics decouple. Considering a monotonically increasing safety factor in a cylinder, both harmonics m and $m + 1$ are expected to cross for $\omega_{dc}^2 = \omega^2$ (Eqn. 2.24) as shown in figure 2.6 (left; dashed lines) at the surface r_0 determined by the condition

$$k_{\parallel,m}(r_0) = -k_{\parallel,m+1}(r_0) .$$

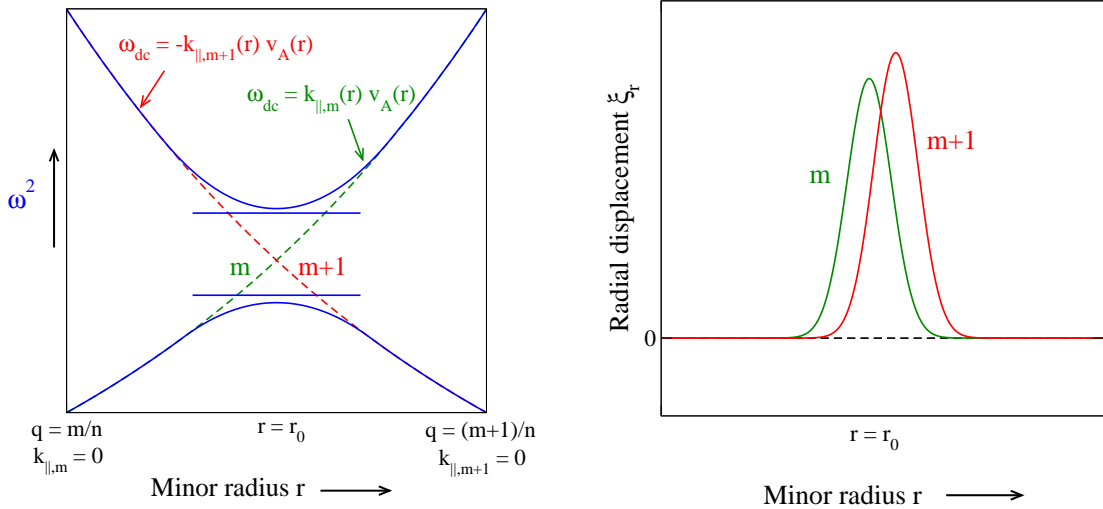


Figure 2.6.: *Left: Coupling of the poloidal harmonics m and $m + 1$ in a torus (blue) producing a gap in the shear Alfvén continuum. Additionally, two discrete global eigenmodes, TAE, exist within the gap. In the cylindrical limit, the shear Alfvén continua $k_{\parallel,m}$ (green) and $-k_{\parallel,m+1}$ (red) cross at the surface r_0 . Right: The corresponding TAE eigenfunction of the two dominant poloidal harmonics is plotted.*

This is approximately equivalent to the position where the safety factor is

$$q(r_0) = \frac{m + \frac{1}{2}}{n} . \quad (2.25)$$

However, toroidicity resolves this degeneracy at the intersection point and produces gaps, called TAE gaps, in the shear Alfvén continuum (Fig. 2.6 left; blue curved lines) due to the poloidal coupling. The gap is located at the frequency,

$$\omega_{TAE} = \frac{v_A}{2q(r_0)R} . \quad (2.26)$$

It has been found [6] that within the TAE gap two discrete eigenmodes, called TAEs, above the maximum and below the minimum of the shear Alfvén continuum are present as shown in figure 2.6 (left; blue straight lines). The corresponding eigenfunctions of the two dominant poloidal harmonics are shown in figure 2.6 (right). Since each TAE lies within the gap and does not satisfy the local shear Alfvén resonance condition, it is not subject to continuum damping. It is extended globally and weakly damped [26].

2.3.3. Beta-induced Alfvén Eigenmodes

It has been shown in equation (2.19) that the inclusion of plasma compressibility within the MHD equations introduces a coupling between the shear Alfvén waves and the compressible acoustic waves in the low frequency range. Due to finite β (Eqn. 2.21), this leads to a coupling between the shear Alfvén continuum with the poloidal mode number m and the sound continuum with the mode numbers $m - 1$ and $m + 1$. The coupling condition [27] is given by

$$\omega = \frac{v_A}{R} \left| n - \frac{m}{q(r_0)} \right| = \frac{v_S}{R} \left| n - \frac{m \pm 1}{q(r_0)} \right| .$$

As explained in section 2.3.2, the coupling produces gaps which are approximately localized at the beta-induced Alfvén eigenmode frequency $\omega_{BAE,MHD}$,

$$\omega_{BAE,MHD}^2 = \frac{2v_S^2}{R_0^2} \left(1 + \frac{1}{2q^2} \right) . \quad (2.27)$$

Including kinetic effects, the dispersion relation $\omega_{BAE,kin}^2$ [28, 29] is given by

$$\omega_{BAE,kin}^2 = \frac{v_{th,i}^2}{R_0^2} \left[\frac{7}{4} + \tau \left(1 + \frac{1}{2q^2} \right) \right] \quad (2.28)$$

where $v_{th,i}$ is the thermal speed of the background ions and $\tau = T_e/T_i$ is the ratio between the electron and the ion background temperature.

Within the gap, a discrete global BAE eigenmode [7, 30] is present. In contrast to the TAE, the coupling produces an eigenfunction with one dominant poloidal harmonic m for the perpendicular component ξ_{\perp} which corresponds to the shear Alfvén continuum. Due to the compressibility, the eigenmode has an additional parallel component ξ_{\parallel} with the poloidal harmonics $m - 1$ and $m + 1$. However, in the low β -limit, the perpendicular displacement is larger than the parallel displacement, $\xi_{\perp} > \xi_{\parallel}$. So, this eigenmode is similar to the TAE but it is neither pure Alfvénic nor pure acoustic.

2.3.4. Growth and Damping of Alfvén Eigenmodes

The following discussion describes the dominant damping mechanisms which can be experienced by Alfvénic waves due to the bulk plasma. Due to the consideration of gap modes, most damping mechanisms however are of the order of a few per cent or less. Afterwards, the driving mechanism which acts as an energy source for the waves and the required conditions for a wave-particle interactions are introduced.

Continuum damping

It was mentioned in section 2.3.2 that due to an inhomogeneous plasma the dispersion relation (Eqn. 2.24) leads to a resonant absorption of Alfvénic waves, known as continuum damping [24]. Since toroidal Alfvén eigenmodes are localized within toroidal gaps where the continuum damping associated to the poloidal mode numbers m and $m + 1$ is absent, these modes are weakly damped. However, if the eigenmode spreads over a large radial range, it is possible that the tail of the eigenfunction intersects with a local Alfvén resonance. It can experience a small residual amount of continuum damping [31, 32]. By the consideration of toroidicity induced gaps which spread to the plasma edge, this damping effect vanishes.

Ion Landau damping

In the plasma, a Maxwellian distribution of thermal ions contains a vanishing amount of background ions which can resonate with Alfvénic waves due to high velocities, $v_{\parallel} = v_A$ (Eqn. 2.22). However, it has been shown [8] that the resonance condition due to the magnetic curvature is modified to

$$\omega - k_{\parallel}v_{\parallel} - \mathbf{k}_{\perp} \cdot \mathbf{v}_{di} = 0 ,$$

where \mathbf{v}_{di} is the magnetic drift velocity. The last term reduces effectively the frequency of the eigenmode so that the bulk particles are able to resonate at the $v_{\parallel} = v_A/3$ resonance.

Electron Landau Damping

For typical tokamak plasma parameters, the background electron velocity is much greater than the Alfvén velocity, $v_e \gg v_A$. Thus, electron Landau damping [33] is present only due to a small fraction of electrons with $v_{\perp,e} \gg v_{\parallel,e}$ so that the toroidal electron velocity is comparable to the wave velocity. These electrons satisfy the resonance condition $\omega - k_{\parallel,m\pm 1}v_e \approx 0$. The resonance layer is radially localized beside the TAE gap so that the tails of the TAE eigenfunction only are affected. Similar to continuum damping, this effect can be neglected for not too large radial eigenmode extents.

Radiative Damping of TAE

Due to the inclusion of finite Larmor radius effects (FLR), the ideal MHD TAE can couple to a kinetic Alfvén wave so that the dispersion relation modifies to [34]

$$\omega = \pm k_{\parallel,m}v_A \left[1 + \left(\frac{3}{4} + \frac{T_e}{T_i} \right) (k_{\perp}\rho_i)^2 \right] .$$

The dispersion relation reveals a finite radial group velocity for the term within the squared bracket. This indicates the coupling to a radiative kinetic Alfvén wave. It carries energy away from the TAE localization so that the effect is known as radiative damping [35].

Linear Theory of the Mode Growth

For the drive of an Alfvénic instability, it is assumed that the energy of the eigenmode is small compared to the energy of the background plasma [10]. In this case, a perturbative approach as described in section 2.3 can be applied which adds a small imaginary value, the growth rate γ , to the frequency of the eigenmode with $\gamma \ll \omega$. Under the consideration of an exponentially growing wave, the increasing wave amplitude A and the corresponding wave energy, $E \sim A^2$, can be expressed by

$$A = A_0 e^{\gamma t} \quad \text{and} \quad E = E_0 e^{2\gamma t} .$$

Since the growth rate can be described by the power transfer P from the fast particles to the mode, it follows

$$\begin{aligned} \frac{\partial E}{\partial t} &= 2\gamma E \\ \Rightarrow \gamma &= \frac{1}{2E} \frac{\partial E}{\partial t} = \frac{P}{2E} \end{aligned}$$

where $P = P_{fp} - P_{damp}$ is the difference of power transfers from the fast particle P_{fp} and the background damping P_{damp} . Thus, the linear growth rate consists of contributions driving the mode unstable and damping the wave,

$$\gamma = \gamma_{fp} - \gamma_{damp} = \frac{P_{fp} - P_{damp}}{2E} .$$

To contribute to the growth of the Alfvén wave, the fast particles have to be resonant with the eigenmode. It is known [36] that the resonance condition can be written as

$$\omega - n\omega_{tp} - p\omega_{po} \approx \Omega_{n,p} , \tag{2.29}$$

where ω is the frequency of the Eigenmode, ω_{tp} the toroidal precession frequency and ω_{po} the poloidal orbit frequency. The toroidal mode number and the poloidal orbit number are given by n and p , respectively. A bidirectional energy exchange is possible if $\Omega_{n,p}$ is approximately zero.

If the resonance condition is fulfilled the growth of a TAE mode driven by fast particles for a typical slowing-down distribution can be estimated [25] as

$$\frac{\gamma}{\omega_0} = \frac{9}{4} \beta_{fp} \left(\frac{\omega_{*,i}}{\omega} - \frac{1}{2} \right) F \tag{2.30}$$

where $\omega_{*,i}$ is the ion diamagnetic drift frequency

$$\omega_{*,i} = \frac{m_i c}{eB} \mathbf{k} \times \mathbf{B} \frac{\nabla f_0}{f_0} \quad (2.31)$$

and

$$F(x) = x (1 + 2x^2 + 2x^4) e^{-x^2} \quad \text{with} \quad x = \frac{v_A}{v_i}.$$

In equation (2.30), the first term in the brackets denotes the energy source which is associated to the radial gradient in the fast particle distribution in $\omega_{*,i}$. The fixed second term is due to the damping of the energetic ions for a slowing-down or Maxwellian distribution since $\partial f_0 / \partial E < 0$. The function F is an approximation for the more complicated expression of the growth rate. Thus, a further condition for the modes to be unstable is $\omega_{*,i} / \omega > 1/2$.

The expression for the growth rate (Eqn. 2.30) was derived for a small particle orbit width Δ_b ¹. If the particle orbit width is comparable to the mode width Δ_m , the growth rate scales linearly [37] with the poloidal mode number m , i.e. $\gamma \sim \omega_{*,i} \sim m$. The mode width is defined as

$$\Delta_m = \frac{r_m^2}{msR} \approx \epsilon \frac{r_m}{m} \quad (2.32)$$

where s is local magnetic shear and r_m is the radial position of the TAE mode. For particle orbit widths larger than the mode width, it was found [34] that the growth rate decreases with m^{-2} so that a maximal mode growth is obtained for $\Delta_b / \Delta_m \approx 1$.

With respect to the linear growth rate, many assumptions are required for an analytical description. For an arbitrary magnetic field geometry and a general fast particle distribution, the linear growth rate must be determined by means of numerical simulations.

2.3.5. Neoclassical Tearing Mode

A variety of MHD instabilities can be excited in an equilibrium plasma causing changes in its topology. These changes occur at surfaces with rational values of the safety factor q as explained for the TAE (section 2.3.2) or the BAE (section 2.3.3). However, it is also possible that due to a so-called tearing mode the magnetic field lines break and reconnect to form magnetic islands (Fig. 2.7). It has been found [38, 39] that these formations cause a significant reduction of fast particles in the centre and thus reduce the plasma heating. Therefore, it is necessary that the interaction between the magnetic island and the fast particles is understood.

In this section the theoretical background and the island properties are introduced. Later in section 4.6, the experimental results are compared to the numerical simulations of a NBI distribution in the presence of a magnetic island.

¹This expression will be clarified in connection with the particle motion in section 2.4.

The excitation of the islands is associated with resistivity in the plasma. Their dynamical evolution is determined by the Rutherford equation [40] but for the following investigations the topology of the island only is of interest. Since toroidicity is a so-called 'neoclassical' effect, the island formations present in a tokamak are referred to as neoclassical tearing modes (NTM) [2].

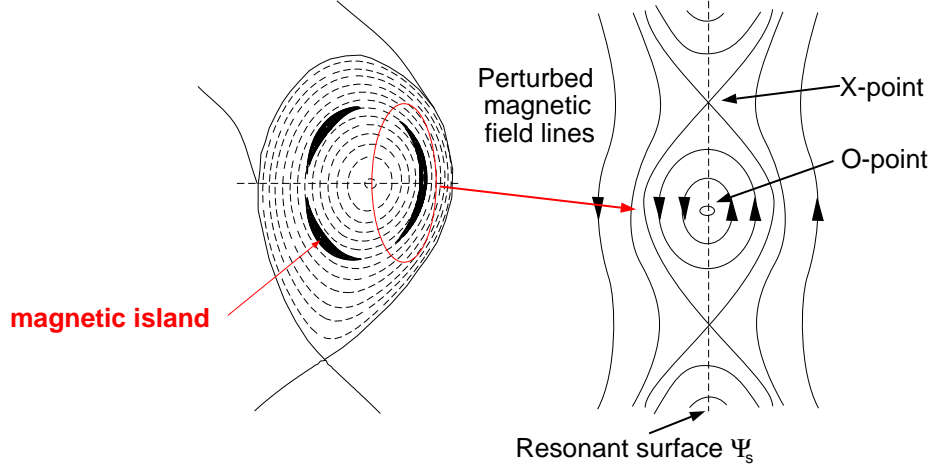


Figure 2.7.: Magnetic islands and the resulting magnetic field.

As shown in figure 2.7, the perturbation constitutes an island chain at the resonant surface ψ_s with $q_s = m/n$ which stretches along the unperturbed magnetic field line. Due to the toroidal and poloidal periodicity, the island chain forms m islands at a poloidal cross section. The point between different islands is called X-points, the centre of the island is the O-point. The resulting magnetic field within the island forms a helix around the O-point so that a helical angle ξ can be defined as

$$\xi = \theta - \frac{n}{m}\zeta. \quad (2.33)$$

The helical angle is directed parallel to the line which connects neighbouring O-points as shown in figure 2.8.

For a large aspect ratio, $R_0/r_0 \gg 1$, the helical component of the magnetic field is approximately given by

$$B_h = B_\theta \left(1 - \frac{n}{m}q(\psi) \right)$$

where B_θ is the poloidal component of the magnetic field. The tearing mode represents the mainly radial field component to generate this formation which can be written as

$$\delta B = B_\psi \sin m\xi \quad (2.34)$$

Due to these assumptions, the magnetic field line is determined by the equation [2]

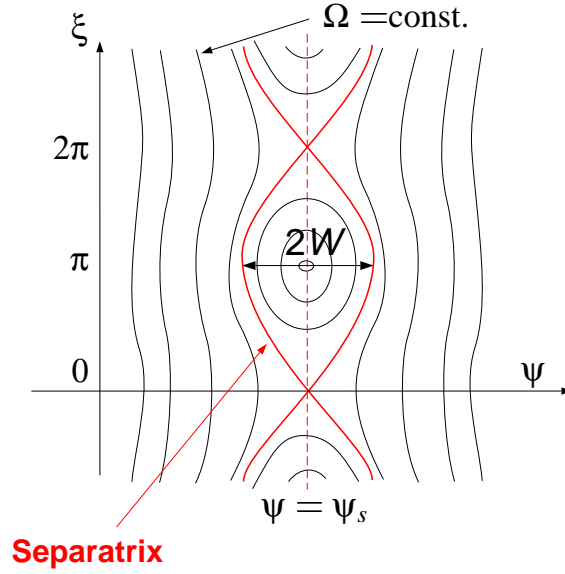


Figure 2.8.: Definition of the helical angle ξ , the half island width w and the flux label Ω of the NTM.

$$\frac{1}{\psi_s} \frac{d\psi}{d\xi} = \frac{\delta B}{B_h}.$$

The magnetic field perturbation caused by the NTM is small except for the vicinity of the resonant surface. Deriving the equation for the field lines by a Taylor's series yields

$$\Omega = \frac{2(\psi - \psi_s)^2}{w^2} - \cos m\xi$$

where Ω is a perturbed flux surface label, as shown in figure 2.8. The value $\Omega = 1$ defines the label at the X-point. For $-1 < \Omega < 1$, the flux surface is within the magnetic island whereas for $\Omega > 1$ a flux surface is determined which is beyond the island separatrix. The crucial value is the half island width w ,

$$w = 2\sqrt{\frac{\psi q B_\psi}{m B_\theta q'_s}}, \quad (2.35)$$

which determines the radial extension of the perturbation. The half width is derived under the assumption of a constant perturbation B_ψ generating a symmetric island. However, it has been detected in the experiment [41] that asymmetric islands are present in ASDEX Upgrade. This requires an asymmetric radial perturbation profile which will be described in section 4.6 in detail.

2.4. Fast Particles in a Tokamak

After the description of the background ions in the MHD model, the highly energetic ions are described by an kinetic approach in this section. This allows for an adequate treatment of the resonant wave-particle interactions. It is assumed that no dissipative processes like collisions are present since the mean free path of the energetic ions is of the order of $\mathcal{O}(10^3 \text{ m})$ compared to the mode size $\mathcal{O}(m)$. In tokamak geometry, this leads to the particle's constants of motion. At the end, the guiding centre approach is introduced which will reduce the simulation time significantly.

The general equation of motion of a non-relativistic charged particle in the presence of an electromagnetic field and an external force \mathbf{F} is given by

$$m \frac{d\mathbf{v}}{dt} = \mathbf{F} + e(\mathbf{E} + \mathbf{v} \times \mathbf{B}) . \quad (2.36)$$

Considering only the effect of the magnetic field upon the fast particle, the equation of motion is

$$m \frac{d\mathbf{v}}{dt} = e\mathbf{v} \times \mathbf{B} . \quad (2.37)$$

The magnetic force cannot change the particle velocity and thus its energy. This is obtained by dotting equation (2.37) with \mathbf{v} ,

$$m \frac{d\mathbf{v}}{dt} \cdot \mathbf{v} = \frac{d}{dt} \left(\frac{m}{2} v^2 \right) = \frac{dE}{dt} = 0. \quad (2.38)$$

This result is valid for an arbitrary magnetic field $\mathbf{B} = \mathbf{B}(\mathbf{r})$ but requires that the magnetic field does not vary with the time. Thus, the particle energy E is a constant of motion. Nevertheless, an accelerated charged particle loses energy in form of an electromagnetic wave due to the gyration and the curvature of the torus. This effect is very small [42] and can be neglected in this thesis.

Homogeneous Magnetic Field

In a homogeneous magnetic field, the particle motion is determined by equation (2.37) which can be separated in a motion parallel and perpendicular to the magnetic field,

$$\frac{d\mathbf{v}_{\parallel}}{dt} = 0 , \quad (2.39a)$$

$$\frac{d\mathbf{v}_{\perp}}{dt} = \frac{e}{m} (\mathbf{v}_{\perp} \times \mathbf{B}) . \quad (2.39b)$$

This shows that the parallel velocity along the field line is constant. The equation (2.39b) can be rewritten as

$$\frac{d\mathbf{v}_\perp}{dt} = \mathbf{v}_\perp \times \omega_c \quad \text{with} \quad \omega_c = \frac{e\mathbf{B}}{m}$$

where ω_c is the cyclotron- or gyro frequency. It describes the rotation with a constant angular velocity around the magnetic field line. Taking $\mathbf{v}_\perp = d\rho_\perp/dt$, the integration of the equation above yields

$$\mathbf{v}_\perp = \rho_\perp \times \omega_c$$

with ρ_\perp being the particle position vector with respect to the centre of the rotation in a plane perpendicular to the magnetic field. The superposition of the parallel and the perpendicular particle velocities reveals a helical trajectory around the magnetic field line.

In a typical tokamak plasma, the magnetic field has a magnitude of a few Tesla. This indicates that the ion cyclotron frequency is of order $\mathcal{O}(10^8 \text{ s}^{-1})$. The absolute value for the radius of the circular orbit, called gyro radius, is given by

$$\rho_\perp = \frac{mv_\perp}{|e|B}$$

so that the gyro radius has a magnitude of a few millimetres for a particle energy of the order of $\mathcal{O}(10^2 \text{ keV})$.

External Force

Including an external force and taking the cross product with \mathbf{B} , the equation of motion (2.37) gives

$$m \frac{d\mathbf{v}}{dt} \times \mathbf{B} = e \left[\frac{\mathbf{F}}{e} \times \mathbf{B} + (\mathbf{v} \cdot \mathbf{B}) \mathbf{B} - B^2 \mathbf{v} \right].$$

Averaging over one complete circular orbit yields

$$0 = \frac{\mathbf{F}}{e} \times \mathbf{B} - B^2 \mathbf{v}_{\perp,ave} \quad \Rightarrow \quad \mathbf{v}_{\perp,ave} = \mathbf{v}_D = \frac{\mathbf{F} \times \mathbf{B}}{eB^2}. \quad (2.40)$$

This velocity \mathbf{v}_D is an averaged drift perpendicular to the magnetic field due to a given force \mathbf{F} . It is independent of the mass so that the magnitude is the same for electrons and single-ionized ions.

$\mathbf{E} \times \mathbf{B}$ Force

Considering now an electric field \mathbf{E} which is perpendicular to the magnetic field, a charged particle experiences a change in its motion due to the electric force. The particle is accelerated if the perpendicular particle motion is in the same direction as the electric field and it

is decelerated in the opposite direction. As shown in figure 2.9, the gyro radius increases as the particle is accelerated and conversely. Therefore, a change in the gyration is produced so that the centre of the gyration drifts in the direction perpendicular to both fields. Inserting the electric force $\mathbf{F} = e\mathbf{E}$ in expression (2.40) yields

$$\mathbf{v}_{\mathbf{E} \times \mathbf{B}} = \frac{\mathbf{E} \times \mathbf{B}}{B^2} .$$

This implies that the drift is in the same direction for electrons and ions without respect to mass and charge.

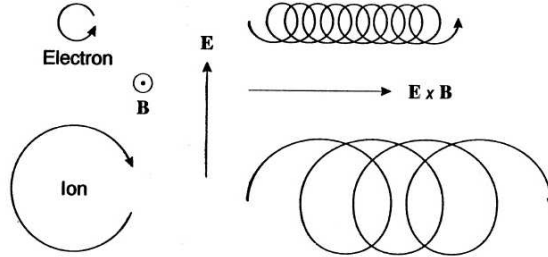


Figure 2.9.: $\mathbf{E} \times \mathbf{B}$ drift of an ion and an electron (from [12]).

Mirror Force

Due to the circular motion around the magnetic field line, the gyrating particle is associated to a circular electric current, I . This enables the possibility to define a magnetic moment μ for the charge particle

$$\mu = I \cdot A = \frac{e\omega_c}{2\pi} \cdot \pi \left(\frac{v_{\perp}}{\omega_c} \right)^2 = \frac{\frac{1}{2}mv_{\perp}^2}{B} = \frac{E_{\perp}}{B} , \quad (2.41)$$

whereby A is the surface which is surrounded by the circular motion. It can be shown [2] that under the assumption of a slowly varying magnetic field for a complete gyro orbit the magnetic moment is invariant and is therefore a constant of motion,

$$\Delta \left(\frac{E_{\perp}}{B} \right) = \Delta \mu = 0 . \quad (2.42)$$

In the presence of a varying magnetic field, it can be derived that a charged particle experiences a force [43] of the form

$$\mathbf{F} = -\mu \nabla B .$$

Inserting this expression into the general form yields

$$v_{\nabla B} = -E_{\perp} \frac{\nabla B \times \mathbf{B}}{eB^3}$$

which is known as the grad-B drift.

As a consequence of the magnetic moment's invariance, the perpendicular particle velocity increases as the charged particle moves into a region of increased magnetic field strength. Simultaneously, the parallel velocity decreases to keep the total energy constant. This implies that if the magnetic field strength is strong enough the parallel motion reduces to zero. Then, the particle is accelerated in the direction of the weaker field. This effect is known as Mirror force.

Curvature Force

Since the magnetic field lines wind helically around the toroidal plasma, the curvature [20] defined by

$$\kappa = (\mathbf{B} \cdot \nabla) \mathbf{B}$$

gives rise to a centripetal force onto the particle

$$\mathbf{F}_{\kappa} = -mv_{\parallel} \kappa = -mv_{\parallel} (\mathbf{B} \cdot \nabla) \mathbf{B}$$

where the curvature radius can be determined as the distance between the torus axis to the actual particle position in lowest order. From equation (2.40), the curvature drift is given by

$$\mathbf{v}_{\kappa} = \frac{mv_{\parallel}}{eB^2} (B \cdot \nabla B \times \mathbf{B} - \mathbf{B} \times \nabla \times \mathbf{B})$$

Although in the straight field line representation no curvature term is present, it is considered because the drift is hidden in the transformation to the laboratory reference frame.

Guiding Centre Motion

In this section so far, it has been shown that the particles gyrate around the magnetic field lines whilst the centre of the gyration, called guiding centre, experiences drifts perpendicular to the magnetic field due to various forces. The 6-dimensional description of the particle motion can be reduced to 5-dimensions by a coordinate transform [44] (Appendix A.2). If the gyro radius is much smaller than the scale length on which the field varies and the gyro frequency is much larger than any characteristic field frequency, the guiding centre approximation can be applied. In this approach it is assumed that the helical particle motion can be reduced to a drift motion of the guiding centre as shown in figure 2.10. The corresponding guiding centre equations of motion were first derived by Alfvén [5]. This 5-d description of the motion is much more computationally feasible than the full particle

motion. Since the gyration is neglected, the treatment allows for larger time steps for the particle evolution. Involving all drift mechanisms it has been found [11] that the guiding centre velocity can be written as

$$\mathbf{v} = v_{\parallel} \hat{\mathbf{b}} + \frac{\hat{\mathbf{b}}}{eB} \times \left[mv_{\parallel}^2 (\hat{\mathbf{b}} \cdot \nabla) \hat{\mathbf{b}} + \mu \nabla B + e \nabla \Phi \right] \quad (2.43)$$

where $\hat{\mathbf{b}}$ is the unit vector of the magnetic field. The first term represents the guiding centre motion along the magnetic field line. The second term consists of the three drifts perpendicular to \mathbf{B} . The first drift is due to the curvature, the second due to the inhomogeneity in the magnetic field strength and the last due to an electric field expressed by the electric potential Φ .

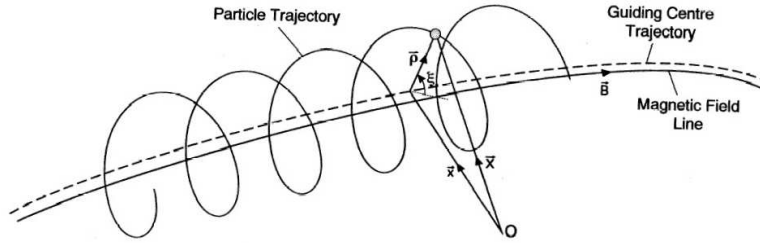


Figure 2.10.: *Helical particle trajectory around a magnetic field line with the corresponding guiding centre trajectory (from [12]).*

Characteristic Fast Particle Trajectories

The curvature and the ∇B -drift determine the characteristic classes of the fast particles - passing and trapped. Due to the poloidal magnetic field, the particles follow the helical magnetic field line and traverse the poloidal cross section. Since the upper and lower half of the torus have the same effects in the same direction for each particle, the drifts cancel after a complete particle orbit, i.e. no net drift.

For trapped particles, the parallel velocity is too small to penetrate into the high field (HF) side of the torus. The condition for particle trapping [2] is

$$\frac{v_{\parallel}}{v_{\perp}} < \sqrt{\frac{B_{max}}{B_{min}} - 1} \quad (2.44)$$

where B_{max} and B_{min} are the maximal magnetic field strength experienced by the particle at the HF side and the minimal magnetic field strength at the low field (LF) side, respectively. The particle is reflected at the particular magnetic field strength B_{max} due to the mirror force and is therefore mainly located at the LF side as shown in figure 2.11 (left). The energetic ions bounce forwards and backwards between their turning points which results in a net toroidal motion due to the inhomogeneous magnetic field. The projection of the

particle trajectory into the poloidal cross section reveals an orbit which is appropriately named banana orbit.

The orbit width Δ_b is determined by the difference between the largest to the lowest flux surface (red arrow in figure 2.11) on which the guiding centre is present. For low magnetic shear, it has been found analytically [15],

$$\Delta_{b,trapped} \approx 2q\rho_{\perp} , \quad (2.45)$$

so that the banana orbit width is proportional to the gyro radius ρ_{\perp} .

Passing particles are not reflected anywhere. Therefore, the guiding centres propagate around the torus on helical trajectories. Like the trapped particles, the trajectory is superimposed by drifts but the poloidal projection (Fig. 2.11 right) reveals a nearly circular orbit with an orbit width of

$$\Delta_{b,passing} \approx q\rho_{\perp} \quad (2.46)$$

which is approximately half the size of the banana orbit width (Eqn. 2.45) [15]. A further particle distinction can be made depending on the direction of propagation. If a particle propagates with the magnetic field it is named co-passing, against the magnetic field counter-passing.

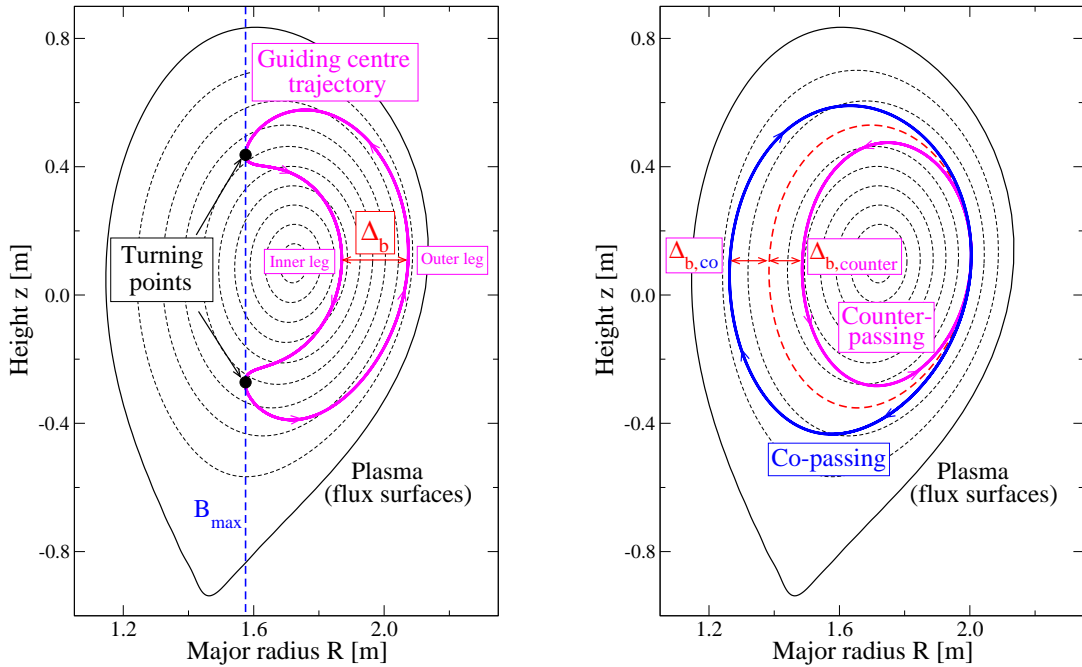


Figure 2.11.: Poloidal projection of the guiding centre trajectories for a trapped (left) and a co-passing as well as a counter-passing particle (right).

2.5. Heating Systems and Diagnostics at ASDEX Upgrade

In a future fusion device, the energy losses in an ignited $D - T$ plasma have to be balanced by the plasma heating from the slowing down process of the α -particles which are generated by fusion reactions. However, the fusion rate is strongly dependent on the temperature and is ineffective for low temperatures. Thus, additional heating is necessary to reach the required temperature. In this section two important heating methods with the underlying physics are presented which generate fast particles to heat the background plasma. Due to wave-particle interactions, a part of these energetic ions is lost and is detected by the fast ion loss diagnostic also introduced here.

2.5.1. Ion Cyclotron Resonance Heating

Radio frequency heating transfers energy from an external source to the plasma via electromagnetic waves. These waves propagate through the plasma and accelerate charged particles which heat the plasma via collisions subsequently. In general, there are three radio frequency heating schemes possible in a fusion device: ion cyclotron resonance heating at frequencies of 30 – 80 MHz, lower hybrid resonance heating at a frequency of a few Giga Hertz and electron resonance heating at a frequency in the range of 100 GHz. But for the investigation of fast particle losses during this thesis only the ion cyclotron resonance heating (ICRH) [45] is of interest.

An antenna launches a wave into the plasma with a frequency which matches the ion cyclotron frequency. Since the cyclotron frequency (section 2.4) depends mainly on the toroidal magnetic field $B \approx B(R)$, a resonant absorption of the charged ions is spatially localized at a major radius R as shown in figure 2.12. The resonance condition $\omega(R)$ is given by

$$\omega - k_{\parallel} v_{\parallel} \approx l \omega_c$$

where $l = 1, 2, \dots$ is the number of the harmonic. Due to Doppler broadening, a spatial region with a resonance width δR is induced,

$$\delta R = \frac{k_{\parallel} v_i}{\omega_c} R .$$

Since the resonance width is much smaller than the plasma extent, ICRH has the desirable feature that the absorption region can be controlled by matching the wave frequency to the magnetic field.

With respect to the absorption, a crucial property is the polarization of the wave. Due to the gyro motion of the particles, the wave must have a circularly polarized component. With inclusion of finite Larmor radius (FLR) effects, it has been shown [46] that the absorption at the fundamental harmonic ($l = 1$) is small due to an unfavourable polarization. The absorption has its maximum at the second harmonic ($l = 2$) and decreases for higher harmonics. The mean energy exchange $\langle \delta E \rangle$ for $l = 2$ is given by

$$\langle \delta E \rangle \sim \left| \frac{k_{\perp} v_{\perp}}{\omega_c} \right|^2 (E_{+})^2$$

where E_{+} is the circularly polarized component of the wave electric field in the direction of the ion gyro motion. The equation shows that the harmonic heating accelerates particles with $k_{\perp} \rho_{\perp} \gg 1$ better than the bulk ions. So, it creates a tail in the distribution function for high energies deviating from the Maxwellian.

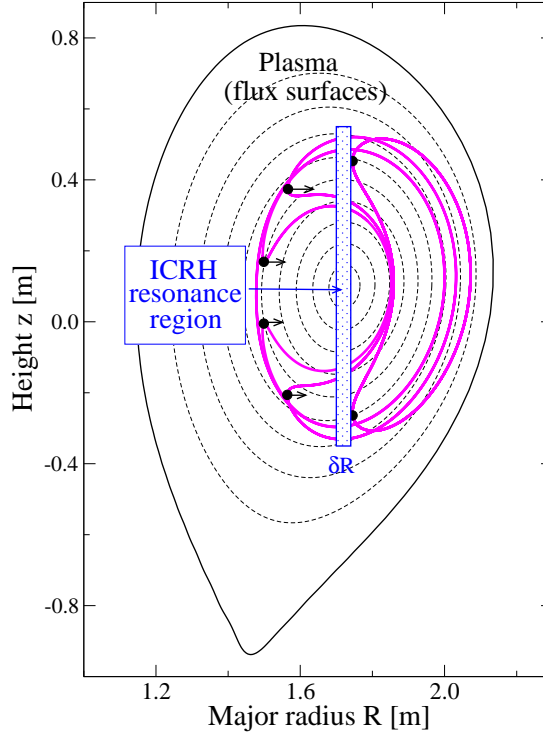


Figure 2.12.: Resonance region (shaded blue box) of the fast particles due to on-axis ICRH.

Minority Heating

If the plasma (deuterium) consists of a further particle species (hydrogen) in a low concentration, the absorption at the minority resonance becomes very strong. All frequencies and absorption parameters are determined by the deuterium ions. This implies that in the vicinity of the hydrogen resonance a considerable fraction of the wave power is left polarized because of the polarization caused by the deuterium. This heating scheme is called minority heating. Since the frequency is set so that all the power is absorbed by the hydrogen, a strong tail is created in the distribution function. The ions relax by collision with background electrons because of the high velocities.

Due to the absorption, the perpendicular energy of the particle is increased. This means that not only the total energy is increased but also the ratio v_{\parallel}/v_{\perp} (Eqn. 2.44) decreases. Due to this, former passing particles change their orbit topology to a trapped orbit as shown

in figure 2.12. Furthermore, the turning points of the trapped particles shift to the LF side since the orbit is still within the absorption region. This continues until the turning points are located at the edge of the resonance region. Therefore, ICRF heating creates a highly anisotropic fast particle distribution in both energy and orbit topology.

2.5.2. Neutral Beam Injection

The neutral beam injection (NBI) is a fast particle source which injects a beam of fast neutral atoms with high energy into the plasma. The energetic neutral atoms are created by extracting positive hydrogen or deuterium ions from an ion source. These ions are accelerated by an electric field to high velocities and neutralized by collisions with a gas target. However, not only hydrogen H^+ or deuterium D^+ ions are produced in the ion source but also ionized molecules like H_2^+ , H_3^+ , D_2^+ and D_3^+ . Since the electric potential is constant during the acceleration, the injected beam consists of atoms and molecules with an acceleration energy E_a according to the number of atoms, i.e. E_a , $E_a/2$ and $E_a/3$. Afterwards, the atoms and molecules propagate on straight lines into the plasma unaffected by the magnetic field. In the plasma, the atoms and molecules are ionized by collisions and charge exchange.

For the ASDEX Upgrade discharge #20853, deuterium was injected by NBI delivering a total power of 20 MeV. The acceleration energies were $E = 93$ keV, $E = 46.5$ keV and $E = 31$ keV for D^+ , D_2^+ and D_3^+ . The corresponding fast particle distribution can be calculated by the FAFNER code [47]. For discharge #20853 at the time $t = 5.0$ s, the NBI distribution [48] for approximately 19.000 particles is shown in figure 2.13.

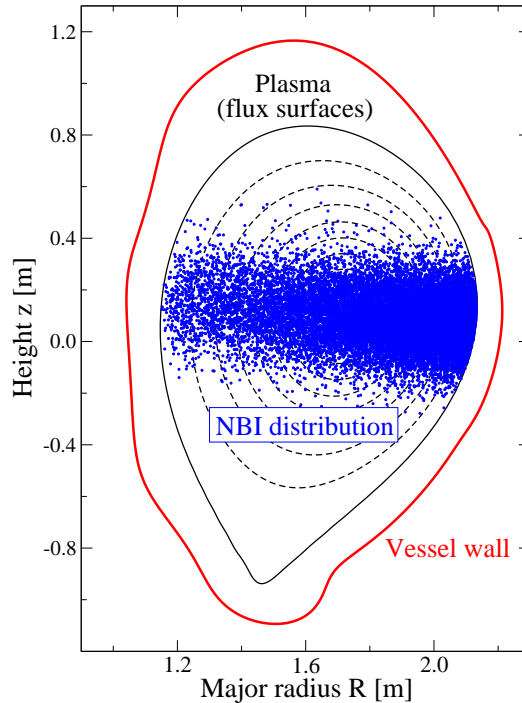


Figure 2.13.: ASDEX Upgrade: Fast particle distribution in the plasma due to neutral beam injection for discharge #20853 at time $t = 5.0$ s.

The particles are injected from the low field side (from the right side) at midplane. The deposited particle density decays exponentially with respect to the distance from its injection point into the plasma. The particles are mainly passing particles since the ratio between the parallel to the total velocity v_{\parallel}/v is between 0.3 till 0.8.

Such a particle distribution is able to interact with a NTM introduced in section 2.3.5. As a consequence, the heating of the background plasma is reduced at the NTM position. This will be investigated in section 4.6.

2.5.3. Fast Ion Loss Detector

Due to wave-particle interaction, it is possible that highly energetic particles are pushed onto loss trajectories, i.e. the ions leave the plasma and are lost at the vessel wall. These particles can be detected with a fast ion loss detector FILD [18] which is installed at ASDEX Upgrade. From the properties of the lost particles, it can be deduced where the particle orbits were located before they were lost and which particular wave has ejected the particles. For a better understanding of the deduced information, a short introduction into the functionality and the parameter range of the FILD is presented here.

At ASDEX Upgrade, the detector is located within the vessel above midplane on the LF side as shown in figure 2.14. The detector consists of a collimator, a scintillator plate and a CCD camera. It is able to measure gyro radii and pitch angles of highly energetic ions with a high temporal resolution. The sampling rate of 10 MHz gives the opportunity to determine in addition the loss frequency. This allows identifying the wave which ejects the ions. The spatial resolution is determined by a CCD camera recording the light pattern of the losses on the scintillator plate.

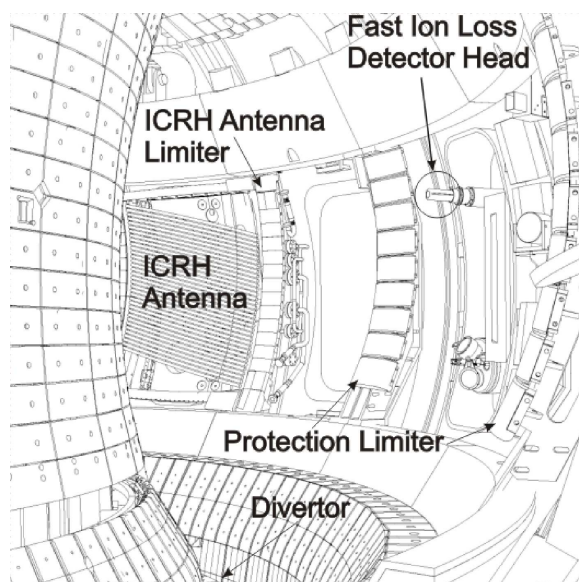


Figure 2.14.: Position of the FILD in the vessel of ASDEX Upgrade (sector 8). The detector head is movable towards the plasma.

2. Theoretical Background

The energetic ions enter the detector through the aperture slit and strike on the scintillator plate as shown in figure 2.15. The gyro radius of the fast particles determines the distance from the slit (Fig. 2.15 left). The pitch angle α defines the striking point on the plate (Fig. 2.15 right). With these values, the particle loss orbit in a reconstructed plasma equilibrium can be simulated.

The chosen geometry of the collimator enables the detection of fast ions with a gyro radius of $\rho_{\perp} \in [3 \text{ cm}, 12 \text{ cm}]$ and a pitch angle between $\alpha = 30^{\circ}$ (passing) and $\alpha = 87^{\circ}$ (trapped).

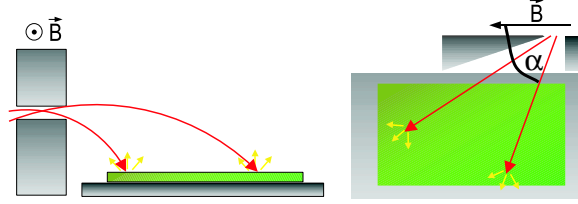


Figure 2.15.: *Schematic outline of the FILD functionality (left: side view, right: top view). The fast particles enter through the aperture slit and strike on the scintillator plate (green).*

Due to the magnetic field geometry introduced in section 2.2, the field line next to the detector is tilted against the horizontal plane. Therefore, the detector head is aligned parallel to \mathbf{B} , i.e. tilted by an angle of $\gamma \approx 13^{\circ}$, and is fixed during a discharge. Since the magnetic field evolves during a discharge, the slope of the magnetic field line next to the detector can vary by a small deviation of $\pm 2^{\circ}$.

Furthermore, it has been assumed [18] that the fast particles which enter the detector slit are propagating exactly along the magnetic field lines, i.e. no drifts. This is only valid in lowest order. In section 4.5, it will be shown that drifts have to be considered for a comparison between numerical simulations and experimental results.

3. Code Development

Based on the theoretical background introduced in the previous chapter a numerical model will be presented to study the interactions between highly energetic particles and Alfvén Eigenmodes. It is apparent that the wave-particle interaction is non-linear since both the MHD modes and the particles evolve in response to the collective motion of each other and thus require a self-consistent approach. Especially, the consequential change in the wave amplitude and the redistribution of fast particles are of tremendous interest. The model presented here is implemented in the non-linear, drift-kinetic, perturbative HAGIS code (HAmiltonian GuIding centre System) [12, 13] which is very well adapted to the problem. A limit of the original code is the spatial restriction of the simulation domain up to the separatrix. The redistributed particles crossing the last closed flux surface are not followed up to the first wall so that the determination of the wall load and the comparison with experimental fast ion loss diagnostics are impossible. In addition, not all particles are lost immediately, but re-enter the plasma again. Neglecting these fast ions corresponds to a serious underestimation of the mode drive. Furthermore, the conditions for the initialization of a particle distribution driving the modes unstable are not developed to full extent for the various heating schemes.

In this chapter the original state of the HAGIS code will be presented, followed by the code extension introducing a new coordinate system, the equations of motion outside the separatrix and an additional functional form for a fast particle distribution. A comparison between both coordinate systems implemented in the code will reveal the advantages and limits.

3.1. Introduction to the HAGIS code

Originally, the HAGIS code was developed by Simon Pinches in 1996. A similar implementation of the physics was carried out in the ORBIT code by White [49] before but the code uses different integration methods. For a better understanding of the following extension and improvements, the main aspects of the HAGIS code (version 2007) are summarized in this section. The depictions are lean to the work [12] in the broadest sense.

The HAGIS code solves a system of first order ordinary differential equations with initial conditions. Evolving the equations simultaneously advances the spatial location of the particles, their parallel velocity and the change in the particle distribution as well as the amplitude and the phase of the modes on the simulation grid. The domain and its appending equilibrium quantities are supplied by the equilibrium code HELENA [22] that solves the Grad-Shafranov equation [2]. Furthermore, the stability code CASTOR [50] provides the frequency and the spatial profiles of the MHD perturbation which is maintained to be fixed in its shape. The initial distribution and conditions of the energetic particles are specified in an input file supplied by the user.

Dealing with such a complex problem a representation has to be chosen that simplifies the equilibrium description and exploits as much as possible the symmetry properties of the magnetic field. As a consequence the equations of motion will be simplified but require a non-orthogonal coordinate system.

Using a Hamiltonian approach, the dynamical equations will be found by Newton's second law evolving the particle's coordinates under the influence of a given force and determining the constants of motion. An analogous procedure will reveal the wave equations for the evolution of the amplitudes and phases. The fast particle distribution represented by the particles acts on the waves and is modified by them, simultaneously. The representation of the distribution function will close the self-consistent description.

3.1.1. Boozer Coordinates

The coordinate system was primarily developed for the approximation of the guiding centre equations of motion. However, the coordinate construction becomes more important because it constitutes the neighbourhood conditions for the vacuum extension. For this reason, particular attention must be emphasized to the coordinate generation to reveal the best connection between both grids.

As indicated in section 2.2, an adoption of flux coordinates which are suited to the geometry of the magnetic field simplifies the dynamical equations significantly. A coordinate system which represents the magnetic field line as straight lines and expresses their components in flux functions as much as possible enables a desired description. Such a representation - referred to as Boozer coordinates - was found by Boozer [51] by using a specific choice of the Jacobian.

In general, the magnetic field determines the nested flux surfaces in a plasma. If in addition the magnetic field has a toroidal symmetry all equilibrium quantities such as the metric tensor and the magnetic field components are independent of the toroidal angle ζ , i.e. $\partial \mathbf{B} / \partial \zeta = 0$, so that the magnetic field (2.9) can be represented [21] in an equilibrium by

$$\mathbf{B} = \nabla \psi \times \nabla \theta + \nabla \zeta \times \nabla \psi_p, \quad (3.1)$$

where ψ_p and ψ are radial flux labels determined by the poloidal and toroidal flux, respectively. The poloidal angle is given by θ . Assuming that the contravariant radial magnetic field component vanishes, i.e. $\mathbf{B} \cdot \nabla \psi = 0$, \mathbf{B} can also be described by any two vectors orthogonal to the radial gradient [52],

$$\mathbf{B} = B_G \nabla \psi_p \times \nabla \theta + B_H (\nabla \psi_p \times \nabla \theta) \times \nabla \psi_p. \quad (3.2)$$

The magnetic components B_G and B_H are functions of ψ_p and θ only and need to be determined. From $\nabla \cdot \mathbf{B} = 0$, it is found that

$$B_H = \frac{h}{\mathcal{J} (\nabla \psi_p \times \nabla \theta)^2} \quad \text{and} \quad B_G = \frac{g}{\mathcal{J} (\nabla \psi_p \times \nabla \theta)^2}$$

with $h = h(\psi_p)$ and $g = g(\psi_p)$ being flux labels. Rewriting equation (3.2) yields

$$\mathbf{B} = \frac{1}{\mathcal{J} (\nabla\psi_p \times \nabla\theta)^2} \left[g(\psi_p) \nabla\psi_p \times \nabla\theta + h(\psi_p) (\nabla\psi_p \times \nabla\theta) \times \nabla\psi_p \right]. \quad (3.3)$$

The poloidal flux $\Psi_{\text{pol}} = 2\pi\psi_p$ can be calculated from the poloidal magnetic field component,

$$2\pi\psi_p = \frac{1}{2\pi} \int \int \int (\mathbf{B} \cdot \nabla\theta) \mathcal{J} d\psi_p d\theta d\zeta,$$

which is determined by equation (3.3) to be,

$$\mathbf{B} \cdot \nabla\theta = \frac{h(\psi_p)}{\mathcal{J}}. \quad (3.4)$$

Inserting into the integral reveals that

$$\begin{aligned} 2\pi\psi_p &= \frac{1}{2\pi} \int \int \int h(\psi_p) d\psi_p d\theta d\zeta \\ &= 2\pi \int h(\psi_p) d\psi_p \\ \Rightarrow h(\psi_p) &= 1. \end{aligned} \quad (3.5)$$

Using the covariant notation of a vector, the magnetic field can also be written as

$$\mathbf{B} = B_{\psi_p} \nabla\psi_p + B_{\theta} \nabla\theta + B_{\zeta} \nabla\zeta.$$

The covariant component can be found by taking the scalar product of equation (3.3) with the corresponding contravariant basis vectors,

$$B_{\psi_p} = \frac{1}{(\nabla\psi_p \times \nabla\theta)^2} \left[g (\nabla\psi_p \times \nabla\theta) \cdot (\nabla\theta \times \nabla\zeta) - \frac{(\nabla\psi_p \times \nabla\theta)}{\mathcal{J}} \right], \quad (3.6)$$

$$B_{\theta} = \frac{1}{(\nabla\psi_p \times \nabla\theta)^2} \left[g (\nabla\psi_p \times \nabla\theta) \cdot (\nabla\zeta \times \nabla\psi_p) + \frac{(\nabla\psi_p)^2}{\mathcal{J}} \right], \quad (3.7)$$

$$B_{\zeta} = g(\psi_p), \quad (3.8)$$

whereby it shows up that the toroidal covariant field component is already a flux label. One can choose the coordinate ζ so that the field lines are straight by defining

$$\zeta = -\phi - \nu(\psi, \theta) \quad (3.9)$$

where ϕ is the cylindrical angle and ν is a toroidal shift angle depending on the radial and poloidal position. Then, the local helicity $d\zeta/d\theta$ is defined via the magnetic fluxes derived

from equation (3.1),

$$\begin{aligned} \frac{d\zeta}{d\theta} &= \frac{\partial\psi_p}{\partial\psi} \\ \frac{\mathbf{B} \cdot \nabla\zeta}{\mathbf{B} \cdot \nabla\theta} &= \frac{B^\zeta}{B^\theta} = q(\psi_p) . \end{aligned} \quad (3.10)$$

The resulting safety factor $q(\psi_p)$ is independent of the poloidal angle θ and yields with (3.4) and (3.5) for the contravariant magnetic field components to

$$B^\theta = \frac{1}{\mathcal{J}} \quad \text{and} \quad B^\zeta = \frac{q(\psi_p)}{\mathcal{J}} . \quad (3.11)$$

Calculating the absolute value of the magnetic field by $B^2 = B_\theta B^\theta + B_\zeta B^\zeta$ together with some straight-forward calculation [12] and reorganizing the poloidal magnetic field component carries out that

$$B_\theta(\psi_p, \theta) = \mathcal{J}B^2 - gq . \quad (3.12)$$

Since the Jacobian is yet not defined, the quantity B_θ is set to a flux function $B_\theta \equiv I(\psi_p)$ by choosing the Jacobian \mathcal{J} to be

$$\mathcal{J} = \frac{I + gq}{B^2} . \quad (3.13)$$

So, the final covariant representation of \mathbf{B} is given by

$$\mathbf{B} = \delta(\psi_p, \theta)\nabla\psi_p + I(\psi_p)\nabla\theta + g(\psi_p)\nabla\zeta , \quad (3.14)$$

whereby the covariant component δ is a measure of non-orthogonality of the coordinate system and vanishes for circular equilibria. Again, it is worth to mention that the dependence of the covariant quantities g and I on the radial coordinate ψ_p only is due to the choice of the Jacobian. This is the important fact to simplify the following Hamiltonian formalism significantly. Furthermore, both quantities are related by definition to the toroidal current $2\pi I/\mu_0$ inside the flux surface ψ_p and the poloidal current $2\pi g/\mu_0$, respectively.

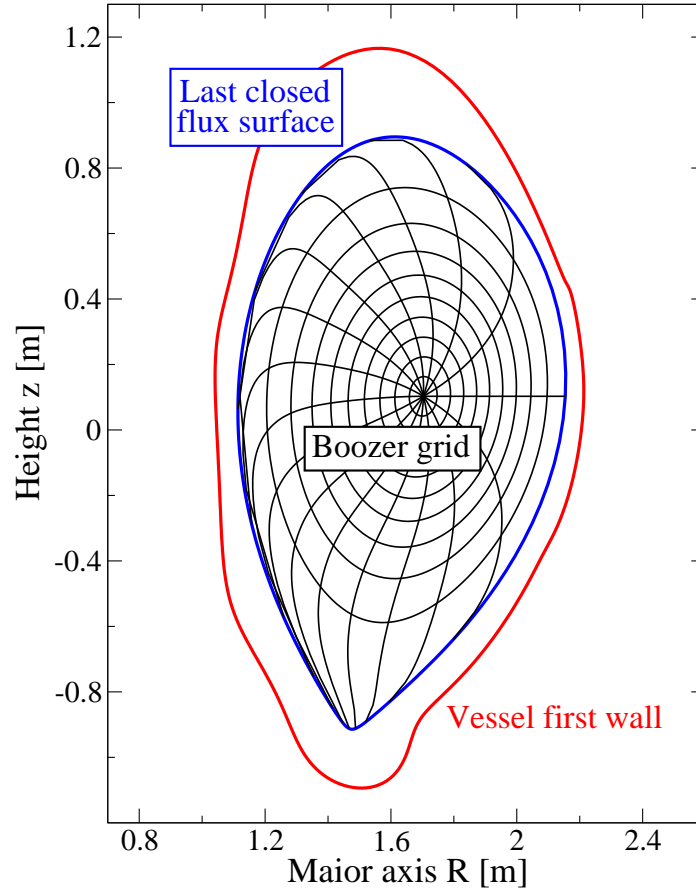


Figure 3.1.: *Boozer grid generation for ASDEX Upgrade discharge #21083. The last closed flux surface represents 99.9% of the radial distance from the magnetic axis to the separatrix.*

3.1.2. Wave-Particle Equations

After providing an equilibrium-adopted coordinate system, the wave-particle equations are derived from the Lagrangian of the complete system. For completeness, a short overview over the Lagrangian's constituents and the final set of equations are presented in this section. (For a detailed derivation see Appendix A.2 or [12])

The complete system can be expressed by a total Lagrangian \mathcal{L}_{sys} which consists of four components: a fast particle Lagrangian \mathcal{L}_{traj} describing the unperturbed trajectory of the ions, a wave-particle interaction Lagrangian \mathcal{L}_{int} calculating the perturbation for both in the presence of each other, a bulk Lagrangian \mathcal{L}_{bulk} taking into account the contributions of the background plasma and an electromagnetic Lagrangian \mathcal{L}_{em} involving the electromagnetic Alfvén wave itself.

$$\begin{aligned}
\mathcal{L}_{sys} &= \underbrace{\overbrace{\mathcal{L}_{traj}}^{\text{Particle Lagrangian}} + \mathcal{L}_{int}}_{\text{Wave equations}} + \underbrace{\overbrace{\mathcal{L}_{bulk} + \mathcal{L}_{em}}^{\text{Wave Lagrangian}}} \\
\end{aligned} \tag{3.15}$$

The only channel over which particles and waves can interact with each other is by transferring energy or toroidal momentum via the interaction Lagrangian. The transferred contributions are placed either into \mathcal{L}_{traj} or \mathcal{L}_{em} which depends on the gradients of the fast particle distribution and the resonance condition as explained in section 2.3.4. The bulk Lagrangian \mathcal{L}_{bulk} is considered to be static due to an invariant equilibrium.

Starting with the Lagrangian of the fast particles, the gyro-averaging procedure of Littlejohn [53] which reduces the canonical phase-space coordinates to be evolved, has shown that the guiding centre Lagrangian can be written as,

$$\mathcal{L}_{fp} = e \left(\mathbf{A} + \frac{v_{\parallel}}{\omega_c} \mathbf{B} \right) \cdot \dot{\mathbf{x}} + \frac{m}{e} \mu \dot{\xi} - \mathcal{H} , \tag{3.16}$$

where \mathcal{H} is the guiding centre Hamiltonian and \mathbf{x} and ξ are the spatial coordinates and the gyro-phase, respectively. The term inside the brackets is known as the modified vector potential $\mathbf{A}^* = \mathbf{A} + \rho_{\parallel} \mathbf{B}$ [11] using the parallel gyro radius $\rho_{\parallel} = v_{\parallel}/\omega_c$. The corresponding Hamiltonian is defined by

$$\mathcal{H} = \frac{m}{2} v_{\parallel}^2 + \mu B , \tag{3.17}$$

From the Lagrangian, the derived constants of motion for a guiding centre are the energy E which coincides with the Hamiltonian (3.17), the toroidal angular momentum P_{ζ} and the magnetic moment μ ,

$$P_{\zeta} = \rho_{\parallel} g - e \psi_p \tag{3.18}$$

$$\mu = \frac{m v_{\perp}^2}{2B} . \tag{3.19}$$

By a straight-forward derivation of the Hamiltonian done by White and Chance [49], the guiding centre equations of motions are

$$\begin{aligned} \dot{\psi}_p &= \frac{1}{D} \left[\rho_{\parallel} B^2 \left(g \frac{\partial \tilde{\alpha}}{\partial \theta} - I \frac{\partial \tilde{\alpha}}{\partial \zeta} \right) - \left(g \frac{\partial \tilde{\Phi}}{\partial \theta} - I \frac{\partial \tilde{\Phi}}{\partial \zeta} \right) \right. \\ &\quad \left. + \left(\rho_{\parallel}^2 B + \mu \right) \left(I \frac{\partial B}{\partial \zeta} - g \frac{\partial B}{\partial \theta} \right) \right], \end{aligned} \quad (3.20)$$

$$\dot{\theta} = \frac{1}{D} \left[\rho_{\parallel} B^2 (1 - \rho_c g' - g \alpha') + g \left\{ \left(\rho_{\parallel}^2 B + \mu \right) B' + \tilde{\Phi}' \right\} \right], \quad (3.21)$$

$$\dot{\zeta} = \frac{1}{D} \left[\rho_{\parallel} B^2 (\rho_c I' + q + I \alpha') - I \left\{ \left(\rho_{\parallel}^2 B + \mu \right) B' + \tilde{\Phi}' \right\} \right], \quad (3.22)$$

$$\begin{aligned} \dot{\rho}_{\parallel} &= \frac{1}{D} \left[\left(I \frac{\partial \tilde{\alpha}}{\partial \zeta} - g \frac{\partial \tilde{\alpha}}{\partial \theta} \right) \left\{ \left(\rho_{\parallel}^2 B + \mu \right) B' + \tilde{\Phi}' \right\} - (\rho_c I' + q + I \alpha') \frac{\partial \tilde{\Phi}}{\partial \zeta} \right. \\ &\quad \left. - (1 - \rho_c g' - g \alpha') \left\{ \left(\rho_{\parallel}^2 B + \mu \right) \frac{\partial B}{\partial \theta} + \frac{\partial \tilde{\Phi}}{\partial \theta} \right\} \right] - \frac{\partial \tilde{\alpha}}{\partial t}, \end{aligned} \quad (3.23)$$

whereby $\tilde{\alpha}$ is the amplitude of the vector potential along the magnetic field. The perturbed parallel gyro radius ρ_c and the denominator D are defined as

$$\rho_c = \rho_{\parallel} + \tilde{\alpha} \quad \text{and} \quad D = \rho_c (g I' - g' I) + I + g q.$$

The prime denotes the derivation with respect to the radial coordinate ψ_p . If the equilibrium functions $g(\psi_p)$, $I(\psi_p)$, $q(\psi_p)$ and $B(\psi_p, \theta)$ and the perturbation variable $\tilde{\alpha}(\psi_p, \theta, \zeta, t)$ are given a particle trajectory in a magnetic field with an electromagnetic wave present can be calculated.

The corresponding wave is described by the wave Lagrangian and can be written in general [43] as

$$\mathcal{L}_w = \underbrace{\sum_i \left[\frac{m}{2} v_i^2 + e (\mathbf{A}_i \cdot \mathbf{v}_i - \Phi_i) \right]}_{\mathcal{L}_{bulk}} + \underbrace{\frac{1}{2\mu_0} \int_V \left(\frac{1}{c^2} E^2 - B^2 \right) d^3x}_{\mathcal{L}_{em}}. \quad (3.24)$$

The equation expresses that a MHD perturbation is a balance between the plasma inertia represented by the bulk plasma particles labelled with i and the magnetic field line tension. It is assumed that the electrostatic potential Φ_i is cancelled everywhere in the plasma due to mobile electrons. The resulting Lagrangian [34] is expressed by

$$\mathcal{L}_w = \sum_k \frac{A_k^2 \dot{\sigma}_k}{\omega_k} E_k \quad \text{with} \quad E_k = \frac{1}{2\mu_0} \int_V \frac{|\nabla_{\perp} \Phi_k|^2}{v_A^2} d^3x, \quad (3.25)$$

where E_k is referred to as the wave energy of the k -th wave. The waves' degrees of freedom are described by the amplitude A_k and the phase σ_k which are combined in a complex amplitude term, $A_k(t) \cdot \exp[-i\sigma_k(t)]$, so that the phase is expressed by

$$\sigma_k = \arctan \left(\frac{\mathcal{I}m\{A_k e^{-i\sigma_k}\}}{\mathcal{R}e\{A_k e^{-i\sigma_k}\}} \right) = \arctan \left(\frac{R_k}{I_k} \right) \Rightarrow \dot{\sigma}_k = \frac{R_k \dot{I}_k - \dot{R}_k I_k}{A_k^2}. \quad (3.26)$$

It is worth to mention that only A_k and σ_k are able to vary but the eigenfunction of the mode which is supplied by the code CASTOR is fixed. Its representation is explained in the following.

The interaction Lagrangian for a particle ensemble n_p consists of two parts related to the vector and the scalar potential,

$$\mathcal{L}_{int} = \sum_{j=1}^{n_p} \left(\tilde{\mathbf{A}}_j \cdot \mathbf{v}_j - \tilde{\Phi}_j \right), \quad (3.27)$$

where the subscript j denotes the particle index. The quantity v_j is the inherent velocity of the particle whereas the perturbed vector and scalar potential $\tilde{\mathbf{A}}_j$ and $\tilde{\Phi}_j$ represent all contributions of the wave ensemble n_w acting on the particle j . Each wave labelled with k is composed by a sum of distinct poloidal eigenfunctions $\tilde{\phi}_{km}$ determined by the poloidal mode number m ,

$$\tilde{\Phi}_k = \sum_m \tilde{\phi}_{km}(\psi_p) e^{i(n_k \zeta - m\theta - \omega_k t)} = \sum_m \tilde{\phi}_{km}(\psi_p) e^{i\Theta} \quad (3.28)$$

with the wave vector \mathbf{k} and the corresponding parallel wave number k_{\parallel} ,

$$\mathbf{k} = n\nabla\zeta - m\nabla\theta \quad \text{and} \quad k_{\parallel} = n_k \zeta - m\theta. \quad (3.29)$$

so that the vector potential of the wave can be expressed by

$$\tilde{\alpha}_{km} = \frac{k_{\parallel}}{\omega_k B} \tilde{\phi}_{km}. \quad (3.30)$$

Substituting all expressions into the interaction Lagrangian (3.27) yields

$$\mathcal{L}_{int} = \sum_{j=1}^{n_p} \sum_{k=1}^{n_w} \frac{1}{\omega_k} \sum_m (k_{\parallel} v_{\parallel j} - \omega_k) \tilde{\phi}_{km}(\psi_p) e^{i\Theta}. \quad (3.31)$$

The Lagrangian calculates the full potential of all perturbations n_w at the position of each particle. Together with the wave Lagrangian, the Lagrangian becomes to

$$\mathcal{L}_{w+int} = \sum_{k=1}^{n_w} \frac{1}{\omega_k} \left[\sum_{j=1}^{n_p} \sum_m (k_{\parallel} v_{\parallel j} - \omega_k) \tilde{\phi}_{km}(\psi_p) e^{i\Theta} + E_k \left(R_k \dot{I}_k - \dot{R}_k I_k \right) \right]. \quad (3.32)$$

Varying the Lagrangian with respect to R_k and I_k results in

$$\dot{R}_k = \frac{1}{2E_k} \sum_{j=1}^{n_p} \sum_m (k_{\parallel} v_{\parallel j} - \omega_k) \mathcal{I}m\{\tilde{\phi}_{km}(\psi_p) e^{i\Theta}\}, \quad (3.33)$$

$$\dot{I}_k = \frac{1}{2E_k} \sum_{j=1}^{n_p} \sum_m (k_{\parallel} v_{\parallel j} - \omega_k) \mathcal{R}e\{\tilde{\phi}_{km}(\psi_p) e^{i\Theta}\}. \quad (3.34)$$

The wave equations form a set of $2 \times n_w$ first order differential equations evolving the amplitude A_k and the phase σ_k in time.

3.1.3. The δf Method

Although the set of equations for the fast particles and the waves has been derived, the model is still inappropriate for the simulation of a particle distribution in the presence of multiple waves. Initialising each particle of a realistic ensemble to fill the phase-space adequately, large computer resources are required leading into unfeasibility. Therefore, an approach is applied to reduce the number of differential equations by introducing quasi-particles which represent a particular ensemble of particles. The ansatz and the incorporation into the wave equations is described in this section.

In the ansatz of quasi-particles, called markers, it is assumed that each marker possesses a weight representing a different part of particle distribution function. This removes the initial condition of loading the markers as required for the fast particle distribution but gives rise of the possibility to accumulate in the region where the wave is present. The weight can alter in time, depending on the marker position governed by the equations of motion so that the represented part of the distribution changes. This technique is known as the δf method [14, 54, 55]. The crucial approach is the decomposition of the fast particle distribution into two parts: an analytically described background part f_0 and a small varying component δf ,

$$f = \underbrace{f_0(\Gamma^{(p)})}_{analytic} + \underbrace{\delta f(\Gamma^{(p)})}_{markers}, \quad (3.35)$$

where $\Gamma^{(p)}$ denotes the physical six dimensional phase-space consisting of the space and velocity components. The advantage of the δf method is that only the change of the distribution function f is represented by the markers. This method assumes that the background distribution f_0 is only slightly distorted through any interaction with a perturbation which is usually valid. This assumption leads to a substantial noise reduction in simulations [56].

The background part f_0 will be described by the unperturbed constants of motions,

$$f_0 = f_0(P_{\zeta}^{(0)}, E^{(0)}, \mu), \quad (3.36)$$

and yields in absence of any wave integrating over the whole phase-space to

$$n_0 = \int_V f_0(P_\zeta^{(0)}, E^{(0)}, \mu) d\Gamma^{(p)},$$

where n_0 is the total number of particles which is time-independent. So, it follows that without a sink or source

$$\delta n = \int_V \delta f d\Gamma^{(p)} = 0.$$

At that point it is obvious why δf has the property to be the change in the value of the distribution function describing the difference in the number of particles. It is supposed that a particle redistribution will occur due to a perturbation but without particle losses. The assumption is valid as long as the losses are much smaller than the total number of particles.

The evolution of δf is derived from the Vlasov equation which in the absence of sources and sinks becomes

$$0 = \frac{df}{dt} = \frac{df_0}{dt} + \frac{d\delta f}{dt} \quad \Rightarrow \quad \frac{d\delta f}{dt} = -\frac{df_0}{dt}.$$

Rewriting δf with respect to the ensemble of markers labelled with j and associated with distinct energies E_j and toroidal angular momentum $P_{\zeta j}$ leads to

$$\delta \dot{f}_j = \dot{E}_j \frac{\partial f_0}{\partial E_j} + P_{\zeta j} \dot{P}_{\zeta j} \frac{\partial f_0}{\partial P_{\zeta j}}, \quad (3.37)$$

whereby E_j and $P_{\zeta j}$ of each marker can vary due to wave-particle interaction, however the total energy of the system is conserved. The temporal change of both the energy and toroidal momentum is given [57] by

$$\frac{dE_j}{dt} = \frac{\partial \tilde{\Phi}_j}{\partial t} - \rho_{\parallel} B \cdot \frac{\partial \tilde{\alpha}_j}{\partial t} \quad \text{and} \quad \frac{dP_{\zeta j}}{dt} = \rho_{\parallel} B \cdot \frac{\partial \tilde{\alpha}_j}{\partial \zeta} - \frac{\partial \tilde{\Phi}_j}{\partial \zeta}. \quad (3.38)$$

Due to a finite number of markers the change in the number of particles δn_j by the discretization of the integral gives

$$\delta n_j(t) = \delta f_j(t) \cdot \Delta \Gamma_j^{(p)}(t). \quad (3.39)$$

After defining the change in the distribution function, the physical phase-space $\Gamma_j^{(p)}$ for each marker position needs to be determined revealing the difficulty that the volume element is compressible, i.e. it changes with the marker flow. The problem can be solved by defining the marker volume within the canonical phase-space $\Gamma_j^{(c)}$ which is incompressible due to Liouville's theorem and only needs to be calculated once. The canonical volume element relates to the physical phase-space by a Jacobian $J^{(pc)}$,

$$\Delta\Gamma_j^{(p)} = J^{(pc)} \cdot \Delta\Gamma_j^{(c)} . \quad (3.40)$$

Due to different particle distribution functions both in energy and space which are generated by several heating mechanisms described in section 2.5, an additional phase-space $\Gamma_j^{(u)}$ is required in which the markers are uniformly loaded due to their heating prerequisites. This offers the possibility to choose the phase-space coordinates adapted to the problem so that they coincide with the quantities in which the fast particle distribution, $f_0 = f_0(s, E, \lambda)$, is determined. The total relationship between the phase-spaces gives

$$\Delta\Gamma_j^{(p)} = J^{(pc)} \cdot J^{(cu)} \cdot \Delta U_j , \quad (3.41)$$

The uniformly loaded phase-space volume element is determined by

$$\Delta U_j = \frac{\int dU}{n_p} = \frac{(2\pi)^2 (v_{max} - v_{min}) (\lambda_{max} - \lambda_{min}) (s_{max} - s_{min})}{n_p} , \quad (3.42)$$

where $\lambda = v_{\parallel}/v$ is the ratio between parallel to total velocity and $s = \sqrt{\psi_p/\psi_p(a)}$ is the normalized radial coordinate. The index a denotes the last closed flux surface.

The derivation of the Jacobians $J^{(pc)}$ and $J^{(cu)}$ is straight-forward [12] but is not unique due to different initial velocity conditions. In general, for an isotropic distribution the Jacobians are expressed as

$$J^{(pc)} = \frac{\mathcal{J}B^2}{D} \quad \text{and} \quad J^{(cu)} = \frac{4\pi s\psi_p(a)Dv^2}{B^2} . \quad (3.43)$$

The inclusion of the δf method derived above into the wave equations is implemented intuitively yielding to

$$\dot{R}_k = \frac{1}{2E_k} \sum_{j=1}^{n_p} \delta f_j \Delta\Gamma_j^{(p)} \sum_m (k_{\parallel} v_{\parallel j} - \omega_k) \mathcal{I}m\{\tilde{\phi}_{km}(\psi_p) e^{i\Theta}\} , \quad (3.44)$$

$$\dot{I}_k = \frac{1}{2E_k} \sum_{j=1}^{n_p} \delta f_j \Delta\Gamma_j^{(p)} \sum_m (k_{\parallel} v_{\parallel j} - \omega_k) \mathcal{R}e\{\tilde{\phi}_{km}(\psi_p) e^{i\Theta}\} . \quad (3.45)$$

The only difference to the wave equations (3.33) - (3.34) is a weighting factor $\delta f_j \Delta\Gamma_j^{(p)}$ representing the change in the distribution function. This means that a fifth equation of motion (3.37) for each marker must be evolved in addition. The set of equations is now complete.

3.2. Extension of the HAGIS Code

In the previous section the relevant concepts with the corresponding model implemented in the original HAGIS code were introduced. But as mentioned before the code is only able to follow particle trajectories up to the last closed flux surface. Thus, significant information about the fast particle losses due to the wave-particle interactions is forfeit. They represent the crucial connection between the experimental measurements at the first wall and the redistribution of fast particles in the plasma centre. In addition, it allows a calculation of the heat loads to the walls by energetic ions. The extension in the vacuum region is not only relevant for a detailed comparison with fast ion losses in the experiment but it also gives the possibility to improve the initialization of a fast particle distribution deduced from ion losses.

In the following the concept of the vacuum coordinates will be presented which are extended from the Boozer coordinates. Together, both coordinates systems cover the whole domain up to the first wall. Then, the additional equations of motion required in the vacuum system will be derived from the general formalism [11] and validated with respect to the constants of motion's conservation. Finally, a implementation of an ICRH-generated fast particle distribution will provide the opportunity to simulate the wave-particle interactions under more realistic conditions. This allows for comparison to isotropic and NBI-generated distribution functions.

3.2.1. Vacuum Coordinates

Inside the vessel as shown in figure 2.1 the whole space can be divided into two regions: the plasma with closed flux surfaces and the vacuum region with open magnetic field lines. As shown in the section 3.1.1, inside the last closed flux surface the advantage of the Boozer coordinate system is the alignment to the magnetic field lines. Due to the problem-adaption, the equations of motion are simplified which results in a speed-up of the simulation time. Since the safety factor q increases to infinity at the separatrix, the coordinate system is not defined at the singularity which refuses a description by a solitary Boozer coordinate system. Nevertheless, field-aligned coordinates can still be applied in the vacuum region which necessitates a separation of the whole simulation domain into at least three particular coordinate systems under the retention of the singularity. This would produce numerical errors for particle trajectories crossing the coordinate boundaries several times.

However, the vacuum region can be represented by a single coordinate system if field alignment is given up. Thus, the speed-up in the simulation time related to field-aligned coordinates is lost but the coordinate system is extended consistently from the Boozer coordinates inside the plasma. The advantages of such a representation are not only the simulation of the wall load but also to account for fast particles with broad orbits re-entering into the plasma without numerical errors in particular. So, the complete fast particle distribution driving the mode unstable is considered. For these reasons, a consistent field-unaligned coordinate system is chosen.

The notation of the new vacuum coordinate system $\{\psi_v, \theta_v, \zeta_v\}$ denoting the radial, poloidal and toroidal coordinate resembles to the Boozer coordinate system $\{\psi_p, \theta, \zeta\}$ but differs significantly in its content. The key point is to remove the flux label predefinition

applied to straight-field line coordinates but to retain the radial coordinate label approximately in the vacuum region for an exact contiguous connection to the Boozer coordinates at an intersection surface ψ_i . This chosen flux surface is both the outermost radial Boozer coordinate ψ_{\max} and the innermost radial vacuum coordinate $\psi_{v,\min}$ as shown in figure 3.2.

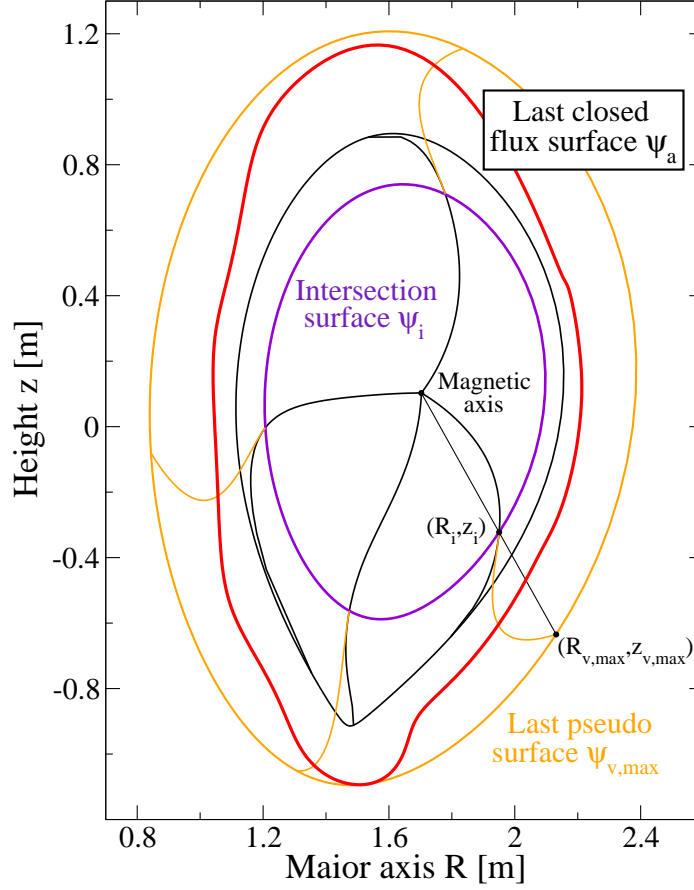


Figure 3.2.: Vacuum grid generation for an ASDEX Upgrade discharge. Exemplary radial Boozer coordinate lines are prolonged into the vacuum region.

It is favourable to define the radial curves in the cylindrical coordinate system $\{R, \phi, z\}$ by analytical functions which connect exactly to each Boozer coordinate line and thus prolongate smoothly from the intersection surface. The continuity conditions for the prolongation of a radial coordinate line into the vacuum region referring to the cylindrical coordinate R are summarized under

$$R_i|_{\psi_i} = R_{v,\min}|_{\psi_i}, \quad \frac{\partial R}{\partial \psi_p}|_{\psi_i} = \frac{\partial R}{\partial \psi_v}|_{\psi_i}, \quad \frac{\partial^2 R}{\partial \psi_p^2}|_{\psi_i} = \frac{\partial^2 R}{\partial \psi_v^2}|_{\psi_i}, \quad R_{v,\max}, \quad (3.46)$$

whereby these conditions are also applied to z and ϕ , respectively. The left-hand sides of the first three conditions, the position and the derivatives, are known on the Boozer coordinate system. The fourth condition determines the outermost radial point on the last pseudo flux surface (Fig. 3.2). This surface is an enlargement of the intersection surface including

the vessel wall. The corresponding $(R_{v,\max}, \phi_{v,\max}, z_{v,\max})$ -coordinates to each radial coordinate line on this surface $\psi_{v,\max}$ are generated by a straight line through the magnetic axis and the coordinates (R_i, ϕ_i, z_i) on the intersection surface. The procedure avoids grid coarsening at the outboard midplane as shown in figure 3.1 where significant fast particle losses are expected.

It is convenient to apply cubic polynomials $R^j = R^j(\psi_v)$, $\phi^j = \phi^j(\psi_v)$ and $z^j = z^j(\psi_v)$ to the set conditions. The analytical functions trace out each radial vacuum coordinate line denoted by the index j . All coordinate lines only depend on the vacuum coordinate ψ_v which is determined to be,

$$\psi_v \in [\psi_{v,\min} = \psi_i, \psi_{v,\max}] , \quad (3.47)$$

to avoid radial discontinuities at the intersection surface. The maximal limit $\psi_{v,\max}$ can be greater than the flux ψ_a at the last closed flux surface. It is worth to mention that an equal spacing of the radial coordinate ψ_v for all polynomials creates nested pseudo surfaces (Figure 3.3)! Finally, the whole simulation domain inside the vessel is divided among the Boozer and the vacuum grid.

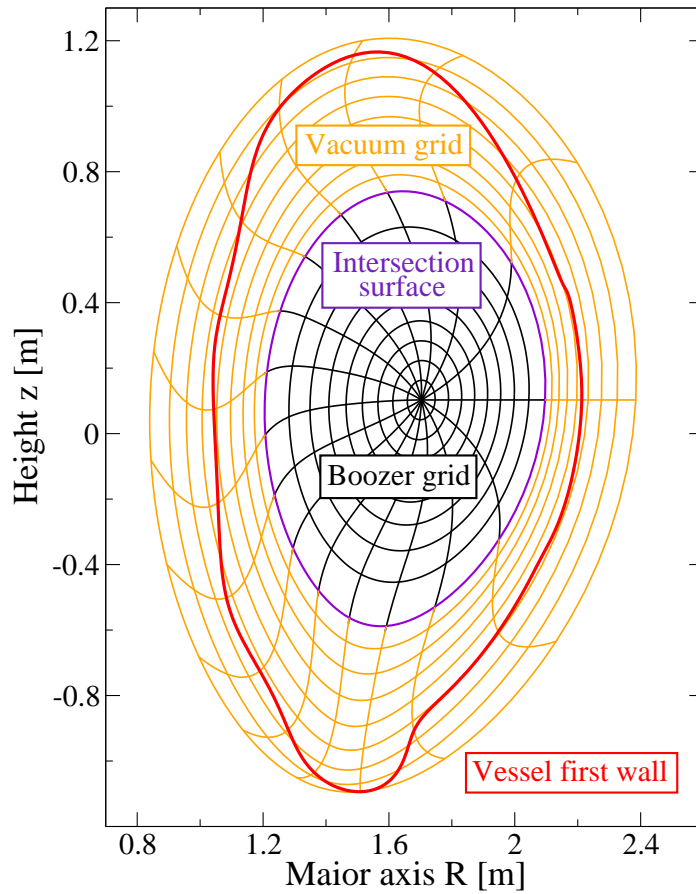


Figure 3.3.: Final vacuum grid with nested pseudo surfaces.

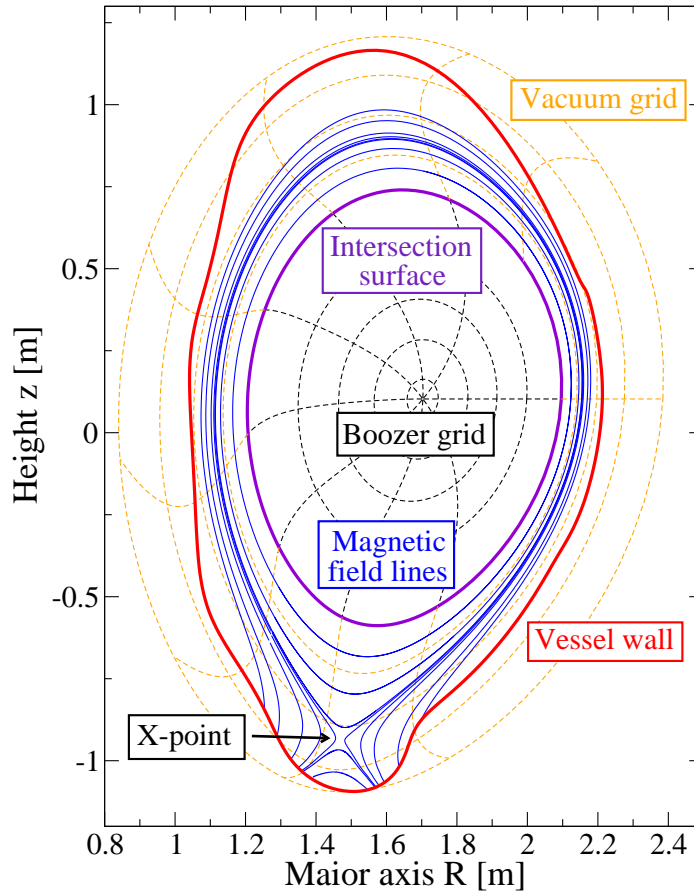


Figure 3.4.: *Electron trajectories which coincide with the magnetic field lines are calculated on the vacuum grid. The X-point is clearly visible.*

Although the radial pseudo surfaces in the vacuum region diverge from the open flux surfaces (Fig. 2.1), especially near the X-point, particle trajectories can be precisely followed in the vacuum region. This is shown at the example of simulating electron trajectories (Fig. 3.4) near the separatrix which coincide with the magnetic field lines nearly perfectly due to their small mass. So, the X-point becomes visible as a repulsion point for each particle trajectory.

Near the intersection surface, a part of the Boozer coordinate system is replaced by the vacuum grid. This is due to the fact that the metric coefficients given on the Boozer grid (3.46) exhibit a strong oscillatory behaviour as the safety factor increases strongly near the separatrix, $q \rightarrow \infty$. By a truncation, the more inward located metric coefficients from which the derivatives are extracted provide a sufficient basis.

As mentioned before, the first derivatives, together with the absolute value on the intersection surface, determine the condition for a consistent grid extension. However, the prescription of the second derivative accounts for the consistent extension of the magnetic field because the components of the magnetic field are composed with the metric coefficients.

After the generation of the vacuum grid, the corresponding basis vectors of the vacuum

coordinate system are derived from the cylindrical basis vectors via the transformation rule,

$$\mathbf{e}_{i'} = \mathbf{e}_j \frac{\partial w^j}{\partial u^{i'}} , \quad (3.48)$$

where the prime denotes the tangent-basis vector of the new coordinate system. (If the subscript and the superscript appear in an equation on the same side always the summation convention is used as in (3.48).) Written explicitly, the vacuum tangent-basis vectors are

$$\begin{aligned} \mathbf{e}_{\psi_v} &= \mathbf{e}_R \frac{\partial R}{\partial \psi_v} + \mathbf{e}_\phi \frac{\partial \phi}{\partial \psi_v} + \mathbf{e}_z \frac{\partial z}{\partial \psi_v} , \\ \mathbf{e}_{\theta_v} &= \mathbf{e}_R \frac{\partial R}{\partial \theta_v} + \mathbf{e}_\phi \frac{\partial \phi}{\partial \theta_v} + \mathbf{e}_z \frac{\partial z}{\partial \theta_v} , \\ \mathbf{e}_{\zeta_v} &= \mathbf{e}_R \frac{\partial R}{\partial \zeta_v} + \mathbf{e}_\phi \frac{\partial \phi}{\partial \zeta_v} + \mathbf{e}_z \frac{\partial z}{\partial \zeta_v} . \end{aligned}$$

Since a poloidal cross section of the Boozer coordinate system for a fixed toroidal angle ζ is curved, the poloidal vacuum plane has also to be curved for an contiguous extension. Therefore, the toroidal vacuum angle is determined similar to Boozer coordinates (3.9) by

$$\zeta_v = -\phi - \nu_v(\psi_v, \theta_v) , \quad (3.49)$$

where ν_v is a toroidal shift angle. The transformation rules simplify to

$$\mathbf{e}_{\psi_v} = \mathbf{e}_R \frac{\partial R}{\partial \psi_v} - \mathbf{e}_\phi \frac{\partial \nu}{\partial \psi_v} + \mathbf{e}_z \frac{\partial z}{\partial \psi_v} , \quad (3.50)$$

$$\mathbf{e}_{\theta_v} = \mathbf{e}_R \frac{\partial R}{\partial \theta_v} - \mathbf{e}_\phi \frac{\partial \nu}{\partial \theta_v} + \mathbf{e}_z \frac{\partial z}{\partial \theta_v} , \quad (3.51)$$

$$\mathbf{e}_{\zeta_v} = -\mathbf{e}_\phi . \quad (3.52)$$

All derivatives which appear in equation (3.50) are calculated analytically due to the cubic polynomials whereas the derivations with respect to the poloidal angle in equation (3.51) are determined by bi-cubic splines evaluated at each vacuum grid node.

Generating the metric coefficients $g_{ij} = \mathbf{e}_i \cdot \mathbf{e}_j$ for the vacuum coordinate system is simplified because the tangent-basis vectors within the cylindrical coordinates are orthogonal and defined to be unit vectors, except the angular basis vector,

$$\mathbf{e}_\phi = \frac{1}{R} \hat{e}_\phi ,$$

so that the metric coefficients are written as

$$\begin{aligned}
 g_{\psi_v \psi_v} &= \left(\frac{\partial R}{\partial \psi_v} \right)^2 + R^2 \left(\frac{\partial \nu}{\partial \psi_v} \right)^2 + \left(\frac{\partial z}{\partial \psi_v} \right)^2, \\
 g_{\psi_v \theta_v} &= \frac{\partial R}{\partial \psi_v} \frac{\partial R}{\partial \theta_v} + R^2 \frac{\partial \nu}{\partial \psi_v} \frac{\partial \nu}{\partial \theta_v} + \frac{\partial z}{\partial \psi_v} \frac{\partial z}{\partial \theta_v}, \\
 g_{\psi_v \zeta_v} &= R^2 \frac{\partial \nu}{\partial \psi_v}, \\
 g_{\theta_v \theta_v} &= \left(\frac{\partial R}{\partial \theta_v} \right)^2 + R^2 \left(\frac{\partial \nu}{\partial \theta_v} \right)^2 + \left(\frac{\partial z}{\partial \theta_v} \right)^2, \\
 g_{\theta_v \zeta_v} &= R^2 \frac{\partial \nu}{\partial \theta_v}, \\
 g_{\zeta_v \zeta_v} &= R^2.
 \end{aligned}$$

So, the determinant g of the metric is defined as

$$\begin{aligned}
 g &= \begin{vmatrix} g_{\psi_v \psi_v} & g_{\psi_v \theta_v} & g_{\psi_v \zeta_v} \\ g_{\theta_v \psi_v} & g_{\theta_v \theta_v} & g_{\theta_v \zeta_v} \\ g_{\zeta_v \psi_v} & g_{\zeta_v \theta_v} & g_{\zeta_v \zeta_v} \end{vmatrix} \\
 &= \left(\left(\frac{\partial R}{\partial \psi_v} \right)^2 + \left(\frac{\partial z}{\partial \psi_v} \right)^2 \right) \left(\left(\frac{\partial R}{\partial \theta_v} \right)^2 + \left(\frac{\partial z}{\partial \theta_v} \right)^2 \right) - \left(\frac{\partial R}{\partial \psi_v} \frac{\partial R}{\partial \theta_v} + \frac{\partial z}{\partial \psi_v} \frac{\partial z}{\partial \theta_v} \right)^2 \\
 &= \left(\frac{\partial R}{\partial \psi_v} \right)^2 \left(\frac{\partial z}{\partial \theta_v} \right)^2 + \left(\frac{\partial z}{\partial \psi_v} \right)^2 \left(\frac{\partial R}{\partial \theta_v} \right)^2 - 2 \frac{\partial R}{\partial \psi_v} \frac{\partial R}{\partial \theta_v} \frac{\partial z}{\partial \psi_v} \frac{\partial z}{\partial \theta_v}.
 \end{aligned}$$

Further simplification leads to

$$\begin{aligned}
 g &= \left(g_{\psi_v \psi_v} - \frac{g_{\psi_v \zeta_v}^2}{g_{\zeta_v \zeta_v}} \right) \left(g_{\theta_v \theta_v} - \frac{g_{\theta_v \zeta_v}^2}{g_{\zeta_v \zeta_v}} \right) - 2 \left(g_{\psi_v \theta_v} - \frac{g_{\psi_v \theta_v} g_{\theta_v \zeta_v}}{g_{\zeta_v \zeta_v}} \right) \\
 &= g_{\psi_v \psi_v}^* g_{\theta_v \theta_v}^* - 2 g_{\psi_v \theta_v}^*. \tag{3.53}
 \end{aligned}$$

revealing that g does not depend on the toroidal shift angle ν_v or its derivatives. The angle was introduced to the vacuum coordinates for an contiguous connection. Since its original function for straight-field lines in the Boozer coordinate system is dispensable, the angle is chosen in such a way that the extreme values of the Jacobian are minimized for a well-behaved metric.

It has been shown that the generation of the vacuum grid and its metric represents a contiguous connection to the Boozer coordinate system and its magnetic field components. Nevertheless, the X-point behaviour is covered. It has to be mentioned that an experimental sign convention for all quantities has been carried out strictly so that a comparison to the experiment is possible.

3.2.2. Connection of two Equilibrium Reconstructions

After the generation of the vacuum grid, the required magnetic field components have to be provided by an equilibrium code. The original code implementation only requires an equilibrium reconstruction within the separatrix which is not extendable into the vacuum region. Therefore, two equilibria have to be mapped at the intersection surface.

For the whole simulation domain, an equilibrium reconstruction is supplied by the CLISTE code [58] which solves the Grad-Shafranov equation,

$$\nabla^* \psi_p = R \frac{\partial}{\partial R} \left(\frac{1}{R} \frac{\partial \psi_p}{\partial R} \right) + \frac{\partial^2 \psi_p}{\partial z^2} = -\mu_0 R^2 p' - \mu_0^2 f f' \quad (3.54)$$

where the prime denotes the derivation with respect to the poloidal flux label ψ_p . The two scalar functions $p = p(\psi_p)$ and $f = f(\psi_p)$ are the pressure and the relation to the toroidal magnetic field,

$$f = \frac{RB_\phi}{\mu_0} . \quad (3.55)$$

The profiles of the right-hand side in equation (3.54) are supplied by measurements and assumptions about their shape. The poloidal flux label on the left-hand side is solved for the profiles with a free boundary. The final result ψ_p and the corresponding equilibrium quantities depend on (R, z) . The last closed flux surface ψ_a and the profiles serve as input to the equilibrium code HELENA [22] which solves the Grad-Shafranov equation for a fixed boundary condition. The key point is that the results are given inverted, i.e. $R(\psi_p, \theta)$. So, the transformation from a straight field line coordinate system to the Boozer coordinates is much less influenced by interpolation errors than a transformation from the cylindrical to the Boozer coordinate system. This procedure generates a sufficiently well-behaved metric in the Boozer coordinate system from which an extension into the vacuum region is possible. So, the HELENA-generated equilibrium is maintained inside the intersection surface, the CLISTE-generated equilibrium [59] provides the magnetic field components required for the vacuum region.

Due to the equilibrium representation, a tiny discontinuity appears at the intersection surface which has to be fixed. Although the deviation in the sub-per cent area in the poloidal flux is very small, discontinuities in the second derivative may become intolerably large. Thus, an adaption of the CLISTE-generated poloidal flux Ψ_{pol} given on a rectangular (R, z) -grid to the radial flux function $\psi_p = \Psi_{\text{pol}}/2\pi$ within the intersection surface is required. The modification is accomplished in such a way that following conditions

$$\begin{aligned} 2\pi\psi_p|_{\psi_i} &= \Psi_{\text{pol}}|_{\psi_i} , \\ \frac{\partial}{\partial \psi_p} (2\pi\psi_p) \Big|_{\psi_i} &= \frac{\partial \Psi_{\text{pol}}}{\partial \psi_v} \Big|_{\psi_i} , \\ \frac{\partial^2}{\partial \psi_p^2} (2\pi\psi_p) \Big|_{\psi_i} &= \frac{\partial^2 \Psi_{\text{pol}}}{\partial \psi_v^2} \Big|_{\psi_i} = 0 , \end{aligned}$$

are fulfilled exactly at the intersection surface. The so constructed poloidal flux Ψ_{pol}^* deviates slightly from the originally generated flux matrix by CLISTE near the intersection surface. Away from the intersection surface at larger radial coordinates, the flux matrix approaches the equilibrium reconstruction by CLISTE again. This approximate quantity also deviates from the equilibrium reconstruction only in the sub-per cent area and represents the basis of the magnetic field components' derivation.

According to Maxwell's equation, a divergence-free magnetic field is ensured at each node of the vacuum grid. Due to axisymmetry, $\partial/\partial\zeta_v = 0$, the equation is

$$\nabla \cdot \mathbf{B} = \frac{1}{J_v} \frac{\partial}{\partial u^i} (J_v B^i) = \frac{\partial}{\partial \psi_v} (J_v B^{\psi_v}) + \frac{\partial}{\partial \theta_v} (J_v B^{\theta_v}) = 0, \quad (3.56)$$

where J_v is the Jacobian in the vacuum coordinate system,

$$J_v = \mathbf{e}_{\psi_v} \cdot \mathbf{e}_{\theta_v} \times \mathbf{e}_{\zeta_v} = \sqrt{g(g_{i,j})}. \quad (3.57)$$

The equation (3.56) is fulfilled by the fact that the radial and poloidal contra-variant components are defined by the modified poloidal flux,

$$B^{\psi_v} = -\frac{2\pi}{J_v} \frac{\partial \Psi_{\text{pol}}^*}{\partial \theta_v} \quad \text{and} \quad B^{\theta_v} = \frac{2\pi}{J_v} \frac{\partial \Psi_{\text{pol}}^*}{\partial \psi_v}. \quad (3.58)$$

It is worth to mention that at the intersection surface the radial contra-variant component equals zero due to the definition of Ψ_{pol}^* being a flux function,

$$0 = B^{\psi_p} = \mathbf{B} \cdot \nabla \psi_p = \mathbf{B}_v \cdot \nabla \psi_v = B^{\psi_v}, \quad (3.59)$$

but this is not valid on the residually vacuum grid due to the absence of flux surface alignment so that

$$\mathbf{B}_v \cdot \nabla \psi_v = B^{\psi_v}(\psi_v, \theta_v) \neq 0 \quad \text{for} \quad \psi_v \in]\psi_i, \psi_{v,\text{max}}]. \quad (3.60)$$

This arising radial magnetic field components highlights that the coordinate grid is not a straight-field line system, in contrast to the Boozer system.

Furthermore, the toroidal magnetic component is supplied by the function f (equation 3.55) yielding the co-variant component,

$$B_{\zeta_v} = R B_\phi, \quad (3.61)$$

which is connected to the corresponding Boozer component by the conditions,

$$B_\zeta|_{\psi_i} = B_{\zeta_v}|_{\psi_i} \quad \text{and} \quad \left. \frac{\partial B_\zeta}{\partial \psi_p} \right|_{\psi_i} = \left. \frac{\partial B_{\zeta_v}}{\partial \psi_v} \right|_{\psi_i} . \quad (3.62)$$

The other co- and contravariant magnetic field components are generated via the transformation equation, $B_i = B^j g_{ij}$, and the metric coefficients,

$$B^{\zeta_v} = \left(B_{\zeta_v} - B^{\psi_v} g_{\psi_v \zeta_v} - B^{\theta_v} g_{\theta_v \zeta_v} \right) / g_{\zeta_v \zeta_v} , \quad (3.63)$$

$$B_{\psi_v} = B^{\psi_v} g_{\psi_v \psi_v} + B^{\theta_v} g_{\psi_v \theta_v} + B^{\zeta_v} g_{\psi_v \zeta_v} , \quad (3.64)$$

$$B_{\theta_v} = B^{\psi_v} g_{\psi_v \theta_v} + B^{\theta_v} g_{\theta_v \theta_v} + B^{\zeta_v} g_{\theta_v \zeta_v} . \quad (3.65)$$

In contrast to straight-field line systems, the magnetic field depends on both the radial and poloidal coordinate. Accordingly, this also applies to the total magnetic field strength which is calculated by

$$B_v^2 = B^{\psi_v} B_{\psi_v} + B^{\theta_v} B_{\theta_v} + B^{\zeta_v} B_{\zeta_v} . \quad (3.66)$$

Since the modified poloidal flux and the grid of the vacuum coordinate system coincide up to the second derivative with the corresponding quantities of the Boozer coordinate system at the intersection surface, all vacuum magnetic field components match to their correspondents up to the first derivative. This supplies a continuous and differentiable magnetic field everywhere.

The procedure for the combination of two reconstructed equilibria has created an approximate equilibrium which satisfies the condition of a consistent, slowly locally-varying magnetic field connection allowing for the conservation of the magnetic moment [2],

$$\frac{d\mu}{dt} = 0 . \quad (3.67)$$

This constitutes the requirement for the invariance of the guiding centre energy [53] in the absence of a perturbation. Due to the modification of the poloidal flux Ψ_{pol} and the function f , the Grad-Shafranov equation is not fulfilled up to the precision the original reconstructed CLISTE equilibrium but the sub-per cent deviation does not interfere relevant physics.

In contrast to that negligible deviation, an unfavourable issue arises due to the interpolation of physical quantities. As shown before, the magnetic field is divergence-free at the vacuum grid points. At intermediate grid points, the components and the Jacobian are calculated by separate bi-cubic splines. This procedure generates a resulting magnetic field which is not divergence-free exactly so that the over-all numerical error affects the invariance of the toroidal angular momentum P_ζ . However, increasing the grid resolution allows to control the invariance of P_ζ .

So, it has to be validated by benchmarks between the Boozer and the vacuum coordinate system (section 3.3) that the usage of the constructed magnetic field in the vacuum region

is applicable. It will be demonstrated that the deviation from the invariance of P_ζ is acceptable and much less than the effects of an MHD perturbation. Thus, the vacuum coordinate system justifies its application for the simulation of fast particles beyond the separatrix.

3.2.3. Equations of Motion

The gyro-averaging procedure which leads to the drift kinetic equations of motion has been described by Littlejohn [60, 53] and Northrop [61] explicitly. The resulting equations and the corresponding constants of motion are used as a starting point and transferred into the vacuum coordinate system.

By the derivation of the gyro-averaged Lagrangian (Appendix A.2), the guiding centre equations of motion (in normalized units) are

$$\dot{\mathbf{X}} = \frac{1}{B_{\parallel}^*} \left[U \mathbf{B}^* + \epsilon \hat{b} \times \mu \nabla B \right], \quad (3.68)$$

$$\dot{U} = -\frac{\mu}{B_{\parallel}^*} \mathbf{B}^* \cdot \nabla B, \quad (3.69)$$

with

$$\mathbf{B}^* = \nabla \times \mathbf{A}^* = \mathbf{B} + \epsilon U \nabla \times \hat{b}, \quad (3.70)$$

$$B_{\parallel}^* = B + \epsilon U (\hat{b} \cdot \nabla \times \hat{b}), \quad (3.71)$$

whereby \mathbf{X} and U are the three components of the spatial location and the parallel velocity of the guiding centre along the magnetic field line in general. The quantity \mathbf{B}^* is the modified magnetic field and its absolute value along the field line is described by B_{\parallel}^* . The quantity ϵ is defined as

$$\epsilon = \frac{\rho_{\perp}}{L} \quad \text{with} \quad L = \frac{|\nabla B|}{B}. \quad (3.72)$$

It is the ratio of the particle's gyro radius to scale length L over which the magnetic field varies but acts to describe the order of various terms.

A closer investigation of the modified magnetic field (3.70) has to be undertaken to clarify its meaning. In the Boozer coordinate system, the additional term results in

$$\epsilon U \nabla \times \hat{b} = \frac{\epsilon U}{JB} \begin{pmatrix} 0 \\ -\frac{\partial g}{\partial \psi_p} \\ \frac{\partial I}{\partial \psi_p} - \frac{\partial B_{\psi_p}}{\partial \theta} \end{pmatrix},$$

which is the deviation of the equilibrium field line within the flux surface. Since the toroidal angular momentum (3.18) in the absence of a perturbation only consists of variables depending on the radial coordinate, this small additional term would only marginally affect P_ζ .

Due to the misalignment of the vacuum coordinate surfaces with the flux surfaces, the term has still to be maintained although it is of order $\mathcal{O}(\epsilon)$. The neglect would corrupt the conservation of the angular momentum P_ζ [53] in an axisymmetric system.

Starting from the basic equation (3.68)

$$\dot{\mathbf{X}} = \frac{U (\mathbf{B} + \epsilon U \nabla \times \hat{b})}{B_{\parallel}^*} + \frac{\epsilon \mu \hat{b} \times \nabla B}{B_{\parallel}^*},$$

the first term can be converted via the vector relation (A.1) so that the equation of motion is written as

$$\begin{aligned} \dot{\mathbf{X}} &= \frac{U \left\{ \mathbf{B} + \epsilon U \left[\hat{b} (\hat{b} \cdot \nabla \times \hat{b}) + \hat{b} \times (\hat{b} \cdot \nabla) \hat{b} \right] \right\}}{B + \epsilon U (\hat{b} \cdot \nabla \times \hat{b})} + \frac{\epsilon \mu \hat{b} \times \nabla B}{B_{\parallel}^*} \\ &= U \hat{b} + \frac{\epsilon \mu \hat{b} \times \nabla B}{B_{\parallel}^*} + \frac{\epsilon U^2 \hat{b} \times (\hat{b} \cdot \nabla) \hat{b}}{B_{\parallel}^*}. \end{aligned} \quad (3.73)$$

It can be seen that the parallel velocity U can be separated from the modified magnetic field B^* and is parallel to B exactly. Using vector relation (A.1) for the third term again the equations are rewritten to

$$\dot{\mathbf{X}} = \underbrace{U \hat{b}}_{\text{Parallel motion}} + \underbrace{\frac{\epsilon \mu \hat{b} \times \nabla B}{B_{\parallel}^*}}_{\text{Mirror force}} + \underbrace{\frac{\epsilon U^2}{B_{\parallel}^*} \left[\nabla \times \hat{b} - \hat{b} (\hat{b} \cdot \nabla \times \hat{b}) \right]}_{\text{Curvature force}} \quad (3.74)$$

As mentioned before, the first term represents the guiding centre propagation along the magnetic field line. The second and third term are drift terms due to the mirror force acting on the perpendicular velocity and the curvature force $\kappa = (\mathbf{B} \cdot \nabla) \mathbf{B}$, respectively. The curvature force appears due to toroidicity and pressure induced effects which are represented by the first and the second part of the third term.

Considering the equation of motion (3.69) for the parallel velocity U , it would be advantageous to transform the equation of motion to the parallel gyro radius ρ_{\parallel} implemented in the code yet. The result is

$$\begin{aligned} \dot{\rho}_{\parallel} &= \frac{d}{dt} \left(\frac{U}{B} \right) = \frac{1}{B} \frac{dU}{dt} - \frac{U}{B^2} \frac{dB}{dt} \\ &= \frac{1}{B} \left(\dot{U} - \rho_{\parallel} \mathbf{v} \cdot \nabla B \right). \end{aligned}$$

A detailed decomposition into co- and contravariant components which are implemented in the HAGIS code is shown in the appendix A.3. The final equations of motion in physical

units are given by

$$v^{s_v} = (C_1 - C_3 K) b^{s_v} - \frac{C_2}{J_v} \cdot b_{\zeta_v} \frac{\partial B}{\partial \theta_v} + \frac{C_3}{J_v} \frac{\partial b_{\zeta_v}}{\partial \theta_v} \quad (3.75a)$$

$$v^{\theta_v} = (C_1 - C_3 K) b^{\theta_v} + \frac{C_2}{J_v} \cdot b_{\zeta_v} \frac{\partial B}{\partial s_v} - \frac{C_3}{J_v} \frac{\partial b_{\zeta_v}}{\partial s_v} \quad (3.75b)$$

$$v^{\zeta_v} = (C_1 - C_3 K) b^{\zeta_v} + \frac{C_2}{J_v} \cdot \left(b_{s_v} \frac{\partial B}{\partial \theta_v} - b_{\theta_v} \frac{\partial B}{\partial s_v} \right) + \frac{C_3}{J_v} \left(\frac{\partial b_{\theta_v}}{\partial s_v} - \frac{\partial b_{s_v}}{\partial \theta_v} \right) \quad (3.75c)$$

$$\dot{\rho}_{\parallel} = \frac{1}{\omega_c} \left[\dot{v}_{\parallel} - \rho_{\parallel} \frac{q_c e}{m} \left(v^{s_v} \frac{\partial B}{\partial s_v} + v^{\theta_v} \frac{\partial B}{\partial \theta_v} \right) \right]. \quad (3.75d)$$

with the equation of motion for the parallel velocity \dot{v}_{\parallel} written as

$$\dot{v}_{\parallel} = C_{\parallel} \left[\left(b^{s_v} + \frac{\rho_{\parallel}}{J_v} \frac{\partial b_{\zeta_v}}{\partial \theta_v} \right) \frac{\partial B}{\partial s_v} + \left(b^{\theta_v} - \frac{\rho_{\parallel}}{J_v} \frac{\partial b_{\zeta_v}}{\partial s_v} \right) \frac{\partial B}{\partial \theta_v} \right]. \quad (3.76)$$

The variables are determined by

$$K = \hat{b} \cdot (\nabla \times \hat{b}),$$

and

$$C_{\parallel} = -\frac{\mu}{m(1 + \rho_{\parallel} K)}, \quad C_1 = \rho_{\parallel} \omega_c,$$

$$C_2 = \frac{\mu}{q_c e B (1 + \rho_{\parallel} K)}, \quad C_3 = \frac{\omega_c \rho_{\parallel}^2}{(1 + \rho_{\parallel} K)}.$$

Here, the radial coordinate ψ_v (3.47) is finally transformed to

$$s_v = \sqrt{\frac{\psi_v}{\psi_a}} \quad \text{with} \quad s_v \in [s_i, s_{v,\max}] \quad (3.77)$$

for normalization advantages. A smooth connection for the normalized coordinate s_v is also guaranteed whereby the maximal value can exceed 1.

Given the equilibrium function B and the unit vectors b^{s_v} , b^{θ_v} , b^{ζ_v} , b_{s_v} , b_{θ_v} and b_{ζ_v} , particle trajectories can be accurately followed in the vacuum region. This is achieved by remaining the constants of motion invariant during the integration path. The magnetic momentum and the energy of the guiding centre were obtained before

$$\mu = \frac{mv_{\perp}^2}{2B} \quad , \quad E = \frac{mv_{\parallel}^2}{2} + \mu B . \quad (3.78)$$

The toroidal angular momentum can be derived directly from the Lagrangian by

$$\begin{aligned} P_{\zeta_v} &= \frac{\partial \mathcal{L}}{\partial \dot{\zeta}_v} = \frac{\partial}{\partial \dot{\zeta}_v} \left[e (\mathbf{A} + \rho_{\parallel} \mathbf{B}) \cdot \mathbf{v} - \frac{m}{2} v_{\parallel}^2 - \mu B \right] \\ &= \frac{\partial}{\partial \dot{\zeta}_v} \left[\frac{m}{2} v_{\parallel}^2 + e \mathbf{A} \cdot \mathbf{v} - \mu B \right] \\ &= m b_{\zeta_v} v_{\parallel} + e A_{\zeta_v} \\ &= m b_{\zeta_v} v_{\parallel} - e R A_{\phi, phys} \\ &= e (\rho_{\parallel} b_{\zeta_v} B - \Psi_{pol}) . \end{aligned} \quad (3.79)$$

It seems that the result is identical to equation (3.18) which is applied for Boozer coordinates. The subtle difference is that all variables are functions of the radial and poloidal coordinate, $b_{\zeta_v} = b_{\zeta_v}(\psi_v, \theta_v)$, $B = B(\psi_v, \theta_v)$ and $\Psi_{pol} = \Psi_{pol}(\psi_v, \theta_v)$. This implies a more difficult conservation of P_{ζ} due to more dependencies. Its conservation is investigated when the vacuum region is benchmarked against the original version.

3.2.4. Virtual Fast Ion Loss Diagnostic

Having derived the equations which describe the motion of highly energetic ions in the vacuum region and the corresponding constants of motion it is almost possible to perform simulations and the corresponding losses. But due to the fact that the equations are derived for the guiding centre of a particle, the gyro motion has to be dealt with separately. The geometrical and physical effects related to this aspect are discussed in the following.

From the equations of motion (3.74) it can be clearly seen how the guiding centre evolves in the magnetic field. However, the particle gyrates around the guiding centre. So, the strike point of a lost particle on the vessel first wall (Fig. 3.5) is a point which is separated from the position of the guiding centre trajectory by the current gyro radius. Therefore, the treatment of the gyro radius is important over the whole vacuum region to determine realistic losses.

Without the treatment of gyromotion, some particles in the vacuum region would be treated as confined which are actually lost as shown in figure 3.6. This is especially valid for highly energetic particles with energies of $E \geq 1$ MeV with a corresponding gyro radius of approximately $\rho_{\perp} \geq 9$ cm. In addition, an unrealistic interaction of these particles with the MHD modes would result in an unphysical drive mechanism. If these ions are finally lost, the strike points on the vessel wall can be different.

Simulating the gyrating particles as a ring which is oriented perpendicular to the magnetic field line and propagates along the guiding centre resolves the problem. This is a good approximation to the helix because the gyro frequency $\omega_c = eB/m_i$ is at least one order higher than the poloidal precession frequency ω_{θ} , $\omega_c \gg \omega_{\theta}$. If a particle is lost, the inter-

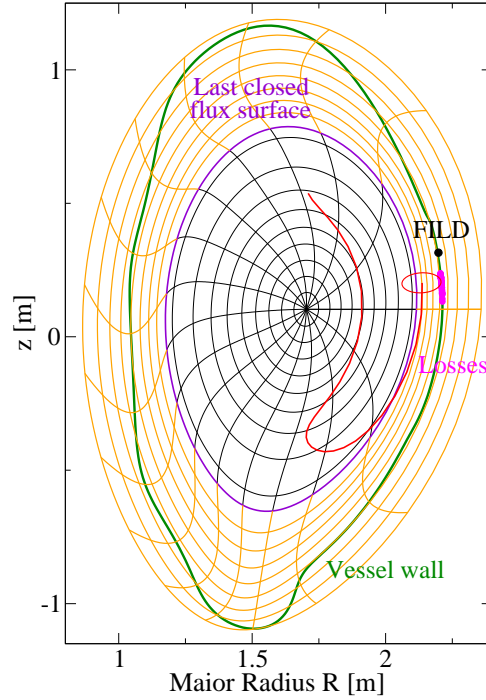


Figure 3.5.: Trajectory of a lost trapped ion with an energy $E = 800$ keV taking into account its gyro motion. Further hitting points of lost particles are displayed for slightly different start conditions. The entrance slit of the fast ion loss diagnostic FILD (section 2.5.3) is plotted.

section of the ring with the first wall determines its hitting point (R_{fw}, z_{fw}) . Furthermore, the following values are determined for each marker:

- t : Time after the initialization
- E : Energy $E = E(t)$ which might deviate from the initial energy $E_0 = E(t_0)$
- ρ_{\perp} : Gyro radius of the lost particle
- λ : Cosine of the pitch angle α , $\lambda = \cos \alpha = v_{\parallel}/v$
- δf : Change in the fast particle distribution
- B_{gc} : Magnetic field at the last guiding centre position

The lost particle positions are distributed over the whole vessel so that a virtual fast particle diagnostic exists everywhere, not only at the position of the entrance slit of the FILD as shown in figure 3.5. However, a single point will not deliver sufficient loss data due to its spatial restriction. Therefore, an extended range at the first wall must be chosen. Regarding to the figure 3.6, a trapped energetic ion with an energy of $E = 800$ keV is lost which has been started at its bounce point, i.e. $\lambda = 0$. Changing either the starting position horizontally or vertically by 1 cm or the energy by 20 keV, different impacts points over a

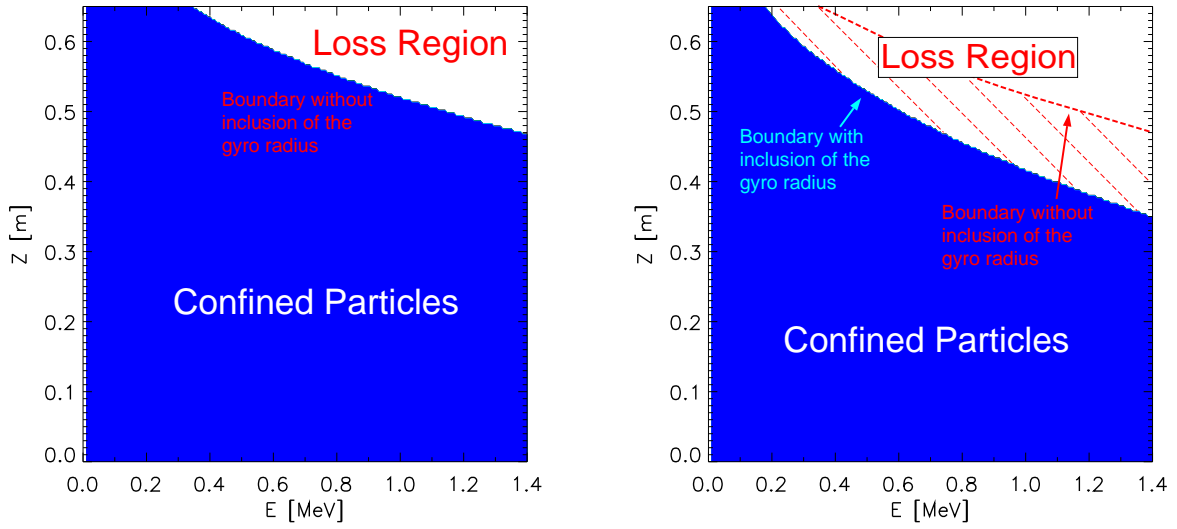


Figure 3.6.: Trapped particles having their bounce points above the magnetic axis are initialized for various vertical positions z and energies E . The confinement of the guiding centres without (left) and with inclusion of FLR effects (right) are shown. Only the latter leads to the correct loss boundary.

vertical range at the first wall of $\Delta z \approx 13$ cm appear. The hitting points are very sensitive to small deviations at the particle initialization. Therefore, the detector range has to be considered accordingly.

3.2.5. ICRH-generated Fast Particle Distribution

Auxiliary heating methods like ICRH or neutral beam injection are applied for the production of a hot plasma in ASDEX Upgrade. Thereby, different distribution functions of fast particles are generated which differ significantly in space, energy and pitch angle regarding to the heating method. As a consequence, MHD modes which are present in the plasma will be driven unstable [25, 34] in differential manner by the varying fast particle initializations so that the losses of energetic particles can also differ strongly. In the original version of the HAGIS code, two distributions of fast particles are available: a NBI-generated function and an isotropic function in the pitch angle variable. Thus, an implementation of a distribution generated by ICRF heating is advantageous and allows for comparison to existing distribution functions.

The distribution functions implemented in the original HAGIS code are described by analytical functions and are separable in space, energy and pitch variable λ ,

$$f_0(P_\zeta, E, \mu) \rightarrow f(s) \cdot f(v) \cdot f(\lambda) \quad (3.80)$$

Both initializations allow for arbitrary functions in energy E and radial coordinate s but fill the angular phase-space equally. The unique difference is determined by the pitch variable λ . For the isotropic case, the distribution is $f(\lambda) = \text{const.}$ whereas for the NBI-generated

distribution the pitch variable is singular at $\lambda = 1$.

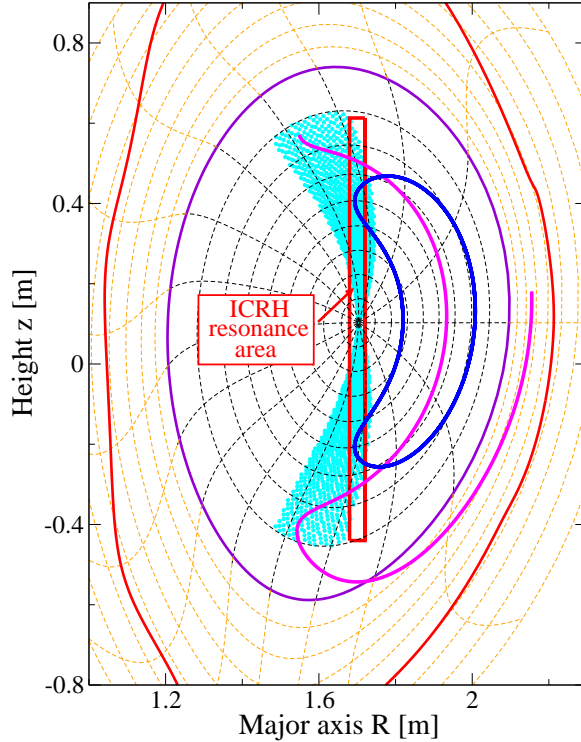


Figure 3.7.: The resonance area of the on-axis ICRF heating (red) is represented by a spatial distribution function which is limited in poloidal angle (cyan). Most particles (magenta) which are not inside the resonance layer are lost immediately. Thus, only particles (blue) are maintained which represent the ICRH-generated distribution in good approximation.

The mechanism of an on-axis ICRF heating was explained in section 2.5.1. Due to a localized resonance conditions at the magnetic axis, the resulting fast particle distribution differs from both functions above, especially in the spatial poloidal initialization. The red square in figure 3.7 illustrates the plasma region at which the ICRH power is deposited, i.e. where the bounce points of the trapped particles are located. In practice, a distribution function which represents such an area exactly can not be described by an analytical function. For the sake of feasibility, two poloidal angle segments are chosen which represent the upper and lower half of the ICRF heated region. Near the magnetic axis the segments coincide sufficiently whereas the condition is not fulfilled at larger radial positions. Fortunately, many particles whose turning points are on the high field side are promptly lost (magenta) so that the ICRH-generated distribution is represented in good approximation [45].

The functions $f(\theta)$ and $f(\lambda)$ are shown in figure 3.8 and correspond to the spatial distribution as shown in figure 3.7. The markers are isotropically initialized around two angles, $\theta_1 = 1.4$ and $\theta_2 = 4.9$, within an interval of $\Delta\theta = 0.3$ poloidally and around $\lambda = 0.0$ within an interval of $\Delta\lambda = 0.2$ for the pitch variable in the uniformly distributed phase-space ΔU_j (3.42). Determining the phase-space adapted to a single marker yields

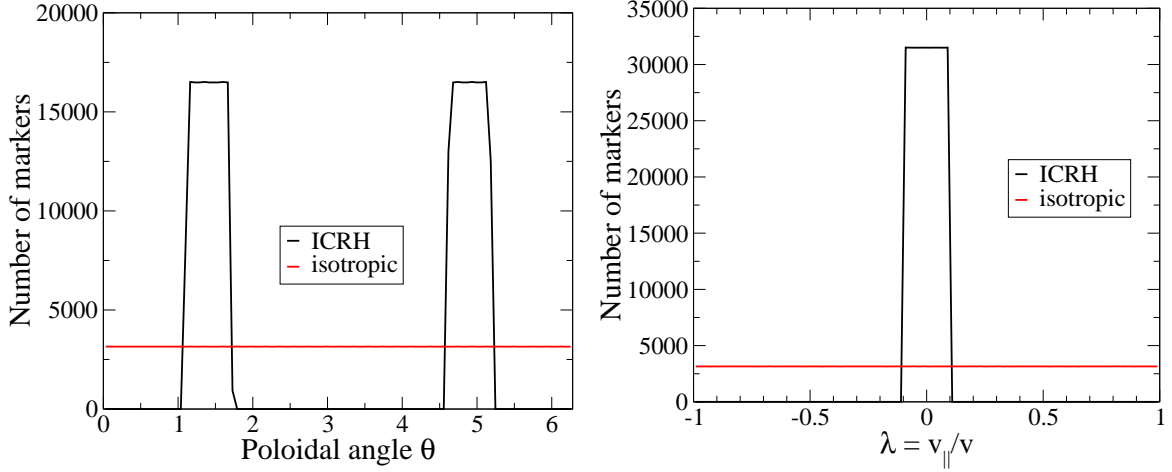


Figure 3.8.: Initial functions $f(\theta)$ and $f(\lambda)$ for an isotropic and an ICRH generated fast particle distribution in the uniformly-loaded phase-space \mathcal{U} . The integral of the curves equals the total number of initialized markers (315000).

$$\begin{aligned}
 \Delta U &= \frac{\int dU}{n_p} \\
 &= \frac{2\pi \sum_i (\theta_{i,max} - \theta_{i,min}) (s_{max} - s_{min}) (v_{max} - v_{min}) (\lambda_{max} - \lambda_{min})}{n_p} \\
 &= \frac{4\pi \Delta\theta (s_{max} - s_{min}) (v_{max} - v_{min}) \Delta\lambda}{n_p}. \tag{3.81}
 \end{aligned}$$

Although the markers are loaded around two poloidal angles, the whole poloidal domain on the low field side will be rapidly filled after the initialization by particles. Since the poloidal angle ranges between 0 and 2π , the poloidal domain consists of two poloidal segments between $[0, \theta_1 + \Delta\theta/2]$ and $[\theta_2 - \Delta\theta/2, 2\pi]$. The equi-distribution of the fast particles in space is the sufficient criterion to maintain the Jacobians (3.43) derived for an isotropic distribution. Thereby, integral boundaries for the poloidal and pitch variable has to be taken into account for the determination of the volume-averaged fast particle beta, $\langle\beta_f\rangle$,

$$\begin{aligned}
 \langle\beta_f\rangle_V &= C \cdot \left\langle \frac{2p}{B^2} \right\rangle = C \cdot \left\langle \frac{2n_0 \int v^2 f_0 d^3v}{B^2} \right\rangle \\
 &= C \cdot \left\langle \frac{8\pi^2 n_0 f(s) f(\theta) \cdot \int v^2 f(v) f(\lambda) d^3v}{B^2} \right\rangle \\
 &= C \cdot 8\pi^2 n_0 \frac{\int_{\theta_2 - \frac{\Delta\theta}{2} - 2\pi}^{\theta_1 + \frac{\Delta\theta}{2}} \int_{-\frac{\Delta\lambda}{2}}^{\frac{\Delta\lambda}{2}} \left(\frac{v}{B}\right)^2 f_0 \mathcal{J} ds d\theta dv d\lambda}{V_{Torus}} \tag{3.82}
 \end{aligned}$$

with the separation of the fast particle distribution of

$$f_0 \rightarrow f(s) \cdot f(\theta) \cdot f(v) \cdot f(\lambda) . \quad (3.83)$$

The fast particle beta determines the number of particles represented by a marker and therefore has an influence on the mode drive. The parameter C in equation (3.82) is a normalization quantity determined by a prescribed $\langle \beta_f \rangle$.

The implementation of a simplified ICRH generated distribution function implies a first step for a realistic fast particle distribution. But for the current status of the code, it is more important that it gives the opportunity for a comparison to an isotropic distribution function. This allows for an inspection which particle species is responsible for the drive of an MHD mode and to which amount.

3.3. Validation of Vacuum Coordinates

The drift kinetic particle orbits of the HAGIS code were benchmarked extensively against the analytical theory [12]. Since the extension of the HAGIS code exhibits a completely different representation of the coordinate system and the equations of motion, the first step is to compare the particle trajectories and the constants of motion in particular with orbits calculated on the Boozer coordinate system.

The first investigation directs to particle trajectories performed on the vacuum and the Boozer coordinate grid separately. Therefore, a large inward-extension of the vacuum coordinates is performed to verify an entire particle trajectory as shown in figure 3.9. Only the simulation domain between the intersection surface and the last closed flux surface is important because only this space is covered by both grids. It can be observed that the poloidal projection of the particle orbit simulated on the vacuum grid matches nearly perfectly the trajectory on the Boozer grid. The difference accounts for the use of two different equilibrium reconstructions from CLISTE and HELENA for the different coordinate systems.

In this context, a key issue for the treatment of fast particles is the conservation of the constants of motion, the magnetic momentum μ , energy E and the toroidal angular momentum P_ζ . As pointed out in section 3.2.2, the magnetic field is exactly divergence-free at the grid points only. Since, the magnetic momentum is conserved intrinsically and the particle energy does not depend on the magnetic field strength, the toroidal angular momentum only is affected. The effect can be minimized by a high grid resolution.

To test the angular momentum conservation, a trapped highly energetic particle (Fig. 3.9) with an energy of $E = 800$ keV is simulated for several poloidal orbits on both grids investigating the deviation of the energy δE and the momentum δP_ζ defined by

$$|\delta E| = \left| \frac{E(t) - E(t_0)}{E(t_0)} \right| \quad \text{and} \quad |\delta P_\zeta| = \left| \frac{P_\zeta(t) - P_\zeta(t_0)}{P_\zeta(t_0)} \right|. \quad (3.84)$$

From figure 3.10 it can be seen that both constants of motion are conserved up to $\delta E = \delta P_\zeta \approx 10^{-8}$ on the Boozer coordinate system for a radial and poloidal grid reso-

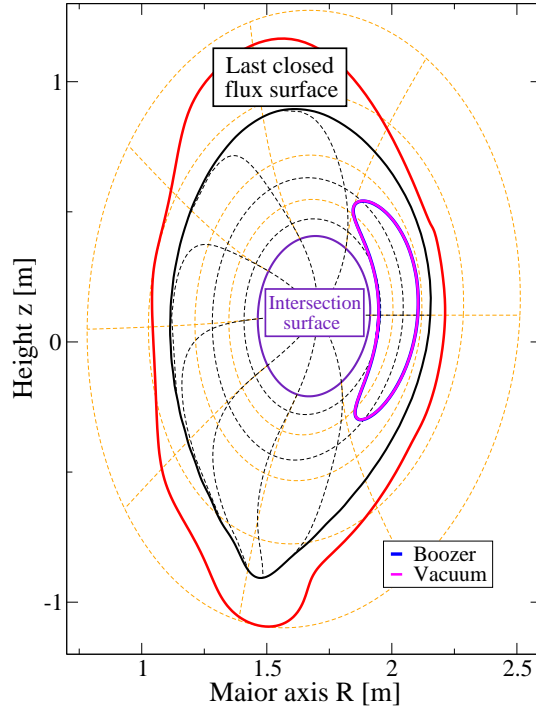


Figure 3.9.: Two trapped particle trajectories with identical start conditions ($E = 800$ keV) but one is performed within the Boozer grid (blue), the other within the vacuum grid (magenta).

lution of (200x256). The conservation of the energy in the vacuum grid is guaranteed at least to the same order, mostly better. This is due to the inclusion of order $\mathcal{O}(\epsilon)$ within the modified magnetic field (3.70) in the equations of motion.

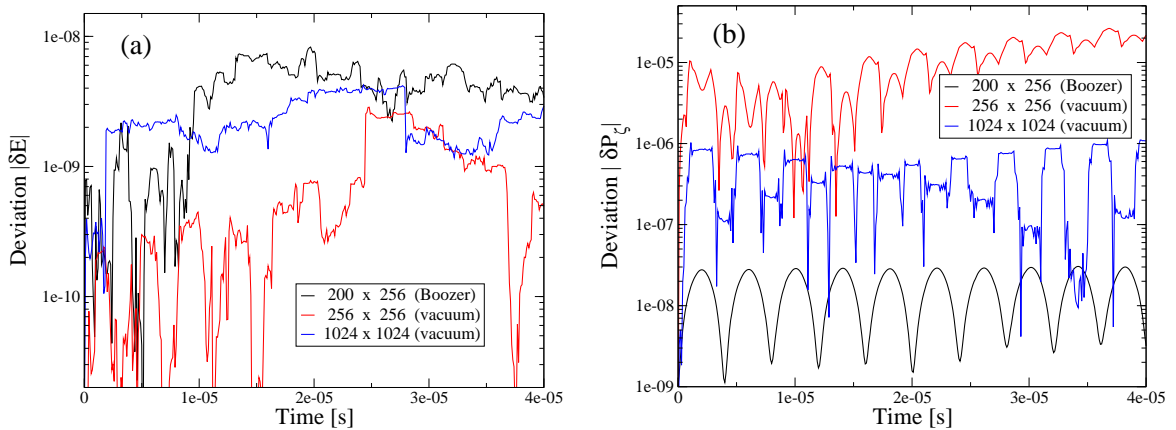


Figure 3.10.: Deviation of the constants of motion, energy (a) and toroidal momentum (b), for a trapped particle with $E = 800$ keV (Fig. 3.9) performed for different vacuum grid resolutions.

On the contrary, the time traces for the conservation of P_ζ show a different accuracy and shape. Within the curve calculated on the Boozer grid, a single particle orbit can be well detected. After a complete orbit, the deviation in P_ζ is minimal and at least one orders of magnitude smaller than at the position of greatest radial distance from the start position. The changes in the curve on the vacuum grid are however sharp and refer to the particle motion along a pseudo surface. This indicates that the poloidal spacing is more relevant than the radial resolution.

Altogether, the toroidal momentum is only conserved up to an order of 10^{-5} for the lowest and 10^{-6} for the highest grid resolutions. The difference to the Boozer coordinate system amounts to two till three orders of magnitude. The size of the grid cell varies from four times to half the size of the corresponding Boozer grid cell. If the distribution of the whole simulation domain between both coordinate systems is chosen as shown in figure 3.3, the size of the grid cells in a (200x256)-Boozer grid resembles to a resolution of (512x512) in the vacuum grid. Such a resolution is sufficient to ensure a maximal deviation of 10^{-6} in the toroidal angular momentum so that changes of at least $\delta P_\zeta \approx 10^{-3}$ due to MHD modes can be well-distinguished.

Since no mode and therefore no wave-particle interaction are present on the vacuum coordinate grid, a very poor resolution would be sufficient in principle. The constants of motion for lost particles would only exhibit a small numerical error due to the resolution. However, the conservation for the particles which enter the plasma again is crucial so that the mode drive inside the plasma is not corrupted. It would be underestimated in the original code version without the vacuum extension as these particles are not taken into account.

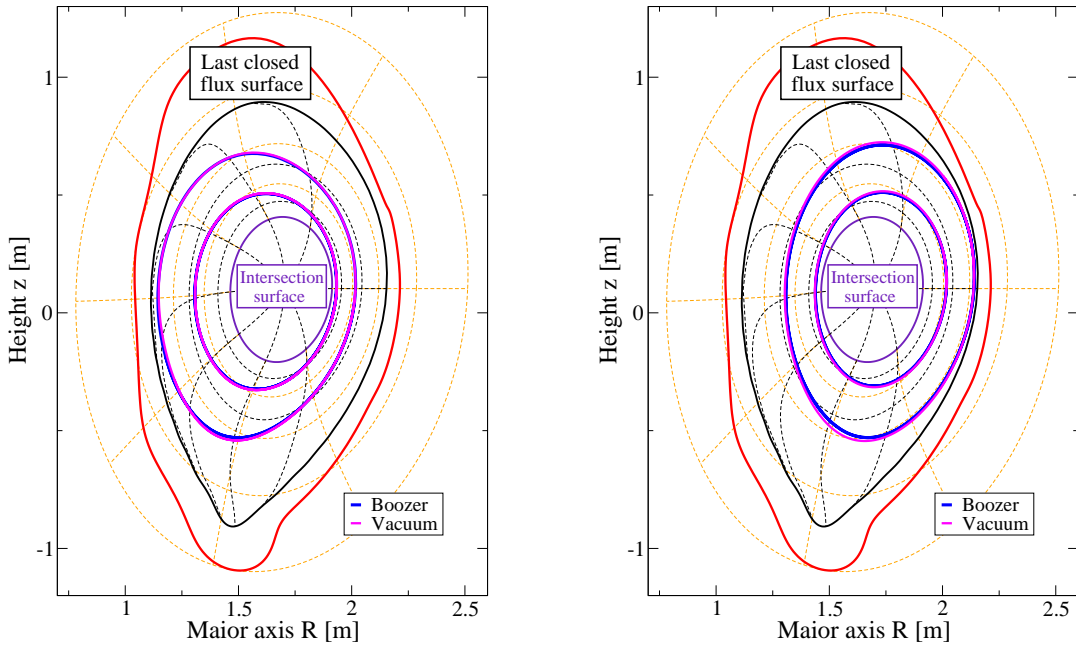


Figure 3.11.: Co-passing (left) and counter-passing (right) particle traces with identical start conditions ($E = 800$ keV, midplane, low field side). In each case one trace is performed within the Boozer grid (blue), the other within the vacuum grid (magenta).

3. Code Development

Furthermore, trajectories of passing particles at various radial positions are performed, both on the Boozer and the vacuum grid with a grid resolution of (256x256). The particle trajectories at radial surfaces near the intersection surface are nearly congruent but trajectories at larger radial positions are only slightly deviating as well. The reason for the deviation is the use of different equilibrium reconstructions which resemble in the vicinity of the intersection surface better than near the separatrix.

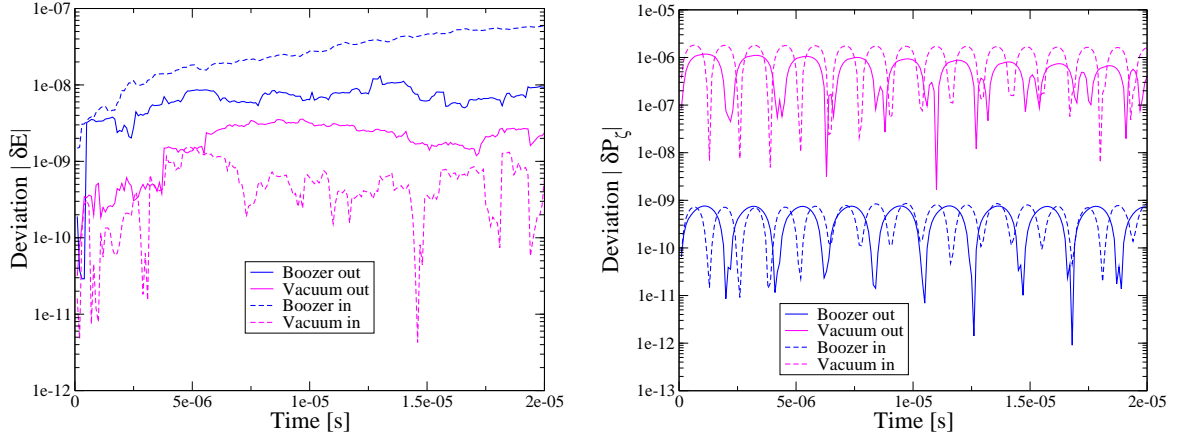


Figure 3.12.: Deviation of the energy and the toroidal momentum for the co-passing particles (Fig. 3.11 left) performed on both coordinate grids with the same resolution (256x256).

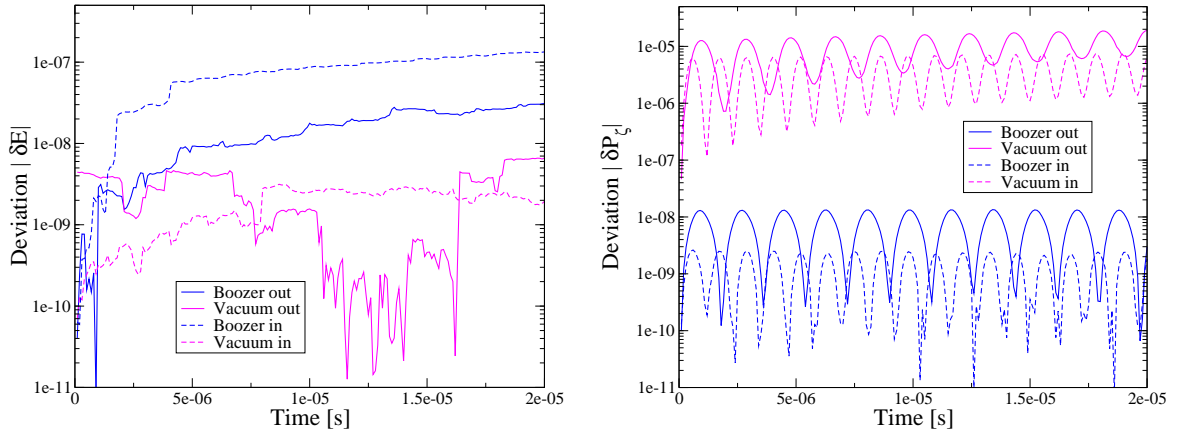


Figure 3.13.: Deviation of the energy and the toroidal momentum for the counter-passing particles (Fig. 3.11 right) performed on both coordinate grids with the same resolution (256x256).

The corresponding conservation of the constants of motion reveals the same behaviour as for the trapped particles. The particle energy is conserved at the same order of magnitude on both grids for particles which are near the last closed flux surface. For particles located more at the centre, the energy conservation is better by one order of magnitude on the vacuum grid. Again, the reason is due to higher terms in the equations of motion whose effects diminish on a greater grid cell near the last closed flux surface.

Considering the angular momentum, the discrepancy between the conservation on both coordinate systems is three orders of magnitude. For counter-passing particles, the conservation is worse compared to co-passing ions and degrades even more for a larger radial position.

After the comparison of an identical particle trajectory on both coordinate grids, the spatial grid distribution as in figure 3.3 is considered. Examples of possible trajectories for energies of $E = 300$ keV and $E = 800$ keV for all three particle species are simulated crossing the intersection surface multiple times. Assuming a similar cell size for both grids, the resolution for the Boozer coordinate system amounts to (256x256), for the vacuum coordinate system to (256x512).

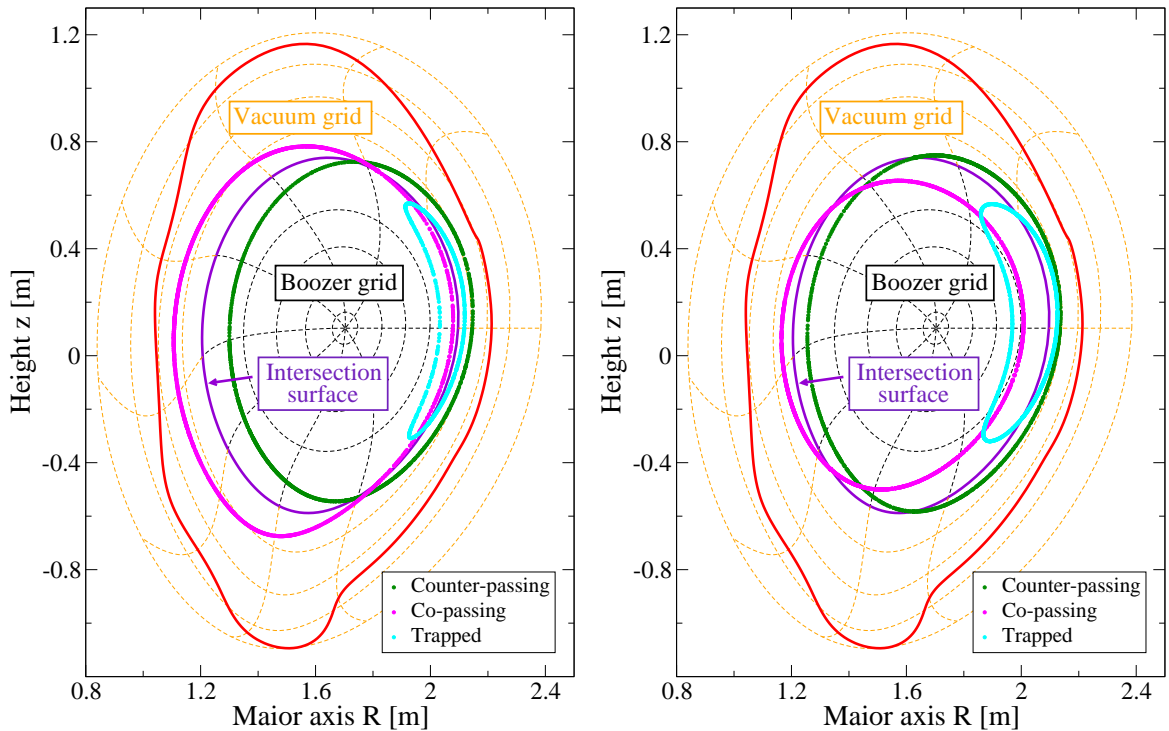


Figure 3.14.: Trajectories of ions with $E = 300$ keV (left) and $E = 800$ keV (right) for all three particle species (counter-passing, co-passing, trapped).

The corresponding graphs (Fig. 3.15) for the conservation of the constants of motion exhibit the same behaviour as shown before for each particle species on a grid separately. The invariants are conserved at the order of magnitude according to the worse properties of each grid. So, the energy is conserved at the order of magnitude which corresponds to the resolution of the Boozer coordinate system, the deviation of the toroidal angular momentum depends on the vacuum grid resolution.

In figure 3.15 (right) the crossing of the particle trajectory over the intersection surface is visible. The deflections in the graphs mark the time which the particle is within the vacuum region. Thereby, an unfavourable increase of the deviation after each poloidal orbit is detected for all particle species. The reason is that the particle cannot fulfil a complete orbit on the vacuum grid over which the deviation is minimized (figures 3.10, 3.12, 3.13) but

3. Code Development

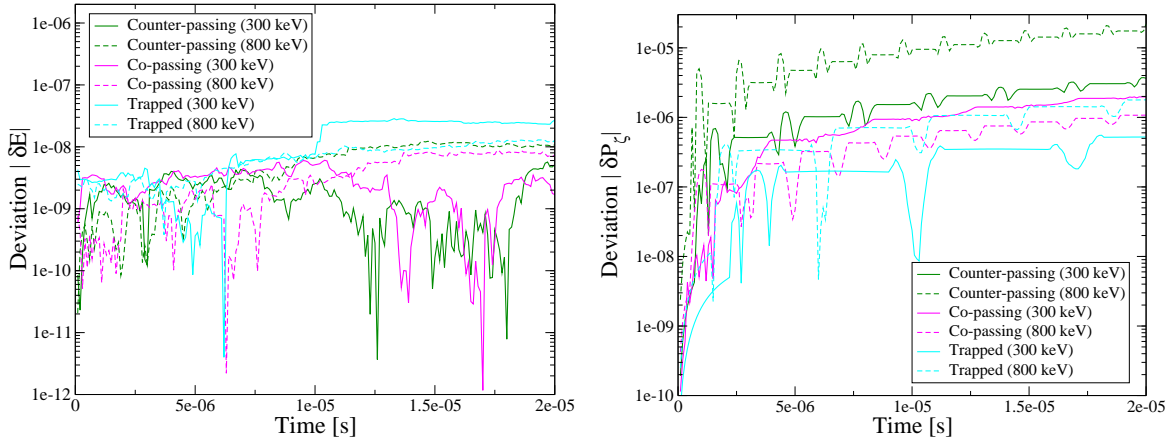


Figure 3.15.: Deviation of the constants of motion, δE and δP_ξ , for the particle trajectories as shown in figure 3.14.

pick up an error during the orbit leg. Except the highly energetic counter-passing particle with $E = 800$ keV, all particles degrade the conservation of P_ξ by an amount of a few 10^{-7} . Thus, it is not negligible if the error approaches the order of an excursion due to an MHD mode, $\delta P_\xi \approx 10^{-3}$. In the worst case, this has to be taken into account for re-entry particles first when at least 1000 orbits are completed. This corresponds to a mean simulation time of $\Delta t \approx 2 \cdot 10^{-3}$ s and therefore provides a sufficiently long time.

After the validation that the constant of motion are conserved sufficiently by controlling the grid resolution, the equations of motions are now allowed to be applied in the vacuum region. Together with the inclusion of the gyro motion effects, the implemented model supplies a complete system to simulate fast particle losses over the whole vessel first wall.

4. Simulation Results

After the implementation of the model, the extended code is used to simulate fast particle driven modes in particular discharges at ASDEX Upgrade. The main goal of the nonlinear simulations is the comparison of the simulated fast ion losses with the experimental measurements of the FILD [18]. For the first time, not only quantitative, but qualitative statements are aimed for. The comparison however is restricted due to limitations of the model. In the experiment, a continuous heating source generates a quasi steady-state fast particle distribution that is balanced by dissipation. In the simulation, the distribution function is initialized at the beginning and will be altered due to wave-particle interaction. An implementation of a self-consistent fast particle distribution generated by a continuous source is being developed in the frame work of another PhD thesis at the moment. Nevertheless, the present fast particle distribution permits qualitatively correct fast ion losses in energy and pitch angle but restricts the quantitative validity. The results allow for conclusions about the evolution of the fast ion loss distribution and the comparison to the experiment.

The model is applicable for the understanding of surprising recent FILD results [17] in detail. In the experiment, MHD modes like the BAE and the TAE have been detected which oscillate at very different frequencies, but generate enhanced fast particle losses. Although it is extensively reported in the literature [15, 16] that a significantly increased fast particle redistribution is caused by multiple modes with radial overlap and similar frequencies, it has to be proven if the same behaviour can be observed in the simulations due to modes with different frequencies. For this reason, the experimental data represent a fundamental challenge not only for the comparison of the fast ion losses but also for an investigation of open questions concerning collective fast ion redistribution in the plasma. In this context, a new coupling mechanism of two waves due to double-resonant particles has been identified which differs significantly from the conventional fast particle transport.

In the first simulations shown in this chapter, a fast particle population which is isotropic in the pitch variable λ has been used to include all possible topologies of fast particle orbits. In contrast to these simulations, in the experiment the auxiliary ICRF heating method is applied to generate a highly anisotropic fast particle population. For this reason, the first implementation of an ICRF-generated distribution introduced in section 3.2.5 is used as a first approach to reproduce the physical drive and loss mechanisms more realistically.

The fast particle losses cannot only be used for a comparison to the experimental loss data but also provide a validation of the initialized fast particle distribution in the simulations. Thus, a powerful tool has been developed that allows to benchmark theoretical models of the fast particle distribution function against the experiment. Additionally, this means that the wall load can be calculated over the whole vessel correctly which gives information about possible vessel damages.

In this chapter, the experimental measurements of a selected discharge in ASDEX Upgrade will be presented in section 4.1 which constitutes the modelling input for the numerical simulations. In section 4.2, the influence of a single TAE is investigated to explain the conventional drive mechanism in the presence of an isotropic fast particle distribution. The fast particle losses are analysed for different points in time. In section 4.3, the results of the nonlinear simulations of multiple modes in the presence of the same isotropic fast particle distribution are discussed. In this context, both the new drive mechanism and the change in the loss distribution compared to a single TAE are explained in detail. In the following section, the same mode constellation is investigated in the presence of a simple model for an ICRF-generated distribution. The fast ion losses will be compared to the previous cases. At the end, the fast particle losses of all cases are compared to the experimental results in section 4.5. This allows for conclusions concerning the validity and accuracy of the initialized distribution functions. Beside the shear Alfvén eigenmodes, the fast particle redistribution caused by neoclassical tearing modes is also studied in section 4.6.

4.1. Experimental Measurements

This section summarizes the experimental set-up for a specific discharge in ASDEX Upgrade. Especially, the experimental results of the fast ion loss detector FILD [18] are of interest. Together with soft X-ray measurements for mode localization and its amplitude as well as results from the Mirnov pick-up coils for the mode frequency, the physics mechanisms involved can be deduced.

The plasma discharge #21083 in ASDEX Upgrade is chosen due to the fact that informative measurements of fast ion losses and multiple MHD modes are present at the same time. The results were extensively described by García-Muñoz [17]. The discharge was performed with a toroidal plasma current $I_p = 1.2$ MA, a toroidal field $B_{tor} = 2.0$ T and a safety factor at the edge of $q_{95} = 3.6$. As main heating method, on-axis minority ICRH with a power of 5 MW was applied generating highly energetic hydrogen ions in a deuterium background plasma ($n_H/n_D \approx 6\%$) with a fast particle beta of $\beta_f = 0.3\%$.

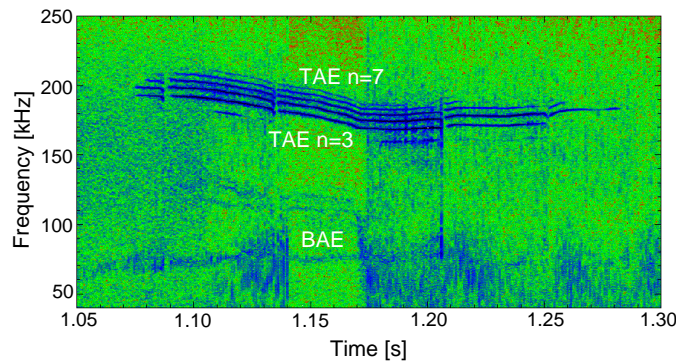


Figure 4.1.: Spectrogram of a Mirnov pick-up coil. Several TAEs with toroidal mode numbers $n = 3 - 7$ and a $n = 4$ -BAE are visible.

Figure 4.1 shows the Fourier spectrogram for a magnetic pick up coil located at mid plane.

It measures the magnetic fluctuation at the plasma edge. Since a TAE is globally extended over a large radial range up to the plasma edge, several dominant TAEs [26] with toroidal mode numbers of $n = 3 - 7$ at frequencies $\omega_{\text{TAE}} = 160 - 200$ kHz are clearly visible at about $t = 1.19$ s. Due to its core-localization, the BAE [7] with a toroidal mode number $n = 4$ at a frequency $\omega_{\text{BAE}} = 70$ kHz is hardly visible. It is clearly detected by the high resolution multichord soft X-ray system [62]. In figure 4.2 the spectrogram of a soft X-ray channel whose line of sight is near to the magnetic axis shows an explicit signal of the BAE.

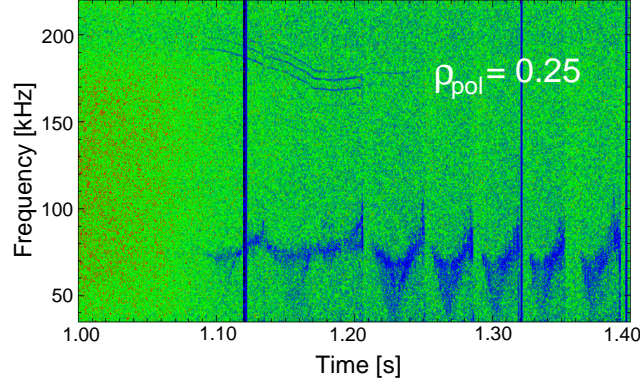


Figure 4.2.: Spectrogram of a soft X-ray measurement (line of sight near the plasma centre). The BAE is clearly visible, together with TAEs $n = 3 - 5$ due to the line of sight.

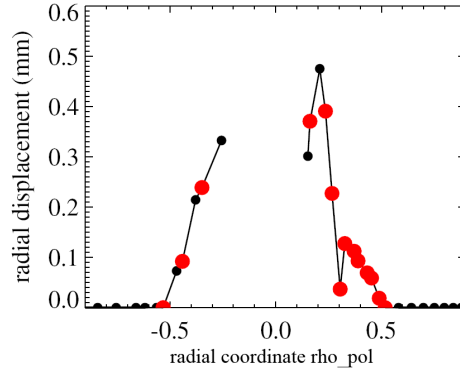


Figure 4.3.: Mode reconstruction by the MHD-IC code [63] based on soft X-ray measurements. Since the line of sight crosses the magnetic axis, positive and negative values for the radial coordinate denote positions on both sides of the plasma centre.

It has been detected by a soft X-ray reconstruction of the MHD-IC code [63] that the BAE is approximately located around the magnetic surface $\rho_{\text{pol}} = 0.25$, as shown in figure 4.3. Up to the time $t = 1.2$ s, the mode frequency is nearly unaffected neither by changes of the magnetic field nor by changes in the electron density. This indicates that the mode is a gap mode as introduced in section 2.3.3. As the equilibrium evolves in time, the mode frequency is almost fixed. This is consistent with the dispersion relation (Eqn. 2.28) [29]. Later for time $t > 1.2$ s, sawtooth crashes appear due to a safety factor $q < 1$ at the plasma centre which results in rapid frequency changes. This confirms the fact that the mode is core-localized.

4. Simulation Results

The $n = 4$ -TAE is a global mode with the maximum of the amplitude at about $\rho_{\text{pol}} = 0.55$, and an amplitude of $\delta B_r / B_{\text{tor}} = 0.2 - 5.0 \cdot 10^{-4}$ was deduced from the radial displacement measured by the soft X-ray system.

The fast ion losses measured by the FILD detector (Fig. 4.4) can be divided into two distinct spots. The 'small' spot is determined by a pitch angle $\alpha \approx 69^\circ - 70^\circ$ and gyro radii of $\rho_\perp \approx 40 - 50$ mm which corresponds to energies $E = 240 - 380$ keV. The measurements of the 'large' spot yield pitch angles between $\alpha \approx 62^\circ - 68^\circ$ and gyro radii of $\rho_\perp \approx 60 - 100$ mm (energy $E = 550 - 1300$ keV).

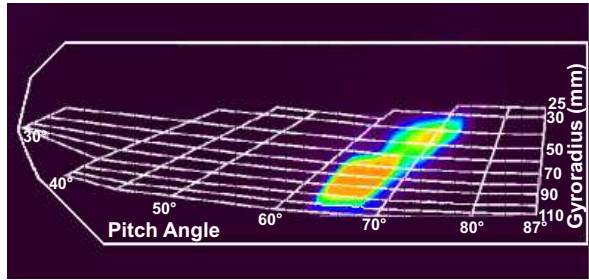


Figure 4.4.: Measurements of the FILD at time $t = 1.19$ s (figure from [17]).

Compared to other ASDEX Upgrade discharges where exclusively TAEs were present, the 'small' spot only emerges in the presence of a BAE and the total loss amplitude due to the TAEs is increased by a factor of 3. The Fourier spectrogram of the fast ion losses shows that the losses of the small 'spot' are only ejected at frequencies corresponding to the TAEs seen in figure 4.1. The fast particles of the 'large' spot are ejected at the frequency of both the BAE and the TAE. Due to the increased loss amplitude caused by the TAE it is claimed by reference [17] that fast particles are redistributed from the position of the BAE towards the TAE because of their radial overlap.

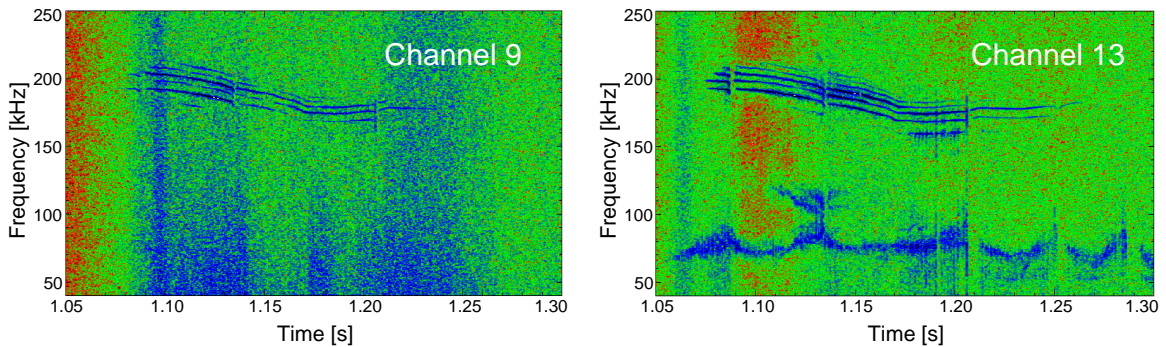


Figure 4.5.: Fourier spectrograms of the particular photomultiplier channels in FILD. Channel 9 is detecting particles with smaller gyro radii, channel 13 ions with larger gyro radii.

In the next sections, these experimental results and the corresponding assumption are investigated by means of numerical simulations with the extended HAGIS code.

4.2. TAE-induced Fast Particle Losses

In order to understand the complete loss mechanism observed in the experiment and discussed before, it is important to describe first the influence of a single TAE on the fast particle redistribution [25] first. Therefore, the mode drive and the saturation behaviour of a single TAE are investigated. Since no self-consistent background damping mechanism such as Landau damping is implemented in the code, a saturation of the mode is achieved by the gradient flattening [15] in the fast particle distribution. This is the best available model at the moment. Nevertheless, detailed drive mechanisms like resonant wave-particle interaction [25, 16] can be understood by the nonlinear simulations. The coherent particle redistribution and the TAE-induced fast particle losses are analyzed to confirm the known mechanisms. The results constitute the basis which is compared to possible enhanced losses due to multiple modes investigated in the later sections.

4.2.1. Initial Conditions and Mode Drive

At first, the stability code CASTOR [50] is applied to provide the shear Alfvén continuum (2.24) and the corresponding eigenmodes for the equilibrium of AUG discharge #21083 at time $t = 1.19$ s. The required profile of the reconstructed safety factor is shown in figure 4.6.

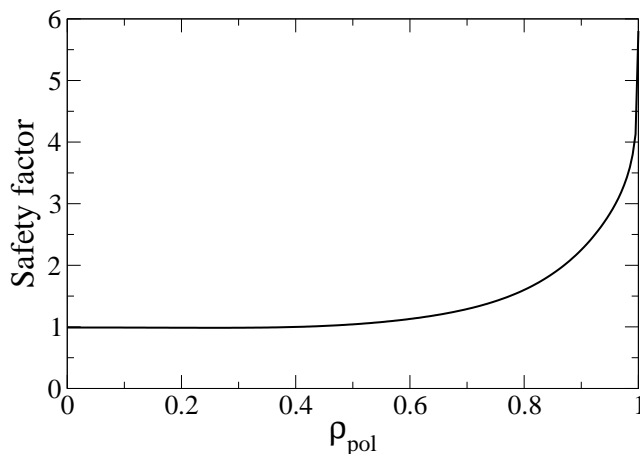


Figure 4.6.: Profile of the safety factor q . The $q = 1$ -surface is located at the radial position $\rho_{pol} = 0.4$.

Due to the determination of the sawtooth inversion radius ρ_{inv} by electron cyclotron emission (ECE) measurements and the relation $q(\rho_{inv}) \approx 1$, the $q = 1$ -surface is located at the radial position $\rho_{pol} \approx 0.40$. The corresponding shear Alfvén frequency continuum is shown in figure 4.7. As explained in section 2.3.2, gaps are generated within the continua due to poloidal coupling where discrete TAE modes can be excited. It is found that the TAEs with a toroidal mode number $n = 3 - 5$ have frequencies of $\omega = 145$ kHz, $\omega = 150$ kHz and $\omega = 153$ kHz in the rest frame of the plasma. This coincides with the experimental findings if an additional plasma rotation of 5 kHz per toroidal mode number is added. The plasma rotation frequency has been deduced from measurements of sawtooth precursors. The eigenfunctions (Fig. 4.8) of the modes are provided by the CASTOR code. The TAEs consists of two dominant poloidal harmonics, m and $m + 1$, which couple to further outer

4. Simulation Results

TAE gaps due to higher harmonics, i.e. $(m + 1, m + 2)$, $(m + 2, m + 3)$, etc. The maximal amplitude of the TAE is located between $\rho_{\text{pol}} \approx 0.55 - 0.60$ which fits to the experimental data ($\rho_{\text{pol,exp}} \approx 0.55$) detected by the soft X-ray system [17].

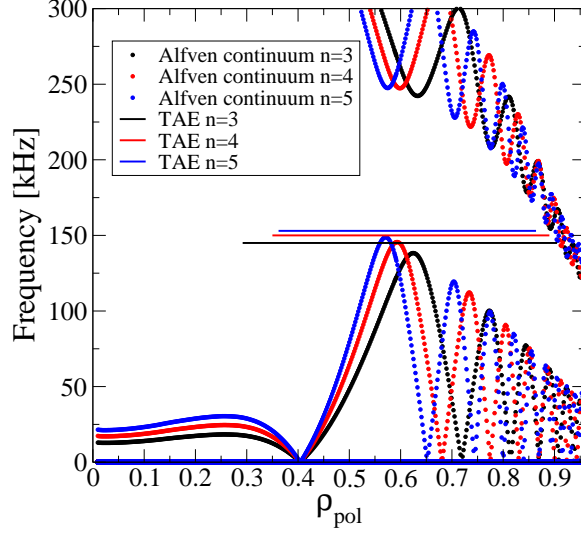


Figure 4.7.: Frequency spectrum showing the shear Alfvén continua for several toroidal mode numbers. In addition, the radial extents of the TAE eigenfunctions (Fig. 4.8) which are defined by the drop of the amplitude to a tenth of its maximal amplitude are plotted at their discrete frequencies in this figure.

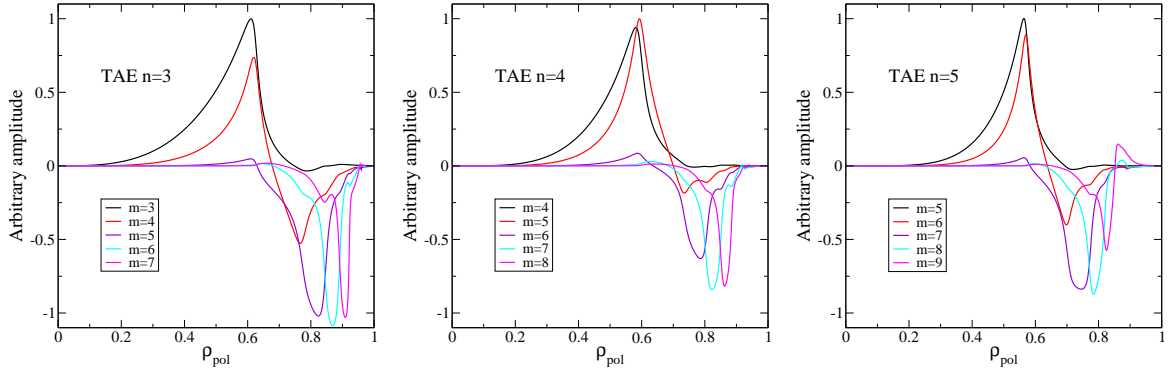


Figure 4.8.: Eigenfunctions of the TAEs with toroidal mode numbers $n = 3 - 5$ (corresponding to figure 4.7).

For the interaction of the mode with the fast particles, the resonance condition [36] has to be fulfilled, as introduced in section 2.3.4. For trapped particles, it is defined by

$$\omega - n\omega_{tp} - p\omega_b = \Omega_{n,p} , \quad (4.1)$$

where ω is the frequency of the Eigenmode, ω_{tp} the toroidal precession frequency and

ω_b the bounce frequency of the trapped ions. The toroidal mode number and the bounce number are given by n and p , respectively. A bidirectional energy and momentum exchange is possible if $\Omega_{n,p}$ is approximately zero.

In figure 4.9, trapped particles which have their bounce points above the magnetic axis R_{mag} are initialized for different energies E and vertical positions z . The corresponding resonance lines (red) for a $n = 4$ -TAE with a frequency of $\omega = 150$ kHz and bounce harmonics between $p = -2$ and $p = 1$ (from left to right) are shown. The intersection of the resonance lines with the loss boundary is expected to be the fast particle loss region. With the inclusion of FLR effects, the loss boundary shifts significantly (Fig. 4.9 right) as shown in figure 3.6 in section 3.2.4. Therefore, the intersection of the $p = 1$ -resonance with the loss boundary at an energy of $E \approx 500$ keV (Fig. 4.9 left) changes to an energy of $E \approx 800$ keV (Fig. 4.9 right). Furthermore, the $p = 0$ -resonance forms an intersection with the loss boundary now.

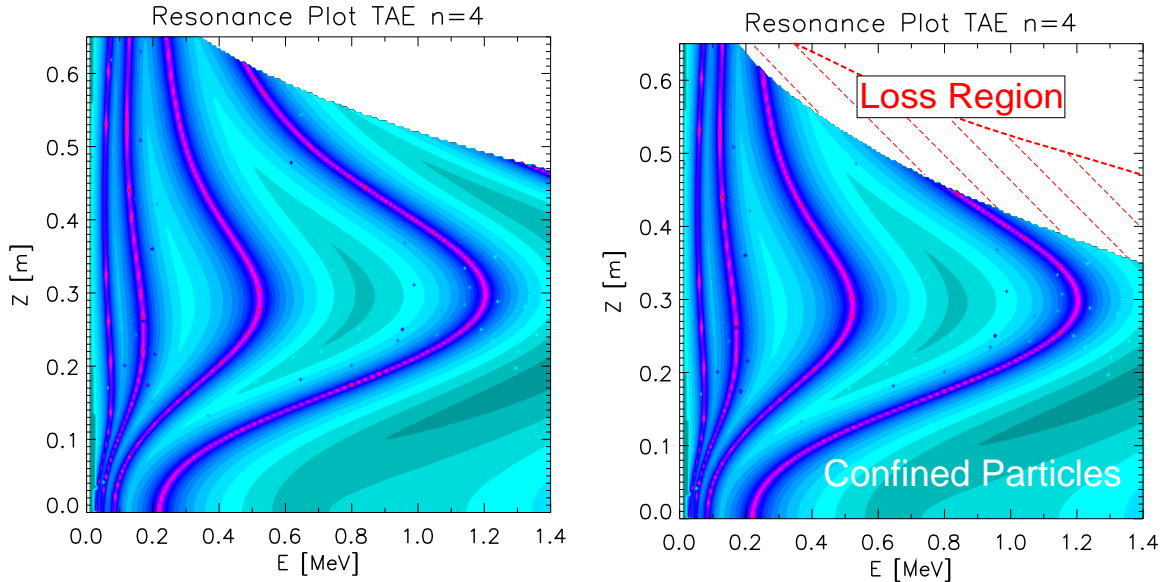
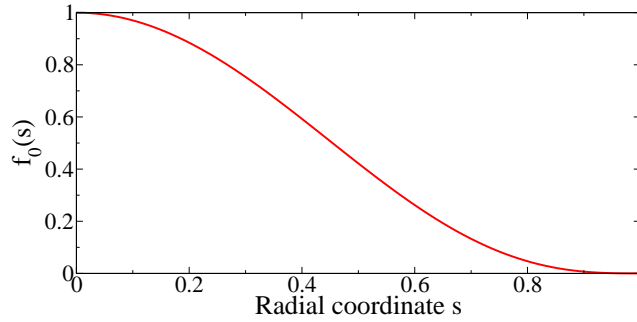
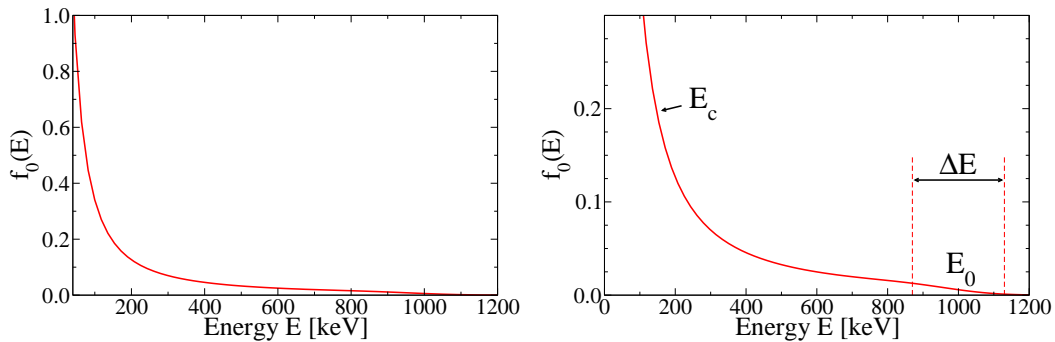


Figure 4.9.: AUG discharge #21083 at time $t = 1.19$ s: The resonance lines of a single $n = 4$ -TAE. The confinement of the guiding centres without (left) and with inclusion of FLR effects (right) are shown. The latter figure shows clearly the increase of the loss region.

For the nonlinear simulation, first a fast particle distribution function f_0 (3.80) represented by 315000 markers is used which is isotropic in the pitch variable λ , i.e. $f(\lambda) = const.$ This allows for the investigation of the mode drive caused by all particles, i.e. co-passing, counter-passing and trapped particles. The fast particle beta is $\beta_f = 0.3\%$ consistent with the experimental measurements. The radial Fermi-like distribution function is described by

$$f_s = (1 - s)^3 \quad (4.2)$$

whereby the particles are loaded between $s = 0.01 - 0.9$.


 Figure 4.10.: *Initialized radial distribution function $f(s)$.*

 Figure 4.11.: *Slowing-down distribution function in energy $f(E)$, in total (left) and enlarged in the lower ordinate range (right).*

Furthermore, a slowing-down distribution in energy [64] is chosen. However, it is adjusted to the ASDEX Upgrade parameters,

$$f_E = \frac{1}{E^{3/2} + E_c^{3/2}} \operatorname{erfc} \left(\frac{E - E_0}{\Delta E} \right), \quad (4.3)$$

whereby $E_0 = 1 \text{ MeV}$ is the most probable maximal energy generated by ICRF heating. The spread of energy around E_0 is given by ΔE which depends on the background plasma temperature. The cross-over energy E_c denotes the drag of the electrons on the fast ions depending on the background electron temperature T_e . This is due to the fact that the electron collisions dominate for highly energetic particles. For $T_e = 2 \text{ keV}$, the values are $E_c = 14.4 \text{ keV}$ and $\Delta E = 129.8 \text{ keV}$.

The cross-over energy also determines the gradient of the distribution function, $\partial f / \partial E$, for lower energetic particles, i.e. the smaller E_c , the steeper the gradient. The gradient decreases significantly at energies above $E \approx 400 \text{ keV}$ due to the vanishing effect of E_c in the denominator of equation (4.3).

It has been shown [25] that the mode growth described by equation (2.30) is proportional to $\gamma \sim \omega_*$. From equation (2.31), this indicates that the gradient of a slowing-down distribution function in energy damps the mode,

$$\frac{\partial f_0}{\partial E} < 0 \quad \Rightarrow \quad \omega_* < 0, \quad (4.4)$$

whereas the gradient of the radial Fermi-like distribution function drives the mode unstable since $P_\zeta \sim -\psi_p$ (Eqn. 3.18),

$$-\frac{\partial f_0}{\partial \psi_p} \sim \frac{\partial f_0}{\partial P_\zeta} > 0 \quad \Rightarrow \quad \omega_* > 0. \quad (4.5)$$

With respect to equation (2.30), the mode is growing if $\omega_*/\omega_0 \geq 0.5$. The total distribution function f_0 leads to a mode growth and a saturation at amplitudes between $\delta b_r/B_0 = 5.5 - 6.7 \cdot 10^{-4}$ for various toroidal mode numbers n (Fig. 4.12). The simulated amplitudes coincide very well with the experimental TAE amplitudes. During the linear growth phase up to the time $t < 3.0 \cdot 10^{-4}$ s, the growth rate is around $\gamma/\omega_0 \approx 2\%$. Afterwards, the growth rate decreases until it is $\gamma \approx 0\%$ at time $t > 6.0 \cdot 10^{-4}$ s (saturation phase). The behaviour is very similar for the $n = 3, \dots, 5$ -TAEs but in the following only the physical mechanisms caused by the $n = 4$ -TAE are discussed in detail.

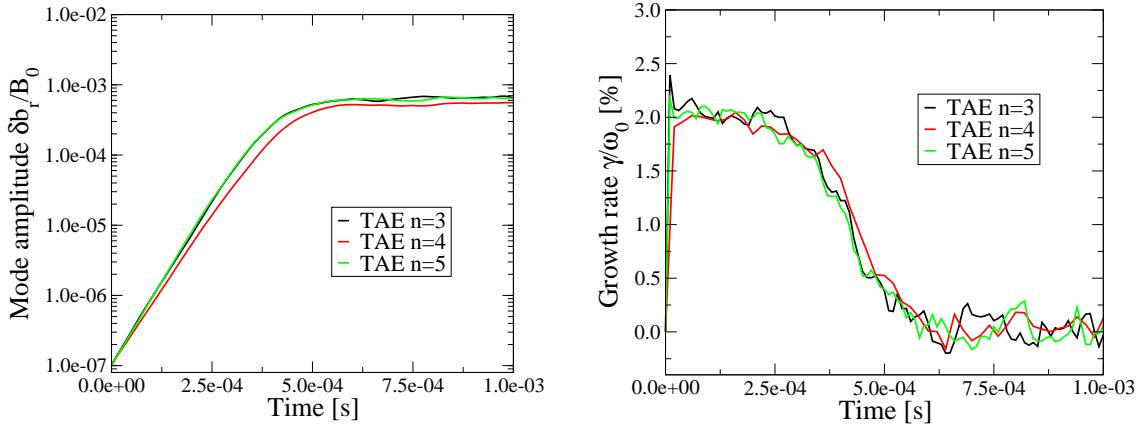


Figure 4.12.: Evolution of the TAE amplitudes and the corresponding growth rates.

Due to the interaction of the fast particle distribution with the mode, energy of the resonant hydrogen ions is transferred due to the radial gradient to the wave [15]. In response, the resonant fast ions are redistributed radially outwards since for a single particle j in the presence of a perturbation it is valid [12] that

$$E_j - \frac{\omega}{n} P_{\zeta,j} = const.$$

It is worth to note here that the relative change in toroidal momentum is much larger than the relative change in the particle energy. Due to the equation above, the relative change is given by

$$\frac{\Delta P_\zeta}{P_\zeta} = \frac{n E}{\omega P_\zeta} \cdot \frac{\Delta E}{E}.$$

4. Simulation Results

Typically, for Alfvénic waves like the TAEs with $v_{\parallel} \approx v_A/3$ and $\omega = v_A/2qR$ (section 2.3.2), the term reduces to

$$\frac{n}{\omega} \frac{E}{P_{\zeta}} \approx \frac{n}{\omega} \frac{m_i \left(\frac{v_A}{3}\right)^2}{m_i R \frac{v_A}{3}} = \frac{n}{\omega} \frac{v_A}{3R} \approx n.$$

This reveals that for large toroidal mode numbers n the relative change in energy compared to the relative change in toroidal momentum [65] is of the order

$$\frac{\Delta E}{E} = \mathcal{O}\left(0.1 \frac{\Delta P_{\zeta}}{P_{\zeta}}\right). \quad (4.6)$$

So, the change in the distribution function provides direct information about the regions in the fast particle phase-space which are interacting with the MHD modes. In figure 4.13, the radial change in the fast particle distribution given by the perturbed particle density δn (Eqn. 3.39) is shown over the total simulation time.

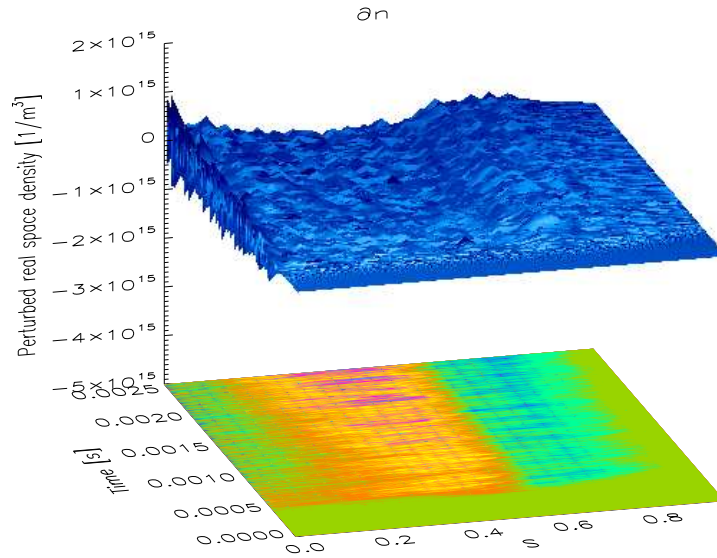


Figure 4.13.: Radial fast particle redistribution in time due to a $n = 4$ -TAE. Resonant fast particles change their phase-space position from a smaller (magenta/yellow) to larger radial position (blue).

Fast particles are redistributed from $s = 0.2 - 0.6$ (magenta) to $s = 0.6 - 0.8$ (blue) for a time $t > 4.0 \cdot 10^{-4}$ s since the mode amplitude is too small before. The redistribution stretches over a wide plasma range due to the large radial extent of the global TAE. In plasma physics, it is common to represent the change in the fast particle distribution by the perturbed fast particle pressure defined by

$$\delta p = C \cdot n \int v^2 \delta f d^3v \quad (4.7)$$

where n is the total particle density at the radial position. The quantity C is a normalization factor. The fast particle pressure profile and the profile of the radial particle population are related to each other.

In figure 4.14 (left), the perturbed particle density δn is plotted with respect to the radial coordinate. The corresponding fast particle pressure $p + \delta p$ is shown in figure 4.14 (right). Both graphs are averaged over the time interval $t = 1.9 - 2.1 \cdot 10^{-3}$ due to large fluctuations in the density δn or δf at a point in time. It is seen that the radial gradient in the fast particle pressure profile at the position of the maximal TAE amplitude flattens. Since the gradient of the fast particle pressure ∇p is also proportional to the diamagnetic frequency,

$$\omega_* = \frac{Tc}{eB^2} \mathbf{k} \times \mathbf{B} \frac{\nabla p}{p}, \quad (4.8)$$

the mode drive decreases. For the time $t > 6.0 \cdot 10^{-4}$ s, the mode drive due to gradients both in energy and radius cancel each other (Eqn. 4.4 and 4.5) and the mode saturates.

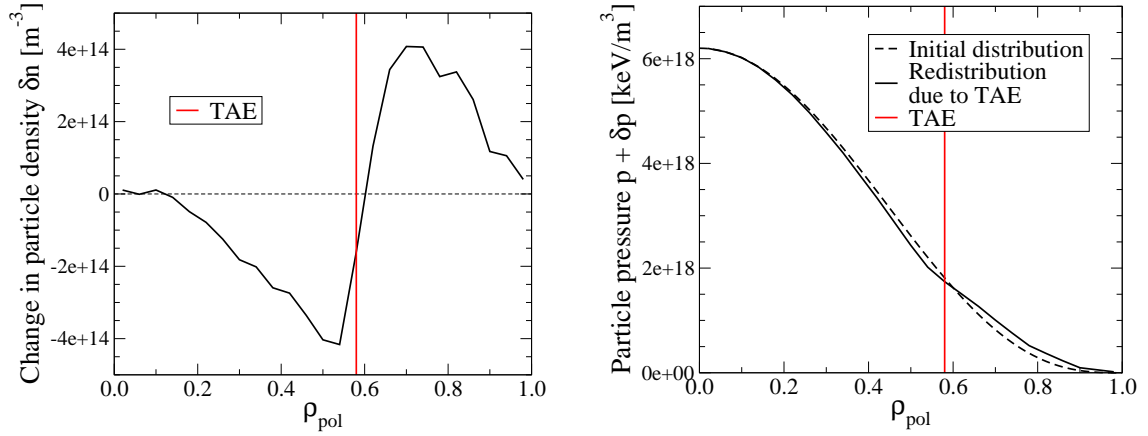


Figure 4.14.: Mean radial redistribution of the fast particles between $t = 1.9 - 2.1 \cdot 10^{-3}$ s caused by the single TAE (left). The fast particle redistribution caused by a TAE generates a flattened gradient in the fast particle pressure (right) compared to the initial state.

Simultaneously, the change in the density of the energy distribution function δn (Fig. 4.15) shows the resonant fast particles. A broad particle population up to an energy of $E \approx 800$ keV is affected. Especially, fast ions with energies of $E \approx 130$ keV and $E \approx 420$ keV (yellow regions) have transferred energy to the mode. As a consequence, the particles change their localization in the phase-space from higher to lower energies.

Since for the fast particles, the relative change in the energies (4.6) is much smaller than the radial change, the increase of the gradient in the distribution function in energy due to the fast particle redistribution is negligible. This indicates that the saturation of the mode is mainly determined by the flattening of the gradient in the radial distribution or the fast particle pressure profile, respectively.

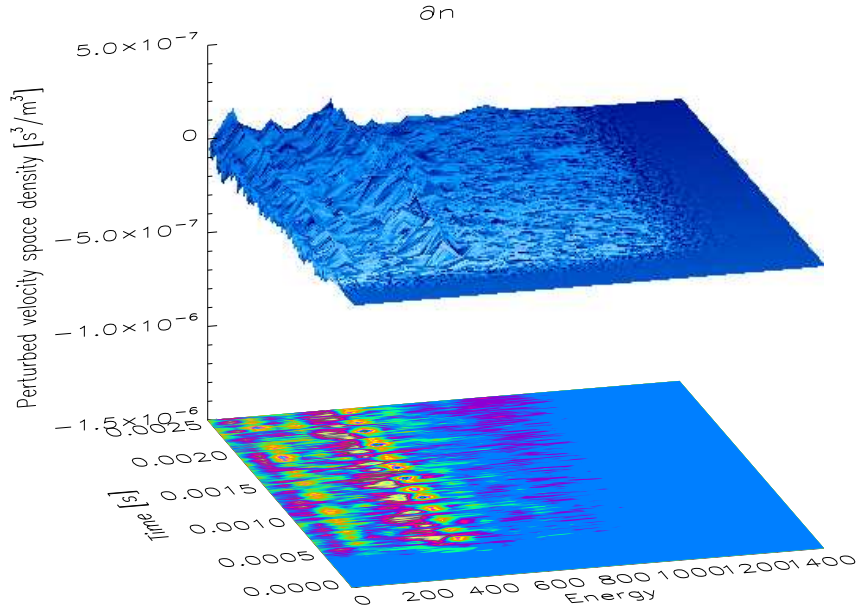


Figure 4.15.: *Redistribution of fast particles in energy caused by a $n = 4$ -TAE. The eigenmode interacts with fast ions of $E \approx 130$ keV and $E \approx 420$ keV (yellow regions). The particles transfer energy to the mode and change their phase-space position to lower energies as a consequence.*

Up to this point, the mode growth and the redistribution mechanisms are analysed by available tools in the original HAGIS code. Due to a recently incorporated diagnostic, more detailed information about the driving mechanisms in energy and space can be obtained when the redistributions in energy and radial space are combined. In addition, the particles of the total ensemble are classified with respect to their orbit topology.

It turns out that the mode drive is mainly due to trapped particles compared to the mode drive by co- or counter-passing particles as shown in figure 4.16. According to the fast particle redistribution in energy (Fig. 4.15), three particle regions within the (s, E) -phase-space are of interest: particles at energies between $E = 300 - 500$ keV in the radial range of $s = 0.4 - 0.9$, at an energy of $E \approx 130$ keV between $s = 0.3 - 0.6$ and between $s = 0.65 - 0.85$. Only the first region is clearly visible, and fast particles are redistributed from an inner (blue) to an outer (yellow/red) radial position.

Under the assumption that the fast particle density n is constant in each phase-space region, the quantity $\delta f \cdot v^2$ is a measure for the fast particle pressure (4.7) and therefore for the mode drive. This indicates that for particle energies of $E = 300 - 500$ keV, the mode drive due to these fast ions is much more important than the mode drive due to fast particles with $E \approx 130$ keV. Nevertheless, the resonant fast ions of both energies are redistributed (Fig. 4.15).

Although fast particles with energies up to $E = 1.4$ MeV have been initialized, particles with higher energies do not contribute to the mode drive and therefore are neglected in figure 4.16. Furthermore, it is clearly seen that the outward shift in the radial position which corresponds to a change in P_ζ is larger than the loss of the fast particle energy as indicated in equation 4.6.

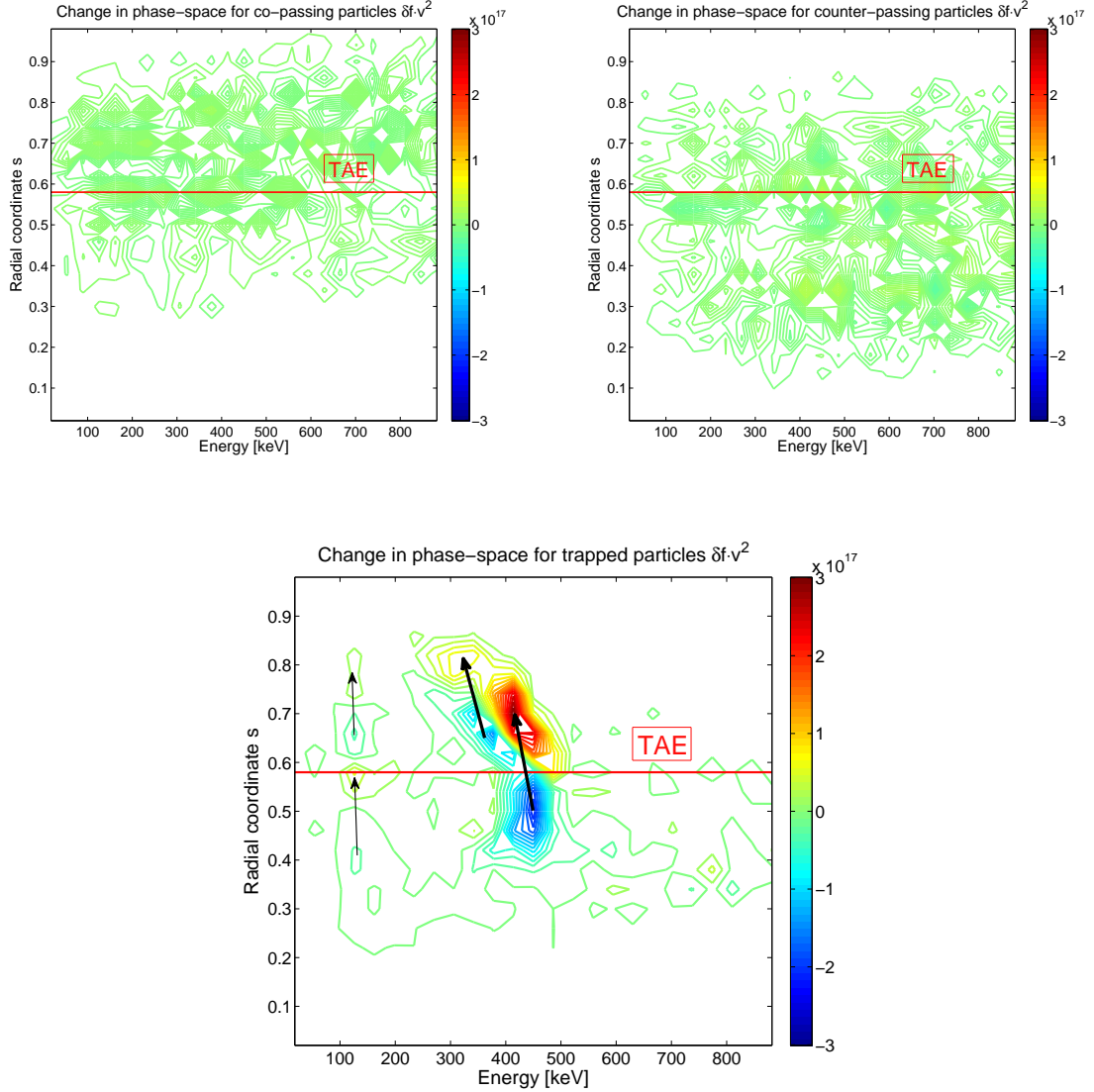


Figure 4.16.: Change in the distribution function, $\delta f \cdot v^2$, due to the $n = 4$ -TAE at time $t = 8.0 \cdot 10^{-4} s$ separated by each particle species. The mode drive due to trapped particles is much stronger than the drive due to passing particles (colour scale). The red lines denote the radial position of the $n = 4$ -TAE amplitude.

Comparing the results to the resonance plots of trapped particles (Fig. 4.9 right) shows that the resonance lines coincide very well with the redistribution regions (Fig. 4.17). Since the trapped particles in the resonance plot have their bounce point above the magnetic axis R_{mag} at a vertical position z , it can be approximately assumed that the normalized poloidal flux ρ_{pol} corresponds to the normalized radius \hat{r} , $s = \rho_{pol} \approx \hat{r} = z/z_{max}$. This relation allows for comparison between the resonance plot and the redistribution in phase-space (E, s). The regions of the redistributed particles for $E = 300 - 500$ keV are located at the resonance

line with the bounce harmonic $p = 0$, i.e. the mode frequency is equal to a multiple of the precession frequency of the trapped particles, $\omega \approx n \cdot \omega_{tp}$ (Eqn. 4.1). For particles with energy $E = 130$ keV, two intersections with the resonance line $p = -1$ exist. Especially, the outer redistribution region shows exact radial agreement between figure 4.16 (lower box) and 4.17. For all three resonant phase-spaces, trapped fast particle from these regions have been simulated. The characteristic orbits are shown in figure 4.19. It is seen that the localization of the orbit width Δ_b for the trapped particle with $E = 420$ keV (red) coincides with the mode width. For the trapped particles with $E = 130$ keV, either the localization of the orbit (blue) is at another radial position or the orbit width (cyan) is smaller compared to the mode width.

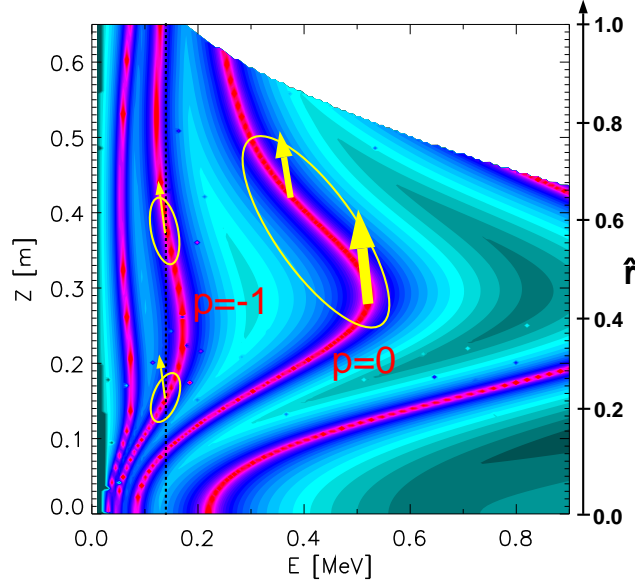


Figure 4.17.: Resonance plot for trapped particles in the presence of the $n = 4$ -TAE. The yellow regions show the regions of the redistributed particles. (The black line denotes the energy $E = 130$ keV.)

With regard to figure 4.16, the resonance line with $p = 0$ is decisive for the mode drive for two reasons: First, the resonance depends on the precession frequency only due to $p = 0$. For $p = -1$, both the toroidal precession and the bounce frequency are involved. For high energies, the frequencies are given [39] by

$$\omega_{tp} = \frac{qv_{\perp}^2}{2\epsilon R^2 \omega_c} \quad \text{and} \quad \omega_b = \frac{v_{\perp}}{qR} \sqrt{\frac{\epsilon}{2}}. \quad (4.9)$$

so that $\omega_{tp} \sim E_{\perp}$ and $\omega_b \sim \sqrt{E_{\perp}}$. Rewriting equation (4.1) reveals the relation for deeply trapped particles, $E_{\perp} \gg E_{\parallel}$,

$$C_1 \cdot nE_{\perp} - C_2 \cdot p\sqrt{E_{\perp}} \approx C_3 \cdot (E_{wave} + \Delta E), \quad (4.10)$$

where ΔE denotes the deviation in energy and C_1, \dots, C_3 are normalization factors. If the resonance condition is fulfilled exactly, the deviation in energy is zero. In figure 4.18,

the graph shows the dependence of the resonance condition on frequency and ΔE . For a particular deviation in the particle energy ΔE , a greater deviation in frequency is obtained for the $p = -1$ -resonance compared to $p = 0$ due to the additional term of \sqrt{E} . It has been demonstrated [66] that a maximal frequency mismatch of $\Delta\omega \approx 7$ kHz for TAEs are allowed to still fulfil the resonance condition (4.1). For this reason, the resonance condition for $p = 0$ is satisfied for a greater range in the particle energy compared to the $p = -1$ -resonance.

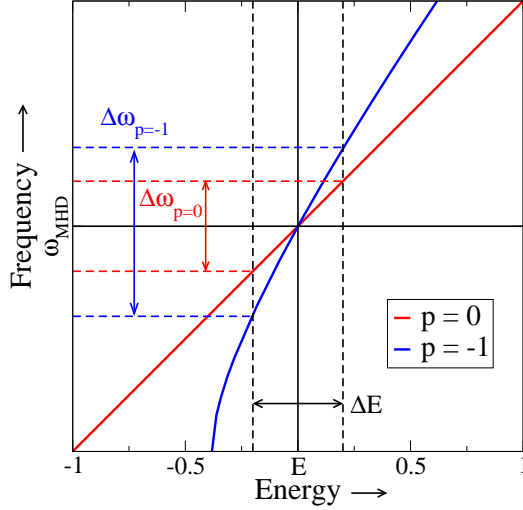


Figure 4.18.: Dependence of the resonance condition (4.1) on the particle energy. A deviation in energy results in a smaller deviation in frequency for $p = 0$ compared to the $p = -1$ -resonance so that the resonance condition is still fulfilled for greater ΔE .

The second reason for the decisive mode drive of the $p = 0$ -resonance is due to finite orbit width effects. It has been found [37] that the growth rate for small orbit widths Δ_b (2.45) is

$$\gamma \sim \frac{\Delta_b}{\Delta_m} \approx \frac{m}{q} \rho_{\perp} \approx k_{\theta} \rho_{\perp} , \quad (4.11)$$

where Δ_m is the scale length of the eigenmode and $k_{\theta} = m/q$ is the poloidal wave number. The growth rate for large orbit widths scales with m^{-2} [34]. An optimum in the mode drive is reached for $k_{\theta} \rho_{\perp} \approx 1$.

In figure 4.19 it can be seen that the particle orbit width for the resonance $p = 0$ (red) is comparable with the mode width. For the $p = -1$ -resonance, the orbit widths of the fast particles are smaller than the mode width (cyan) or localized at a different radial position (blue). The mode is thus driven less effectively by the $p = -1$ -resonance than by the $p = 0$ -resonance (4.11). Therefore, the mode is still slightly growing after the saturation of the main resonance (Fig. 4.12).

Due to the m^{-2} -scaling for $k_{\theta} \rho_{\perp} > 1$, trapped particles with an energy of $E \geq 1$ MeV do not contribute to the mode drive. Thus, no particle redistribution is detected for these energies. For this reason, the corresponding phase-space region has been neglected in the previous plots (Fig. 4.16).

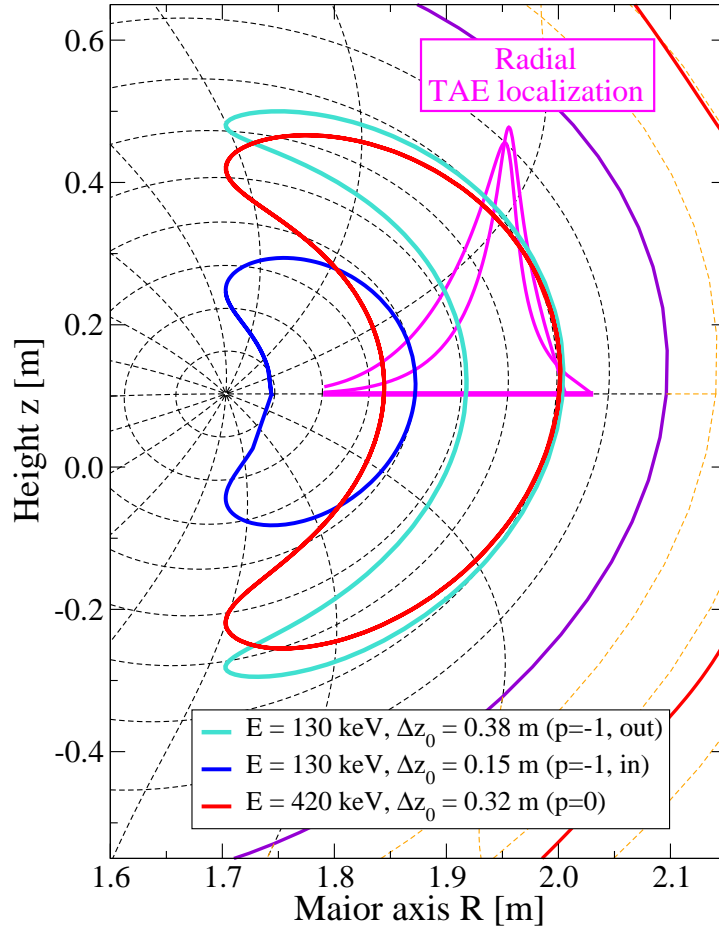


Figure 4.19.: Examples of unperturbed particle trajectories for each redistribution region as shown in Fig. 4.17. The magenta line shows the radial extension of the $n = 4$ -TAE.

4.2.2. Fast Particle Losses

In this section the fast particle losses caused by a TAE mode are investigated at different points in time. It is expected in the simulations that fast particles are ejected by the mode as the amplitude of the eigenmode increases. Due to the fact that no particle source is available, the fast ion losses will stop as the mode saturates.

From figure 4.21 it can be seen that at the beginning of the linear growth phase no fast particles are ejected due to the TAE. As an amplitude of $A \approx 5.0 \cdot 10^{-5}$ at $t = 3.2 \cdot 10^{-4}$ s is reached, particle losses appear (red). The maximal loss amplitude occurs at time $t = 5.0 \cdot 10^{-4}$ where the mode amplitude has almost reached a saturated level. Thereby, the fast particle losses show an over-shoot due to weakly-confined particles in the outer plasma region. After the ejection of these particles, a mean loss amplitude of $\delta f = 1.5 \cdot 10^{12}$ is still present due to the continuing growth of the amplitude caused by the $p = -1$ -resonance (section 4.2.1). Although the amplitude increases slightly further, the period $t > 6.5 \cdot 10^{-4}$ s is denoted as saturation phase (Fig. 4.20).

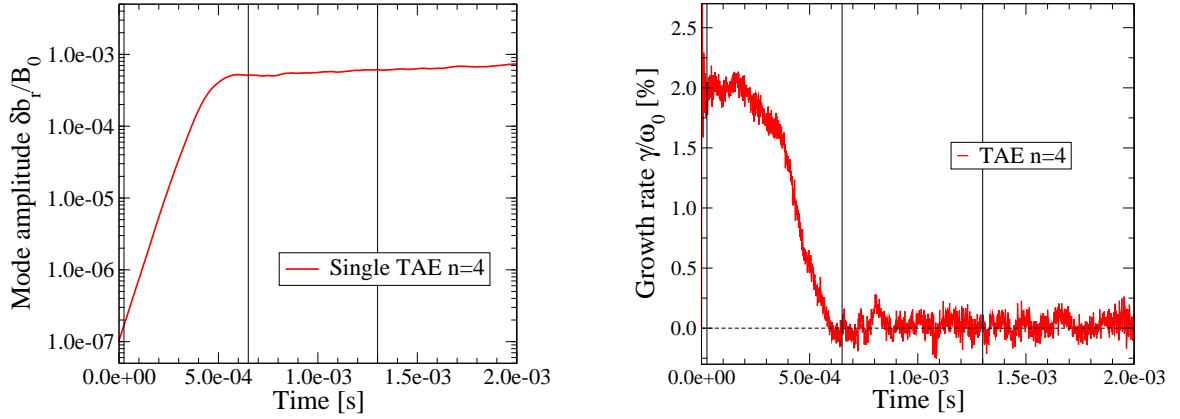


Figure 4.20.: Mode evolution of the TAE amplitude (left) with toroidal mode number $n = 4$ and the corresponding growth rate (right). The vertical lines mark the time intervals over which the fast particle losses are examined.

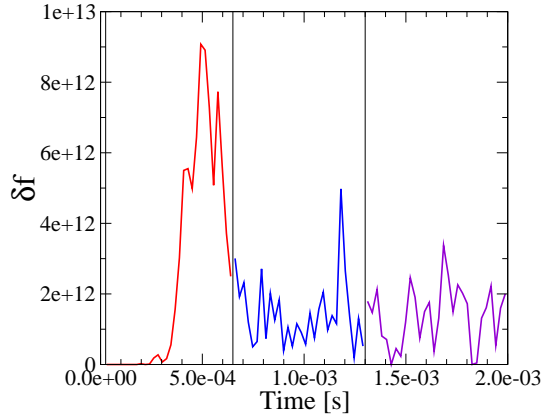


Figure 4.21.: Total fast particle losses over the vessel wall caused by the $n = 4$ -TAE.

In figure 4.22 it is shown that almost all fast particle losses are located in the lower half of the vessel. Especially on the high field (HF) side, the wall load is below the mid plane. The main losses are concentrated on the low field (LF) side slightly above the mid plane, i.e. the position of the FILD is well-chosen. This is due to the fact that the first wall has the smallest distance to the plasma at this position. Further loss regions are detected on the HF side above and at the position of the inner divertor as well as on the LF side below the mid plane.

The investigation of the total fast particle losses as a function of energy reveals that hydrogen ions between $E = 200 \text{ keV}$ to $E = 1.1 \text{ MeV}$ are lost as shown in figure 4.23. The total losses at the vessel wall are divided into two ranges: a low energetic range from $E \approx 200 - 500 \text{ keV}$ and a highly energetic range from $E \approx 500 - 1100 \text{ keV}$. Particles of the first range are lost over the whole lower half of the vessel. However, particles with high energy $E > 500 \text{ keV}$ are only lost near the detector due to the small plasma-wall distance. The fast particle losses are divided into intervals between characteristic points in time ($t_1 = 2.0 \cdot 10^{-5} \text{ s}$, $t_2 = 6.5 \cdot 10^{-4} \text{ s}$, $t_3 = 1.3 \cdot 10^{-3} \text{ s}$, $t_4 = 2.0 \cdot 10^{-3} \text{ s}$) to investigate the loss

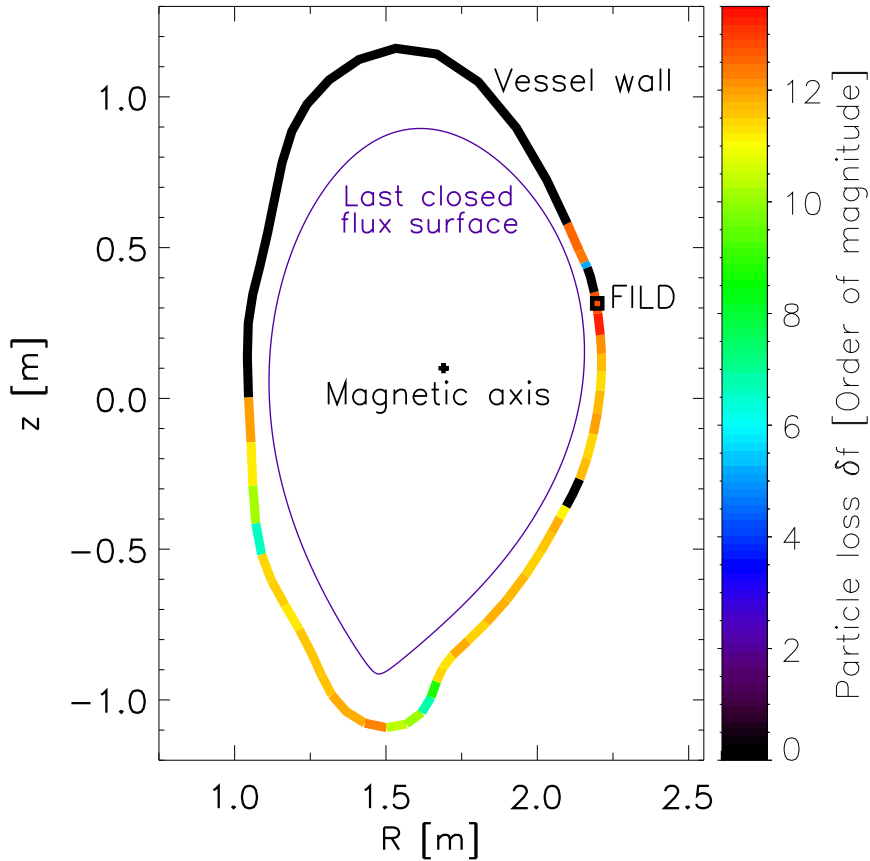


Figure 4.22.: Fast particle losses δf at the vessel wall over the total simulation time. (The colourbar is scaled logarithmically.)

behaviour. The ratio between low and highly energetic particles changes from the overshoot (red) to the saturation phase (violet). The losses at large energies decrease significantly whereas the loss amplitude at small energies remains the same over the total simulation time.

The loss distribution as a function of the pitch angle α (Fig. 4.24) shows that fast particles with a pitch angle of $\alpha = 47^\circ$ up to $\alpha = 82^\circ$ are lost at the vessel wall (dashed line). The main particle losses at the detector position are concentrated between $\alpha = 55^\circ - 70^\circ$. The outer peaks of the fast ion losses at the vessel wall (dashed black) for $\alpha = 50^\circ$ and $\alpha = 80^\circ$ refer to low energetic particles at the pronounced loss regions below the mid plane, i.e. inner divertor region and the LF side below the mid plane (Fig. 4.22).

The corresponding resonance plot (Fig. 4.25) for trapped particles with energies of $E = 10 - 1400$ keV and a single $n = 4$ -TAE shows two possible, separate loss regions at an energy range of $E = 650$ keV to $E = 1.1$ MeV and between $E = 200 - 300$ keV. Since the TAE amplitude is too small, the loss region of the low energetic range ($p = 0$) does not occur. However, the observed losses at the detector (Fig. 4.23) coincide very well with the expected loss region due to the $p = 1$ -resonance for highly energetic particles. These lost ions do not

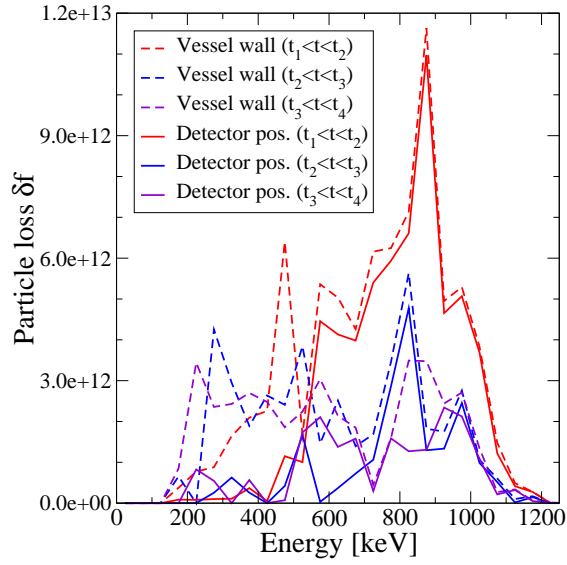


Figure 4.23.: Integrated fast particle losses δf as a function of energy between characteristic points in time. The dashed lines denote the particle losses over the whole vessel wall, the solid lines at the position of the FILD. The colours refer to the time intervals in figure 4.21.

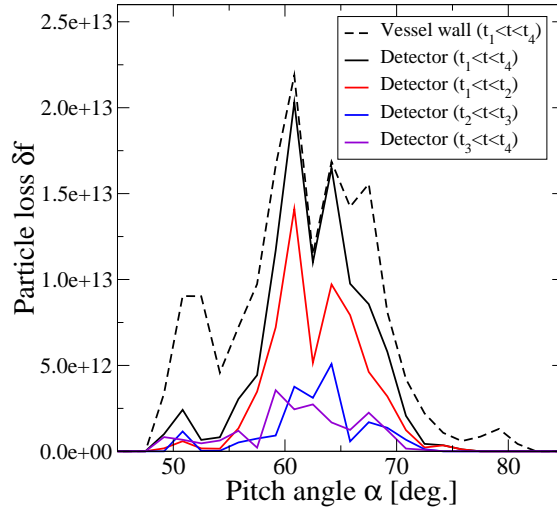


Figure 4.24.: Integrated fast particle losses δf as a function of pitch angle between characteristic points in time. The solid lines denote the fast ion losses at the detector position. The colours refer to the time intervals in figure 4.21. The dashed black line shows the total particle loss at the vessel wall over the total simulation time.

contribute to the mode drive due to $k_{\theta}\rho_{\perp} > 1$ [34], as explained in section 4.2.1. This shows that there can be a significant difference between particles that drive the mode and ejected particles.

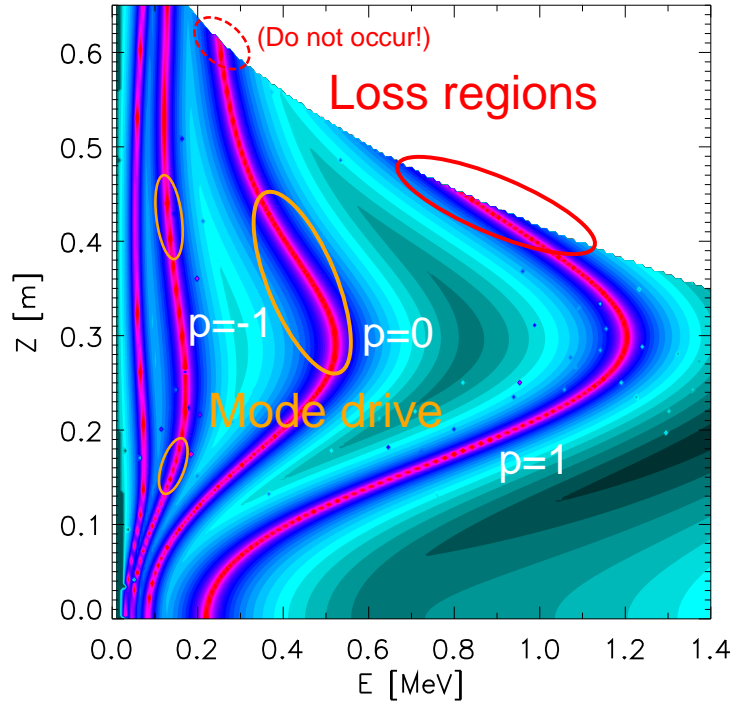


Figure 4.25.: Loss region of trapped fast particles caused by a single $n = 4$ -TAE whose bounce points are located at the radial position R_{mag} . The energetic ions are ejected by the $p = 1$ -resonance but the mode is driven via the $p = 0$ -resonance.

4.3. Enhanced Fast Particle Losses due to Multiple Modes

As shown in section 4.1, multiple TAEs with different toroidal mode numbers are present at the same time in most ASDEX Upgrade discharges. Including finite compressibility effects as described in section 2.3.3 results in the coupling of the shear Alfvén waves with the acoustic waves. Due to the coupling, BAE gaps are generated whose gap widths scale with the plasma beta. A kinetic analysis has shown that a global BAE [7] can be excited in this gap [29, 67] which is also present in the experiment.

It is well-documented [15, 16] that multiple TAEs excited at similar eigenfrequencies lead to a broader redistribution of fast particles due to their radial overlap. However, the interplay between a TAE and a BAE has not been investigated by means of numerical simulations so far. Therefore, in this section the mode drive of both modes and the corresponding particle redistribution in the presence of a fast particle population are examined. In this context, two aspects are of particular interest: It is open if significantly different mode eigenfrequencies (factor of 3 between the TAE and the BAE) also lead to a collective transport inside the plasma and if the redistribution caused by the BAE and TAE results in an enhanced fast particle loss. The corresponding particle losses are analysed in the following.

4.3.1. Mode Drive and Transport Phenomena

The inclusion of finite compressibility effects into the calculation of the frequency spectrum with CASTOR gives rise to a coupling between the shear Alfvén and the sound continuum. From the Mirnov pick-up coils, the determination of the toroidal mode number for the

BAE reveals that the mode signal consists of a mixture of eigenmodes with a dominant $(n, m) = (4, 4)$ component.

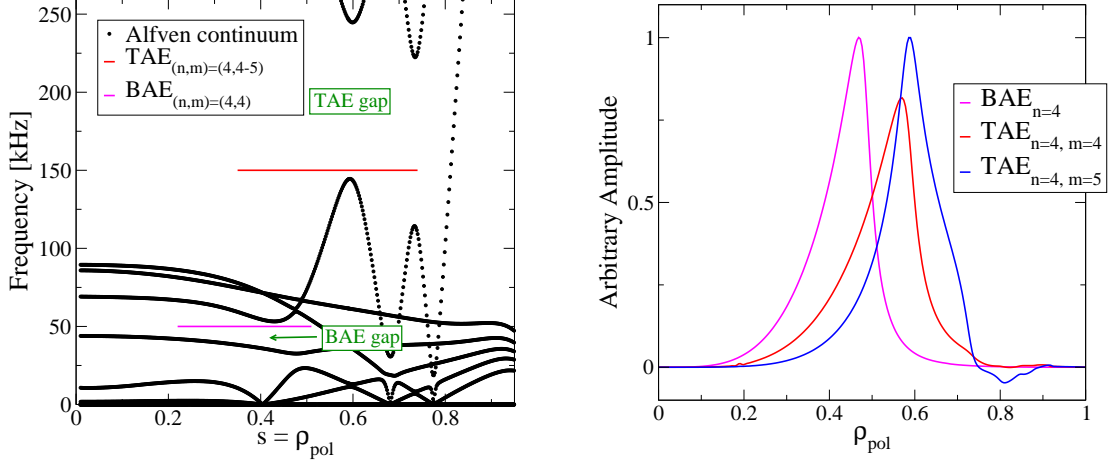


Figure 4.26.: Frequency spectrum showing the Alfvén and sound continuum (left) and the corresponding eigenfunctions of the BAE and the TAE, both $n = 4$ (right). The radial extensions of the BAE and TAE eigenfunctions are drawn at their discrete frequencies.

The frequency continua for $n = 4$ are shown in figure 4.26. The BAE is found at the upper edge of the BAE gap. The corresponding eigenfunction only consists of one dominant poloidal harmonic $m = 4$. The mode is localized at the radial position $\rho_{\text{pol}} \approx 0.45$ and overlaps radially with the $n = 4$ -TAE. The radial position of the BAE amplitude deviates from the experimental measurement $\rho_{\text{pol,exp}} \approx 0.25$ (Fig. 4.2). The difference can be caused by an inexact q -profile from the equilibrium reconstruction or by the missing of kinetic effects in the MHD code CASTOR. Calculations with the gyrokinetic code LIGKA [68] have shown that the radial BAE position shifts to the plasma centre [29]. Since the mode is also detected clearly at $\rho_{\text{pol}} \approx 0.45$ in the experiment (Fig. 4.27), this allows for the application of the simulated MHD eigenmode for the following simulations.

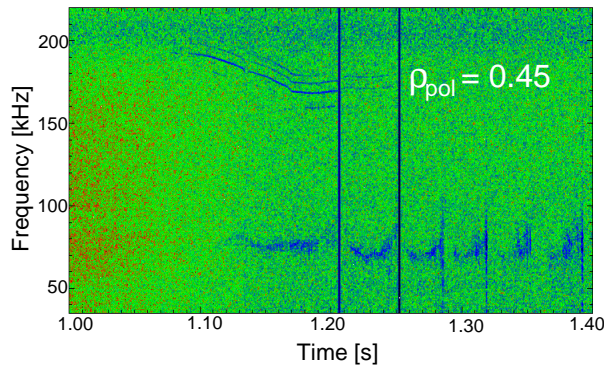


Figure 4.27.: Spectrogram of a soft X-ray measurement (line of sight at half minor radius). The $n = 4$ -BAE and the TAEs with toroidal mode number $n = 3 - 5$ are clearly visible.

4. Simulation Results

As for the single $n = 4$ -TAE in section 4.2, the same simulation conditions (315000 markers, fast particle beta $\beta_f = 0.3\%$) and the same fast particle distribution functions in real space and energy (Fig. 4.10 and 4.11) are applied.

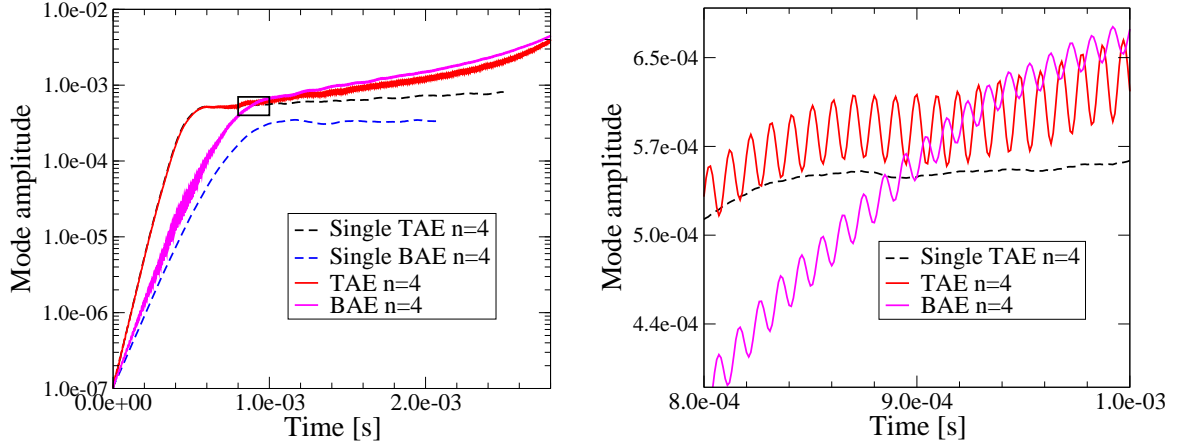


Figure 4.28.: Mode evolution of the BAE and the TAE, both $n = 4$, which are simulated simultaneously (left). Right: Enlargement of the mode evolution (black box on the left side).

At the beginning (Fig. 4.28), the TAE amplitude grows nearly with the same growth rate as for the single TAE case and starts to saturate. However, the BAE starts at a higher growth rate compared to the single simulation (dashed blue line) which saturates at an amplitude of $A = 3.4 \cdot 10^{-4}$. The BAE amplitude grows up to the TAE amplitude, $A = 5.4 \cdot 10^{-4}$. From this point on, $t \approx 9.0 \cdot 10^{-4}$ s, both mode amplitudes increase further and do not reach a saturated level. For the time $t > 2.3 \cdot 10^{-3}$ s both modes also show an additional nonlinear growth.

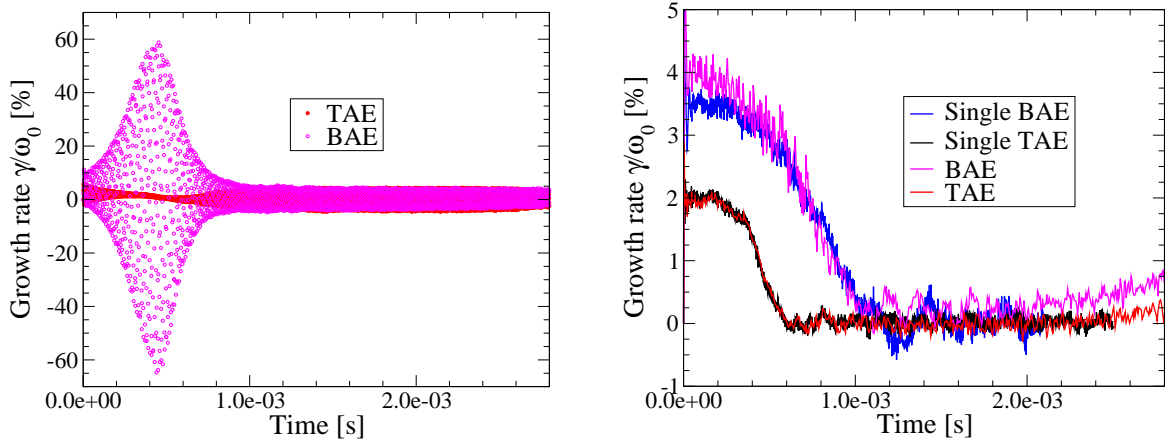


Figure 4.29.: Temporary and mean growth rate of the BAE and the TAE, both $n = 4$, which are simulated simultaneously. For comparison, the growth rates for the single eigenmodes are also displayed.

Superimposed on both amplitudes is an oscillation with a frequency of $\omega \approx 100$ kHz which is phase-shifted by π between the BAE and the TAE (Fig. 4.28, right). The oscillation is

seen in the growth rates for both modes clearly (Fig. 4.29). The maximal oscillation in the BAE growth ranges from $\gamma/\omega_0 = -60\%$ to 60% and is at the point in time when the ratio between the BAE to the TAE amplitude is minimal. Simultaneously, the oscillation amplitude for the TAE is minimal. If both modes have the same amplitude, the excursion of the oscillation is equal for both modes.

The mean growth rates which are calculated by an averaging procedure are shown in figure 4.29 (right). During the linear growth phase for $t < 4.0 \cdot 10^{-4}$ s, the mean growth rate of the BAE is increased but approaches the value of its single simulation at a time $t > 6.0 \cdot 10^{-4}$ s. After $t > 1.0 \cdot 10^{-3}$ s the mean growth rate is larger than zero and deviates from the single BAE value in the saturated phase. On the contrary, the mean growth rate of the TAE is not affected significantly by the presence of the BAE till the nonlinear behaviour sets in.

To exclude numerical errors, the oscillation has been resolved by a scan in the marker number (Fig. 4.30). It has been found that for all marker numbers the amplitude oscillations in both modes are present. For a marker number $N > 63000$, the oscillation amplitude between $t = 3.0 - 5.0 \cdot 10^{-4}$ s where the oscillation in the BAE growth rate is largest converges to a maximal excursion value of $|\gamma/\omega_0| \approx 50\%$. This indicates that the oscillation is not subject to numerical resolution.

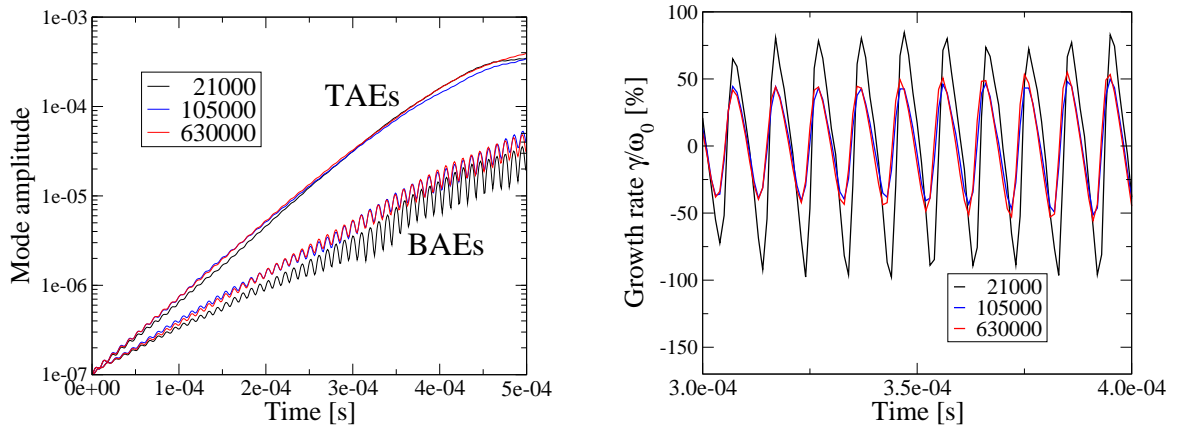


Figure 4.30.: Temporal evolution of the TAE and BAE amplitudes, both $n = 4$, for different marker resolutions (left). Right: Enlargement of the BAE growth rate for the time interval with the largest oscillations.

According to the known collective particle transport phenomenon [15], both eigenmodes should increase to higher amplitudes compared to their single simulations. Due to their radial overlap and the corresponding redistribution of energetic particles, the modes interact with a larger fast ion volume in phase-space which results in a broader total redistribution. After the gradient is flattened, the modes should saturate. However, the observed mode behaviour (Fig.4.28) cannot be explained completely with the described conventional theory. Therefore, an additional phenomenon has to be present simultaneously. In order to distinguish both mechanisms and to estimate their influence on the mode drive, the conventional gradient-driven mode growth with the coherent collective particle transport is investigated first.

Gradient-driven Mode Growth

At the beginning, the TAE is driven unstable by the $p = 0$ -resonance for highly energetic trapped particles (Fig. 4.31) as discussed for the single TAE case (Fig. 4.16). The BAE amplitude is one order of magnitude smaller than the TAE and therefore does not affect the TAE induced redistribution significantly. On the contrary, the BAE mode is influenced significantly by the redistribution caused by the TAE due to the radial localization as shown in figure 4.32. At the position of the BAE mode an increased radial gradient is generated by the TAE compared to the initial distribution function. This implies a stronger growth compared to a single BAE since $\omega_* \sim \nabla p$ (Eqn. 4.8).

The fast particles are redistributed by the BAE within a radial range of $s = 0.5 - 0.7$ only (Fig. 4.32 left). This radial region is partially located between both modes so that the TAE redistributes the ions further radially outwards if the fast particles are also in resonance with the TAE. This mechanism continues until the gradient flattens over the whole radial BAE-TAE range generating a broader radial plateau than for a single mode [15]. It has to be emphasized that the radial overlap of the modes is necessary for the collective particle transport. If the BAE eigenfunction is localized much more to the plasma centre, both the collective transport and the increased mode growth of the BAE caused by the TAE induced particle redistribution vanish.

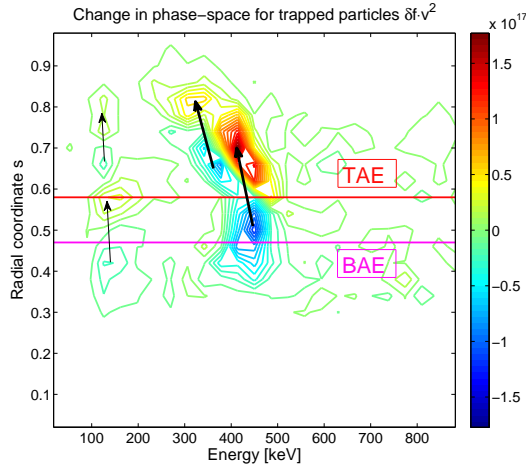


Figure 4.31.: *Redistribution of trapped particles caused by the BAE and the TAE in the linear growth phase for time $t = 4.0 \cdot 10^{-4} s$. The TAE amplitude is one order of magnitude larger than that of the BAE. The horizontal lines denote the radial positions of both modes.*

Such a collective transport is to be expected for fast particles which are resonant with both modes simultaneously. Since the main contribution to the mode drive is due to trapped particles, the resonance lines for both modes are drawn in the same resonance plot (Fig. 4.33 left). Intersections of resonance lines indicate the phase-space regions where fast ions can be further redistributed by the TAE. As the BAE amplitude increases up to $t = 8.0 \cdot 10^{-4} s$, the fast particle phase-space at the radial BAE position $s = 0.47$ and an energy around $E = 130 \text{ keV}$ (Fig. 4.33 right, black ellipse) is redistributed due to the enhanced BAE mode growth caused by the increased gradient (Fig. 4.32, right). The fast particles are further redistributed by the TAE so that the radial gradient at the BAE position remains.

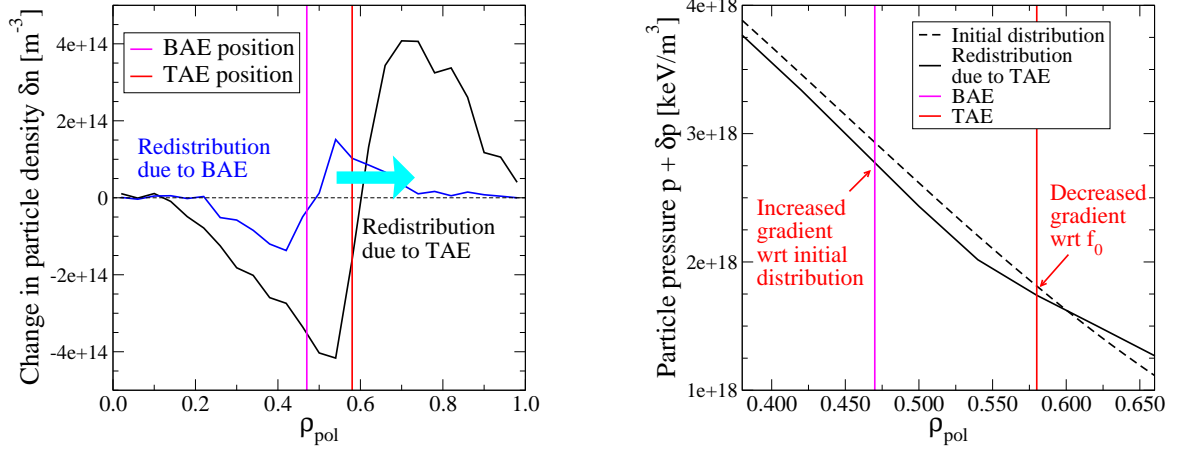


Figure 4.32.: Total radial redistributions of the fast particles at time $t = 2.0 \cdot 10^{-3}$ s (averaged over $t = 1.9 - 2.1 \cdot 10^{-3}$ s) caused by a single TAE (black; as shown in Fig. 4.14) and a single BAE (blue). If both modes are present, the BAE induced particle ensemble between both modes is further redistributed by the TAE. Right: Due to the radial localization of the BAE, the BAE mode growth is increased because of an increased radial gradient caused by the TAE.

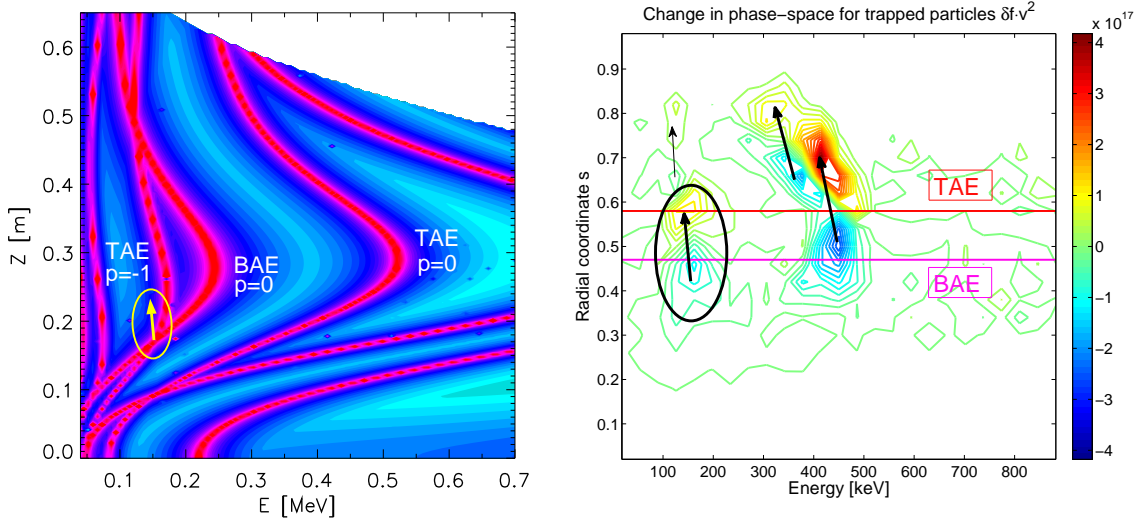


Figure 4.33.: Resonance lines for the BAE and the TAE for different bounce harmonics p (left). Right: The redistribution of trapped particles caused by the BAE and the TAE for the point in time, $t = 8.0 \cdot 10^{-4}$ s (left). The redistribution for the low energetic ions with $E = 130$ keV is increased due to the larger radial gradient and the intersection of the resonance lines (left).

This process increases the mean gradient in the fast particle pressure profile ∇p from equation (4.8) at the radial BAE position by about 8% but does not explain the increase of the BAE growth rate by about 14%. An additional drive mechanism must be present simultaneously to resolve all observations.

Double-resonant Mode Coupling

Regarding the oscillation in the mode growth as seen in figure 4.28, the behaviour indicates that a particular particle ensemble is exchanging energy and momentum in a bidirectional way. It is found by loading only trapped or passing particles that trapped particles cause this modulation in the amplitude. A specific ensemble of particles (Fig. 4.34) is radially localized between both waves whereby their trajectories pass through both modes. These particles are resonant with both modes so that equation (4.1) is satisfied for each mode simultaneously. This leads to

$$\omega_{tp} (n_{TAE} - n_{BAE}) - \omega_b (p_{TAE} - p_{BAE}) = \omega_{TAE} - \omega_{BAE} = \Delta\omega, \quad (4.12)$$

where $\Delta\omega$ is the beat frequency of the two modes.

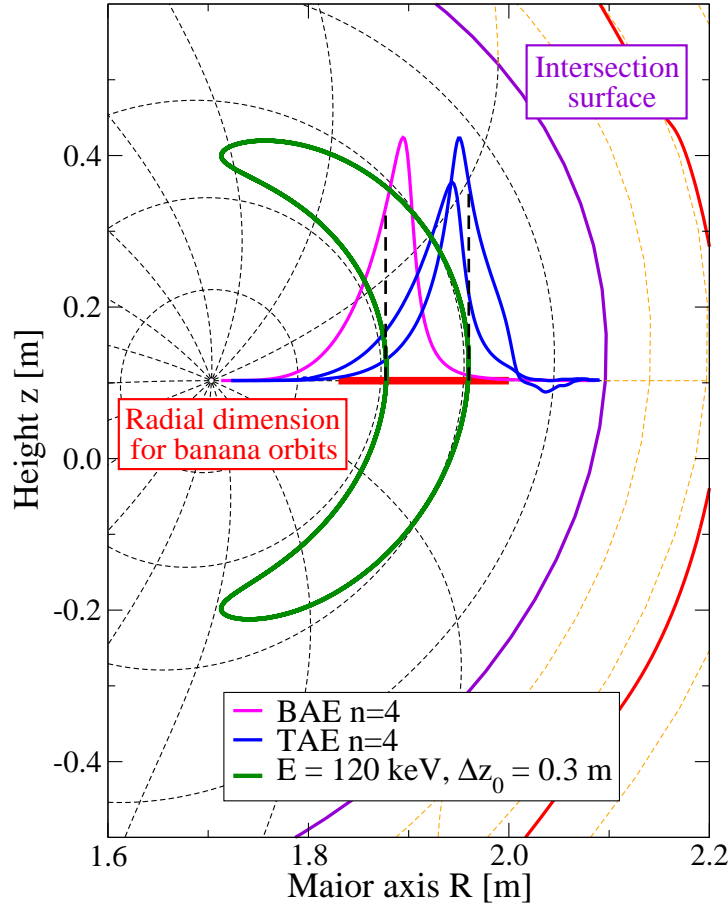


Figure 4.34.: Example of the specific trapped particle ensemble which is localized radially between both mode amplitudes with a bounce frequency of $\omega_b = 100$ kHz. The red line denotes the radial localization where the particle orbits have to be located to generate an oscillatory behaviour.

In figure 4.35, the resonance plot for the general resonance condition (4.1) is shown for the TAE and the BAE, both with $n = 4$, and for comparison also with $n = 3$ and $n = 4$. The

BAE frequency is $\omega = 50$ kHz, for the $n = 3$ - and $n = 4$ -TAEs the corresponding frequencies are $\omega = 145$ kHz and $\omega = 150$ kHz, respectively. Due to the radial localization of the trapped particles, the bounce harmonics for both mode combinations are $p = 0$ for the BAE and $p = -1$ for the TAE. This simplifies the resonance condition (4.12) to

$$\begin{aligned}\omega_b &= \Delta\omega = 100 \text{ kHz} && (\text{both } n=4) \\ -\omega_{tp} + \omega_b &= \Delta\omega = 95 \text{ kHz} && (n = 4\text{-BAE}, n = 3\text{-TAE})\end{aligned}$$

In both cases, the resonance line of the beat frequency is crossing the resonance lines of the single modes at their intersections. But only if the toroidal mode numbers are equal, an oscillatory behaviour was found in the simulation. This phenomenon has also been seen for all pairs of eigenmodes with the same toroidal mode number $n = 3, \dots, 5$. This indicates that different particle precession drifts with respect to each mode corrupt the 'double-resonant' interaction between both modes via fast particles.

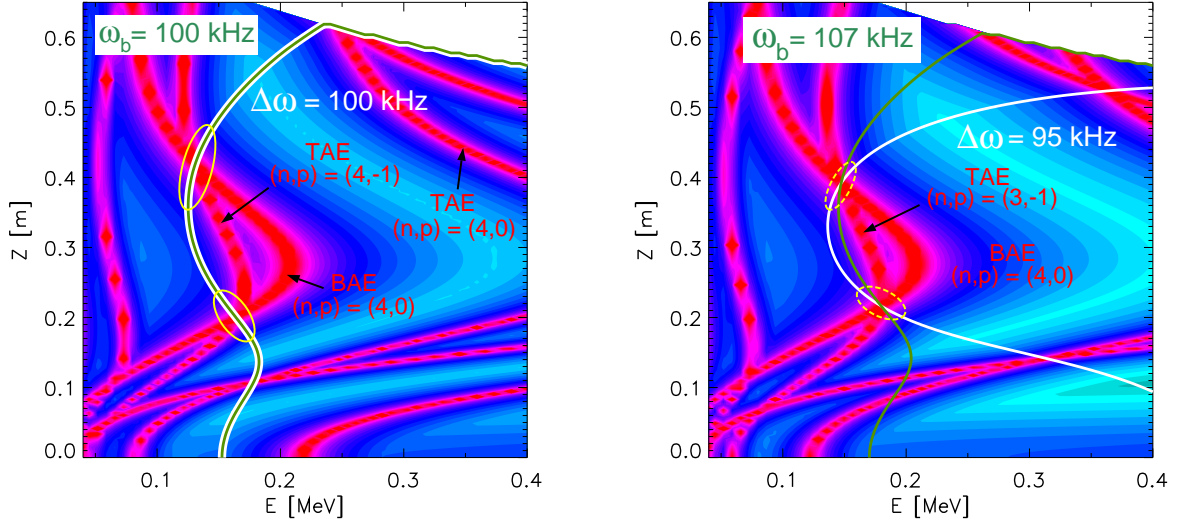


Figure 4.35.: The beat frequency $\Delta\omega$ (white) is displayed in the resonance plot for the TAE and the BAE, both $n = 4$ (left) and $n = 3$ as well as $n = 4$ (right), crossing the general resonance intersections (yellow ellipses). But only for the first case, the particles in the yellow ellipses generate the oscillations.

Transforming into the frame of reference which moves with the BAE $\omega_{BAE} = n \cdot w_{tp}$, the banana centres of these double-resonant particles and the BAE phase are fixed for the $p = 0$ -resonance (Fig. 4.36). In this reference frame, the TAE propagates with the frequency difference of the modes, the beat frequency. A trapped particle from the phase-space (Fig. 4.35 left, yellow solid ellipse) is passing through both radial mode localizations and it is resonant with both modes. The energetic ion is considered to be started at the TAE position at the midplane, its bounce time is T . The TAE is initialized with a certain phase ϕ_0 . At time $T/2$, the particle completes half of its poloidal orbit, leaves the wave potential of the TAE due to its radial drift and is trapped in the wave potential of the BAE. After a complete orbit at time T , it returns to the radial TAE position.

If ω_b and $\Delta\omega$ are equal (Fig. 4.35 left), the particle re-enters the TAE position with the initial phase ϕ_0 (Fig. 4.36). For the case of different toroidal mode numbers (Fig. 4.35 right), the bounce frequency of a double-resonant fast particle (yellow dashed circles) is larger than the beat frequency $\Delta\omega$. Thus, the particle experiences a different phase of the TAE after one bounce orbit.

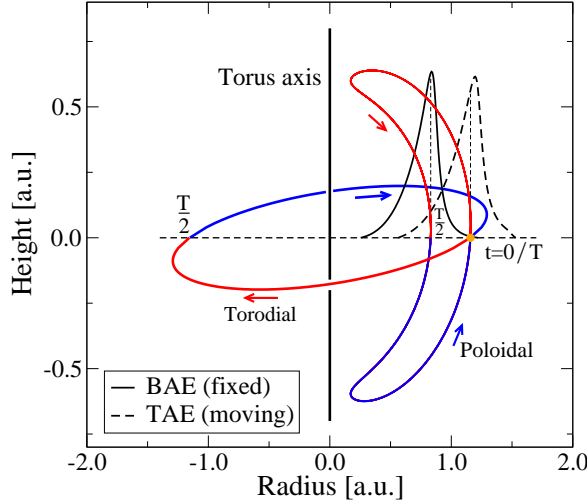


Figure 4.36.: 3D schematic view of the frame of reference for the BAE and a particle from figure 4.35 (left; yellow ellipse). In this system, the TAE propagates toroidally with the beat frequency $\Delta\omega$ whereas the particle propagates with the bounce frequency, $\omega_b = \Delta\omega$. The particle is trapped in both wave potentials with a fixed phase.

This means that the toroidal precession drift of the particle has to be equal with respect to both modes so that the resulting resonance condition for energy exchange is defined by

$$\begin{aligned} -(p_1 - p_2) \cdot \omega_b &= \Delta\omega \\ P \cdot \omega_b &= \Delta\omega \quad \text{for} \quad n_1 = n_2, \end{aligned} \quad (4.13)$$

where P is the difference of both bounce harmonics. However, not all particles which fulfil the above mentioned conditions exchange energy between both modes. Only the particles with an initial phase ϕ_0 that gain energy from the TAE (slight inwards 'shift') and transfer the energy to the BAE (slight outwards 'shift') stay in resonance (no net shift). The particles that lose part of their energy to the TAE are redistributed radially outwards.

In figure 4.28, the BAE amplitude is smaller than that of the TAE before $t = 9.0 \cdot 10^{-4}$ s and the BAE oscillation is the largest when the ratio between both modes is largest. The double-resonant particles transfer an amount of energy which is small compared to the TAE energy but large compared to the BAE energy. Therefore, the BAE amplitude modulation is large. Not before both wave energies are equal, the opposite oscillation amplitude is also nearly equal but is slightly larger for the mode which gains energy. This balancing phenomenon is depending on the difference in amplitude for the interacting modes and transfers net energy to the eigenmode whose amplitude is smaller.

Due to the phase locking of the energetic ions, a redistribution of the double-resonant particles does not happen which is in significant contrast to the gradient-driven mode growth. A further distinction between both mechanisms is the radial direction of the transfer. Whilst the radially outward redistributed particles transfer their energy to the waves at the radial mode position, the particles trapped in the exchange mechanism can transfer net energy radially both inwards and outwards depending on the ratio of the amplitudes. The crucial condition is only a double-resonant wave-particle-coupling. However, the process is always superposed by the gradient-drive mode growth and cannot be treated separately. Considering a radially constant fast particle distribution, the wave-particle interaction Lagrangian determined by the equations (3.44) and (3.45) would be zero since the change in the fast particle distribution δf (Eqn. 3.37) is governed by the gradients.

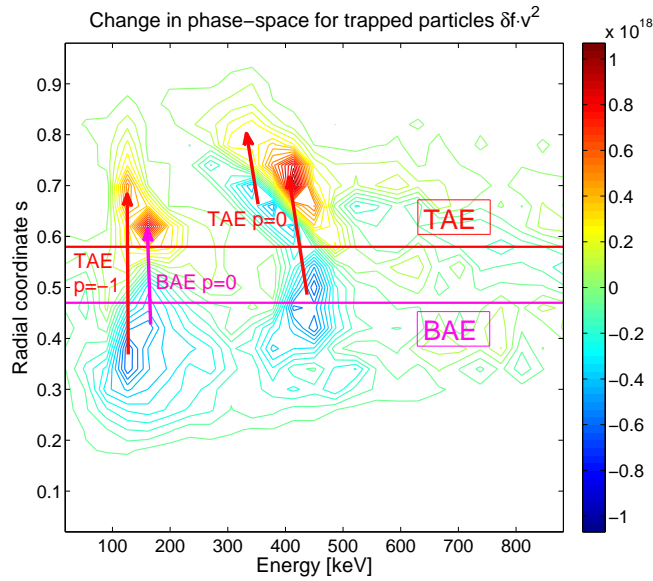


Figure 4.37.: Various mode resonances are responsible for the redistribution of fast particles caused by the BAE and the TAE at time $t = 2.0 \cdot 10^{-3}$ s. The collective particle redistribution is caused by the interplay between the $p = 0$ -BAE and $p = -1$ -TAE resonance.

Because of both transfer mechanisms which are of the same order in this case, the BAE amplitude approaches the TAE amplitude at the time $t = 8.0 \cdot 10^{-4}$ s and continues to grow. It is found that the fast particle redistribution caused by the $p = 0$ -BAE resonance is enlarged radially due to the increased BAE amplitude (Fig. 4.37). Again, the particles are further shifted by the TAE via the $p = -1$ -resonance so that an extended plateau is created between both modes as shown in figure 4.38.

Due to the enlarged mode amplitude and the radial extension of the TAE, fast particles are redistributed by various TAE resonances with a bounce number from $p = -1, \dots, 1$. At time $t = 2.0 \cdot 10^{-3}$ s, the redistribution strength due to the $p = -1$ -resonance is as large as the strength due to the $p = 0$ -resonance (Fig. 4.37). This differs from the redistribution due to $p = 0$ at the beginning (Fig. 4.31) and is caused by the previously explained interplay with the $p = 0$ -BAE resonance as shown in figure 4.33.

4. Simulation Results

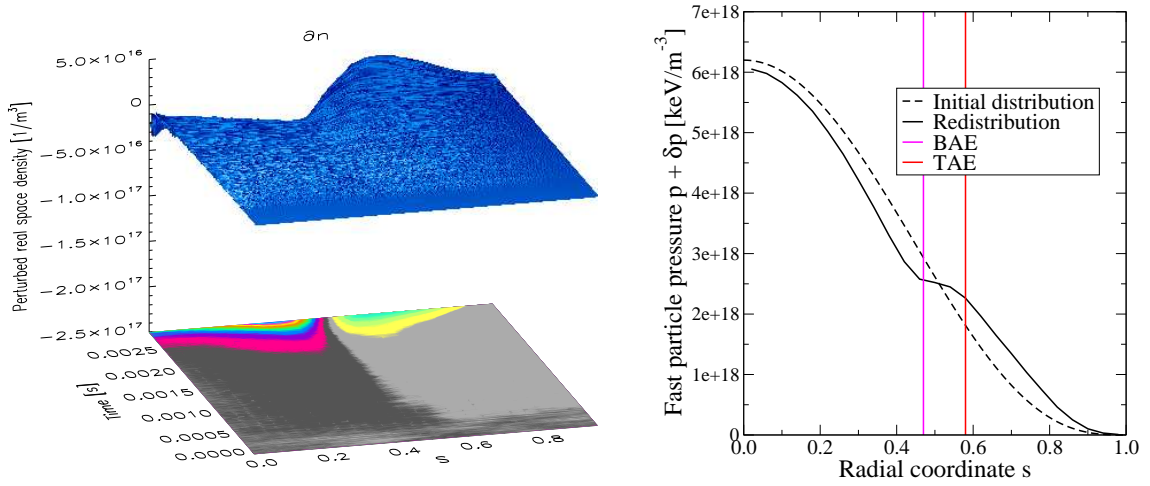


Figure 4.38.: Fast particle redistribution in density (left) and pressure (right) at the time $t = 2.0 \cdot 10^{-3}$ s.

At times $t > 2.0 \cdot 10^{-3}$ s, the fast particle redistribution extends over the whole plasma radius showing a remarkable drop at the magnetic axis (Fig. 4.38). Due to large amplitudes, both modes continue to redistribute particles.

4.3.2. Fast Ion Losses

Compared to the single mode case, the fast ion losses are expected to be strongly increased due to the large mode amplitudes which give also rise to diffusive losses [69, 70, 71]. The stochastic threshold for a single mode is $\delta B_{\psi}/B \approx 10^{-3}$ although that may be greatly reduced to $\delta B_{\psi}/B \approx 10^{-4}$ in the multiple mode case [69]. With respect to these findings, the simulated fast ion losses are investigated and compared to the single mode case.

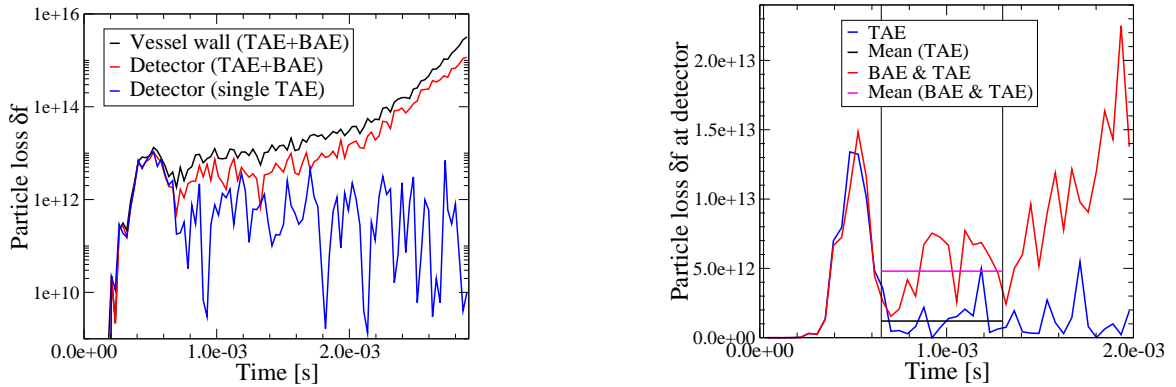


Figure 4.39.: Time evolution of the fast ion losses caused by the both modes and by a single TAE (left). At the detector, the loss amplitude due to both modes is already enhanced by a factor of 3 during the saturation phase of the single TAE (right).

Again, the fast ion losses at the virtual detector position (Fig. 4.39) are divided into

three time intervals ($t_1 = 2.0 \cdot 10^{-5}$ s, $t_2 = 6.5 \cdot 10^{-4}$ s, $t_3 = 1.3 \cdot 10^{-3}$ s, $t_4 = 2.0 \cdot 10^{-3}$ s) to compare the results to the losses of a single TAE. During the overshoot phase, the loss signals of both modes (red) and the single mode (blue) match up nearly perfectly because the amplitude of the BAE is still small compared to the TAE amplitude. When the BAE amplitude approaches the order of magnitude of the TAE amplitude during the time interval $t = 0.65 - 1.30 \cdot 10^{-3}$ s of the saturation phase, the mean fast ion losses are already larger by a factor of 3. Afterwards, the losses continue to grow exponentially.

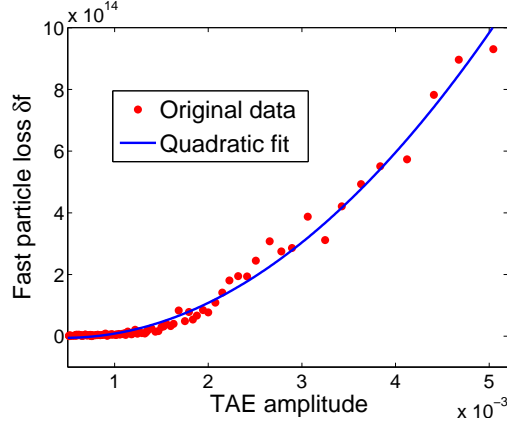


Figure 4.40.: Dependence of the fast particle loss δf at the detector position on the mean TAE amplitude.

It was shown [69] that the stochastic fast ion losses scale with $(\delta B_\psi/B)^2$ if the mode amplitude is above the threshold. To investigate at which mode amplitudes stochastic losses are observed, the fast particle losses δf at the detector position (Fig. 4.39 left; red line) are compared with the corresponding mean TAE amplitudes (4.28) for the same points in time. In figure 4.40, the fast particle losses show a quadratic dependence. Since the stochastic behaviour is clearly seen only after the TAE has reached an amplitude of $\delta B_r/B_0 \approx 10^{-3}$, the threshold for a single mode seems to be valid in this case. The reduction of the threshold [69] to 10^{-4} in the presence of multiple modes was detected for modes with similar mode amplitudes and radial positions. Since the BAE is core-localized and the BAE amplitude is one order of magnitude smaller than the TAE amplitude as the TAE amplitude reaches the threshold of $\delta B_r/B_0 \approx 10^{-4}$ at $t \approx 4.0 \cdot 10^{-4}$ s, the threshold conditions for stochastic losses due to multiple modes are not satisfied.

In figure 4.41 (left), the fast ion losses at the detector position with respect to the energy are shown. During the overshoot phase for $t_1 < t < t_2$ (red), the loss signals caused by both modes (solid) compared to the single mode (dashed) match up nearly perfectly because of the small BAE amplitude. In the linear saturation of $t = 0.65 - 1.30 \cdot 10^{-3}$ s (blue), the loss distribution due to both modes which ranges from $E = 200$ keV - $E = 1.2$ MeV is different from the fast ion losses caused by the single TAE. The loss amplitude is larger by a factor of 3 as seen in the time trace before (Fig. 4.39). The range of the main losses between energies of $E = 500$ keV and $E = 1$ MeV has increased compared to the peak around $E = 800$ keV for the single mode. After $t_3 = 1.30 \cdot 10^{-3}$ s, the loss amplitude for $E = 250 - 400$ keV has increased significantly compared to the losses around $E = 400 - 1100$ keV. Compared to the

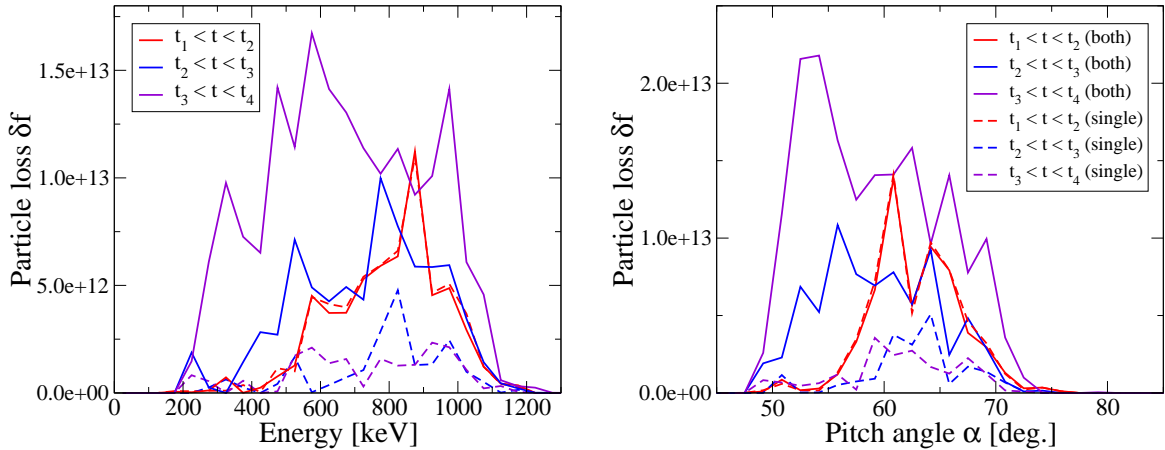


Figure 4.41.: Fast ion loss signal of the energy (left) and the pitch angle (right) during the specific time intervals. The dashed lines show the corresponding detector signals caused by a single TAE.

single mode case, the increase of the fast ion losses with energies $E = 250 - 400$ keV is the main difference, in addition to the large total amount of the fast ion losses.

In figure 4.41 (right), the pitch angle of the loss signal ranges from $\alpha = 48^\circ - 72^\circ$ after the overshoot which deviates significantly from the loss distribution (Fig. 4.24) caused by a single TAE, $\alpha = 54^\circ - 71^\circ$. Especially with the start of the nonlinear fast ion losses, most fast particles are ejected at a pitch angle around $\alpha = 52^\circ$. In the saturation phase of the single mode case, the fast ion losses are concentrated between $58^\circ - 70^\circ$.

Normalizing the amplitudes of the fast ion losses to unity for different points in time reveals a qualitative change in the energy distributions as shown in figure 4.42. It is seen that during the linear growth phase the main losses are detected at an energy around $E = 900$ keV. During the saturation phase, the amplitude maximum changes from $E = 750$ keV to $E = 550$ keV at the end of the nonlinear growth ($t = 2.9 \cdot 10^{-3}$ s). The loss range in energy during these three stages widens as the minimum limit is decreased to lower energies, from $E = 550$ keV to $E = 200$ keV. The maximal loss energy remains around 1.1 MeV. A further difference is the form of the distribution which changes from distinct peaks to a broader shape with two small peaks at $E = 250$ keV and around $E = 800$ keV. Because of the large mode amplitudes $\delta B_\psi/B > 10^{-3}$, such a change in the distribution can result from stochastic losses for which all fast particles are ejected without a preference in energy [70].

A comparison of the lost fast ions (Fig. 4.42) to the corresponding resonances shows that the distinct peak at an energy around $E = 800$ keV which is present for all points in time coincides very well with the intersection of the $p = 1$ -TAE resonance with the loss boundary (Fig. 4.43 left). The loss region at $E = 250$ keV caused by the $p = 0$ -TAE resonance appears when the TAE amplitude reaches $\delta B_\psi/B \approx 10^{-3}$. Then, fast particles in the outer plasma region are expelled by the dominant poloidal harmonics in the outer TAE gaps at $s = 0.7 - 0.9$ (Fig. 4.8 mid). Since the trapped particle orbit width Δ_b for $E = 300$ keV in the outer plasma region is larger than the mode width Δ_m for the poloidal harmonics $m + 2, \dots, m + 4$ and therefore the mode interaction scales with m^{-2} [34], these lost fast

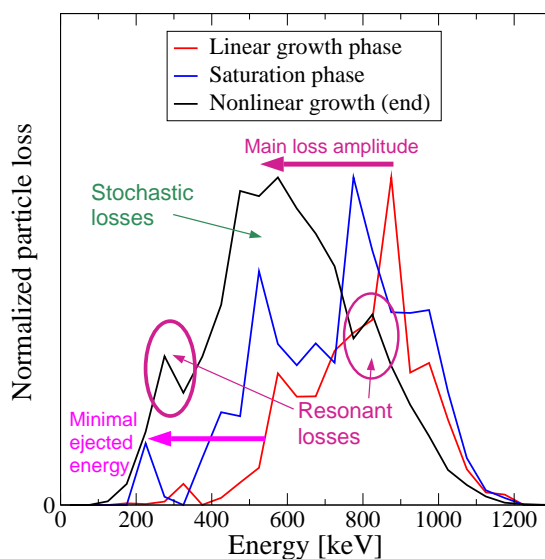


Figure 4.42.: Normalized loss distributions with respect to the energy for different states of the modes. The main loss amplitude changes its dependence on the energy to a lower value. The distribution in energy is broader for a later point in time than at the beginning.

particles are only present for a large TAE amplitude. This is in contrast to the single mode case (Fig. 4.23) where no significant fast ion losses are detected.

Although the BAE resonance line (Fig. 4.43 right) intersects with the loss boundary, the mode cannot eject fast particles at $E = 250$ keV due to its core-localization, even for mode amplitudes above $\delta B_\psi/B = 10^{-3}$. However, at the end of the nonlinear growth the main fast particle losses are detected at energies $E = 400 - 700$ keV (Fig. 4.42, black line). These particles can partly be expelled by the $p = 1$ -BAE resonance due to the large BAE amplitude.

4.3.3. Summary

In this section it has been shown that a radial transport of fast particles between modes of different types due to resonance overlap at very different eigenfrequencies is as possible as for multiple TAEs [16]. The gradient in the radial fast particle distribution drives both modes unstable. However, the mode drive due to the increased gradient at the radial position of the BAE amplitude caused by the TAE mode is larger than that compared to the single BAE case. The collective particle transport due to both modes generates a flat gradient region at the position of the modes. An additional mechanism has been identified that transfers energy and momentum via double-resonant trapped particles between two modes. The mode that has the smaller amplitude is driven by the mode with the larger amplitude independently on the radial mode position. Since the increase of the mode drive for the BAE is approximately twice as large as the increase of the radial gradient in the particle distribution, the influence of the double-resonant mode coupling on the mode drive is of the same order as that of the gradient-driven mode growth.

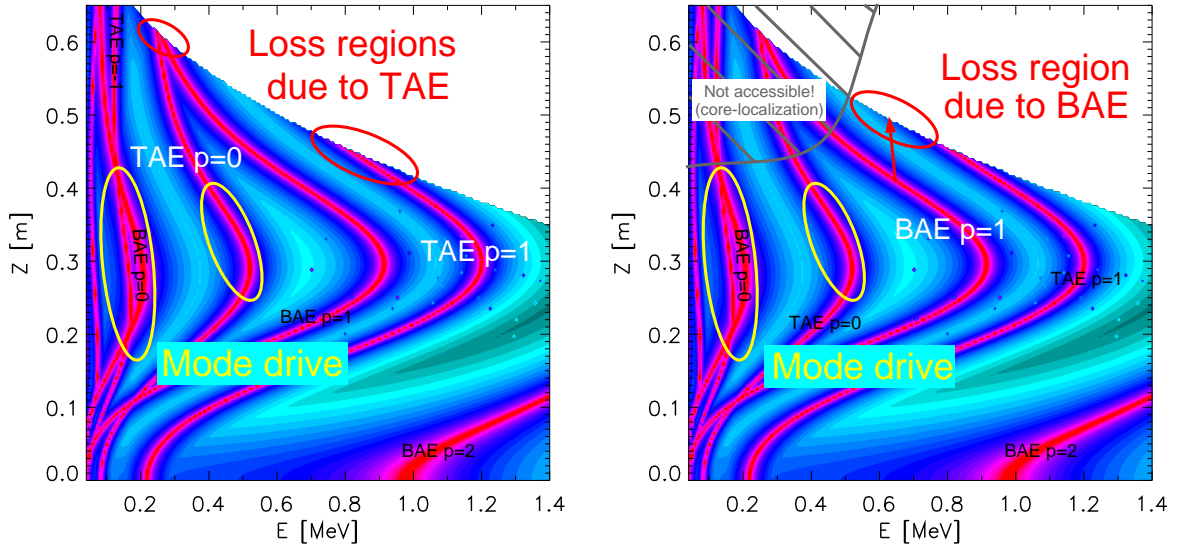


Figure 4.43.: Resonance plots of both modes but the fast ion losses caused by the TAE (left) and the BAE (right) are treated separately. A difference between fast particles that drive the modes and particles which are ejected is clearly observed.

Due to both mechanisms, the TAE amplitude is increased further as the BAE amplitude reaches the TAE amplitude. Due to the significantly increased TAE amplitude, an additional region in the low energetic fast ion loss range appears as the TAE reaches the stochastic threshold for a single mode. A broader shape of the loss distribution indicates an increasing influence of stochastic losses. Nevertheless, a striking difference is observed between fast particles that drive the modes and particles that are ejected (Fig. 4.43).

4.4. Fast Particle Losses for ICRH-generated distributions

In order to compare the fast ion losses with the experimental data, an implemented ICRH-generated fast particle distribution is used in the following. It has to be investigated how realistic the implemented distribution is and if all experimental observations can be explained. Therefore, both single modes and multiple modes in the presence of the anisotropic distribution function are studied. The results of the mode drive and the fast ion losses are compared to the simulated results of the isotropic loading first.

The anisotropic ICRH-generated fast particle distribution was introduced in section 3.2.5 and deviates from its isotropic counterpart especially by the narrow initialization of the pitch angle variable around $\lambda = 0$ as shown in figure 3.8. In addition, the particles are loaded within small poloidal angle segments which are localized around the magnetic axis position (Fig. 3.7). The same slowing-down distribution in energy as for the isotropic distributions is used (Eqn. 4.3).

The volume-averaged fast particle beta $\langle \beta_f \rangle$ (Eqn. 3.82) which is related to the distribution function determines the particle density. Due to the anisotropy in poloidal space and in the pitch angle in an ICRH-generated distribution, an increased particle density increases the constant C in the equation so that an enhanced weight is represented by each marker for

a given $\langle\beta_f\rangle$ compared to the isotropic distribution. For this reason, the growth rates of a single TAE are investigated in dependence on different fast particle pressures first.

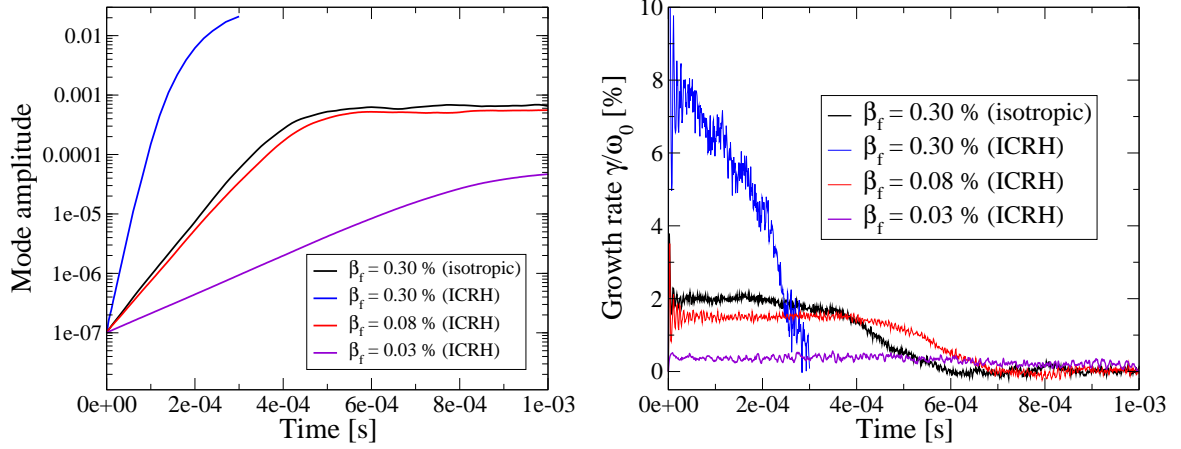


Figure 4.44.: Evolution of the amplitudes and the growth rates for different fast particle betas using the example of a single TAE.

From figure 4.44 it can be seen that for the same $\langle\beta_f\rangle = 0.3\%$ as used in the isotropic case a single TAE which is driven by an ICRH-generated distribution does not saturate. Its amplitude reaches a value of $A > 10^{-2}$. At such amplitudes the code is out of validity since the perturbation is not small compared to the background magnetic field any longer, $\delta B_\psi = \mathcal{O}(10^{-2} - 10^{-1} \cdot B)$. The same fast particle beta for an isotropic distribution increases the mode's amplitude up to $A \approx 6.0 \cdot 10^{-4}$ followed by a saturation phase which agrees very well with the experimental findings in section 4.1. For an ICRH-generated distribution, the same behaviour is seen approximately for $\langle\beta_f\rangle = 0.08\%$ (Fig. 4.44). This result shows that the fast particle beta that generates the same mode amplitude in the simulation is far below the experimental value. The mismatch is probably due to the lack of a background damping mechanism and a continuous fast particle source.

In the following, all simulations with an ICRH-generated distribution are carried out with a fast particle beta of $\langle\beta_f\rangle = 0.08\%$. A difference compared to the isotropic loading with $\langle\beta_f\rangle = 0.3\%$ is seen in the evolution of the growth rates. The ICRH-driven mode increases slower but over a longer time scale compared to the mode driven by an isotropic distribution. Decreasing the fast particle beta by a factor of 10 to $\langle\beta_f\rangle = 0.03\%$ shows that the amplitude decreases approximately about four orders of magnitude.

The mode is driven unstable by the same trapped particle ensembles as in the isotropic case (Fig. 4.16). The fast ions with an energy between $E = 420 - 550$ keV interact with the TAE via the $p = 0$ -resonance as well as particles with energies around $E = 130$ keV via the $p = -1$ -resonance. However, the amount of redistributed particles changes for the two specific particle ensembles as shown in figure 4.45 in comparison to the isotropic case (Fig. 4.15). The resulting radial fast particle redistribution for the anisotropic case is similar to that for the isotropic case (Fig. 4.13).

The initial distribution in the pitch angle variable (Fig. 3.8 right) which is centred around $\lambda = 0$ broadens as the particles evolve in time. The final range is $\lambda \in [-0.6, 0.4]$. As shown

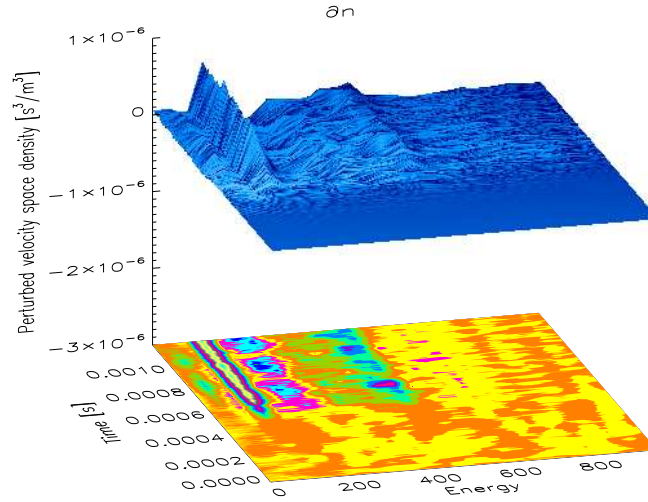


Figure 4.45.: Temporal redistribution in energy for an ICRH-generated fast particle distribution in the presence of a single $n = 4$ -TAE. Fast particles are redistributed around $E \approx 130$ keV (from blue/magenta to green/yellow) and from the energetic range $E \approx 420 - 550$ keV to $E \approx 350 - 420$ keV.

in figure 4.46 (left), two peaks at $\lambda = 0.1$ and $\lambda = -0.4$ evolve. Since a trapped particle propagates in co- and counter-passing direction with respect to the magnetic field lines, it changes its sign of the parallel velocity ($\lambda = v_{\parallel}/v$). The extremum values of λ are both the minimum and maximum between the bounce points ($\lambda = 0$). Thus, the peaks denote the temporary values at the minimal and the maximal radial position. At these radial positions, the ions interact with the TAE.

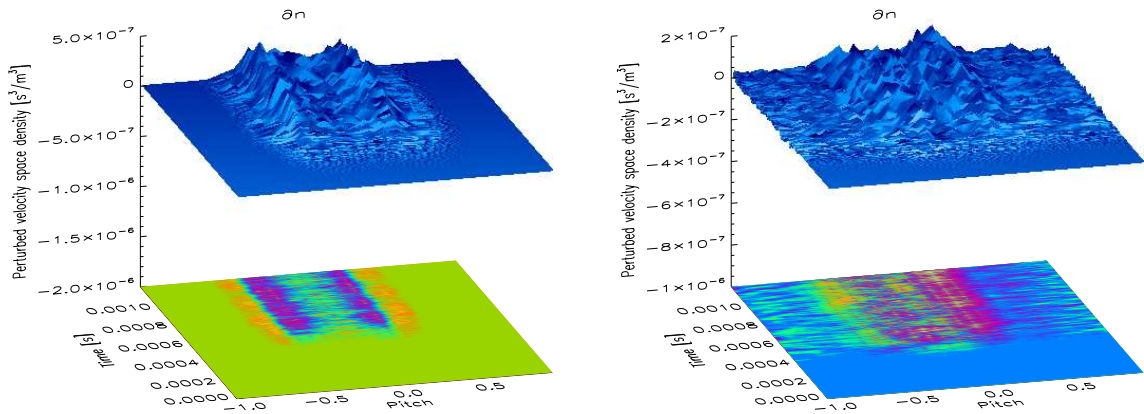


Figure 4.46.: Temporal pitch angle redistribution in the presence of a single $n = 4$ -TAE for an initial ICRH-generated distribution (left) and an isotropic distribution (right).

Comparing with the isotropic marker loading (Fig. 4.46 right), the whole range of the pitch angle variable is affected but the peaks are still visible. As mentioned before, the main drive is due to trapped particles in the isotropic initialization. The absolute values of the

peaks are smaller by a factor of 2 compared to the ICRH-loading, and the difference between both peaks refers to the additional contribution of co-passing particles. These particles increase the amplitude at $\lambda = 0.1$.

For the following simulations, the same parameters as for the BAE and the TAE with a toroidal mode number $n = 4$ are considered. Exceptions are the fast particle distribution and the smaller absolute value of the fast particle beta.

In figure 4.47 both mode amplitudes increase nearly equally during the linear growth phase, i.e. γ_{TAE} is smaller whereas γ_{BAE} is higher compared to the isotropic distribution. This implies that the decrease of the fast particle beta is overcompensated by the ICRH specific loading. The decrease in the TAE growth is due to the absence of passing particles. Since trapped fast particles are loaded which have been identified to cause the main mode drive as shown for the isotropic loading, both modes reach a higher amplitude after the linear growth phase. In addition, the same oscillatory behaviour (Fig. 4.47 right) is detected which drives both modes further unstable without a saturation. The excursions are much smaller than in the isotropic case because both amplitudes are roughly equal.

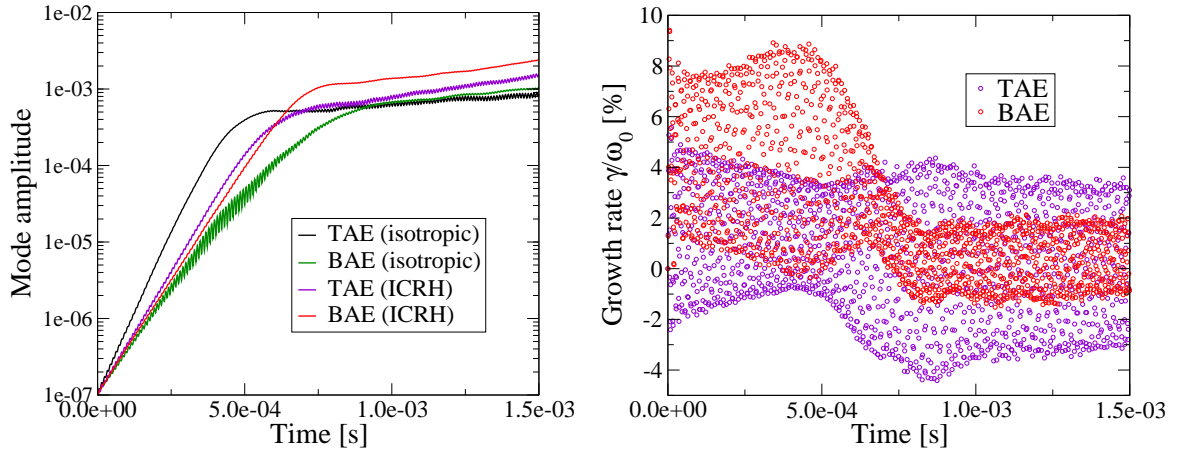


Figure 4.47.: Evolution of the amplitudes for a BAE and a TAE, both $n = 4$, caused by a ICRH-generated and an isotropic distribution (left). The growth rates of both modes due to the ICRH-generated distribution show the same oscillatory behaviour as for the isotropic case (right).

Due to the higher amplitudes after the linear growth phase, the temporal evolution of the loss rate is increased compared to the isotropic initialization (Fig. 4.48). Since there is no saturation phase (Fig. 4.47), the fast ion losses increase exponentially after the overshoot for the time $t > 10^{-3}$ s. For this reason, only two time intervals are chosen, the overshoot phase ($t < 10^{-3}$ s) and the nonlinear growth phase ($t > 10^{-3}$ s). For these time intervals, an analysis with respect to energy and pitch angle is carried out.

In figure 4.49, the energies of the lost particles range from $E = 400$ keV to $E = 1.2$ MeV. In the overshoot phase, the particles are mainly ejected at $E = 850$ keV. This value changes significantly to a lower energy $E = 650$ keV during the nonlinear growth phase. The former peak is due to the resonant losses for $p = 1$ -TAE (Fig. 4.43 left). As indicated in the section

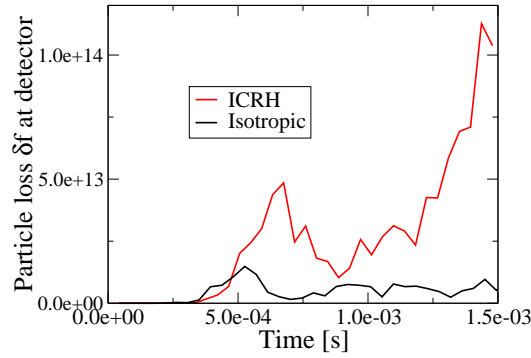


Figure 4.48.: Evolution of the fast particle losses at the detector for the ICRH-generated and the isotropic distribution.

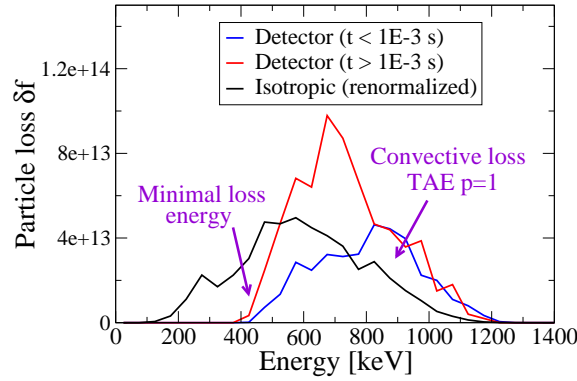


Figure 4.49.: Fast particle loss distribution in dependence on the energy caused by a BAE and a TAE, both $n = 4$. The results are compared to the isotropic case at the end of the nonlinear growth. For a better comparison, the amplitude of the isotropic case is renormalized.

before, the large mode amplitudes of $\delta B_\psi/B > 10^{-3}$ give rise to a stochastic loss behaviour. For this reason, the peak for $t > 10^{-3}$ s is mainly due to the $p = 1$ -BAE resonance (Fig. 4.43 right) and stochastic losses.

For a qualitative comparison of the fast particle losses with the isotropic case at the end of the nonlinear growth phase (Fig. 4.42), the amplitude of the isotropic case has been increased significantly and plotted in figure 4.49. The loss distributions deviate significantly from each other since the main fast ion losses are detected at an energy $E \approx 700$ keV for the anisotropic loading compared to $E \approx 500$ keV for the isotropic loading. Furthermore, the minimal energy of the ICRH-generated distribution, $E \approx 400$ keV, is larger than in the isotropic case, $E \approx 200$ keV. Remember that in the isotropic case these particles are ejected by the dominant poloidal harmonics in the outer TAE gaps (section 4.3.2) because they are located at the outer plasma edge on the LF side. Due to the different loading (Fig. 3.7), such particles do not exist. Thus, the peak at $E \approx 250$ keV due to resonant $p = 0$ -TAE losses in the isotropic case cannot appear but there is still a considerable amplitude at $E \approx 800$ keV due to the $p = 1$ -TAE resonance at all points in time.

A further difference to the isotropic initialization is shown in figure 4.50. The losses with respect to the pitch angle caused by the ICRH-generated fast particle distribution lie between $\alpha = 56^\circ - 66^\circ$ which deviates significantly from the isotropic distribution (Fig 4.41 right) at the end of the nonlinear growth phase. The particles tend to be ejected at smaller pitch angles in both cases for later points in time but this does not increase the range in case of the ICRH-generated distribution. The resonantly lost particles with an energy of $E = 800$ keV are ejected at a pitch angle of $\alpha \approx 60^\circ$ and superpose with the main losses at $t > 10^{-3}$ s.

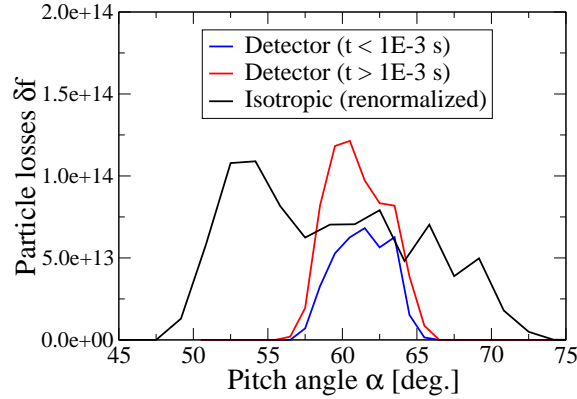


Figure 4.50.: Fast particle losses in dependence on the pitch angle caused by an ICRH-generated (blue and red) and an isotropic distribution (black). For a better comparison, the amplitude of the isotropic case is renormalized.

4.5. Comparison of Fast Ion Losses: Simulation vs Experiment

The fast ion losses caused by different mode activity and initial fast particle distributions were compared to each other in the previous sections. In this section, it is investigated which fast particle distribution agrees best with the experimental measurement. Since the experimental diagnostic FILD measures the pitch angle and the gyro radius of the ejected particles simultaneously on one loss pattern, the separate simulated loss distributions are combined. Afterwards, the simulated fast ion losses are compared to the experimental data.

For the following comparison, only these particle loss distributions of different configurations are investigated in which all loss processes due to resonant or stochastic behaviour are present. This means that each time interval after or at the end of the saturation phase is examined, i.e. for the single TAE with an isotropic distribution at $t = 1.3 - 2.0 \cdot 10^{-3}$ s, for the BAE and the TAE with an isotropic distribution at $t = 1.3 - 2.0 \cdot 10^{-3}$ s as well as for the BAE and the TAE with an ICRH-generated distribution at $t = 1.0 - 1.5 \cdot 10^{-3}$ s. Since the FILD measures the gyro radius of a lost particles, the energy distributions has to be expressed with respect to ρ_{\perp} ,

$$\rho_{\perp} = \sqrt{\frac{2mE[eV](1 - \lambda^2)}{q^2eB^2}}.$$

The corresponding distributions in gyro radius for the above specified time intervals are shown in figure 4.51 (left). For a better comparison, the fast ion losses for different initializations are renormalized. Therefore, the losses with respect to the pitch angle are plotted in figure 4.51 (right) again.

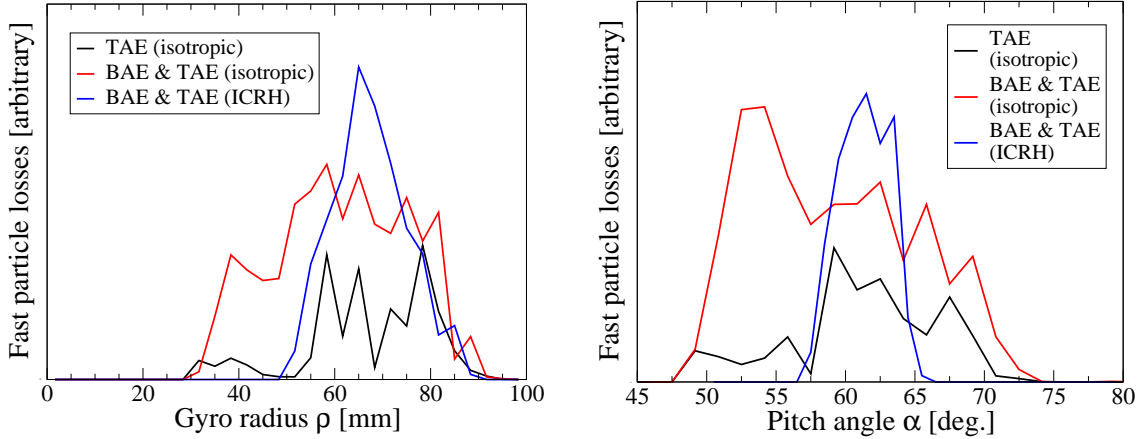


Figure 4.51.: Loss distributions in gyro radius (left) and pitch angle (right) for the single TAE with isotropic loading (black), the BAE and the TAE with isotropic loading (red) as well as the BAE and the TAE with an ICRH-generated distribution (blue). The distributions are renormalized.

The combination of both distributions in a contour plot gives more detailed information about the phase-space from which the fast particles are lost. In figure 4.52 (left), the combined distribution of the pitch angle and the gyro radius for a single TAE and an isotropic distribution is shown colour-coded and normalized to the maximal loss amplitude. Investigations on the pitch angles of the lost trapped particle orbits reveal that fast particles with a pitch angle of $\alpha \approx 63^\circ$ independent of their energy have their bounce points near the magnetic axis before they are lost. This means that fast particles with a higher pitch angle at the detector are completely located on the LF side, trapped ions with a lower pitch angle have their bounce points at the HF side.

Two separated spots are detected, a small spot for a gyro radius from $\rho_{\perp} = 30$ mm to 45 mm and pitch angles between $\alpha = 48^\circ - 52^\circ$ and a large spot for $\rho_{\perp} = 45 - 90$ mm and pitch angles between $\alpha = 52^\circ - 71^\circ$. The small spot consists of lost particles which are barely co-passing. These fast ions change their orbit topology due to the interaction with the mode (Fig. 4.54, red).

The large spot consists of trapped particles only. The black ellipse corresponds to resonant losses with energies between $E \approx 750 - 900$ keV due to the $p = 1$ -resonance and coincides very well with the resonance plot (Fig. 4.52 right) made for the radial position of the magnetic axis R_{mag} . The loss peak with an energy of $E = 500$ keV is due to lost particles whose

turning points are at the HF side, $R < R_{mag}$. For these particles, the bounce and the toroidal precession frequency are smaller than for trapped particles which have their bounce points at the magnetic axis. Therefore, the corresponding resonance lines (Eqn. 4.1) shift to the left side so that these particles are also ejected by the $p = 1$ -TAE resonance.

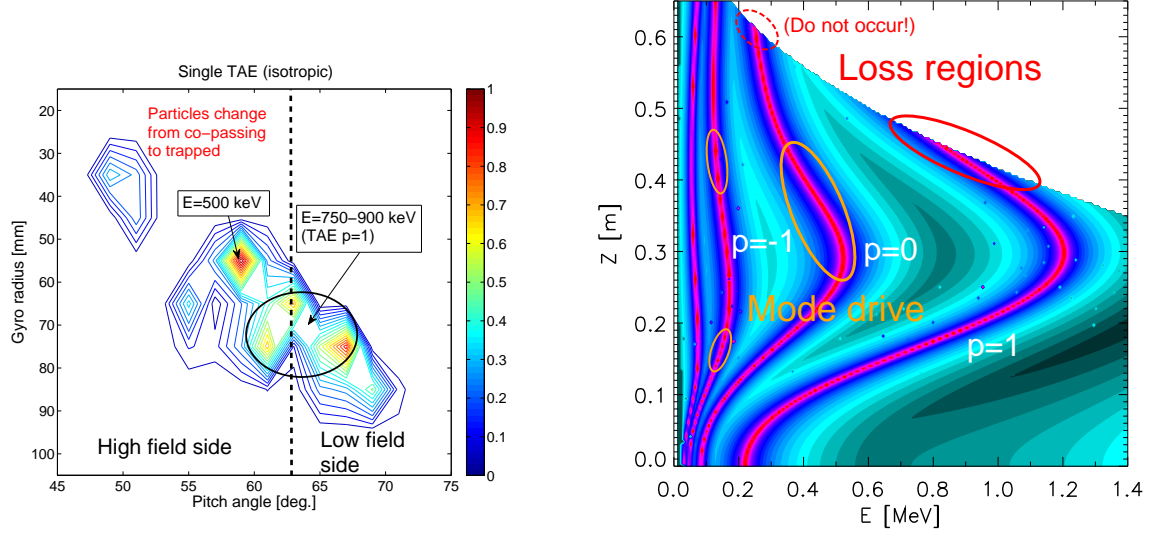


Figure 4.52.: Left: Fast particles losses due to a single TAE in the presence of an isotropic distribution. The main losses are detected due to the $p = 1$ -TAE resonance as well as for particles with $E = 500$ keV with their bounce points on the HF side. Right: The resonance region due to the $p = 1$ -resonance coincides very well with the main losses.

The simulated loss pattern changes significantly if additionally a BAE mode is present, again an isotropic distribution is considered here. One continuous loss region is observed in figure 4.53 which consists of different loss areas. The red ellipse denotes lost particles which change their orbit topology. This was detected for the single TAE (Fig. 4.52 left) before. Furthermore, two peaks are detected for a gyro radius from $\rho_{\perp} \approx 60 - 80$ mm with a pitch angle of $\alpha \approx 63^{\circ}$ (green ellipse) and at a gyro radius of $\rho_{\perp} \approx 45$ mm with a pitch angle of $\alpha \approx 67^{\circ}$ (magenta ellipse). These peaks correspond to the loss regions due to the $p = 0$ and $p = 1$ TAE-resonance shown in figure 4.43. The corresponding guiding centre trajectories for each ellipse are shown in figure 4.54.

Both modes eject particles at an $\rho_{\perp} \approx 52$ mm at a pitch angle of $\alpha \approx 54^{\circ}$ which correspond to a particle energy of $E \approx 600$ keV. The peak was also detected before due to the single TAE and is slightly shifted. The loss peak at a gyro radius $\rho_{\perp} \approx 85$ mm ($E \approx 1$ MeV) with a pitch angle of $\alpha \approx 68^{\circ}$ (cyan ellipse) is also caused by both modes. The highly energetic particles have large orbit widths which are completely on the LF side and traverse the BAE and the TAE amplitude with the inner leg (Fig. 4.54; cyan trajectory).

In total, the loss areas are not strictly separated. Due to stochastic losses, a broadening [69] in the loss pattern can be possible since no clear association of the losses between the resonant loss regions to any resonance can be made.

The behaviour of the fast ion losses (Fig. 4.51 blue) caused by both modes changes for an

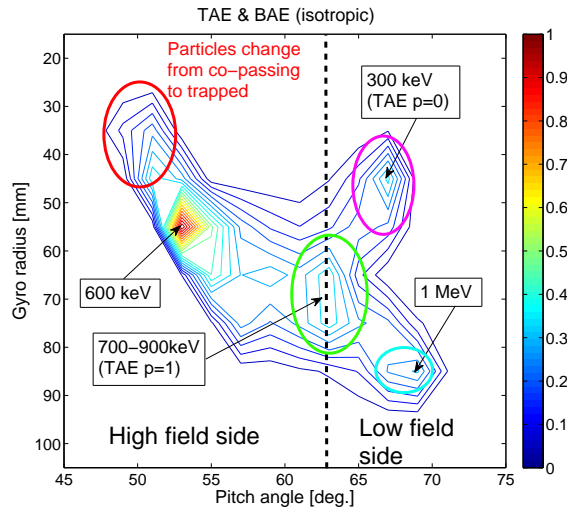


Figure 4.53.: Fast particles losses due to the BAE and the TAE in the presence of an isotropic distribution. The main losses are detected due to the $p = 0, 1$ -TAE resonances as well as for particles with $E = 600$ keV which are ejected by both modes.

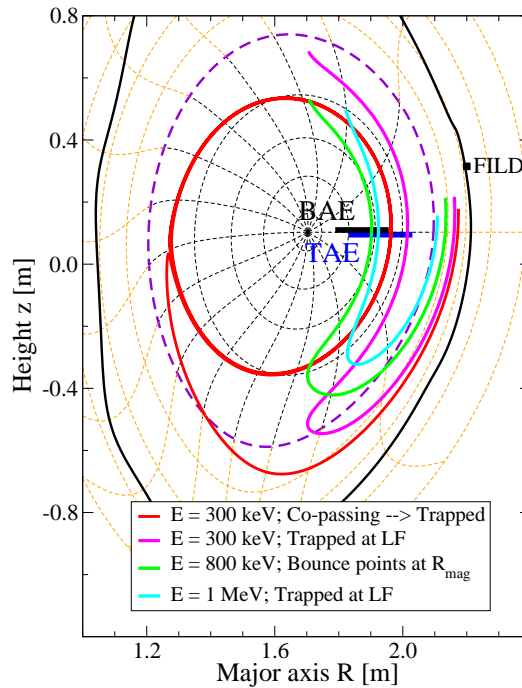


Figure 4.54.: Trajectories of typical fast ions with energies of $E = 300$ keV, $E = 800$ keV and $E = 1$ MeV which contribute to the loss distribution (Fig. 4.53). For $E = 300$ keV, the fast particle (red) which changes its orbit topology and the initial trapped one (magenta) on the LF side are lost with a pitch angle of $\alpha = 51^\circ$ and $\alpha = 67^\circ$. For $E = 800$ keV (green) and $E = 1$ MeV (cyan), the highly energetic ions are lost with $\alpha = 63^\circ$ and $\alpha = 68^\circ$, respectively.

ICRH-generated distribution as shown in figure 4.55. Only one large loss region is detected with gyro radii between $\rho_{\perp} \approx 50 - 90$ mm and pitch angles between $\alpha \approx 56^{\circ} - 66^{\circ}$ which correspond to energies between $E = 500$ keV (upper left corner) to $E = 1.1$ MeV (lower right corner). The main particles are lost at an energy of $E \approx 700$ keV whose bounce points are slightly beyond the magnetic axis on the HF side. In general, the particles are ejected from orbits whose bounce points are near the magnetic axis due to the initialization of the ICRH-generated distribution (Fig. 3.7). Therefore, particle losses which are related to bounce points far away from the magnetic axis as in the isotropic case (Fig. 4.53) are missing.

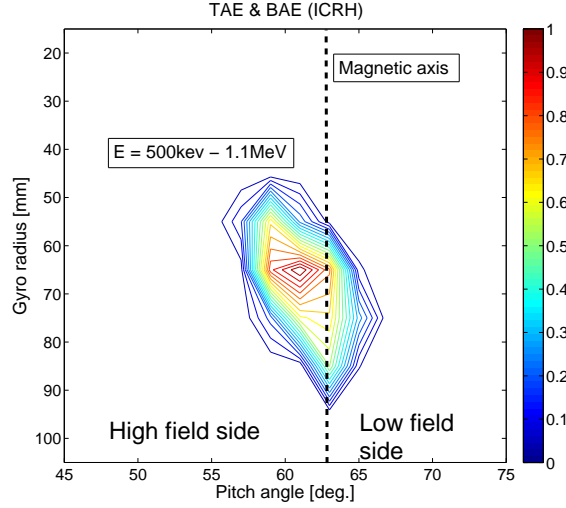


Figure 4.55.: Fast particles losses due to the BAE and the TAE in the presence of an ICRH-generated fast particle distribution. The main losses are detected due to the $p = 1$ -TAE resonance near the magnetic axis because of the chosen spatial loading (Fig. 3.7).

For the following comparison between the simulated and the experimental results, a peculiarity corresponding to the FIELD and the fast particle motion has to be taken into account. The ratio between the drifts and the parallel motion (Eqn. 3.74) is of order $\mathcal{O}(\epsilon)$ (Eqn. 3.72) so that

$$\frac{v_D}{v_{\parallel}} \sim \epsilon = \frac{\rho_{\perp}}{R} \approx 5\% .$$

Since the main losses are obtained for deeply trapped particles, the perpendicular velocity is larger than the parallel velocity, $v_{\perp} > v_{\parallel}$. Assuming that $v_{\perp} = 4v_{\parallel}$ yields for the angle β (Fig. 4.56) which determines the deviation of the guiding centre motion from the motion along the magnetic field line in $-z$ -direction

$$\frac{v_D}{v_{\parallel}} \lesssim \epsilon \frac{\sqrt{v_{\parallel}^2 + \frac{1}{2}v_{\perp}^2}}{v_{\parallel}} = 3\epsilon \quad \Rightarrow \quad \beta \approx 9^{\circ} ,$$

which is the maximum value of the deviation.

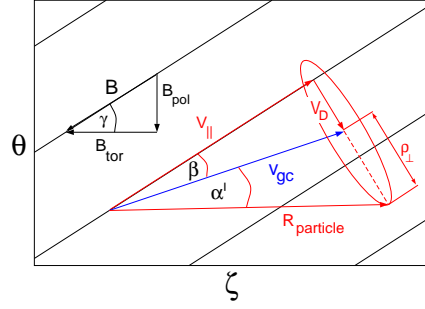


Figure 4.56.: View of a flux surface in the region of the outboard midplane: Motion \mathbf{v}_{gc} of the guiding centre across the magnetic field lines \mathbf{B} within the flux surface.

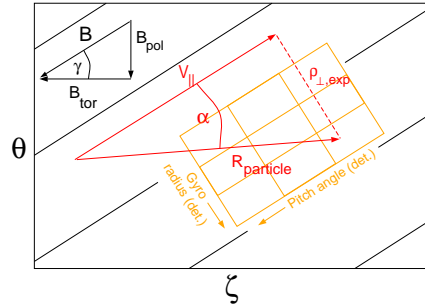


Figure 4.57.: Experimental set-up of the FILD loss pattern: Since the side of the pattern responsible for the pitch angle is assumed to be parallel to v_{\parallel} , the gyro radius $\rho_{\perp,exp}$ and the pitch angle α are determined as plotted in the figure.

As introduced in section 2.5.3, the detector is located at midplane and is tilted against the horizontal plane by $\gamma \approx 13^\circ$ (Fig. 4.56). So, the loss pattern is parallel to the magnetic surface at midplane and the side of the loss plate responsible for the pitch angle is parallel to the magnetic field line (Fig. 2.15). It is assumed in the experimental analysis that the particle is propagating along the magnetic field line with v_{\parallel} without a drift so that the gyro radius $\rho_{\perp,exp}$ and the pitch angle α are measured as shown in figure 4.57. Including the drift motion for deeply trapped particles is however very important and leads to a deviation from the measurement. Since the diagnostic is located at midplane, the drift motion ($-z$ -direction) is in poloidal direction, i.e. a drift within the flux surface. This indicates that the guiding centre motion v_{gc} does not coincide with the parallel motion any longer which results in a smaller pitch angle and a smaller gyro radius as shown in figure 4.58.

Comparing the angle between the magnetic field line and the vector of the fast particle shown in 4.58 reveals that the experimentally detected angle α is

$$\alpha = \alpha' + \beta .$$

This means that each simulated pitch angle α' has to be increased by β for comparison. Since β depends on the fast particle's energy and pitch angle, a numerical simulation has

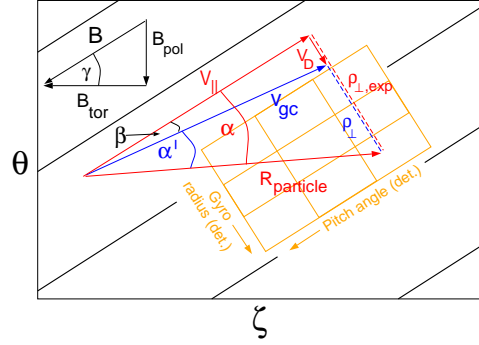


Figure 4.58.: Including drift motion shows that the real gyro radius ρ_{\perp} and the real pitch angle α' are smaller than the measured quantities α and $\rho_{\perp,exp}$.

to be carried out to determine its value. Therefore, trapped particles with energies up to 1.5 MeV have been started over the complete upper half of the plasma with $\lambda = 0$ (Fig. 4.59) but only the lost particles which are detected by the virtual fast ion loss detector are important for the comparison. For better visualization, only 3 energies (300 keV, 700 keV, 1 MeV) are plotted. For the ions which are lost due to interaction with the waves the last position of the bounce point is shown.

In figure 4.59 (a) the shaded areas within the plasma show the initial positions of trapped particles for various energies. The corresponding colour at the (R, z) -position denotes the actual pitch angle α' determined at the detector area. Including the drift motion, the pitch angle α which is measured by the FILD is shown in figure 4.59 (b). The drift correction increases for higher pitch angles α' due to the rising relevance of the drift terms in equation (3.74) and affects fast particles at the low field side up to a correction of $\beta \approx 8^\circ$ in particular. The corresponding change in the gyro radius is within the same percentage range. So, the particle energies which are calculated from the measurements are overestimated up to $\Delta E = 140$ keV.

As shown in section 4.1 (Fig. 4.4), the experimental fast ion losses are separated in two spots ('large' spot: $\rho_{\perp} \approx 60 - 100$ mm, $\alpha \approx 62^\circ - 68^\circ$; 'small' spot: $\rho_{\perp} \approx 40 - 50$ mm, $\alpha \approx 69^\circ - 70^\circ$). In figure 4.60, these original experimentally observed spots (red) are plotted into the simulated fast ion losses due to a TAE (left) and both modes (right) for an isotropic fast ion distribution. With inclusion of the drift effect, the spots shift to smaller pitch angles and gyro radii (blue ellipses). For a single TAE, the corrected 'large' spot coincides very well with the fast ion losses due to the $p = 1$ -resonance. However, the small spot is missing. In the presence of both modes (Fig. 4.60 right), losses with $E \approx 300$ keV due to the $p = 0$ -TAE resonance appear and agree with the corrected 'small' spot. It was found in section 4.3.2 that the $p = 1$ -BAE resonance does not eject fast ions of the same energy due to the core-localization of the mode, although the resonance line intersects the loss boundary at the same position in phase-space as the TAE resonance (Fig. 4.43). This is in good agreement with the FILD spectrogram for low energetic losses (Fig. 4.5) where BAE-induced losses are only detected for high energies. Nevertheless, beside the spots further loss regions are present which are not detected in the experiment.

4. Simulation Results

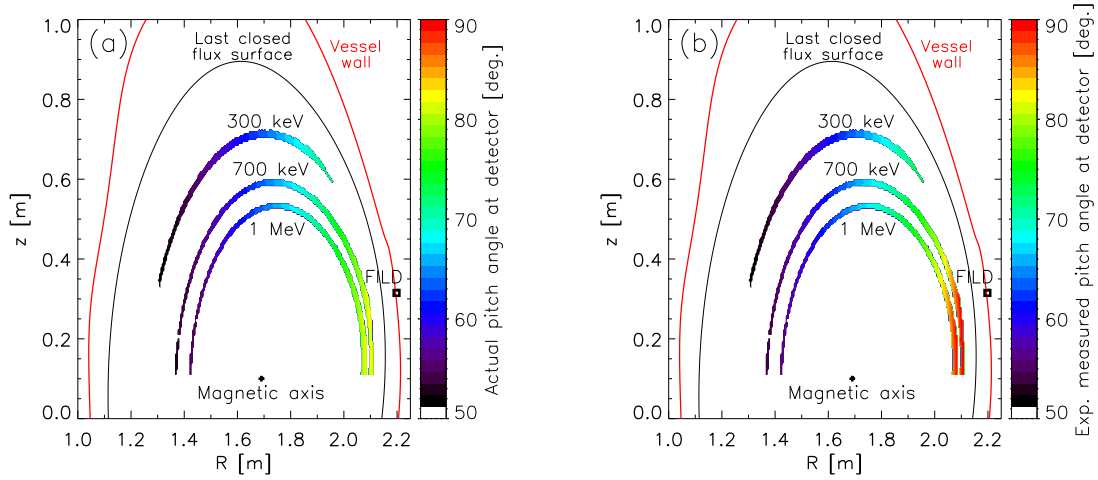


Figure 4.59.: The colour-shaded area denotes the initial positions of the trapped particles with $\lambda = 0$ and energies of $E = 300$ keV, $E = 700$ keV and $E = 1$ MeV which reach the FILD position. The actual pitch angle at the detector to the corresponding starting position is colour-coded and shown on the left side (a), the expected pitch angle measured experimentally and including drifts on the right side (b).

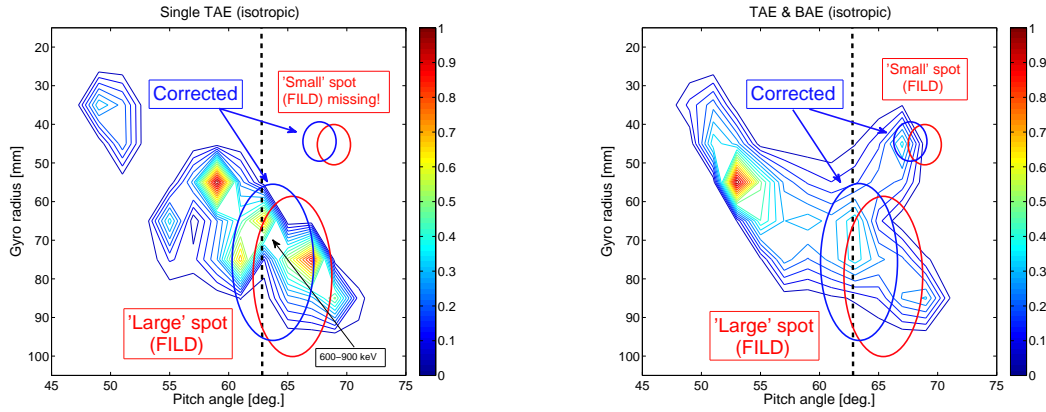


Figure 4.60.: The loss patterns of a single TAE (left) and of both modes (right) are compared to the experimental data (red ellipses) as shown in figure 4.4. With inclusion of the drift effect, the measurements are shifted to smaller gyro radii and pitch angles (blue ellipses). The simulated fast ion losses are normalized to unity.

The reason for this deviation is the use of ICRF heating in the experiment. This generates a highly anisotropic distribution located on-axis which is in contrast to the isotropic fast particle distribution used in the simulation. Due to the increase of perpendicular energy and the corresponding shift of the bounce points to the resonant layer as explained in section 2.5.1, only lost fast particles that have their bounce points near the magnetic axis are relevant for a comparison with the experiment. Assuming that only ions with bounce points between $R = 1.60 - 1.80$ m cause all losses, pitch angles of $\alpha \leq 57^\circ$ and $\alpha \geq 70^\circ$ vanish, as shown in figure 4.61. Under this assumption, the two simulated loss regions due

to resonant TAE losses coincide very well with the experimental measurements. The lost ions with $E \approx 300$ keV are still included as shown in figure 4.54 (blue trajectory). The small deviation in pitch angle and the absence of even higher energetic losses of the 'large' spot can be explained by two reasons: On the one hand, the assumption that the FILD detector is parallel to the magnetic field lines might not be exactly correct. Increasing γ by only 1° (Fig. 4.56) would result in a perfect line up and is within the error bar for a deviation of $\pm 2^\circ$. On the other hand, the distribution function in energy (Eqn. 4.3) underestimates high energies since it is assumed that a maximum energy of $E_0 = 1$ MeV is created by the ICRF heating. An increase of E_0 to larger values could bring the desirable effect.

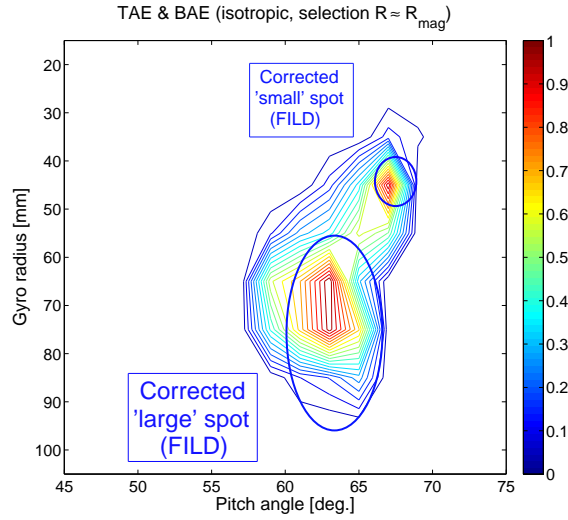


Figure 4.61.: Loss pattern of selected fast ion losses caused by both modes in the presence of an isotropic fast particle distribution. Only trapped particles which have their bounce points between $R = 1.6$ m – 1.8 m are plotted in contrast to the total losses shown in figure 4.60 (right).

The initialization of the ICRH-generated distribution should avoid the need for a loss selection. In figure 4.62, the losses for the two mode case are shown. The loss region coincides partly with the experiment (blue ellipses). The 'small' spot is however missing as for the single TAE with an isotropic loading. The simulated loss region partly agrees with the 'large' spot but has a wrong distribution in pitch angle. The lost particles with smaller pitch angles and the absence of low energetic particles are due to the chosen loading of the fast ions (Fig. 3.7). If trapped particles are initialized near to the plasma edge, they have their turning points at the HF side. This results in smaller pitch angles when the particles are lost (Fig. 4.59). Furthermore, the fast particle initialization near R_{mag} excludes trapped ions with low energies located on the LF side.

Although the 'ICRH-generated' distribution is more realistic, the fast ion losses caused by both modes in the presence of an isotropic distribution coincide much better after the particle selection. This is due to the inclusion of all possible trapped particle orbits but

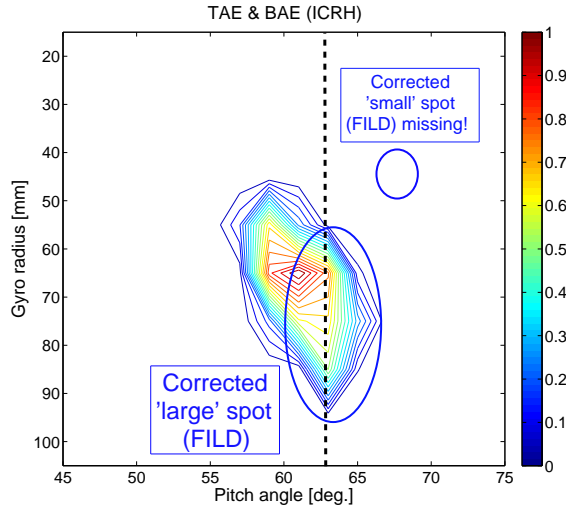


Figure 4.62.: Loss pattern due to both modes in the presence of an ICRH-generated distribution. The corrected, experimental losses are plotted into the figure (blue ellipses) for direct comparison. The 'small' spot from the experiment is missing, the simulated fast ion losses coincide partly with the 'large' spot.

it also generates fast particle losses which are not present in the experiment. It indicates that a connection between the radial and the poloidal coordinate is mandatory to represent on-axis heating. Only in this case and with the inclusion of the drift motion, the simulated fast ion losses can be expected to be equal to the experimental measurements.

4.6. Particle Redistribution due to NTMs

In present-day tokamaks, a fast particle population is often generated by Neutral Beam Injection (NBI) which interacts with a variety of MHD modes. It has been observed that changes in the distribution are caused by Alfvén waves [65] but also by tearing modes [38, 39]. In the context of a NTM, the perturbation generates a beam ion depletion [72] over its radial extension which leads to a significant decrease in the plasma heating. Beside the calculation of the fast particles with shear Alfvén eigenmodes, the HAGIS code can also be applied to simulate an NBI-generated fast particle distribution in the presence of a static tearing mode. Here, particular emphasis is given to the island structure and its displacement mechanism.

For the simulation of a particle distribution in the presence of a single NTM, a reconstructed equilibrium with a slowly increasing safety factor has to be chosen. Otherwise, multiple islands can be excited due to close rational surfaces. Therefore, the ASDEX Upgrade discharge #21083 has been modified so that the monotonic safety factor profile passes through $q(\psi_s = 0.35) = 1.5$ (Fig. 4.63, left). This indicates that a NTM with a poloidal and toroidal mode number of $(m, n) = (3, 2)$ can be present at the resonant surface ψ_s . In section 2.3.5, the structure of the magnetic island was introduced (Fig. 2.8). The island is symmetric under the assumption that the growth of the safety factor q is linear and the radial perturbation B_ψ is constant. However, it has been found in the experiment [41] that

the island structure is asymmetric in the radial coordinate, i.e. the island half width w (Eqn. 2.35) on the inside (towards the centre) is larger than on the outside (towards the plasma edge). Therefore, an asymmetric Gaussian profile for the vector potential \tilde{A} has been implemented in the HAGIS code which is determined by the left and right radial width, Δ_L and Δ_R and its amplitude, \tilde{A}_0 ,

$$\tilde{A}(\psi_p) = \begin{cases} \tilde{A}_0 \cdot \exp\left[-\frac{(\psi_p - \psi_s)^2}{\Delta_L}\right] & \psi_p \leq \psi_s, \\ \tilde{A}_0 \cdot \exp\left[-\frac{(\psi_p - \psi_s)^2}{\Delta_R}\right] & \psi_p > \psi_s. \end{cases}$$

In figure 4.63 (right), both a symmetric profile (blue) with $\Delta_L = \Delta_R = 2.0 \cdot 10^{-2}$ and an asymmetric profile (red) with $\Delta_L = 5.0 \cdot 10^{-2}$ and $\Delta_R = 3.0 \cdot 10^{-3}$ are shown. These vector potentials cause a maximal radial perturbation of $B_\psi/B_0 \approx 2.0 \cdot 10^{-3}$.

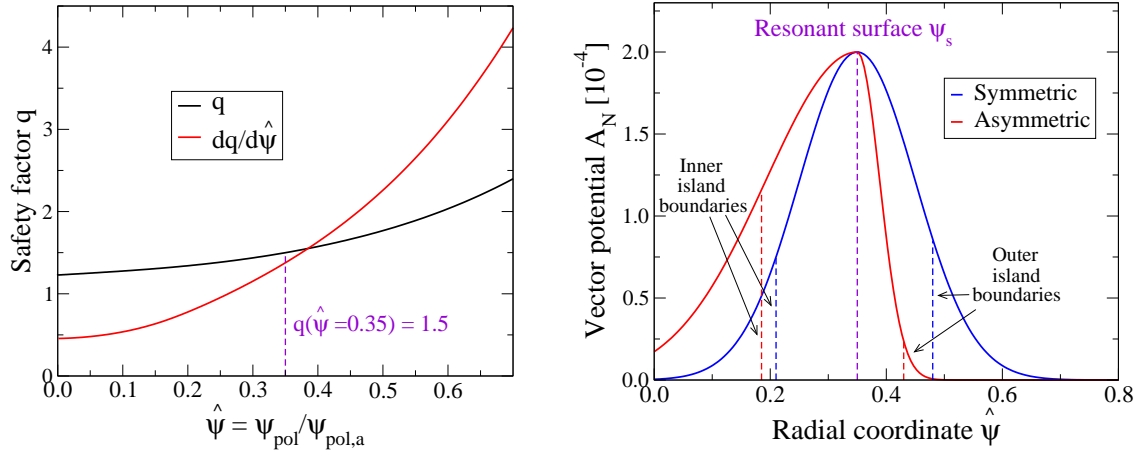


Figure 4.63.: Left: Radial profile of the safety factor q and its derivative q' . Right: Radial profile of the normalized vector potential \tilde{A}_N for a symmetric (blue) and an asymmetric (red) NTM. The dashed, violet line denotes the resonant surface. The other dashed lines represent the minimal and maximal radial surfaces of the corresponding tearing modes.

The corresponding magnetic islands within the magnetic equilibrium field are displayed in figure 4.64 by a Poincaré plot. The island width is $\Delta R_{sym} = 10.1$ cm in the symmetric case and $\Delta R_{asym} = 9.5$ cm in the asymmetric case at the outboard miplane. Since the resonant surface is fixed (violet) at $\psi_s = 0.35$, the radial limits of both islands do not coincide. The asymmetric perturbation profile is much larger towards the plasma centre so that the asymmetric island extends more to the centre. In figure 4.63 (right), the radial extents of the islands are plotted into the vector potential to show how large the amplitude \tilde{A} for such a generation has to be. The vector potential at the symmetric island separatrix is nearly equal since the boundaries are nearly equidistantly away from the resonant surface. This indicates that the smaller the island separatrix is away from the resonant surface, the smaller is the required vector potential.

However, the field lines are also perturbed outside but close to the island. The excursion is

largest for the asymmetric case due to the large remaining vector potential and remains up to the centre (Fig. 4.64 (right), black dots). Reversely, the Poincaré plot of the magnetic field line between the island separatrix and the plasma edge matches perfectly with the flux surfaces in a small radial distance again in the asymmetric case.

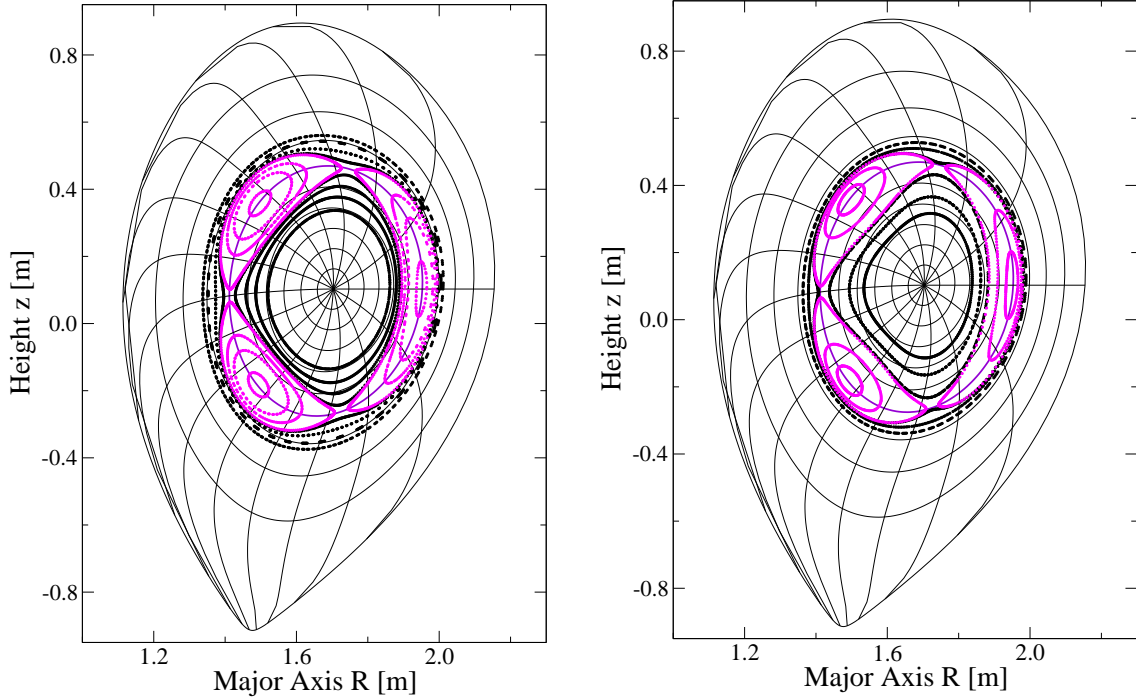


Figure 4.64.: Poincaré plot of a symmetric (left) and an asymmetric (right) island chain due to the corresponding radial perturbation profile shown in figure 4.63 (right). The black dots denote perturbed but not reconnected magnetic field lines in the vicinity of the island chain (magenta).

A tearing perturbation with a nearly constant potential was implemented in the HAGIS code before. However, the introduced radial perturbation profile is an enhancement since the experimental measurements of the perturbed field lines excursions [41] decreases more quickly with increasing distance from the NTM than in the original implementation of the code. Furthermore, the magnetic field strength and the island structure can be treated separately now.

For the simulation, the deuterium NBI distribution which is represented by approximately 19000 markers shown in figure 2.13 is used. The simulation time is $\Delta t = 3.0 \cdot 10^{-4}$ s. Without a NTM present, the radial distribution averaged over $t = 2.8 - 3.0 \cdot 10^{-4}$ s is shown in figure 4.65 (black). In the presence of the NTM, a change in the radial distribution is detected for the symmetric (Fig. 4.65, left) and the asymmetric case (Fig. 4.65, right). Beam particles are redistributed from the inner of the island in both directions, inwards and outwards. This agrees with experimental observations [72] where an increase of the beam ions at the island separatrix has been detected. The increase in the distribution near $\psi = 1.0$ is due to losses caused by unconfined orbits or wave-particle interactions.

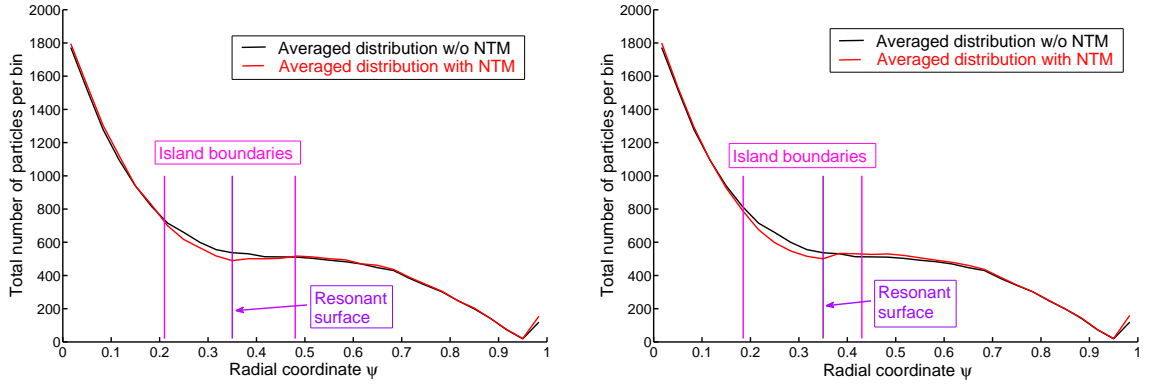


Figure 4.65.: Averaged radial distribution of the beam ions without a NTM (black) and with a NTM (red) at the end of the simulation time for a symmetric (left) and an asymmetric island (right).

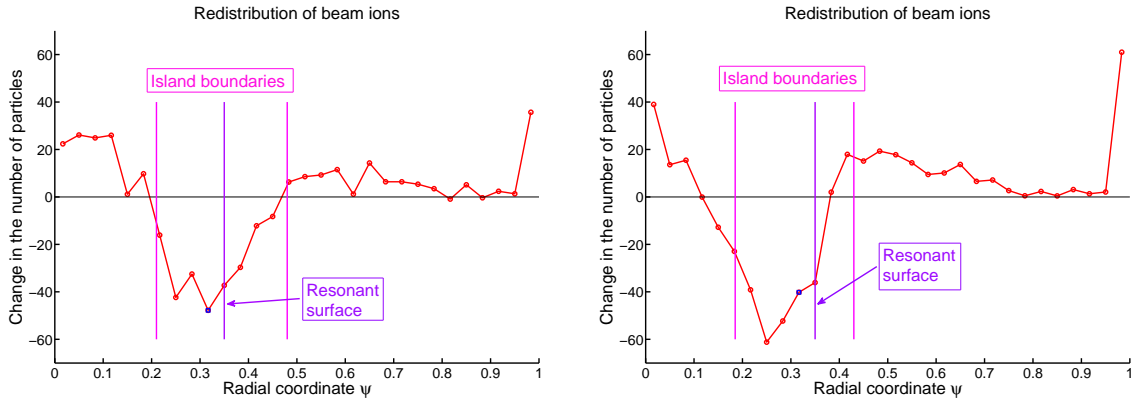


Figure 4.66.: Redistribution of the beam ions in the presence of a symmetric NTM (left) and an asymmetric NTM (right).

Subtracting the perturbed from the unperturbed NBI distribution reveals a better insight of the particle redistribution (Fig. 4.66). Surprisingly, the maximal depletion of the beam ions is not located at the resonant surface for both cases but on the inside of the magnetic island. The particle accumulation points are for the symmetric island (Fig. 4.66 left) outside the island separatrix but for the other case the outward peak is partly within the island boundary (Fig. 4.66 right). The total redistribution and the particle losses are larger for the asymmetric case compared to the symmetric case although the total radial island width ΔR is smaller.

For a better understanding of the redistribution mechanism, the particle orbits of the single deuterium ions in the presence of a symmetric island are investigated. Without island, it is well-known (section 2.4) that drift orbits can be separated into a parallel motion along the magnetic field line and a slow drift motion perpendicular to it. Since the magnetic field perturbation of the island is large, the parallel guiding centre motion is along the perturbed

field line. This indicates that a Poincaré plot of the particle at a poloidal cross section represents approximately the island structure which is superposed by the radial drift as shown in figure 4.67. The whole formation of the perturbed particle trajectory is shifted towards the LF side. The particle is phase-locked to the island structure.

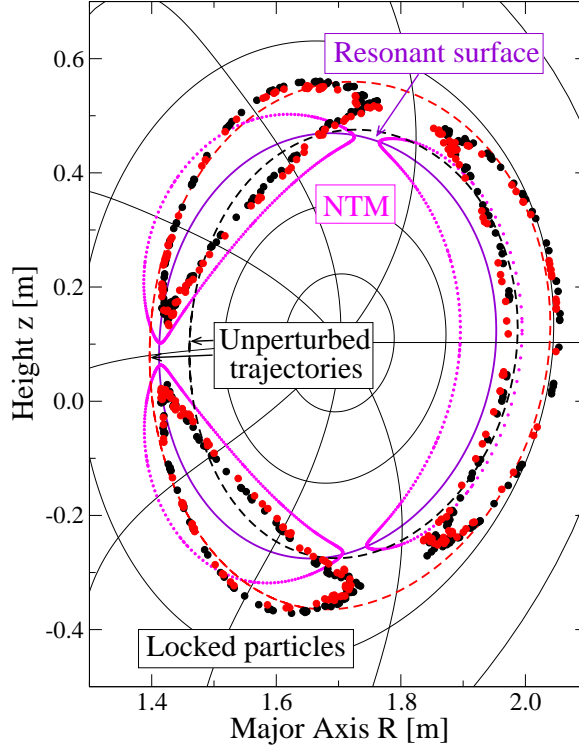


Figure 4.67.: Poincaré plot of the island (magenta) and the perturbed particle trajectories ($E = 93$ keV, black and red dots) which is phase-locked to the mode structure particle. The violet line denotes the resonant surface whereas the dashed lines are the unperturbed trajectories of each particle.

During the investigation of the particle trajectories, it turns out that a part of the passing particles whose mean radial position of the unperturbed trajectory is located within the inner half of the island is redistributed to a larger mean radial position (Fig. 4.67, black). This is clearly seen by plotting the radial position of the perturbed trajectory with respect to the helical angle, as shown in figure 4.68. It has been detected by means of numerical simulations [73] that the closer the ratio v_{\parallel}/v is to the trapped-passing boundary, the larger is the radial shift between the resonant island surface and the perturbed mean radial position (Fig. 4.68).

A particle whose mean radial position of the unperturbed trajectory is localized within the outer half of the island can also be phase-locked to the island (Fig. 4.68, red) as the particle discussed before. In this case, the mean radial position of perturbed trajectory can be even slightly smaller than that of the unperturbed trajectory. The particle trajectory is similar to the particle trace initialized on the island inside. Therefore, the particle exhibits a similar formation for a poloidal cross section, as shown in figure 4.67 (red). Both particles

are located at the outboard side of the island separatrix forming the outer peak in figure 4.66.

Furthermore, it can be shown by numerical simulations that due to the sign of the parallel velocity more counter-passing particles which are located at the island inside are phase-locked with respect to the NTM compared to those which are located at the island outside. Only due to the sign of the parallel velocity, the radial shift of the passing particles is outwards on average whereas the opposite sign would cause an inward radial shift with a particle depletion on the island outside.

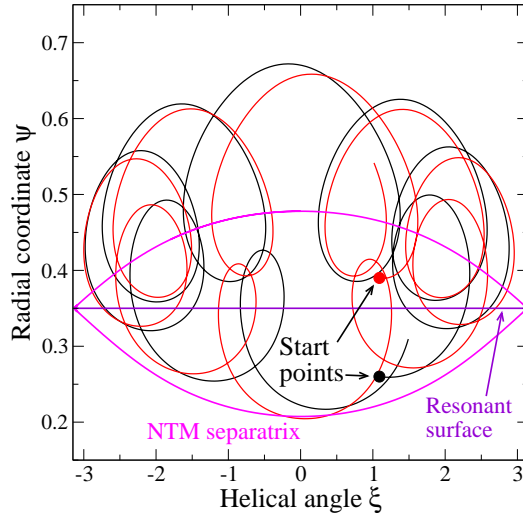


Figure 4.68.: Perturbed particle trajectories (black and red) in the presence of a NTM (magenta) whose mean radial positions do not coincide with the resonant island surface. The particles ($E = 93 \text{ keV}$) are phase-locked with respect to the mode.

The comparison of the particle redistribution to the experimental measurements of a similar ASDEX Upgrade discharge [72] where a beam ion depletion from the island centre of about 40 – 50% was observed reveals a significant deviation. The simulated depletion near the resonant surface is around 10% only. The depletion can be increased by a stronger vector potential \tilde{A} . However, the resulting magnetic field would be of the order $\mathcal{O}(10^{-2} \cdot B_0)$ which is not realistic. This indicates that the particle redistribution in the experiment cannot be explained by phase-locking with respect to a single NTM only. Further effects, e.g. the influence of multiple NTMs which are present in the experiment and the shape of the safety factor, have to be examined. In addition, the consideration of island rotation would include the resonance condition, $\omega - k_{\parallel} v_{\parallel} = 0$, which can give rise to a larger redistribution. Since these results were obtained recently, ongoing investigations are already in progress.

5. Summary and Outlook

5.1. Summary

In this thesis, nonlinear effects due to energetic particle driven Alfvén eigenmodes have been investigated. The consequential fast particle redistribution has been calculated by the drift-kinetic perturbative HAGIS code. The original HAGIS code has been extended to follow fast particles beyond the separatrix up to the vessel wall. This improvement provides a powerful tool for the comparison between numerical simulations and experimental measurements concerning fast ion losses.

A main aspect has been the gradient-driven mode growth and the collective fast particle transport [15, 16] for multiple shear Alfvén eigenmodes. The assumption that the same transport mechanism and flattening in the fast particle distribution for significantly different eigenfrequencies is present has been validated for the interplay of a BAE and a TAE. The investigation revealed an enormous influence of the core-localized BAE on the TAE leading to enhanced fast particle losses caused by the TAE.

Furthermore, a new nonlinear coupling effect has been identified. This mechanism transfers energy and toroidal momentum between two eigenmodes due to double-resonant particles. Only if eigenmodes with the same toroidal mode number are present, both mode amplitudes couple. In contrast to the gradient-driven mode growth, the orbit size of the double-resonant particles determines the radial coupling width, not the radial overlap of the modes. Moreover, the double-resonant particles are not redistributed by this mechanism. The balancing effect of the coupling mechanism is independent on the radial directions and thus can cause a significant increase of the amplitude for core-localized Alfvén eigenmodes. Both the coupling mechanism and the conventional gradient-driven mode growth are superposed and of the same order of magnitude.

During the code extension, a non-flux coordinate system has been developed which enables a contiguous connection to the Boozer coordinate system. Such an implementation allows the possibility for a single grid in the vacuum region on which fast particles are followed beyond the separatrix with a defined control of numerical errors. The coordinate system has been validated by the comparison of guiding centre trajectories against the Boozer coordinate system for different ASDEX Upgrade divertor discharges. It can easily be extended to arbitrary toroidally symmetric geometries.

Both nonlinear wave-particle mechanisms cause a significant fast particle loss at the vessel wall which were compared to recent experimental results [17]. The implementation of a virtual fast ion loss diagnostic allows for direct comparison in pitch angle and gyro radius. In this context, it has been shown that the recent loss results can be explained and that the experimental diagnostic overestimates slightly both pitch angle and gyro radius due to the

neglect of the fast particle drift motion.

Further development of the HAGIS code towards a more realistic fast particle initialization has been made by the implementation of an ICRH-generated distribution. The comparison to an isotropic distribution showed the limitations of both approaches but a spatial restriction within the isotropic loading due to the ICRH resonance region revealed a nearly perfect match to the experimental measurements of the FILD.

The onset of stochasticity in the presence of multiple evolving Alfvén eigenmodes has been studied numerically. It has been shown [69] that the threshold for diffusive fast particle losses decreases when multiple extended modes with similar eigenfrequencies, amplitudes and a large radial overlap are present. Since the BAE however is core-localized and both mode amplitudes are different by at least one order of magnitude during the mode evolution, the threshold for multiple modes is not applicable in this case. The onset is larger than that for the multiple mode case.

Furthermore, neoclassical tearing modes in the presence of a beam ion distribution have been investigated. A radial profile of the vector potential has been implemented to investigate the particle depletion over the radial mode width. It has been shown that an asymmetric magnetic island which is present in the experiment causes larger particle redistribution than a symmetric NTM. A new mechanism for the fast particle redistribution has been identified. The energetic ions are shifted to the island separatrix but are phase-locked onto the island structure.

5.2. Conclusions and Further Work

The main conclusion of this thesis is the demonstration of a fast ion loss comparison between the simulation and the experiment. This introduces the extended HAGIS code as a powerful interface tool. It had been applied to understand both theory and experiment in more detail. On the one hand, it has been shown that the interpretation of the experimental fast ion loss results have to be slightly corrected. On the other hand, the nonlinear wave-particle interaction have been investigated with a deeper insight revealing new coupling mechanisms between multiple waves and fast particle.

Concerning the double-resonant mode coupling, the influence of the radial overlap has to be investigated. Although the mechanism is expected to be independent of the radial mode positions, it has to be proven that only finite orbit width effects are responsible. Especially, the fast particle redistribution caused by each mode and the assumed vanishing collective transport effect due to less radial mode overlap is a subject for future investigations.

The first approach of a ICRH-generated distribution has shown from where fast particles are mainly lost due to the heating method. However, the assumed static distribution function in this thesis is not able to predict exactly the loss pattern observed in the experiment. In order to compare the fast particle losses quantitatively fully accurate, both a self-consistent background damping and a particle source have to be included.

Since the eigenfunction is assumed to be invariant, the combination of the linear gyrokinetic code LIGKA [68] with the HAGIS code is a promising approach to represent a self-consistent wave-particle interaction since it is expected that the structure of the eigenmode evolves in the presence of the fast particle population. By doing so, a further step should be undertaken for a simulation of a fully self-consistent system including sources, sinks and the evolution of the fast particle distribution function as well as the mode structure.

With respect to the neoclassical tearing modes, a detailed comparison of the fast particle redistributions between the experiment and the simulations has to be carried out. Since the energetic ion depletion caused by a single NTM is smaller by a factor of at least 3 compared to similar experimental results, further effects have to be examined. Simulations are planned investigating the influence of multiple islands, radial profile shaping and island rotation.

A. Appendix

A.1. Useful Vector- and Tensor Transformation

From the book of D'haeseleer [20]:

$$\begin{aligned}
 (\hat{b} \cdot \nabla) \hat{b} &= -\hat{b} \times (\nabla \times \hat{b}) \\
 \hat{b} \times (\hat{b} \cdot \nabla) \hat{b} &= -\hat{b} \times (\hat{b} \times (\nabla \times \hat{b})) \\
 &= -\left[\hat{b} (\hat{b} \cdot \nabla \times \hat{b}) - \nabla \times \hat{b} (\hat{b} \cdot \hat{b}) \right] \\
 &= -\hat{b} (\hat{b} \cdot \nabla \times \hat{b}) + \nabla \times \hat{b} \\
 \Rightarrow \nabla \times \hat{b} &= \hat{b} \times (\hat{b} \cdot \nabla) \hat{b} + \hat{b} (\hat{b} \cdot \nabla \times \hat{b})
 \end{aligned} \tag{A.1}$$

A.2. Guiding Centre Lagrangian and Equations of Motion

Gyro averaging procedure of the single particle Lagrangian

In a magnetic field, the motion of a charged particle is strongly anisotropic: it gyrates around the field lines whereas it is free to propagate along the field line. Since the gyromotion is much faster than the parallel motion along the field lines and the drifts caused by the magnetic field, a separation between the gyro motion and the rest is plausible.

The most formal technique to carry out the transformation from single particle to guiding centre coordinates is the Lie-transform [60, 44] which allows a rigorous proceeding. Since for a guiding centre transformation the Lie-transform is too laborious, the same result can be achieved by a more physical approach. The procedure was introduced by Littlejohn [53] and bases upon Hamilton's variational principle,

$$\delta \int \mathcal{L} dt = 0 .$$

As the Lie-transform method, the transformation is completely rigorous up to any order and the averaging procedure is systematic. In general, the **Lagrangian \mathcal{L} for a single particle** in canonical coordinates can be specified as

$$\mathcal{L}(\mathbf{q}, \mathbf{p}, \dot{\mathbf{q}}, t) = \mathbf{p} \dot{\mathbf{q}} - \mathcal{H}_{can}(\mathbf{q}, \mathbf{p}, t) , \tag{A.2}$$

where q , p and t denote the spatial coordinates, the coordinate-conjugate momenta and

the time, respectively. The dot represents the derivation with respect to the time. In the case of a particle in an electromagnetic field, the canonical Hamiltonian \mathcal{H}_{can} is

$$\mathcal{H}_{can}(\mathbf{q}, \mathbf{p}, t) = \frac{1}{2} \left(\mathbf{p} - \frac{1}{\epsilon} \mathbf{A}(\mathbf{q}, \epsilon t) \right)^2 + \Phi_e(\mathbf{q}, \epsilon t), \quad (\text{A.3})$$

where Φ_e is the electromagnetic potential and \mathbf{A} the vector potential. The variable ϵ is the adiabatic ordering parameter,

$$\epsilon = \frac{\rho_{\perp}}{L} \quad \text{with} \quad L = \frac{|\nabla B|}{B}. \quad (\text{A.4})$$

Physically, it is the ratio of the particle's gyro radius to scale length L over which the magnetic field differs. Mathematically, it is a reminder of the order of various terms. (Do not confound the parameter with the aspect ratio!)

The radial position and velocity of the particle are related to the canonical variables by $\mathbf{x} = \mathbf{q}$ and $\mathbf{v} = \mathbf{p} - \mathbf{A}/\epsilon$. So, the particle Lagrangian (A.2) becomes

$$\mathcal{L}(\mathbf{x}, \mathbf{v}, \dot{\mathbf{x}}, t) = \left[\frac{1}{\epsilon} \mathbf{A}(\mathbf{x}, \epsilon t) + \mathbf{v} \right] \cdot \dot{\mathbf{x}} - \left[\Phi_e(\mathbf{x}, \epsilon t) + \frac{1}{2} v^2 \right]. \quad (\text{A.5})$$

Deriving the guiding centre Lagrangian from (A.5) you have to decompose the position vector of the particle and the velocity vector,

$$\mathbf{x} = \mathbf{X} + \epsilon \frac{w \hat{a}}{B} - \mathcal{O}(\epsilon^2) \quad \text{and} \quad \mathbf{v}(\mathbf{x}, t) = u \hat{b} + w \hat{c}, \quad (\text{A.6})$$

where \mathbf{X} is the guiding centre position. In the second term, the position vector \hat{a} describes the gyromotion (oscillatory behaviour) of the particle with its perpendicular velocity w . The velocity is split into the parallel velocity u along the unit vector \hat{b} of the magnetic field and w is the perpendicular velocity along unit vector \hat{c} . Both unit vectors, \hat{a} and \hat{c} are perpendicular to the magnetic field and defined by

$$\hat{a} = \cos \theta \hat{e}_1 - \sin \theta \hat{e}_2 \quad (\text{A.7})$$

$$\hat{c} = -\sin \theta \hat{e}_1 - \cos \theta \hat{e}_2 \quad (\text{A.8})$$

where \hat{e}_1 and \hat{e}_2 are two arbitrary unit vectors perpendicular to the magnetic field line. The angle θ is the gyro phase around the guiding centre. Inserting these assumptions into the Lagrangian yields

$$\begin{aligned} \mathcal{L} = & \left[\frac{1}{\epsilon} \mathbf{A} \left(\mathbf{X} + \epsilon \frac{w \hat{a}}{B} - \mathcal{O}(\epsilon^2) \right) + u \hat{b} + w \hat{c} \right] \cdot \left[\dot{\mathbf{X}} + \frac{d}{dt} \left(\epsilon \frac{w \hat{a}}{B} - \mathcal{O}(\epsilon^2) \right) \right] \\ & - \left[\Phi_e \left(\mathbf{X} + \epsilon \frac{w \hat{a}}{B} - \mathcal{O}(\epsilon^2) \right) + \frac{1}{2} u^2 + \frac{1}{2} w^2 \right]. \end{aligned} \quad (\text{A.9})$$

Now, the result is sorted order by order. The Lagrangian up to order $\mathcal{O}(\epsilon^0)$ is

$$\begin{aligned} \mathcal{L}_0 = & \frac{1}{\epsilon} \mathbf{A}(\mathbf{X}) \cdot \dot{\mathbf{X}} + \frac{w\hat{a}}{B} \cdot \nabla \mathbf{A}(\mathbf{X}) \cdot \dot{\mathbf{X}} + \mathbf{A}(\mathbf{X}) \cdot \frac{d}{dt} \left(\frac{w\hat{a}}{B} \right) \\ & + \left(u\hat{b} + w\hat{c} \right) \cdot \dot{\mathbf{X}} - \Phi_e(\mathbf{X}) - \frac{1}{2}u^2 - \frac{1}{2}w^2 . \end{aligned} \quad (\text{A.10})$$

To proceed, a general property of Lagrangians is applied by the rule that the equations of motions are invariant under the gauge transformation of the form,

$$\mathcal{L} \rightarrow \mathcal{L} + \frac{dS}{dt} .$$

Here, S can be an arbitrary scalar function. This transformation rule will be exploited to simplify the Lagrangian by choosing,

$$S_0 = -\frac{w}{B} \hat{a} \cdot \mathbf{A}(\mathbf{X}) ,$$

which involves all gyro motion terms. In particular, the temporal derivation evaluated at \mathbf{X} yields

$$\frac{dS_0}{dt} = -\mathbf{A}(\mathbf{X}) \cdot \frac{d}{dt} \left(\frac{w\hat{a}}{B} \right) - \frac{w\hat{a}}{B} \cdot \left(\dot{\mathbf{X}} \cdot \nabla \mathbf{A}(\mathbf{X}) \right) ,$$

so that the result of the gauge transformation inserted in (A.10) is given by

$$\begin{aligned} \mathcal{L}_0 = & \frac{1}{\epsilon} \mathbf{A} \cdot \dot{\mathbf{X}} + \frac{w\hat{a}}{B} \cdot \left(\nabla \mathbf{A} \cdot \dot{\mathbf{X}} - \dot{\mathbf{X}} \cdot \nabla \mathbf{A} \right) + w\hat{c} \cdot \dot{\mathbf{X}} + u\hat{b} \cdot \dot{\mathbf{X}} \\ & - \Phi_e - \frac{1}{2}u^2 - \frac{1}{2}w^2 \\ = & \frac{1}{\epsilon} \mathbf{A} \cdot \dot{\mathbf{X}} + \frac{w\hat{a}}{B} \cdot \left(\dot{\mathbf{X}} \times \mathbf{B} \right) + w\hat{a} \times \hat{b} \cdot \dot{\mathbf{X}} + u\hat{b} \cdot \dot{\mathbf{X}} \\ & - \Phi_e - \frac{1}{2}u^2 - \frac{1}{2}w^2 \\ = & \frac{1}{\epsilon} \mathbf{A} \cdot \dot{\mathbf{X}} + u\hat{b} \cdot \dot{\mathbf{X}} - \Phi_e - \frac{1}{2}u^2 - \frac{1}{2}w^2 . \end{aligned} \quad (\text{A.11})$$

It is important to note that oscillatory terms of order $\mathcal{O}(\epsilon)$ have to be inserted in equation (A.9), otherwise the gyro motion terms in the Lagrangian (A.11) would not cancel in zeroth order.

The next term to be considered is the Lagrangian of first order in ϵ written as

$$\begin{aligned} \mathcal{L}_1 = & \left(u\hat{b} + w\hat{c} \right) \cdot \frac{d}{dt} \left(\frac{w\hat{a}}{B} \right) \\ & + \frac{w\hat{a}}{B} \nabla \mathbf{A}(\mathbf{X}) \cdot \frac{d}{dt} \left(\frac{w\hat{a}}{B} \right) - \frac{w\hat{a}}{B} \nabla \Phi_e(\mathbf{X}) . \end{aligned} \quad (\text{A.12})$$

Choosing the scalar function S_1 to be

$$S_1 = -\epsilon \frac{w^2}{2B^2} \hat{\mathbf{a}} \cdot \nabla \mathbf{A} \cdot \hat{\mathbf{a}} ,$$

the temporal derivation is

$$\frac{dS_1}{dt} = -\epsilon \frac{w^2}{2B^2} \left(\frac{d\hat{\mathbf{a}}}{dt} \cdot \nabla \mathbf{A} \cdot \hat{\mathbf{a}} + \hat{\mathbf{a}} \cdot \nabla \mathbf{A} \cdot \frac{d\hat{\mathbf{a}}}{dt} \right) .$$

Following the gauge transformation in phase-space, equation (A.12) becomes

$$\begin{aligned} \mathcal{L}_1 &= w\hat{c} \frac{d}{dt} \left(\frac{w\hat{a}}{B} \right) + \frac{w^2}{B^2} \hat{\mathbf{a}} \nabla \mathbf{A} \cdot \frac{d\hat{\mathbf{a}}}{dt} - \frac{w^2}{2B^2} \left(\frac{d\hat{\mathbf{a}}}{dt} \cdot \nabla \mathbf{A} \cdot \hat{\mathbf{a}} + \hat{\mathbf{a}} \cdot \nabla \mathbf{A} \cdot \frac{d\hat{\mathbf{a}}}{dt} \right) \\ &\quad + u\hat{b} \frac{d}{dt} \left(\frac{w\hat{a}}{B} \right) - \frac{w\hat{a}}{B} \nabla \Phi_e \\ &= \frac{w^2}{B} \hat{c} \frac{d\hat{\mathbf{a}}}{dt} + \frac{w^2}{2B^2} \hat{\mathbf{a}} \nabla \mathbf{A} \cdot \frac{d\hat{\mathbf{a}}}{dt} - \frac{w^2}{2B^2} \left(\frac{d\hat{\mathbf{a}}}{dt} \cdot \nabla \mathbf{A} \cdot \hat{\mathbf{a}} \right) \\ &\quad + u\hat{b} \frac{d}{dt} \left(\frac{w\hat{a}}{B} \right) - \frac{w\hat{a}}{B} \nabla \Phi_e \\ &= \frac{w^2}{B} \hat{c} \frac{d\hat{\mathbf{a}}}{dt} - \frac{w^2}{2B^2} (\nabla \mathbf{A} \cdot \hat{\mathbf{a}} - \hat{\mathbf{a}} \nabla \mathbf{A}) \frac{d\hat{\mathbf{a}}}{dt} \\ &\quad + u\hat{b} \frac{d}{dt} \left(\frac{w\hat{a}}{B} \right) - \frac{w\hat{a}}{B} \nabla \Phi_e \\ &= \frac{w^2}{B} \hat{c} \frac{d\hat{\mathbf{a}}}{dt} - \frac{w^2}{2B^2} (\hat{\mathbf{a}} \times \mathbf{B}) \frac{d\hat{\mathbf{a}}}{dt} + u\hat{b} \frac{d}{dt} \left(\frac{w\hat{a}}{B} \right) - \frac{w\hat{a}}{B} \nabla \Phi_e \\ &= \frac{w^2}{2B} \hat{c} \frac{d\hat{\mathbf{a}}}{dt} + u\hat{b} \frac{d}{dt} \left(\frac{w\hat{a}}{B} \right) - \frac{w\hat{a}}{B} \nabla \Phi_e . \end{aligned}$$

Applying the definitions (A.7) and (A.8) on the first term of the first order Lagrangian leads to

$$\mathcal{L}_1 = \frac{w^2}{2B} \dot{\theta} + u\hat{b} \frac{d}{dt} \left(\frac{w\hat{a}}{B} \right) - \frac{w\hat{a}}{B} \nabla \Phi_e . \quad (\text{A.13})$$

Substituting all results into equation (A.9), the total Lagrangian up to order $\mathcal{O}(\epsilon)$ can be written as

$$\begin{aligned} \mathcal{L} &= \left[\frac{1}{\epsilon} \mathbf{A}(\mathbf{X}) + u\hat{b} + \mathcal{O}(\epsilon) \right] \cdot \dot{\mathbf{X}} + \left[\epsilon \frac{w^2}{2B} + \mathcal{O}(\epsilon^2) \right] \cdot \dot{\theta} \\ &\quad + [\mathcal{O}(\epsilon^2)] \dot{u} + [\mathcal{O}(\epsilon^2)] \dot{w} - \left[\Phi_e(\mathbf{X}) + \frac{1}{2}u^2 + \frac{1}{2}w^2 + \mathcal{O}(\epsilon) \right] . \end{aligned} \quad (\text{A.14})$$

The order of all neglected terms is shown and the Lagrangian only retains terms of $\mathcal{O}(\epsilon^0)$ with one exception. Due to the independence of the Lagrangian on the gyro phase θ , it is stated by Noether's theorem that the quantity

$$\frac{\partial \mathcal{L}}{\partial \theta} = \epsilon \frac{w^2}{2B} = \epsilon \mu \quad (\text{A.15})$$

is a constant, i.e. an invariant of the equations of motion, and is denoted as the magnetic momentum.

To finish the gyro averaging procedure, all variables referring to the particle have to be replaced by the corresponding variables of the guiding centre. In this context, the gyro phase of the particle can be expressed by the gyro phase Ξ of the guiding centre,

$$\theta(\mathbf{x}) = \Xi(\mathbf{X}) + \mathcal{O}(\epsilon) , \quad (\text{A.16})$$

so that the **guiding centre Lagrangian** can be written as

$$\mathcal{L}_{gc} = \frac{1}{\epsilon} \mathbf{A}^* \cdot \dot{\mathbf{X}} + \epsilon \mu \dot{\Xi} - \mathcal{H} \quad (\text{A.17})$$

with the 'modified vector potential' \mathbf{A}^* defined by

$$\mathbf{A}^* = \mathbf{A} + \epsilon U \hat{b} . \quad (\text{A.18})$$

The Hamiltonian \mathcal{H} is expressed as

$$\mathcal{H} = \Phi_e + \mu B + \frac{1}{2} U^2 . \quad (\text{A.19})$$

Note that everything is evaluated at the guiding centre position \mathbf{X} , now. Therefore, every quantity is written in capital letters now. The variables $(U, \mu, \mathbf{X}, \Xi)$ and $(u, w, \mathbf{x}, \theta)$ are equal at least to the lowest order in ϵ .

Derivation of the guiding centre equations of motion

The gyro averaging procedure has supplied a Lagrangian from which the guiding centre equations of motion can easily be derived. The Lagrangian (A.17) is a function of the guiding centre variables $z = (\mathbf{X}, U, \Xi, \mu)$ and their time derivatives $\dot{z} = (\dot{\mathbf{X}}, \dot{\Xi})$. Using the Euler-Lagrange equations,

$$\frac{d}{dt} \left(\frac{\partial \mathcal{L}}{\partial \dot{z}_i} \right) - \frac{\partial \mathcal{L}}{\partial z_i} = 0 , \quad (\text{A.20})$$

and taking $z_i = U, \Xi, \mu$, it follows that

$$U = \hat{b} \cdot \dot{\mathbf{X}} \quad , \quad \dot{\Xi} = \frac{B}{\epsilon} \quad \text{and} \quad \dot{\mu} = 0 . \quad (\text{A.21})$$

This shows again that U is indeed the parallel velocity along the magnetic field, the gyrophase Ξ evolves rapidly and the magnetic moment μ is a constant of motion. Taking $z_i = X_i, i = 1, 2, 3$, we find

$$\mathbf{E}^* + \frac{1}{\epsilon} \dot{\mathbf{X}} \times \mathbf{B}^* = \dot{U} \hat{b} + \mu \nabla B , \quad (\text{A.22})$$

with the modified fields \mathbf{B}^* and \mathbf{E}^* ,

$$\begin{aligned} \mathbf{B}^* &= \nabla \times \mathbf{A}^* = \mathbf{B} + \epsilon U \nabla \times \hat{b} , \\ \mathbf{E}^* &= -\frac{\partial \mathbf{A}^*}{\partial(\epsilon t)} - \nabla \Phi_e = \mathbf{E} - \epsilon U \frac{\partial \hat{b}}{\partial(\epsilon t)} , \end{aligned}$$

Equation (A.22) can be solved for $\dot{\mathbf{X}}$ by crossing with \hat{b} giving

$$\dot{\mathbf{X}} = \frac{1}{B_{\parallel}^*} \left[U \mathbf{B}^* + \epsilon \hat{b} \times (\mu \nabla B - \mathbf{E}^*) \right] . \quad (\text{A.23})$$

Dotting (A.22) with \mathbf{B}^* gives

$$\dot{U} = -\frac{1}{B_{\parallel}^*} \mathbf{B}^* \cdot (\mu \nabla B - \mathbf{E}^*) , \quad (\text{A.24})$$

which is the equation for the parallel acceleration. The quantity B_{\parallel}^* is defined as,

$$B_{\parallel}^* = B + \epsilon U \left(\hat{b} \cdot \nabla \times \hat{b} \right) . \quad (\text{A.25})$$

The equations (A.23) and (A.24) can be further simplified by considering that the velocity of the electrons is fast enough to equal arising macroscale electric fields. So, the resulting equations are

$$\dot{\mathbf{X}} = \frac{1}{B_{\parallel}^*} \left[U \mathbf{B}^* + \epsilon \hat{b} \times \mu \nabla B \right] , \quad (\text{A.26})$$

$$\dot{U} = -\frac{\mu}{B_{\parallel}^*} \mathbf{B}^* \cdot \nabla B , \quad (\text{A.27})$$

with

$$\mathbf{B}^* = \nabla \times \mathbf{A}^* = \mathbf{B} + \epsilon U \nabla \times \hat{\mathbf{b}} , \quad (\text{A.28})$$

$$B_{\parallel}^* = B + \epsilon U \left(\hat{\mathbf{b}} \cdot \nabla \times \hat{\mathbf{b}} \right) . \quad (\text{A.29})$$

The equations (A.26) and (A.27) are the equations of motions derived from the guiding centre Lagrangian (A.17). Although the Lagrangian appears to depend on six phase-space coordinates, only four are independent. This four-dimensional phase-space is called the 'reduced' phase-space and consists of the three components of the spatial location \mathbf{X} and the parallel velocity of the guiding centre, U , along the magnetic field line. The phase-space has reduced due to the fact that the magnetic moment μ is a constant of motion (A.21). The gyrophase Ξ is the coordinate conjugated to μ and therefore it is irrelevant to the guiding motion. The constants of motion are conserved exactly within the guiding centre coordinates and deviate from the constants of motion in real space by an order ϵ .

A.3. Decomposition of the Equations of Motion in the Vacuum

The equations of motion (3.74) use general vector expressions that must be decomposed in co- and contra-variant components explicitly. In this context, a gradient of a value can only be expressed by reciprocal-basis vectors \mathbf{e}^i . Due to axisymmetry, $\partial B / \partial \zeta_v = 0$, the gradient of the magnetic field is given by

$$\nabla B = \frac{\partial B}{\partial s_v} \mathbf{e}^{s_v} + \frac{\partial B}{\partial \theta_v} \mathbf{e}^{\theta_v} . \quad (\text{A.30})$$

The notation of a cross product can be chosen to be

$$\mathbf{F} \times \mathbf{G} = F_i G_j \mathbf{e}^i \times \mathbf{e}^j = \frac{\epsilon^{ijk}}{\sqrt{g(g_{ij})}} F_i G_j \mathbf{e}_k , \quad (\text{A.31})$$

so that all equation terms are expressed by tangent-basis vectors. Then, no additional metric coefficients are used.

The magnetic unity field components are

$$\begin{aligned} \hat{\mathbf{b}} = \frac{\mathbf{B}}{|\mathbf{B}|} &= \frac{B^{s_v}}{B} \mathbf{e}_{s_v} + \frac{B^{\theta_v}}{B} \mathbf{e}_{\theta_v} + \frac{B^{\zeta_v}}{B} \mathbf{e}_{\zeta_v} \\ &= b^{s_v} \mathbf{e}_{s_v} + b^{\theta_v} \mathbf{e}_{\theta_v} + b^{\zeta_v} \mathbf{e}_{\zeta_v} \\ \hat{\mathbf{b}} = \frac{\mathbf{B}}{|\mathbf{B}|} &= \frac{B_{s_v}}{B} \mathbf{e}^{s_v} + \frac{B_{\theta_v}}{B} \mathbf{e}^{\theta_v} + \frac{B_{\zeta_v}}{B} \mathbf{e}^{\zeta_v} \\ &= b_{s_v} \mathbf{e}^{s_v} + b_{\theta_v} \mathbf{e}^{\theta_v} + b_{\zeta_v} \mathbf{e}^{\zeta_v} . \end{aligned}$$

So, the vector expression $\hat{\mathbf{b}} \times \nabla B$ is written as

$$\begin{aligned}
 \hat{b} \times \nabla B &= \begin{pmatrix} b_{s_v} \\ b_{\theta_v} \\ b_{\zeta_v} \end{pmatrix} \times \begin{pmatrix} \frac{\partial B}{\partial s_v} \\ \frac{\partial B}{\partial \theta_v} \\ 0 \end{pmatrix} \\
 &= \frac{1}{\sqrt{g(g_{ij})}} \begin{pmatrix} -b_{\zeta_v} \frac{\partial B}{\partial \theta_v} \\ b_{\zeta_v} \frac{\partial B}{\partial s_v} \\ b_{s_v} \frac{\partial B}{\partial \theta_v} - b_{\theta_v} \frac{\partial B}{\partial s_v} \end{pmatrix}. \tag{A.32}
 \end{aligned}$$

The result is a contravariant representation of the whole vector expression!

Next, $\nabla \times \hat{b}$ has to be expressed using (A.31),

$$\begin{aligned}
 \nabla \times \hat{b} &= \begin{pmatrix} \frac{\partial}{\partial s_v} \\ \frac{\partial}{\partial \theta_v} \\ 0 \end{pmatrix} \times \begin{pmatrix} b_{s_v} \\ b_{\theta_v} \\ b_{\zeta_v} \end{pmatrix} \\
 &= \frac{1}{\sqrt{g(g_{ij})}} \begin{pmatrix} \frac{\partial}{\partial \theta_v} b_{\zeta_v} \\ -\frac{\partial}{\partial s_v} b_{\zeta_v} \\ \frac{\partial}{\partial s_v} b_{\theta_v} - \frac{\partial}{\partial \theta_v} b_{s_v} \end{pmatrix}. \tag{A.33}
 \end{aligned}$$

Furthermore, the rule for a scalar product, $\mathbf{F} \cdot \mathbf{G} = F_i G^i$, is used to decompose the expression in the fourth term, $K = \hat{b} \cdot \nabla \times \hat{b}$. The curl term components are the contravariant ones and $\sqrt{g(g_{ij})} = J$ so that

$$\begin{aligned}
 \hat{b} \cdot \nabla \times \hat{b} &= \begin{pmatrix} b_{s_v} \\ b_{\theta_v} \\ b_{\zeta_v} \end{pmatrix} \cdot \frac{1}{J} \begin{pmatrix} \frac{\partial}{\partial \theta_v} b_{\zeta_v} \\ -\frac{\partial}{\partial s_v} b_{\zeta_v} \\ \frac{\partial}{\partial s_v} b_{\theta_v} - \frac{\partial}{\partial \theta_v} b_{s_v} \end{pmatrix} \\
 &= \frac{1}{J} \left[b_{s_v} \frac{\partial b_{\zeta_v}}{\partial \theta_v} - b_{\theta_v} \frac{\partial b_{\zeta_v}}{\partial s_v} + b_{\zeta_v} \left(\frac{\partial b_{\theta_v}}{\partial s_v} - \frac{\partial b_{s_v}}{\partial \theta_v} \right) \right] = K.
 \end{aligned}$$

Decomposing the vector \mathbf{B}^* , the use of the contravariant representation due to $\nabla \times \hat{b}$ is advantageous leading to

$$\mathbf{B}^* = \mathbf{B} + \epsilon U \nabla \times \hat{b} = \begin{pmatrix} B^{s_v} \\ B^{\theta_v} \\ B^{\zeta_v} \end{pmatrix} + \frac{\epsilon U}{J} \begin{pmatrix} \frac{\partial}{\partial \theta_v} b_{\zeta_v} \\ -\frac{\partial}{\partial s_v} b_{\zeta_v} \\ \frac{\partial}{\partial s_v} b_{\theta_v} - \frac{\partial}{\partial \theta_v} b_{s_v} \end{pmatrix}.$$

Recalling the equations of motion (3.69) and (3.74), it can be seen that every term has been decomposed.

The next step is to remove the ordering parameter ϵ and recover the physical constants.

The modified magnetic field B_{\parallel}^* is

$$B_{\parallel}^* = B + \frac{mv_{\parallel}}{qce}K = B + \frac{v_{\parallel}B}{\omega_c}K = B + \rho_{\parallel}BK = B(1 + \rho_{\parallel}K)$$

and

$$\mathbf{B}^* = \mathbf{B} + \frac{mv_{\parallel}}{qce}\nabla \times \hat{b} = \mathbf{B} + \frac{v_{\parallel}B}{\omega_c}\nabla \times \hat{b} = \mathbf{B} + \rho_{\parallel}B\nabla \times \hat{b}.$$

So, the equation of the parallel velocity is simplified to

$$\begin{aligned} \dot{v}_{\parallel} &= -\frac{\mu}{mB(1 + \rho_{\parallel}K)} \left(\mathbf{B} + \rho_{\parallel}B\nabla \times \hat{b} \right) \cdot \nabla B \\ &= -\frac{\mu}{m(1 + \rho_{\parallel}K)} \left(\hat{b} + \rho_{\parallel}\nabla \times \hat{b} \right) \cdot \nabla B \\ &= C_{\parallel} \left(\hat{b} + \rho_{\parallel}\nabla \times \hat{b} \right) \cdot \nabla B \end{aligned} \quad (\text{A.34})$$

with

$$C_{\parallel} = -\frac{\mu}{m(1 + \rho_{\parallel}K)}. \quad (\text{A.35})$$

The spatial equations of motion are written as

$$\begin{aligned} \dot{\mathbf{X}} &= U\hat{b} + \frac{\epsilon\mu}{B_{\parallel}^*}\hat{b} \times \nabla B + \frac{\epsilon U^2}{B_{\parallel}^*} \left(\nabla \times \hat{b} - K\hat{b} \right) \\ \mathbf{v} &= v_{\parallel}\hat{b} + \frac{\mu}{qceB(1 + \rho_{\parallel}K)}\hat{b} \times \nabla B \\ &\quad + \frac{mv_{\parallel}^2}{qceB(1 + \rho_{\parallel}K)} \left(\nabla \times \hat{b} - K\hat{b} \right) \\ &= C_1\hat{b} + C_2\hat{b} \times \nabla B + C_3 \left(\nabla \times \hat{b} - K\hat{b} \right) \end{aligned} \quad (\text{A.36})$$

with

$$C_1 = v_{\parallel} = \rho_{\parallel}\omega_c \quad (\text{A.37})$$

$$C_2 = \frac{\mu}{qceB(1 + \rho_{\parallel}K)} \quad (\text{A.38})$$

$$C_3 = \frac{mv_{\parallel}^2}{qceB(1 + \rho_{\parallel}K)} = \frac{v_{\parallel}^2}{\omega_c(1 + \rho_{\parallel}K)} = \frac{\omega_c\rho_{\parallel}^2}{(1 + \rho_{\parallel}K)}. \quad (\text{A.39})$$

Substituting all vector expressions, equation (A.36) is expressed by

$$\begin{aligned}
\mathbf{v} &= v^s \mathbf{e}_{s_v} + v^{\theta_v} \mathbf{e}_{\theta_v} + v^{\zeta_v} \mathbf{e}_{\zeta_v} \\
&= C_1 \left(b^{s_v} \mathbf{e}_{s_v} + b^{\theta_v} \mathbf{e}_{\theta_v} + b^{\zeta_v} \mathbf{e}_{\zeta_v} \right) \\
&\quad + \frac{C_2}{J} \left[-b_{\zeta_v} \frac{\partial B}{\partial \theta_v} \mathbf{e}_{s_v} + b_{\zeta_v} \frac{\partial B}{\partial s_v} \mathbf{e}_{\theta_v} + \left(b_{s_v} \frac{\partial B}{\partial \theta_v} - b_{\theta_v} \frac{\partial B}{\partial s_v} \right) \mathbf{e}_{\zeta_v} \right] \\
&\quad + \frac{C_3}{J} \left[\frac{\partial b_{\zeta_v}}{\partial \theta_v} \mathbf{e}_{s_v} - \frac{\partial b_{\zeta_v}}{\partial s_v} \mathbf{e}_{\theta_v} + \left(\frac{\partial b_{\theta_v}}{\partial s_v} - \frac{\partial b_{s_v}}{\partial \theta_v} \right) \mathbf{e}_{\zeta_v} \right] \\
&\quad - C_3 K \left(b^{s_v} \mathbf{e}_{s_v} + b^{\theta_v} \mathbf{e}_{\theta_v} + b^{\zeta_v} \mathbf{e}_{\zeta_v} \right)
\end{aligned}$$

Decomposing the vector equation into the three guiding centre coordinates, it follows

$$v^{s_v} = (C_1 - C_3 K) b^{s_v} - \frac{C_2}{J} \cdot b_{\zeta_v} \frac{\partial B}{\partial \theta_v} + \frac{C_3}{J} \frac{\partial b_{\zeta_v}}{\partial \theta_v} \quad (\text{A.40})$$

$$v^{\theta_v} = (C_1 - C_3 K) b^{\theta_v} + \frac{C_2}{J} \cdot b_{\zeta_v} \frac{\partial B}{\partial s_v} - \frac{C_3}{J} \frac{\partial b_{\zeta_v}}{\partial s_v} \quad (\text{A.41})$$

$$\begin{aligned}
v^{\zeta_v} &= (C_1 - C_3 K) b^{\zeta_v} + \frac{C_2}{J} \cdot \left(b_{s_v} \frac{\partial B}{\partial \theta_v} - b_{\theta_v} \frac{\partial B}{\partial s_v} \right) \\
&\quad + \frac{C_3}{J} \left(\frac{\partial b_{\theta_v}}{\partial s_v} - \frac{\partial b_{s_v}}{\partial \theta_v} \right). \quad (\text{A.42})
\end{aligned}$$

The parallel guiding centre velocity is simplified to

$$\begin{aligned}
\dot{v}_{\parallel} &= C_{\parallel} \left(\hat{\mathbf{b}} + \rho_{\parallel} \nabla \times \hat{\mathbf{b}} \right) \cdot \nabla B \\
&= C_{\parallel} \left[\left(b^{s_v} + \frac{\rho_{\parallel}}{J} \frac{\partial}{\partial \theta_v} b_{\zeta_v} \right) \frac{\partial B}{\partial s_v} + \left(b^{\theta_v} - \frac{\rho_{\parallel}}{J} \frac{\partial}{\partial s_v} b_{\zeta_v} \right) \frac{\partial B}{\partial \theta_v} \right]. \quad (\text{A.43})
\end{aligned}$$

However, this formula shall be expressed in terms of the parallel gyro radius so that the final derivative looks like

$$\begin{aligned}
\frac{d\rho_{\parallel}}{dt} &= \frac{d}{dt} \left(\frac{v_{\parallel}}{\omega_c} \right) = \frac{1}{\omega_c} \frac{dv_{\parallel}}{dt} - \frac{v_{\parallel}}{\omega_c^2} \frac{d\omega_c}{dt} \\
&= \frac{1}{\omega_c} \left[\frac{dv_{\parallel}}{dt} - \rho_{\parallel} \frac{q_c e}{m} \left(\frac{\partial B}{\partial t} + \mathbf{v} \cdot \nabla B \right) \right] \\
&= \frac{1}{\omega_c} \left[\dot{v}_{\parallel} - \rho_{\parallel} \frac{q_c e}{m} \left(v^{s_v} \frac{\partial B}{\partial s_v} + v^{\theta_v} \frac{\partial B}{\partial \theta_v} \right) \right]. \quad (\text{A.44})
\end{aligned}$$

B. Nomenclature

β	Plasma parameter $\beta = 2\mu_0 p / B_0^2$
β_f	Fast particle beta $\beta = 2\mu_0 p_f / B_0^2$
δ	Perturbation; measure for non-orthogonality in the Boozer coordinate system
ϵ	Inverse aspect ratio $\epsilon = r_0 / R_0$; Adiabatic ordering parameter
ϵ_0	Dielectric constant
γ	Adiabatic index; Growth rate
κ	Magnetic curvature
\mathcal{H}	Hamiltonian
\mathcal{L}	Lagrangian
μ	Magnetic moment
ω	Frequency
ω_0	Gyro frequency at the magnetic axis
ω_A	Frequency of the Alfvén continuum
ω_b	Bounce frequency of trapped particles
ω_c	Cyclotron or gyro frequency
ω_{TAE}	TAE frequency
ω_{po}	Poloidal orbit frequency
ω_{tp}	Toroidal precession frequency
ϕ	Cylindrical coordinate
Φ_e	Electric potential
ψ	Toroidal flux label $\psi = \Psi_{\text{tor}} / 2\pi$; radial coordinate
Ψ_{pol}^*	Adapted poloidal flux
ψ_i	Intersection surface between Boozer and vacuum coordinate system
ψ_p	Poloidal flux label $\psi_p = \Psi_{\text{pol}} / 2\pi$; radial coordinate
$\psi_p(a)$	Poloidal flux label at the last close flux surface
Ψ_{pol}	Poloidal flux
Ψ_{tor}	Toroidal flux
ψ_v	Radial coordinate in the vacuum coordinate system
ρ	Mass density of the plasma
ρ_{\perp}	Gyro radius of a charged particles
σ_k	Phase of the amplitude term for the k -th wave
θ	Poloidal coordinate
θ_v	Poloidal coordinate in the vacuum coordinate system
$\tilde{\alpha}$	Scaling factor of the perturbed vector potential
$\tilde{\Phi}$	Perturbed scalar potential
$\tilde{\phi}_{km}$	Poloidal Eigenfunction (m) of the scalar potential for a wave k
$\tilde{\mathbf{A}}$	Perturbed vector potential
\mathbf{A}	Vector potential
\mathbf{A}^*	Modified vector potential
\mathbf{b}	Magnetic unit vector $\mathbf{b} = \mathbf{B} / B $

ξ	Eigenfunction; Gyro-phase
ζ	Toroidal coordinate
ζ_v	Toroidal coordinate in the vacuum coordinate system
a	Index of the last closed flux surface
A_k	Amplitude of the k -th wave
B	Magnetic field
B_{mag}	Magnetic field at the magnetic axis
B_{pol}	Poloidal magnetic field
B_{tor}	Toroidal magnetic field
E	Electric field; Energy
e	Electron; Electric charge
E_k	Wave energy of the k -th wave
J	Jacobian of the Boozer coordinate system
j	Current density
J_v	Jacobian of the vacuum coordinate system
k	Wave number
k_{\parallel}	Parallel wave number
k_{\perp}	Perpendicular wave number
m	Poloidal mode number
m_e	Electron mass
m_i	Ion mass
n	Toroidal mode number
n_0	Total number of fast particles
n_e	Electron particle density
n_i	Ion particle density
P	Power transfer $P = \partial E / \partial t$
p	Plasma pressure; Proton; Bounce harmonic
q	Safety factor
q_0	Value of the q -profile at the magnetic axis
q_{min}	Minimal value of an inverted q -profile
R	Cylindrical coordinate
r	Radial cylindrical coordinate
R_0	Major radius
r_0	Minor radius
R_{mag}	Magnetic axis
s	Normalized radial coordinate $s = \sqrt{\psi_p / \psi_p(a)}$
T	Plasma temperature
t	Zeit
T_e	Electron temperature
T_i	Ion temperature
v	Velocity
v_A	Alfvén velocity
v_S	Sound velocity
v_{\parallel}	Parallel particle velocity
v_{\perp}	Perpendicular particle velocity
x	Spatial coordinate
z	Cylindrical coordinate

C. Acronyms

ASDEX Axialsymmetric Divertor Experiment (Garching, Germany)

BAE Beta-induced Alfvén Eigenmode

ECE Electron Cyclotron Emission

FLR Finite Larmor Radius

HAGIS Hamiltonian Guiding Centre System code

ICRH Ion Cyclotron Resonance Heating

ITER International Thermonuclear Experiment Reactor (Cadarache, France)

JET Joint European Torus (Culham, England)

MHD Magnetohydrodynamic

NBI Neutral Beam Injection

NTM Neoclassical Tearing Mode

TAE Toroidicity-induced Alfvén Eigenmode

Bibliography

- [1] J. D. Lawson. Proc. Roy. Soc. B **70**, 6 (1958).
- [2] J. Wesson. Tokamaks. Clarendon Press, Oxford (2004).
- [3] A. Yoshizawa, S. I. Itoh, and K. Itoh. Plasma and Fluid Turbulence: Theory and Modelling. Taylor & Francis Group (2003).
- [4] E. Strumberger, S. Günter, E. Schwarz, C. Tichmann, *et al.*. New J. Phys. **10**, 023017 (2008).
- [5] H. Alfvén. Ark. Mat. Astron. Fys. **27A**, 1 (1940).
- [6] C. Z. Cheng, L. Chen, and M. S. Chance. Ann. Phys. **161** (1985).
- [7] A. D. Turnbull, E. J. Strait, W. W. Heidbrink, M. S. Chu, *et al.*. Phys. Fluids B **5**, 2546 (1993).
- [8] M. N. Rosenbluth and P. H. Rutherford. Phys. Rev. Lett. **34**, 1428 (1975).
- [9] H. H. Duong, W. W. Heidbrink, E. J. Strait, T. W. Petrie, *et al.*. Nucl. Fusion **33**, 749 (1993).
- [10] J. P. Freidberg. Ideal Magnetohydrodynamics. Plenum Press, New York (1987).
- [11] A. I. Morozov and L. S. Solov'ev. Reviews of Plasma Physics 2. Consultant Bureau, New York (1966).
- [12] S. D. Pinches. Nonlinear Interaction of Fast Particles with Alfvén Waves in Tokamaks. Ph.D. thesis, University of Nottingham, Nottingham (1996).
- [13] S. D. Pinches, L. C. Appel, J. Candy, S. E. Sharapov, *et al.*. C. Ph. Comm. **110**, 133 (1998).
- [14] T. Tajima and F. W. Perkins. In: Proceedings of the 1983 Sherwood Theory Meeting. University of Maryland, Arlington, VA (1983).
- [15] B. N. Breizman, H. L. Berk, and H. Ye. Phys. Fluids B **5**, 3217 (1993).
- [16] H. L. Berk, B. N. Breizman, and M. Pekker. Phys. Plasmas **2**, 3007 (1995).
- [17] M. García-Muñoz, H.-U. Fahrbach, S. Günter, V. Igochine, *et al.*. Phys. Rev. Letters **100**, 055005 (2008).
- [18] M. García-Muñoz. Fast Response Scintillator Based Detector for MHD Induced Energetic Ion Losses in ASDEX Upgrade. Ph.D. thesis, Ludwig-Maximilians-Universität München, Garching (2006).

- [19] O. Gruber, M. Kaufmann, W. Köppendörfer, K. Lackner, *et al.*. J. Nucl. Mater. **121**, 407 (1984).
- [20] W. D. D'haeseleer, W. N. G. Hitchon, J. D. Callen, and J. L. Shohet. Flux Coordinates and Magnetic Field Structure: A Guide to a Fundamental Tool of Plasma Theory. Springer-Verlag, Berlin (1991).
- [21] R. D. Hazeltine and J. D. Meiss. Plasma Confinement. Addison-Wesley Publishing Company, Redwood City, California (1992).
- [22] G. T. A. Huysmans, J. P. Goedbloed, and W. Kerner. In: Conf. on Computational Physics Proc. World Scientific, Singapore (1990).
- [23] I. B. Bernstein, E. A. Frieman, M. D. Kruskal, and R. M. Kulsrud. Proc. Roy. Soc. A **244**, 17 (1958).
- [24] A. V. Timofeev. In: Rev. Plasma Physics, volume 9. Consultants Bureau (1965).
- [25] G. Y. Fu and J. W. Van Dam. Phys. Fluids B **1**, 1949 (1989).
- [26] C. Cheng and M. S. Chance. Phys. Fluids **29**, 3695 (1986).
- [27] B. N. Breizman, M. S. Pekker, S. E. Sharapov, and J. E. contributors. Phys. Plasmas **12** (2005).
- [28] F. Zonca, L. Chen, and R. A. Santoro. Plasma Phys. Control. Fusion **38**, 2011 (1996).
- [29] P. Lauber, M. Brüdgam, D. Curran, V. Igochine, *et al.*. Plasma Phys. Controlled Fusion **51**, 124009 (2009).
- [30] W. W. Heidbrink, E. J. Strait, M. S. Chu, and A. D. Turnbull. Phys. Rev. Letters **71**, 855 (1993).
- [31] H. L. Berk, J. W. Van Dam, Z. Guo, and D. M. Lindberg. Phys. Fluids B **4**, 1806 (1992).
- [32] F. Zonca and L. Chen. Phys. Rev. Lett. **68**, 592 (1992).
- [33] J. Candy. Plasma Phys. Control. Fusion **38**, 795 (1996).
- [34] B. N. Breizman and S. E. Sharapov. Plasma Phys. Controlled Fusion **37**, 1057 (1995).
- [35] R. Mett and S. M. Mahajan. Phys. Fluids B **4**, 2885 (1992).
- [36] S. D. Pinches, V. G. Kiptily, S. E. Sharapov, D. S. Darrow, *et al.*. Nucl. Fusion **46**, S904 (2006).
- [37] H. L. Berk, B. N. Breizman, and H. Ye. Phys. Letters A **162**, 475 (1992).
- [38] E. Carolipio. Nucl. Fusion **42**, 853 (2002).
- [39] E. Poli, M. García-Muñoz, H.-U. Fahrbach, S. Günter, *et al.*. Phys. Plasmas **15**, 032501 (2008).

- [40] P. H. Rutherford. *Phys. Fluids* **16**, 1903 (1973).
- [41] J. P. Meskat. Untersuchung der Struktur und Dynamik magnetischer Inseln im Tokamak ASDEX Upgrade. Ph.D. thesis, Universität Stuttgart, Stuttgart (2001).
- [42] J. D. Jackson. *Classical Electrodynamics*. Wiley (1999).
- [43] L. D. Landau and E. M. Lifschitz. *The Classical Theory of Fields*. Pergamon Press, Oxford (1975).
- [44] R. G. Littlejohn. *J. Math. Phys.* **23**, 742 (1982).
- [45] R. Bilato. Private communication.
- [46] T. H. Stix. *Waves in Plasmas*. American Institute of Physics, New York (1992).
- [47] G. G. Lister. A fully 3-dneutral beam injection code using monte carlo methods. Technical report, Max-Planck-Institut für Plasmaphysik (1985).
- [48] G. Tardini. Private communication.
- [49] R. B. White and M. S. Chance. *Phys. Fluids* **27**, 2455 (1984).
- [50] W. Kerner, S. Poedts, J. P. Goedbloed, G. T. A. Huysmans, *et al.*. In: Proc. 18th European Conference on Controlled Fusion and Plasma Physics. EPS, Berlin (1991).
- [51] A. H. Boozer. *Phys. Fluids* **23**, 904 (1980).
- [52] J. M. Greene. *Commun. Pure Appl. Math* **36**, 537 (1983).
- [53] R. G. Littlejohn. *J. Plasma Phys.* **29**, 111 (1983).
- [54] J. Denavit and J. M. Walsh. *Plasma Phys. Controlled Fusion* **6**, 209 (1981).
- [55] A. M. Dimits and W. W. Lee. *J. Comput. Phys.* **107**, 309 (1993).
- [56] G. Hu and J. A. Krommes. *Phys. Plasmas* **1**, 863 (1994).
- [57] J. Candy, D. Borba, H. L. Berk, G. T. A. Huysmans, *et al.*. *Phys. Plasmas* **4**, 2597 (1997).
- [58] P. J. McCarthy. *Phys. Plasmas* **6**, 3554 (1999).
- [59] W. Schneider. Private communication.
- [60] R. G. Littlejohn. *Phys. Fluids* **24**, 1730 (1981).
- [61] T. G. Northrop and J. A. Rome. *Phys. Fluids* **21**, 384 (1978).
- [62] A. Mueck. Study of the Sawtooth Instability and its Control in the ASDEX Upgrade Tokamak. Ph.D. thesis, Technische Universität München, München (2004).
- [63] V. Igochine, S. Günter, M. Maraschek, and the ASDEX Upgrade. *Nucl. Fusion* **43**, 1801 (2003).

- [64] J. D. Gaffey. *J. Plasma Phys.* **16**, 149 (1976).
- [65] W. W. Heidbrink, M. A. Van Zeeland, M. E. Austin, K. H. Burrell, *et al.*. *Nucl. Fusion* **48**, 084001 (2008).
- [66] S. D. Pinches. In: 9th IAEA Technical Meeting on Energetic Particles, Japan (2005).
- [67] P. Lauber, M. Brüdgam, D. Curran, V. Igochine, *et al.*. In: 36th Conference on Plasma Phys. Sofia (2009).
- [68] P. Lauber. Linear Gyrokinetic Description of Fast Particle Effects on the MHD Stability in Tokamaks. Ph.D. thesis, Technische Universität München, Garching (2003).
- [69] D. J. Sigmar, C. T. Hsu, R. B. White, and C. Z. Cheng. *Phys. Fluids B* **6**, 1506 (1992).
- [70] C. T. Hsu and D. J. Sigmar. *Phys. Fluids B* **6**, 1492 (1992).
- [71] L. Chen and F. Zonca. *Nucl. Fusion* **47**, S727 (2007).
- [72] F. Ryter, E. Poli, M. Brüdgam, M. Maraschek, *et al.*. (to be submitted) (2010).
- [73] E. Poli, M. Brüdgam, F. Ryter, M. Siccino, *et al.*. In: 13th European Fusion Theory Conference (2009).

Publications and Conference Presentations

Conference Presentations

'EXTENSION OF HAGIS INTO THE REGION BETWEEN LAST CLOSED FLUX SURFACE AND FIRST WALL' (Poster)

M. Brüdgam and Ph. Lauber

10th IAEA Technical Meeting on Energetic Particles in Magnetic Confinement Systems, Kloster Seeon (2007)

'THE SYNTHETIC FAST-ION LOSS DETECTOR' (Poster)

M. Brüdgam, Ph. Lauber, M. García-Muñoz, S. Günter and ASDEX Upgrade Team

11th IAEA Technical Meeting on Energetic Particles in Magnetic Confinement Systems, Kiev (2009)

Publications

'NONLINEAR SIMULATION OF FAST PARTICLES BEYOND THE SEPARATRIX AT ASDEX UPGRADE'

M. Brüdgam, Ph. Lauber, M. García-Muñoz and S. Günter

Physics of Plasmas (submitted)

'EVIDENCE OF LOCAL DEPLETION OF THE FAST ION POPULATION BY TEARING MODES IN TOKAMAKS'

F. Ryter, E. Poli, M. Brüdgam, M. Maraschek, G. Tardini and ASDEX Upgrade Team

Physical Review Letters (to be submitted)

'PHASE-SPACE OF CONVECTIVE AND DIFFUSIVE ENERGETIC PARTICLE LOSSES INDUCED BY SHEAR ALFVÉN WAVES IN THE ASDEX UPGRADE'

M. García-Muñoz, N. Hicks, R. van Voornveld, I. G. J. Classen, R. Bilato, V. Bobkov, M. Brüdgam, H.-U. Fahrbach, V. Igochine, S. Jamsae, M. Maraschek, K. Sassenberg and the ASDEX Upgrade Team

Nuclear Fusion (to be submitted)

'KINETIC ALFVÉN EIGENMODES AT ASDEX UPGRADE'

Ph. Lauber, M. Brüdgam, D. Curran, V. Igochine, K. Sassenberg, S. Günter, M. Maraschek, M. García-Muñoz, N. Hicks and the ASDEX Upgrade Team

Plasma Physics and Controlled Fusion, **51**, 124009 (2009)

'REDISTRIBUTION OF BEAM IONS IN THE PRESENCE OF A MAGNETIC ISLAND'

E. Poli, M. Brüdgam, F. Ryter, M. Siccino, G. Tardini and ASDEX Upgrade Team
Proceedings of the 13th EFTC Conference, Riga (2009)

'MHD INDUCED FAST-ION LOSSES ON ASDEX UPGRADE'

M. García-Muñoz, H.-U. Fahrbach, S. D. Pinches, V. Bobkov, M. Brüdgam, M. Gobbin, S. Günter, V. Igochine, Ph. Lauber, M. J. Mantsinen, M. Maraschek, L. Marrelli, P. Martin, P. Piovesan, E. Poli, K. Sassenberg, G. Tardini, H. Zohm and the ASDEX Upgrade Team
Nuclear Fusion **49**, 085014 (2009)

'FAST PARTICLE DRIVEN MODES AT ASDEX-UPGRADE'

Ph. Lauber, M. Brüdgam, H. L. Berk, S. Günter, M. García-Muñoz, V. Igochine, M. Maraschek and the ASDEX-Upgrade Team
Proceedings of the 35th Conference on Plasma Physics (EPS), Hersonissos, **32D** (2008)

'OBSERVATION AND MODELLING OF FAST-ION LOSSES DUE TO HIGH FREQUENCY MHD INSTABILITIES IN THE ASDEX UPGRADE TOKAMAK'

M. García-Muñoz, M. Brüdgam, S. Günter, V. Igochine, Ph. Lauber, M. J. Mantsinen, M. Maraschek, P. Martin, S. D. Pinches, P. Piovesan, K. Sassenberg, H. Zohm and the ASDEX Upgrade Team
Proceedings of the 35th Conference on Plasma Physics (EPS), Hersonissos, **32D** (2008)

Acknowledgements

Zuallerst gilt mein Dank meinem direkten Betreuer Dr. Philipp Lauber. Mit seinen weitreichenden Kenntnissen in und seinem Enthusiasmus für die Plasmaphysik hat er mir stets geholfen. Er ließ mir geduldig alle Freiräume, um 'Spielereien' im Code auszutesten und zeigte mir die Richtung auf, wenn ich abschweifte. Ich hätte mir keine bessere Betreuung sowohl im fachlichen als auch sozialen Bereich vorstellen können.

Ein großer Dank gilt auch meiner Doktormutter Prof. Sibylle Günter. In Gesprächen und physikalischen Diskussionen war sie mir ein sehr große Hilfe. Sie gab mir die Möglichkeit, frei zu arbeiten und nach Culham zu fahren, um neue Erfahrungen zu sammeln. Außerdem möchte ich mich für das Korrekturlesen meiner Arbeit bedanken.

Vielen Dank auch an Emanuele Poli. Er beantwortete immer meine Fragen in bezug auf physikalische Probleme. Durch seine gute Laune und seine scheinbar unendliche Geduld ging ich immer fröhlich aus seinem Büro.

Bedanken möchte ich mich auch bei Manuel García-Muñoz, der mich in die experimentellen Aspekte der Plasmaphysik einweihte. Die reibungsbehaftete Zusammenarbeit erlaubten es mir, die Vorstellungen von Experimentatoren und Theoretikern besser zu verstehen.

Für die angenehme Zeit in Culham möchte ich mich bei Simon Pinches und Lynton Appel bedanken, die sich mit meiner Thematik auseinander setzten und nach Fehlern abklopften. Besonders Simon bin ich für die Hilfe in Computerfragen und der Beantwortung meiner Mails zum Verständnis des Codes dankbar.

Große Inspirationsquellen waren mir durch ihre Begeisterung auf ihren jeweiligen physikalischen Gebieten Prof. Karl Lackner, Prof. Frank Jenko und Bruce Scott.

Außerdem möchte ich mich noch bei den vielen Personen in der TOK-Gruppe bedanken, die mir auf vielfältige Weise geholfen haben. Besonders herausheben möchte ich dabei Erika Strumberger, Wolfgang Schneider, Christian Konz und David Coster.

Besonders lieb möchte ich mich bei Anja Bauer bedanken, die die Bürokratie so gut wie irgend möglich von mir ferngehalten hat. Wenn ich dann doch mal ein Problem hatte, hat sie es gelöst.

Außerdem bedanke ich mich bei Klaus Reuter und Matthias Hölzl für kleinere und größere Hilfen zu Computerfragen und für die Kantinengespräche.

Besonders bedanken möchte ich mich bei Christian Wigger. Geduldig hörte er sich viele physikalische Probleme von mir an und half mir, sie zu lösen. Seine gute Laune und die Freude am Erörtern des Weltgeschehens machten ihn zum idealen Bürokollegen.

Mein letzter Dank gilt meiner Freundin Franziska. Sie sorgte dafür, dass ich in dieser arbeitsreichen Zeit Entspannung fand und baute mich in schwierigen Zeiten wieder auf. Durch ihr Verständnis und ihre Liebe war es überhaupt erst möglich, diese Arbeit zu schreiben.